Advanced diffusion-weighted MRI of breast cancer: response to neoadjuvant chemotherapy and correlation with dynamic contrast-enhanced MRI

Zyad Mansour M. Almutlaq

Submitted in accordance with the requirements for the degree of
Doctorate in Philosophy

The University of Leeds

Faculty of Medicine and Health
Leeds Institute of Cardiovascular and Metabolic Medicine
School of Medicine

November 2024

Intellectual Property and Publication Statement

Acknowledgements

First and foremost, I would like to express my deepest gratitude to my supervisors, Prof. David Buckley, Dr. Daniel Wilson, and Dr. Tatendashe Dondo, for their invaluable guidance, time, and expertise, which enriched me on an academic level and improved my research skills to carry out this work.

A special thanks goes to Prof. David, who dedicated part of his time to addressing my questions, accommodating my meeting requests promptly, and sharing his valuable expertise with remarkable generosity. I am especially grateful to him for performing the quantitative DCE-MRI analysis presented in Chapter 6. His unwavering encouragement and guidance throughout this journey have been truly inspiring. It has been an honour to work under his mentorship, which provided me with a role model to learn from. Prof. David, words cannot adequately convey the depth of my gratitude.

Dr. Daniel, I am sincerely grateful for your warm hospitality during my time at St James's University Hospital. Your kindness in providing me with office space next to yours and supporting my work on the images was greatly appreciated. I am also profoundly thankful to Mrs. Sarah Bacon for her instrumental assistance in developing the programming code I used in my image analysis for this research. Thank you so much, Mrs. Sarah, for your contribution, which made the image analysis process more rigorous and smoother. I wish you every success and fulfilment in your new career.

To my family, I extend my heartfelt thanks for their unwavering support and encouragement over these years. Living abroad was not easy for any of us, but your love and steadfast backing helped bridge the distance and made the challenges more bearable. To my mother, my constant pillar of strength, thank you for enduring my absence with patience and for your endless support, motivation, and optimism. Your words of encouragement lit my path during moments of fatigue and doubt. I am equally grateful to Bero, who stood by me like a shadow throughout this journey. Your encouragement, advice, and shared joyful moments, and comfort during tough times meant a lot to me. I wish you every success and happiness in your future.

I am also deeply thankful to King Saud bin Abdulaziz University for Health Sciences for granting me this opportunity and providing financial support to study

at the University of Leeds and undertake this research. The experience I have gained has been truly invaluable and I am eager to share it upon my return.

Finally, and most importantly, I dedicate this work to my late father, Eng. Mansour Al Mutlaq, my role model and source of inspiration. May God have mercy on him. I wish you were here to share in the joy of completing this thesis. Your words of encouragement and faith in my potential laid the foundation for reaching this point.

Publications and presentations

Derivations of this work have been published in the following citations:

Almutlaq, Z.M., Wilson, D.J., Bacon, S.E., Sharma, N., Stephens, S., Dondo, T. and Buckley, D.L., 2022. Evaluation of Monoexponential, Stretched-Exponential and Intravoxel Incoherent Motion MRI Diffusion Models in Early Response Monitoring to Neoadjuvant Chemotherapy in Patients With Breast Cancer—A Preliminary Study. Journal of Magnetic Resonance Imaging, 56(4), pp.1079-1088.

This work represents an earlier version of Chapter 4. The candidate (Almutlaq, Z.M.) conducted the image analysis, statistical analyses, and drafted the original manuscript under the supervision of Wilson, D.J., Dondo, T., and Buckley, D.L. The image analyses were performed using MATLAB codes written by Bacon, S.E. Tumour delineations on the MRI images were defined by Sharma, N. Stephens, S. seeded the tumour, blinded to the candidate (Almutlaq, Z.M.), for the purpose of agreement analysis. All authors contributed to editing the final draft.

Almutlaq, Z.M., Bacon, S.E., Wilson, D.J., Sharma, N., Dondo, T. and Buckley, D.L., 2024. The relationship between parameters measured using intravoxel incoherent motion and dynamic contrast-enhanced MRI in patients with breast cancer undergoing neoadjuvant chemotherapy: a longitudinal cohort study. Frontiers in Oncology, 14, p.1356173.

This work includes portions of Chapter 3 and the entirety of Chapter 6. The candidate (Almutlaq, Z.M.) conducted the simulation experiments (in part, Chapter 3), image analysis, statistical analyses, and drafted the original manuscript under the supervision of Wilson, D.J., Dondo, T., and Buckley, D.L. The image analyses were performed using MATLAB codes written by Bacon, S.E. Tumour delineations on the MRI images were defined by Sharma, N. The quantitative DCE-MRI analysis was conducted entirely by Buckley, D.L. All authors contributed to editing the final draft.

Scientific meetings

Derivations of this work have been disseminated through poster presentations at:

The International Society for Magnetic Resonance in Medicine (ISMRM) Annual Meeting & Exhibition. 03 June 2023; Toronto, Canda

Almutlaq, Z.M., Bacon, S.E., Wilson, D.J., Sharma, N. and Buckley, D.L. "Does intravoxel incoherent motion MRI measure tumour perfusion? A comparison with DCE-MRI in patients with breast cancer."

ISMRM Workshop on Moving Forward with Intravoxel Incoherent Motion Modeling for Diffusion-Weighted MRI: An Attempt at Consensus. 26 March 2024; Erlangen, Germany

Almutlaq, Z.M., Bacon, S.E., Wilson, D.J., Dondo, T. and Buckley, D.L. "Evaluation of the effect of fitting algorithm on the bias and precision of IVIM parameters in breast cancer: a simulation study."

Almutlaq, Z.M., Bacon, S.E., Wilson, D.J., Sharma, N., Dondo, T. and Buckley, D.L. "The relationship between parameters measured using intravoxel incoherent motion and dynamic contrast-enhanced MRI in patients with breast cancer undergoing neoadjuvant chemotherapy: a longitudinal cohort study"

Abstract

Background

Previous studies showed promising applications of intravoxel incoherent motion (IVIM) and stretched-exponential (SEM) models of diffusion-weighted imaging (DWI) in breast imaging; however, their ability to predict early breast cancer response to neoadjuvant chemotherapy (NACT) was minimally investigated.

Aims

To evaluate accuracy, bias, precision, and in-vivo repeatability of IVIM parameters estimated using different curve-fitting methods and determine the optimum for analysing the acquired clinical breast DWI data. To investigate the value of conventional monoexponential versus advanced (IVIM and SEM) DWI models parameters estimated from whole-tumour, tumour diffusion cold-spot, and perfusion hot-spot regions to assess early breast cancer response to NACT. To explore relationships between IVIM and dynamic contrast-enhanced (DCE)-MRI perfusion-related parameters, and between DWI diffusion coefficients and DCE-MRI cellularity-related measures in the same three tumour regions.

Materials

MRI dataset of primary breast cancer patients acquired at pretreatment and after one and three NACT cycles. Simulated data represent IVIM parameter ranges observed in these patients.

Results

Constrained oversegmented-fitting was the optimum IVIM curve-fitting method, producing parameter estimates with the smallest errors, highest precision, and best repeatability. Tumour volume was significantly larger in non-responders across all time-points and demonstrated reasonable predictive performance (AUC=0.84-0.88; p<0.05). The monoexponential model was unable to predict response (p>0.05), while IVIM and SEM models differentiated response groups at pretreatment tumour hot-spot regions and after one NACT cycle in three tumour regions, displaying reasonable predictive performance (AUC=0.71-0.79 at pretreatment, 0.71-0.83 after one cycle; p<0.05). IVIM and DCE-MRI perfusion-related parameters were uncorrelated (p>0.5), but statistically significant, moderate between-subject (r=0.405-0.461; p<0.05) and within-subject (r_{rm}=0.514-0.619; p<0.05) correlations

between diffusion coefficients and DCE-MRI cellularity-related measures were observed in the whole-tumour regions.

Conclusion

IVIM and SEM models demonstrated better predictive capabilities for response than the monoexponential model. While IVIM and DCE-MRI perfusion-related parameters were uncorrelated, diffusion coefficients and DCE-MRI cellularity-related measures correlated.

Table of Contents

List of Figures

List of Tables

List of Abbreviations

ADC apparent diffusion coefficient

AUC area under the ROC curve

BI-RADS breast imaging reporting and data system

cAIC corrected Akaike information criterion

CIs confidence intervals

DCE dynamic contrast-enhanced

DDC distributed diffusion coefficient

D_p pseudo-diffusion coefficient

D_t true molecular diffusion

DWI diffusion-weighted imaging

EES extravascular-extracellular space

Eq equation

ER oestrogen receptors

f perfused fraction

$f \times D_p$ microvascular blood flow

FA flip angle

F_b blood flow

FoV field of view

Full-C full-fitting method with constraints

Full-woC full-fitting method without constraints

Gd Gadolinium

HER2 human epidermal growth factor receptor 2

HER2+ HER2-positive

HR+ hormone receptor-positive

HSR high spatial resolution

HTR high temporal resolution

iAUC initial area under the time-signal curve

ICC intraclass correlation coefficient

IDC invasive ductal carcinoma

IQR interquartile range

IR inversion recovery

IVIM intravoxel incoherent motion

k$_{ep}$ rate constant of contrast transfer

K^{trans} volume transfer constant

MRI magnetic resonance imaging

NACT neoadjuvant chemotherapy

Overseg-C oversegmented-fitting method with constraints

Overseg-woC oversegmented-fitting method without constraints

pCR pathological complete response

PGSE pulsed gradient spin echo

pNR pathological non-responders

pR pathological responders

PR progesterone receptors

PS permeability–surface area product

RB relative bias

RCB residual Cancer Burden

RE relative error

RECIST response evaluation criteria in solid tumours

rmcorr repeated measures correlation

ROC Receiver operating characteristic

ROI region of interest

S(0) signal intensity with b-value of zero

S(b) signal intensity at a given b-value

SD standard deviation

Seg-C segmented-fitting method with constraints

Seg-woC segmented-fitting method without constraints

SEM stretched-exponential model

SI signal intensity

SNR signal-to-noise ratio

SPAIR spectral attenuated inversion-recovery

ss-EPI single-shot echo-planar imaging

TE echo time

TR repetition time

TTP time to peak enhancement

US ultrasound

v_b blood volume fraction

v_d extracellular volume fraction

v_e interstitial volume fraction

v_p blood plasma volume fraction

wCV within-subject coefficient of variation

α diffusion heterogeneity index

Chapter 1 Introduction

1.1 Background

In 2020, about 2.3 million women were diagnosed with breast cancer, resulting in 685,000 deaths, making it one of the most prevalent cancers affecting women worldwide (1). Patients with primary breast cancer often undergo neoadjuvant chemotherapy (NACT) to reduce the tumour size and increase the chances of breast-conserving surgery; however, the patient response to NACT varies (2). Identifying non-responders before or at an early treatment stage is valuable, allowing clinicians to change the NACT regimen or proceed with surgery without delay, avoiding the toxic side effects of NACT and tumour progression while maintaining the cost-effectiveness of the treatment plan (3).

Patients with breast cancer undergoing NACT often undergo repeated dynamic contrast-enhanced (DCE) magnetic resonance imaging (MRI) scan, a common imaging technique involving serial MRI scans before and after injecting a gadolinium-based contrast agent for treatment assessment (3, 4). The primary need for injecting the contrast agent is for visualising the tumour and its boundaries within surrounding tissues. Nevertheless, the assessment is typically limited to evaluating morphological changes (5). Tumour cellularity and perfusion are two properties of tumours that often change as a response to treatment, preceding morphological changes (4, 6). A quantitative estimation of perfusion-related parameters of breast tumours, including tumour blood flow (F_b), blood volume fraction (v_b), along with haemodynamic and cellularity-related parameters, can be achieved with a pharmacokinetic analysis of the DCE-MRI data (7). However, it is recommended that patients who have had prior allergic reactions to gadolinium-based contrast media or those who present severe renal insufficiency should not be subjected to a DCE-MRI scan (8). Moreover, certain safety concerns exist regarding the administration of gadolinium, particularly for oncology patients who undergo repeated DCE-MRI scans (9). In addition, DCE-MRI is costly in terms of time and money. These concerns and limitations support the need for alternative imaging techniques that can provide equivalent perfusion and cellularity-related measurements without administering a contrast agent.

Conventional diffusion-weighted imaging (DWI), which is not typically used in breast cancer imaging, can be employed in oncology treatment response monitoring via the apparent diffusion coefficient (ADC). The ADC measures the diffusivity of water molecules in the tissue and is assumed to serve as an indicator

of cellular density. As such, as tumour cellularity decreases in response to treatment, the ADC value increases (10). However, intertumoural structural heterogeneity may cause the heterogeneity of water diffusion in the tumour, resulting in non-monoexponential diffusion (11). Moreover, blood within the capillary network can contribute to the ADC value, which may affect its accuracy in describing diffusion (12).

Bennett et al. introduced the stretched-exponential model (SEM) to assess the intravoxel heterogeneity of diffusion by measuring the distributed diffusion coefficient (DDC) and the diffusion heterogeneity index (α) (13). Although evidence has revealed that the SEM is useful for evaluating breast and other tumours, its application in assessing breast cancer response to NACT is still limited (14-19).

Le Bihan et al. introduced the intravoxel incoherent motion (IVIM) model as an approach to diffusion imaging. The IVIM model is proposed to enable the simultaneous assessment of water diffusion and blood perfusion by separating the effects of the microcirculation of blood in the capillary network (so-called pseudo-diffusion) from water diffusion in the rest of the tissue. This separation enables the measurement of the diffusion-related parameter D_t (reflecting tissue diffusion) and perfusion-related parameters, including D_p (reflecting the pseudo-diffusion coefficient), f (reflecting the perfused fraction), and their product $f \times D_p$ (reflecting microvascular blood flow) (12, 20). As such, IVIM is an interesting technique that can assess both tumour cellularity and perfusion without injecting the patient with gadolinium. Studies have demonstrated the potential of the IVIM model in differentiating benign and malignant breast tumours (15, 21, 22); however, few studies have investigated the ability of the model to assess the response of breast cancer to NACT (19, 23).

1.2 Thesis motivation

Two preliminary studies have indicated that, after two or three NACT cycles, the parameters of the SEM and IVIM models obtained from a single region of interest (ROI) drawn freehand on the imaging slice with the largest tumour dimension may predict the breast cancer response to NACT (19, 23). The authors of these studies have recommended further investigation at earlier treatment points (i.e., after one cycle). Furthermore, the International Breast DWI Working Group recommended volumetric sampling when evaluating tumour response (24).

Trial 6698 by the American College of Radiology Imaging Network (ACRIN) is the largest multicentre trial evaluating the effectiveness of the ADC to assess the breast cancer response to NACT. The ACRIN 6698 trial found that a relative increase in the whole-tumour ADC value was only predictive of the breast cancer response to NACT after four cycles (12 weeks). The trial suggests that the SEM or IVIM models may better depict NACT effects. Moreover, the trial recommended further investigation of alternative analytical methods, such as characterising the worst tumour subregion (i.e., the area with the lowest ADC) to improve the detection of changes in tumour cellularity (25). Similarly, the International Breast DWI Working Group suggested using a small ROI on the darkest region of the tumour on ADC maps, occasionally known as the diffusion cold-spot, to calculate ADC values, potentially reflecting the most active part of the tumour (24). This method is indicated to be analogous to that used for DCE-MRI image analyses, which involves selecting the region of greatest mean maximum enhancement, often called a perfusion hot-spot (24, 26). However, the ability of the ADC, along with the parameters of the SEM and IVIM models derived from the diffusion cold-spot and perfusion hot-spot of the tumour, to predict the early breast cancer response to NACT requires further exploration.

The promising applications of IVIM perfusion-related parameters in breast tumours over the past decade have, in turn, reopened the question of whether IVIM could be used as a contrast-agent-free alternative to DCE-MRI for measuring breast tumour perfusion. Few studies have investigated the correlations between IVIM and DCE-MRI perfusion-related parameters in breast tumours and have produced contradictory results (27-29). These studies examined correlations at a single visit, and none of these studies provided an absolute estimation of the tumour blood flow, thus; they did not perform a direct comparison with the IVIM parameter purported to measure microvascular blood flow ($f \times D_p$). In contrast, ADC is expected to be related to DCE-MRI cellularity-related measures. However, one

study on breast tumours has challenged this expectation, suggesting that ADC is incompletely understood (30).

The focus of this thesis, therefore, is to evaluate the relative potential of basic monoexponential and advanced (IVIM and SEM) diffusion models in predicting early responses to NACT in patients with primary breast cancer scheduled to undergo NACT, and to explore the relationships between IVIM and DCE-MRI perfusion-related measures, as well as between DWI tissue diffusion measures and DCE-MRI cellularity-related measures. The experimental works in this thesis utilised a retrospective MRI dataset of patients with breast cancer acquired as part of a Breast Cancer Now-funded project at three points in time: before NACT and after one and three NACT cycles.

1.3 Overview of chapters

Chapter 2 provides an overview of breast cancer, its histological and molecular subtypes and grading, and discusses the tumour microenvironment. This chapter summarises treatment approaches, emphasising NACT and evaluating histopathological responses. The chapter explains the roles of MRI in breast cancer imaging, focusing on DCE-MRI, DWI and the associated models, including basic monoexponential and advanced (IVIM and SEM) models. Each technique is described with a brief overview of its reproducibility and roles in breast cancer imaging. The chapter concludes by reviewing studies that explored the correlation between perfusion parameters estimated by IVIM and DCE-MRI techniques, highlighting gaps in the current literature.

Chapter 3, the first of four experimental chapters, compares commonly used IVIM curve-fitting methods in breast cancer via computer simulations and in vivo measurements to determine the optimum method to analyse the clinical breast DWI data included in this research.

Chapter 4 addresses the points raised in the literature by investigating the value of the monoexponential, SEM, and IVIM models at pretreatment and after one and three NACT cycles, using volumetric sampling to assess early breast cancer response to NACT.

In Chapter 5, the recommendations raised by the ACRIN 6698 trial and the suggestions from the International Breast DWI Working Group were followed by investigating the value of the ADC, along with the parameters obtained from the SEM and IVIM models, derived from diffusion cold-spot and perfusion hot-spot regions of the tumour, to predict early breast cancer response to NACT.

Chapter 6, final and main experimental chapter, addresses the gaps in the literature by systematically investigating whether IVIM could offer a contrast-agent-free alternative to DCE-MRI for breast tumour perfusion measurement, using a novel methodology. Furthermore, the research extended to explore the relationship between ADC and DCE-MRI cellularity-related measures.

Chapter 7 presents a summary of the experimental works, addresses the limitations of the works performed, provides recommendations for future research, and draws the final conclusion.

Chapter 2 Background material: breast cancer, treatment, and role of magnetic resonance imaging

2.1 Breast anatomy

Breasts or mammary glands are component of the female reproductive system. The development of the two mammary glands in females occurs during puberty with the hormone's oestrogen and progesterone secretion. Anatomically, the breast lies on the anterior thoracic wall and the pectoralis major muscle and extends between the second and the sixth ribs (31). The suspensory ligaments (also known as Cooper's ligaments) extend from the skin to the pectoralis fascia offering structural support and allowing movement of the breast (32). The breast is supplied with blood through numerous arteries that deliver oxygen and nutrients to the tissue, and veins that carry away waste products. The internal thoracic artery and its branches are the primary blood supply to the breast (33). Additionally, the breast is efficiently drained by the lymphatic system, which consists of lymphatic vessels and nodes that encircle the nipple (Figure 2.1). This system's roles include draining tissues of dissolved substances such as plasma proteins and contributing to the immune response by producing and releasing immune cells such as lymphocytes (a type of white blood cell) (34). However, cancer cells can exploit both the vascular and lymphatic systems to spread and establish secondary tumours in other parts of the body, such as the brain and lungs.
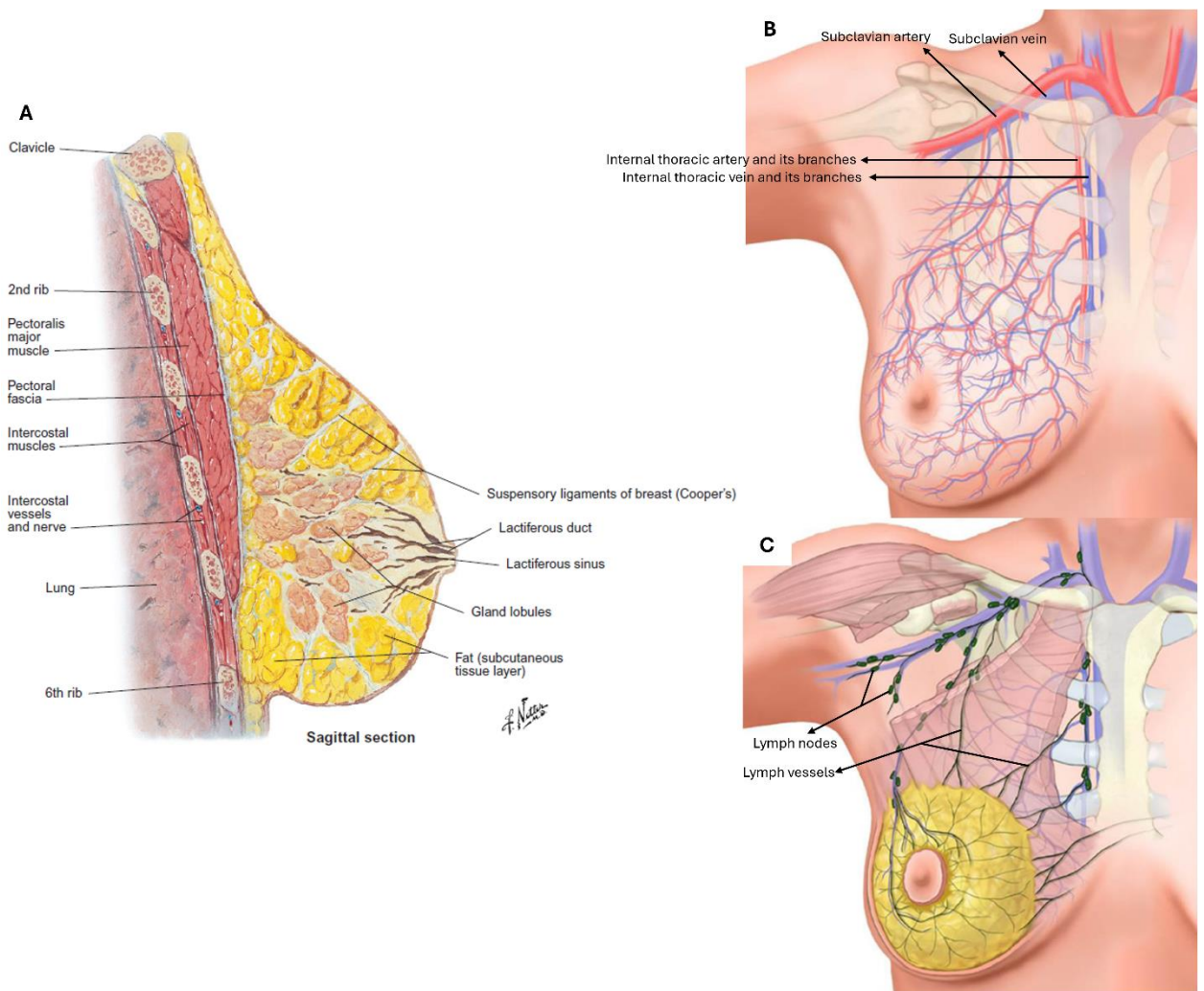
Figure 2.1 Normal female breast anatomy. (A) sagittal plane, (B) arteries and veins network, (C) lymph vessels and nodes network. Figure derived from **(33, 35),** and annotated.

2.2 Background of breast cancer

Breast cancer ranks as the second most frequently diagnosed cancer globally constituting 11.6% of all cancer cases, and it is the most prevalent cancer among females in the world (36). In females, it stands as a primary cause of cancer mortality worldwide, and it is the second highest cause of cancer mortality in UK after lung cancer (36, 37). Around 56,800 females in the UK are diagnosed with breast cancer annually and 1 in 7 females will develop the disease during their lifetime (37). Breast cancer survival are better than before due to improvement of awareness, screening, and treatments, where 85.9% of females diagnosed with the disease survive for 5 years or more, while 75.9% for 10 years or more (38). Nevertheless, approximately 11,400 females still die every year from breast cancer

in UK (37). Therefore, significant efforts for performing research aimed at improving prevention, early diagnosis, and the tailor of most effective treatment plan are still needed.

The detection pathway of breast cancer typically involves a physical examination by a clinician and screening using mammography (39). Ultrasound imaging is often used as a supplementary method to detect a lump in a breast that has not appeared on a mammogram, to characterise abnormalities that have shown up on a mammogram, to probe for nodal metastases, or to guide taking a needle biopsy from the suspicious area for pathological analysis (40). Screening through MRI is often conducted for women who are at high risk of developing breast cancer, such as those with a strong family history of breast cancer (39, 41).

Breast cancer is a heterogeneous disease, and its risk of progression and treatment resistance vary between patients (42). Heterogeneity implies variations in both biological and molecular characteristics between the same tumour type in different patients (inter-tumoural heterogeneity) and within cells of a primary tumour in the same patient (intra-tumoural heterogeneity), such as vascularity, proliferation rate, cellular morphology, and gene expression (42, 43). However, breast cancer can be characterised according to its histopathological subtype, grade, and the expression of particular proteins, which can be utilised in determining the suitable treatment.

2.3 Breast cancer histopathological classification

Breast cancers are classified into two main types: in-situ carcinoma (non-invasive), and invasive carcinoma. In-situ carcinoma is that where cancerous cells have not yet spread into the tissue surrounding the ducts or lobules. It is divided into two subtypes: ductal carcinoma in situ and lobular carcinoma in situ, with breast cancer called ductal or lobular according to where the cancer cells originate in and are restricted, as illustrated in Figure 2.2. In contrast, invasive carcinoma is that where cancerous cells have infiltrated beyond the myoepithelial cells and basement membrane of the ducts and lobules into the surrounding breast tissue and are capable of metastasising to other parts of the body.

The histopathological type of cancer is determined through microscopy of biopsied specimens. The most common histological subtype of invasive breast cancer is invasive ductal carcinoma where it constitutes approximately 75% of all breast cancer cases, while the second most common subtype is invasive lobular carcinoma, comprising 5-15% of all breast cancer cases (44). There are a number

of rare subtypes including tubular, mucinous, papillary, and inflammatory breast cancer (44, 45). Although the histopathologic subtyping of invasive breast cancers provides useful prognostic information, its role in the clinical management decision is generally limited (46).
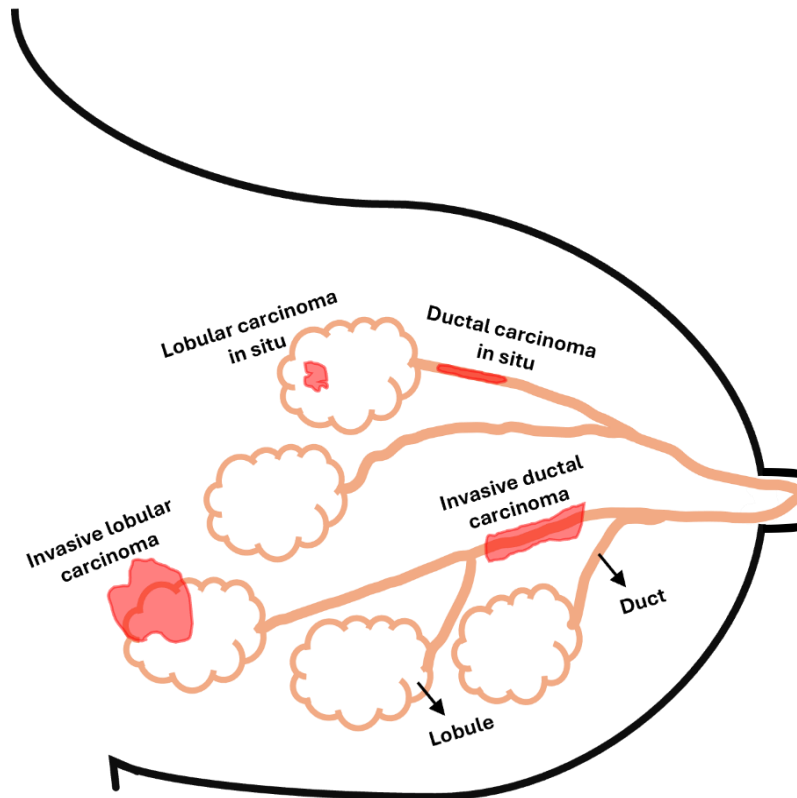
Figure 2.2 Common histopathological types of breast cancer.

2.4 Breast cancer molecular subtypes

Usually, immunohistochemical tests of biopsy specimens are performed to categorise the molecular subtype of breast cancer. These tests determine the expression of oestrogen receptors (ER), progesterone receptors (PR), and the human epidermal growth factor receptor 2 (HER2) in the breast tumour. According to the expression of these molecular markers, breast cancer can be categorised into four molecular subtypes: luminal A, luminal B, HER2-enriched, and triple-negative, as outlined in Table 2.1. Breast cancer is classified as luminal A when the hormone receptor is positive (i.e., ER and/or PR are present in significant quantities) and HER2 is negative, and as luminal B when both the hormone receptor and HER2 are positive. When breast cancer is negative for hormone

receptors (i.e., neither ER nor PR are present) but is HER2 positive, it is categorised as HER2-enriched, whereas when both the hormone receptors and HER2 are negative, it is categorised as triple-negative (47).

Establishing the molecular subtype of breast cancer helps with prognostication and therapeutic strategy. For example, luminal A and B breast tumours can be treated with endocrine therapy, such as tamoxifen (an oestrogen receptor modulator) in addition to chemotherapy, whereas trastuzumab (an anti-HER2 drug) can be used along with chemotherapy for HER2-enriched and luminal B tumours (48). It has been indicated that patients with luminal A tumours are associated with a good prognosis, whereas HER2-enriched and triple-negative tumours have a poorer prognosis compared to luminal tumours (49). Triple-negative cancer particularly accounts for a significant proportion of breast cancer deaths because of its aggressive nature and the lack of targeted treatments (50).

Table 2.1 Classification of molecular subtypes of breast cancer (47).

Molecular subtype	Immunohistochemical properties	Frequency (%) of invasive breast cancers
Luminal A	ER+ and/or PR+, HER2-	~40%
Luminal B	ER+ and/or PR+, HER2+	~20%
HER2-enriched	ER- and PR-, HER2+	~ 15% - 20%
Triple-negative	ER- and PR-, HER2-	~ 10% -15%

2.5 Breast cancer grading

The histologic grading of breast cancer measures the extent to which tumour cells differ from normal breast epithelial cells, reflecting the tumour's potential aggressiveness and correlates with prognosis (51, 52). Three morphological features are evaluated by a pathologist using the Nottingham Grading System where each feature is scored from 1 to 3: tubule formation (the proportion of tumour tissue that forms tubules similar to normal breast tissue), nuclear pleomorphism (the variation in tumour cell nuclei compared to normal cell nuclei), and mitotic count (the number of cells undergoing division in a given tumour tissue area - an indicator of cell proliferation). The total scores obtained determines the overall tumour grade, with scores of 3-5 equating to grade 1, 6-7 to grade 2, and 8-9 to grade 3. Grade 1 tumour cells tend to be small and proliferate slowly

compared to grade 3 tumour cells which are larger and rapidly proliferating, and the survival rate for patients with grade 1 tumours is significantly better than for those with grade 2 or grade 3 tumours (52).

2.6 Breast cancer features

2.6.1 Proliferation in breast cancer

Proliferation of tumour cells is one of the main features of malignancy. Cancer can develop rapidly; the increased proliferation of tumour cells leads to high tumour cellular density, a more confined extracellular space, and loss of structured organization (10), and is linked with prognosis and aggressiveness of tumours (53), (Figure 2.3). Inhibiting tumour cell proliferation is one of the cancer treatment strategies where various drugs are available to inhibit proliferative activity and therapy tumour progression (54). The DWI MRI technique has demonstrated the capability to characterise tumour cellularity, which would assist in both the diagnosis and monitoring of tumour responses (more details in section 2.8.2.1.1).
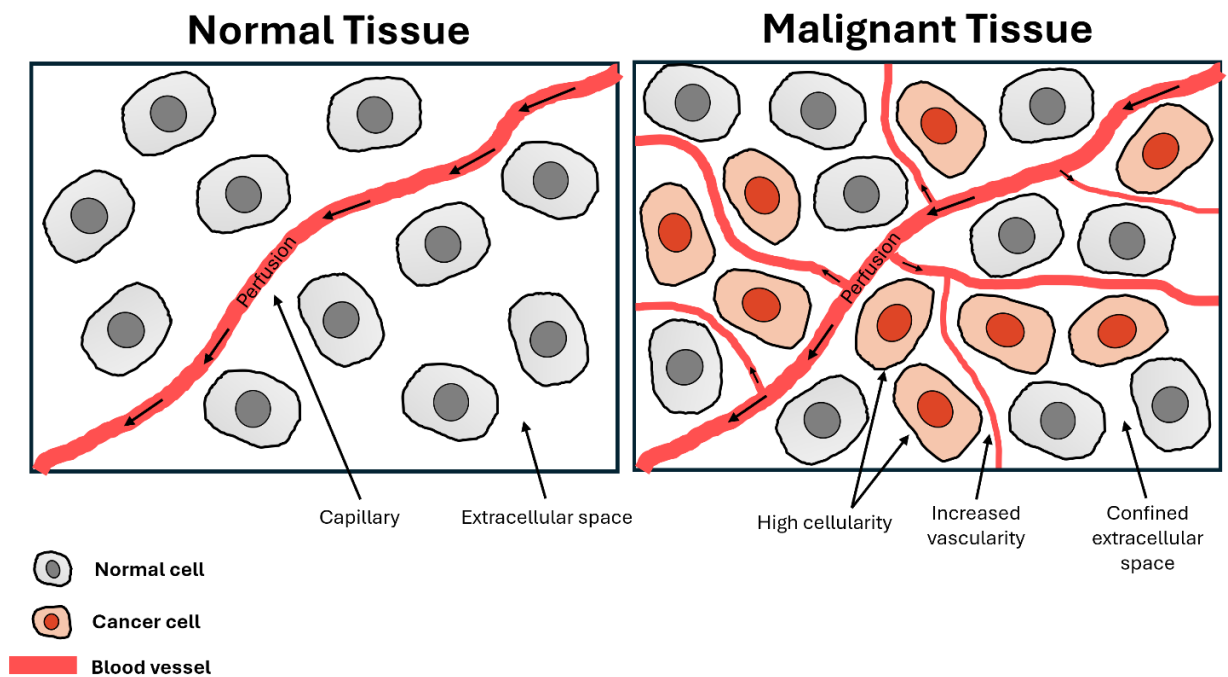
Figure 2.3 Illustration of features of normal and malignant breast tissue microenvironments. Malignant breast tissue (right), contrasting with normal breast tissue (left), is characterized by high cellular density due to cancer cell proliferation, and increased vascularity due to formation of new blood vessels to meet the increased demand for oxygen and nutrients for cancer cell proliferation, which both result in a more confined extracellular space.

2.6.2 Vascularity in breast cancer

Angiogenesis is another cancer characteristics by which new blood vessels are formed from existing vasculature. It is essential for tumour growth, invasion, and metastasis, as it fulfils the increased requirement for oxygen and nutrients needed for cancer cell proliferation (55), (Figure 2.3). Tumours generally do not expand beyond 1-2 mm in diameter without forming new blood vessels (56). In normal tissues, blood is delivered through an orderly and efficient mature vascular network (57). However, tumour vasculature develops in a dysfunctional and disorganised manner due to aggressive cell growth, resulting in irregularly shaped, tortuous, immature, and leaky blood vessels (58).

In the breast, tumours are characterized by an altered general vascular supply, a prominent feeding vessel, and increased regional vascularity (59). Targeting angiogenesis is considered one approach in cancer treatment strategies, where numerous drugs are available to inhibit angiogenesis and thereby impede the delivery of oxygen and nutrients needed for tumour growth (60). The DCE-MRI technique has the ability to characterise tumour vascularity, thereby aiding both diagnosis and monitoring of tumour response (more description in section 2.8.1.1).

2.7 Approaches to treatment

Treatment for breast cancer includes local therapy of surgery with/without radiotherapy, systemic therapy such as targeted chemotherapy and endocrine therapy, or a combination of both approaches. The appropriate treatment plan is determined based on multiple factors, including tumour size, molecular subtype, axillary node status, the presence of metastases, and patient decision. The main objective when treating non-metastatic breast cancer is to eradicate the tumour and remove cancer-affected axillary lymph nodes to a sufficient degree to prevent a local recurrence of the tumour. The local therapy approach for non-metastatic cancer involves surgical eradication of tumour or lymph nodes, with consideration of postoperative radiotherapy to cause necrosis of any residual tumour cells to reduce the risk of local recurrence. Systemic therapy, which includes targeted chemotherapy and endocrine therapy, can be administered before surgery (as neoadjuvant) or after surgery (as adjuvant), or both. In contrast, the main aims for systemic therapy and local therapy in treating metastatic breast cancer are to lengthen a patient's life and palliate symptoms, where it remains incurable in nearly all affected patients (48).

2.7.1 Overview of neoadjuvant chemotherapy (NACT)

Neoadjuvant chemotherapy (NACT) is often used in treating patients with primary breast cancer to:[1] reduce tumour size thereby increasing the chances of breast-conserving surgery instead of mastectomy; [2] rapidly treat any potential micrometastatic disease undetected in preoperative staging; and [3] downstage the axillary lymph nodes potentially reducing the need for axillary lymph node dissection (48, 61). NACT regimens are typically delivered in a series of cycles with intervals between cycles to permit the body to recuperate from side effects.

NACT often involves combination regimens comprising: alkylating agents such as cyclophosphamide that cause cross-linking and breaks in the DNA strands preventing cancer cells from dividing and leading to cell death; anthracyclines such as epirubicin which disrupt DNA synthesis and repair inhibiting cancer cell growth and ultimately leading to cell death; and taxanes such as docetaxel that disrupt the process of cell division, leading to cell cycle arrest and inducing cell death (62). These therapeutic agents are commonly administered in a regimen of cycles of epirubicin and cyclophosphamide for the initial phase of the NACT course, followed by cycles of docetaxel for the last phase (63).

Endocrine therapy and HER2-targeted therapy are considered the main treatments for breast cancers that are hormone receptor-positive (HR+) and HER2-positive (HER2+), respectively. HR+ breast cancers are treated with drugs such as tamoxifen, which is a selective ER modulator that reduces the effect of oestrogen, as well as aromatase inhibitors that can be used to decrease circulating oestrogen levels in the body. Additionally, HER2+ cancers are treated using monoclonal antibody drugs targeting HER2, such as trastuzumab and pertuzumab, which improve disease-free survival and overall survival rates. In contrast, treating triple-negative breast cancers is challenging due to the lack of expression of ER, PR, and HER2, thus making drugs targeted at these receptors ineffective (48).

2.7.1.1 Histological pathological response evaluation

Patient typically undergoes surgery following the completion of NACT to remove the remaining tumour, with either a lumpectomy (removing the tumour and a small margin of surrounding tissue) or a mastectomy (eradicate of the entire breast). Axillary lymph node dissection or sentinel lymph node biopsy is also performed to assess the involvement of lymph nodes. The surgical specimen and excised lymph nodes are collected and examined histologically by a pathologist for the calculation

of the Residual Cancer Burden (RCB) index to grade the tumour response to NACT.

The RCB index is a scoring system that commonly used for quantifying residual disease after NACT to assess response, and it is proposed as an independent predictor of distant relapse-free survival. The index is estimated from pathological sections of the primary breast tumour bed and the regional lymph nodes after NACT completion, including six variables (64):

Primary tumour bed:

- Largest bidimensional diameters of the residual primary tumour bed.
- Percentage of the residual tumour bed area that contains carcinoma.
- Percentage of cancer in the residual tumour bed that is in-situ component.

Lymph nodes:

- Number of positive metastatic axillary lymph nodes.
- Largest diameter of the largest nodal metastasis.

The RCB index is calculated by entering these variables into the online RCB calculator provided by the MD Anderson Centre (http://www.mdanderson.org/breastcancer_RCB). Subsequently, this index is separated into four different RCB classes reflecting the extent of residual disease: RCB-0 (pCR; pathological complete response), RCB-I (minimal residual disease), RCB-II (moderate residual disease), and RCB-III (extensive residual disease). The classification method is as follows: an RCB index of 0 is classified as pCR, which is defined as the absence of residual invasive disease in the breast and axillary nodes; an index greater than 0 but not exceeding 1.36 is categorised as RCB-I; an index between 1.36 and 3.28 is identified as RCB-II; while an index above 3.28 is labelled as RCB-III.

RCB-0/I is associated with a good prognosis, whereas RCB-II is linked with an intermediate prognosis and RCB-III with a poor prognosis (64). Notably, patients with RCB-I share the same excellent 5-year distant relapse-free prognosis as RCB-0 patients, and both groups achieving approximately 89% 8-year distant relapse-free survival rate (64, 65). Thereby the category of responders (patients with a very low risk of relapse) could be extended to include patients with minimal residual disease (RCB-I). Responders (RCB-0 and RCB-I), however, constitute only 37-40% of patients undergoing NACT (64, 65).

2.8 Breast cancer magnetic resonance imaging (MRI)

2.8.1 Background of dynamic contrast-enhanced (DCE) MRI

Breast MRI is a non-invasive imaging technique that plays multiple vital roles in breast cancer care including screening, staging, and monitoring treatment response, due to its ability to image both breasts simultaneously and offer superior soft tissue contrast and detailed cross-sectional anatomical imaging, allowing for high spatial resolution and sensitivity in identifying and characterising breast lesions (66).

The standard protocol for breast MRI includes T2-weighted fast spin echo sequence and dynamic contrast-enhanced (DCE) 3D T1-weighted spoiled gradient echo sequence with fat-suppression before and one or more after the intravenous administration of a gadolinium-based contrast agent (67). DCE-MRI images are highly valuable for detecting breast lesions and characterising lesion morphology and extent (66). T2-weighted images provide diagnostic insights that complement DCE-MRI for aiding in the differentiation between benign (e.g., cysts, fibroadenomas) and malignant lesions and in the assessment of breast anatomy (67).

Gadolinium-based contrast agents used in DCE-MRI function by shortening the T1 relaxation time of water in blood which tends to pool in in cancerous regions because of increased vascularity and leaky blood vessels, key characteristics of cancer, resulting in the tumour appearing bright on T1-weighted images due to enhanced signal intensity. Given the high adipose tissue content in the breast, applying fat suppression is key in breast imaging. Suppressing the fat signal during DCE sequence acquisition enhances the clarity of contrast agent uptake in fibroglandular tissue (68).

Peak enhancement for breast cancer appears within the initial 2 min following contrast agent injection, with tumours possibly losing signal (which called as wash-out) as early as 2 to 3 minutes post-injection. The European Society of Breast Imaging (EUSOBI) thus recommended performing the DCE sequence at least three time points: one before the contrast agent is administered, a second around 2 minutes afterward to capture the peak enhancement, and a third in the late phase to assess if the lesion continues to enhance, reaches a plateau, or exhibits early contrast agent wash-out, though the optimum number of required repetitions remains unknown (67).

DCE-MRI involves balancing temporal and spatial resolution. High spatial resolution is needed for identifying small tumours and accurately characterising tumour morphology, whereas high temporal resolution is necessary for effectively characterising or quantifying contrast agent uptake or performing pharmacokinetic modelling (66). Tumour morphology can be evaluated on the fat-suppressed contrast agent-enhanced images. However, interpretation may be challenged by residual fat signals that appear bright on T1-weighted images due to difficulty in achieving homogeneous fat suppression. Therefore, subtraction images, created by subtracting pre-contrast from post-contrast images, are recommended to further suppress the residual bright fat signal, as fatty tissue hardly enhances, thereby further improving tumour characterisation (67).

2.8.1.1 Roles of the DCE-MRI in breast cancer imaging

<u>Screening</u>

DCE-MRI is currently used as an adjunct imaging method for annual breast screening along with mammography or ultrasound in women who are at high risk for breast cancer, including those with a strong familial risk of breast cancer (first-degree relative such as a mother or sister), inherited BRCA1 or BRCA2 gene mutations, or a history of radiotherapy to the chest (69, 70). Breast screening for women at an elevated risk using MRI alone showed the highest sensitivity and specificity (92.6% and 98.4%) compared to mammography (33.3% and 99.1%) and ultrasound (37% and 98%) and combining MRI with mammography further improved the sensitivity and specificity to 100% and 97.6%, respectively (71). However, MRI is not popular for screening women at low and moderate risk of breast cancer due to concerns about false-positive results often associated with MRI, leading to additional tests and/or biopsies for the patient (70), thus eventually resulting in unnecessary fear to the patient and also costing the healthcare system time and money.

Additionally, DCE-MRI is often used to investigate equivocal (inconclusive) findings on mammograms or ultrasounds (70), and particularly in women with dense breast tissue as dense tissue appear white on a mammogram which can therefor hide similarly white dense tumour tissue. It has been reported that mammography sensitivity in women with largely fatty breasts is approximately 86-89%, but it decreases to 62-68% in those with extremely dense breasts, resulting in a higher rate of cancers that are not detected until the next scheduled screening round, known as interval cancers. However, screening with MRI has been shown to reduce the interval cancer rate by 84% (72).

Staging

Following a biopsy confirming cancer, DCE-MRI can also be used preoperatively to characterise tumour size and extent, including multifocal and multicentric disease, assess involvement of the chest wall and lymph nodes, and evaluate the contralateral breast for additional cancer (73, 74). This information can be utilised to aid in guiding the treatment (75), and for the selection of surgical planning particularly after the completion of NACT (mastectomy or lumpectomy), potentially minimising the need for surgical re-excision (76). Previous study showed that MRI provides the highest level of sensitivity in the pre-operative assessment of breast cancer (77).

Monitoring of NACT response

The primary goal of NACT is tumour size reduction. Monitoring the patient's response during NACT cycles is crucial as it allows the oncologist to change the NACT regimen if the tumour has not manifested a therapeutic response, or proceed to surgery without delay, thereby avoiding unnecessary cytotoxic side effects of NACT and tumour progression while maintaining the cost-effectiveness of the treatment plan. Tumour response is typically assessed by measuring changes in the tumour's size at each stage, often determined by its longest diameter on clinical examination (palpation) and imaging techniques such as mammography, ultrasonography, and DCE-MRI. Clinical assessment of tumour response by palpation is intrinsically subjective and may lack precision (78). Furthermore, breast tissue is inherently pliable, which implies that tumour dimensions may differ depending on the patient's position, potentially causing variations in measurements obtained in upright (mammography), supine (US), and prone (DCE-MRI) positions (79).

The Response Evaluation Criteria in Solid Tumours (RECIST) 1.1 guidelines specify MRI as the preferred imaging modality to follow breast tumours in the neoadjuvant setting and recommend measuring tumour diameter in at least one dimension (the longest diameter in the plane of measurement) to evaluate the therapeutic response, categorised into four types: complete response, partial response, stable disease, and progressive disease (Table 2.2) (5). In cases of multifocal or multicentric breast cancers, up to two of the largest lesions in each breast are measured and classified as target lesions for subsequent follow-up imaging assessments. Other enhancing lesions are classified as non-target lesions, which should be assessed during follow-up imaging, but measurement is not required (5). DCE-MRI provides a more accurate measurement of the longest

tumour diameter than ultrasound, mammography, and clinical examination (79, 80), and demonstrates higher accuracy in predicting tumour response to NACT (80, 81).

Table 2.2 The RECIST criteria for evaluating tumour response to treatment.

Response type	Criteria
Complete response	Disappearance of all target lesions
Partial response	A reduction in target lesion diameter of no less than 30%.
Progressive disease	An increase in target lesion diameter by at least 20%, or the appearance of one or more new lesions.
Stable disease	Lacking sufficient reduction to be classified as a partial response or sufficient increase to be considered progressive disease.

The EUSOBI recommends performing DCE-MRI at three time points: before starting NACT, midway through the NACT course, and after completing the final course (67). Nonetheless, there is still no consensus on the optimal time points for performing MRI assessments during treatment. The EUSOBI suggests that changing the NACT regimen based on MRI results halfway through treatment should be considered only for clear non-responders and those with progressive disease (67).

However, tumour shrinkage patterns vary, and a tumour might shrink asymmetrically, with for example a greater reduction occurring in one dimension than in the dimension of the largest diameter. Additionally, tumours that are irregularly shaped or multifocal may be inadequately evaluated by measuring only the largest diameter. Therefore, relying solely on the largest tumour diameter when monitoring NACT may not fully reflect the extent of the response.

Furthermore, the accuracy of DCE-MRI in measuring the size of residual tumour can be impacted by multiple factors. Tumour molecular subtype can affect the accuracy of DCE-MRI in determining the residual tumour size with luminal tumours found to be more underestimated compared to triple-negative and HER2-positive tumours, potentially due to a low level of contrast enhancement that may make measuring the residual tumour more difficult (82). Changes resulting from the treatment can impact the accuracy of residual tumour size measurement often resulting in over- or underestimation. Fibrosis and inflammatory reactions following

NACT may enhance and resemble the appearance of residual tumour, resulting in overestimation of tumour size on DCE-MRI. In cases where MRI suggested remnant tumour that was not found in the pathological analysis, fibrous granulation tissue containing numerous small vessels and inflammatory cells was accounted for the enhancement (83, 84). In comparison, tumours size that break up into small scattered residual carcinoma may be underestimated on DCE-MRI as residual tumour cells may be too small to be detected by MRI (85). Tumours treated with a NACT regimen that includes taxanes often fragment into scattered small nests of tumour cells which can result in the underestimation of residual tumour size by DCE-MRI, whereas tumours treated with a fluorouracil-epirubicin-cyclophosphamide-based regimen often shrink into single nodular residual lesions, and the measurements of these residual tumour sizes by MRI have been found to correlate highly with those obtained by pathological evaluation (85). Also, the use of a taxane-containing NACT suppresses contrast enhancement in breast cancers due to its antiangiogenic effects, which can also lead to the underestimation of residual tumour extent on DCE-MRI (86). Due to the aforementioned challenges in measuring residual tumour size with DCE-MRI, pathological examination of surgical specimens continues to be the gold standard for assessing tumour response.

Tumour volume measurement can provide a more comprehensive assessment of the extent of tumour response than changes in the longest diameter and tumour size on the section of the longest diameter, particularly with tumours that are irregularly shaped or multifocal. Researchers found that measurement of tumour volume was more predictive than measurement of the tumour's longest diameter for pathologic response (87) and recurrence-free survival (78). Moreover, a systematic review revealed that tumour volume measurements were more accurate in predicting the pathological response compared to uni- or bidimensional tumour size measurements (88).

Characterising tumour physiology

In addition to providing morphological information, DCE-MRI can provide physiological information about breast tumours through qualitative, semi-quantitative, or quantitative analysis of DCE-MRI data, which can aid in the diagnosis of malignant versus benign tumours and in monitoring tumour response. Physiological changes within the tumour often precede changes in volume, indicating early tumour response (89).

The American College of Radiology developed the Breast Imaging Reporting and Data System (BI-RADS) lexicon to standardise breast MRI reports, including the evaluation of lesion morphological features (size, shape, and margins), internal enhancement characteristics of the lesion (homogeneous, heterogeneous, or rim enhancement), and assessment of the lesion's signal intensity-time curve, known also as kinetic curve (90). Acquiring multiple MR images over the course of contrast media injection enables constructing the enhancement kinetic curve by plotting the signal intensity values of a breast lesion over time following the injection, depicting the dynamic contrast flow through the tissue.

DCE-MRI qualitative analysis is based on characterising the shape of two distinct enhancement phases (initial and delayed) of the constructed signal intensity-time curve, as depicted in Figure 2.4. The initial enhancement phase occurs within the first 2 minutes following contrast administration or when the enhancement curve begins to increase; the enhancement shape is determined as either slow, medium, or fast. The delayed enhancement phase occurs following the first 2 minutes of contrast injection or after the enhancement curve peaks; the enhancement pattern is characterised as either persistent, plateau, or washout (90). A persistent gradual increase in signal intensity over time following contrast injection is considered a type I kinetic curve; a fast initial signal enhancement followed by a plateau phase is classified as a type II kinetic curve; and a fast initial signal enhancement followed by a fast washout phase is characterised as a type III kinetic curve (91).
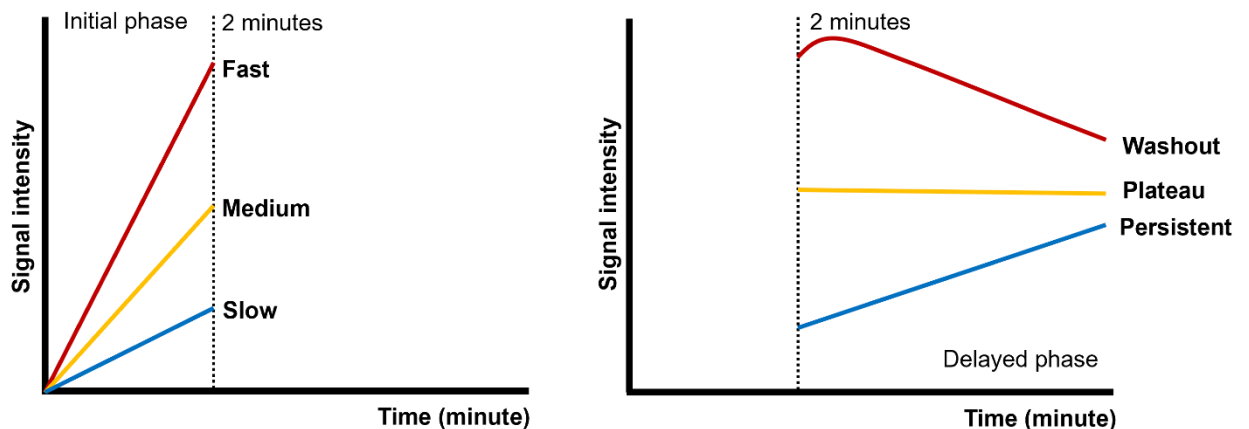
Figure 2.4 Enhancement shapes of initial (left) and delayed (right) phase of breast lesion signal intensity-time curve.

A type I curve was considered indicative of benignity, observed in 83% of benign lesions compared to 8.9% of malignant lesions (91). This could be a reflection of more normal vascularity in benign lesions, where the contrast agent gradually accumulates until saturation. In comparison, type II and III curves were recognised as indicative of malignancy, identified in 91% of malignant lesions (type II: 33.6%; type III: 57.4%) versus 17% of benign lesions (type II: 11.5%; type III: 5.5%) (91). These patterns in malignant lesions could correspond to high but permeable vascularity, where the contrast agent accumulates rapidly but then leaks out. Additionally, the changes in signal intensity-time curve types post-NACT were found significantly correlated with clinical and pathological responses (92).

Semi-quantitative DCE-MRI analysis involves calculating several heuristic parameters using the signal intensity-time curve, such as maximum relative tumour signal intensity enhancement compared to normal tissue, the signal enhancement ratio, time to peak enhancement (TTP), wash-in and wash-out rates, and the initial area under the time-signal curve (iAUC), which have demonstrated the ability to differentiate between benign and malignant tumours (93). Previous studies have also found that iAUC, TTP, and wash-in rate are valuable in predicting pathological response to NACT (94).

Quantitative analysis in DCE-MRI is based on performing mathematical pharmacokinetic modelling, which characterises the passage of the contrast agent through the vasculature into the tumour and its distribution between the intravascular and extravascular spaces (95). There are a number of pharmacokinetic models utilised in the literature for analysing DCE-MRI data in breast cancer, varying from the simple Tofts' model to the extended Tofts model, which provide a range of quantitative parameters describing various physiological aspects of the tumour. Such parameters include: K^{trans} (min^{-1}), indicating the influx mass transfer rate of the contrast agent from the blood plasma to the extravascular-extracellular space (EES); k_{ep} (min^{-1}), representing the flux rate of contrast agent from the EES back to the blood plasma; v_p, representing the fractional blood plasma volume; and v_e, indicating the EES volume fraction (96), (Figure 2.5).
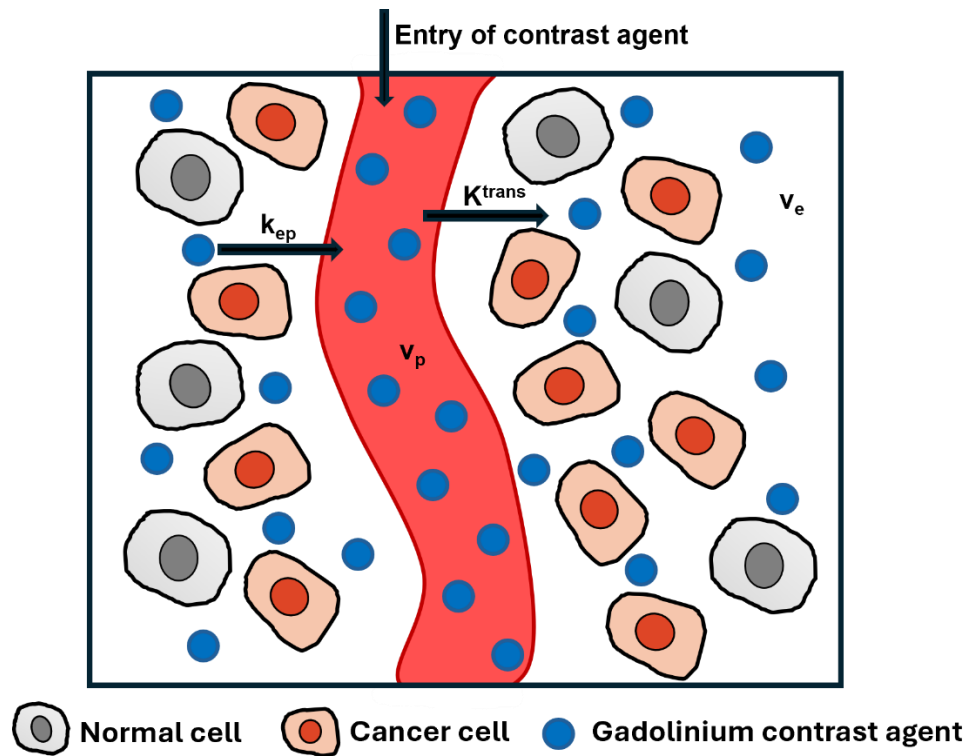
Figure 2.5 Pictorial representation of the extended Tofts model, describing the parameters K^{trans}, k_{ep}, v_p, and v_e in the context of breast cancer tissues.

Researchers have demonstrated that K^{trans}, K_{ep}, and v_p can distinguish between benign and malignant breast lesions with over 80% accuracy, with these parameters found to be higher in malignant lesions compared to benign ones (97, 98). This could be due to malignant lesions being associated with higher perfusion and leaky vascularity than benign lesions. Additionally, other researchers have found that K^{trans} (99-101), K_{ep} (99, 102, 103), and v_e (103) can predict tumour response to NACT when measured at early treatment time points, with responders showing a greater reduction in K^{trans}, K_{ep}, and an increase in v_e in response to treatment. Marinovich et al. indicated that, in addition to tumour volume, a reduction in K^{trans} may outperform uni- or bidimensional size measurements for early response prediction (88). Although a meta-analysis of 14 articles found the sensitivity and specificity of quantitative DCE-MRI for predicting response to NACT to be above 80%, the published studies are noted to be highly heterogeneous and there is a lack of standardization in the field (104). The spontaneous variability range of quantitative DCE-MRI parameter estimates, evaluated using the within-subject coefficient of variation at different anatomic sites, was 7.7-31% for K^{trans} (105-109), 15.4-24% for K_{ep} (105, 107, 108), 6.2-17% for v_e (105-109), and 30-48% for v_b (108, 109). The DCE-MRI data in routine clinical practice is analysed using

the BI-RADS lexicon (i.e., qualitatively), whereas deriving quantitative parameters is typically limited to breast cancer research.

There are safety concerns regarding the administration of gadolinium-based contrast agents, particularly in patients with a history of allergic reactions to gadolinium or those with severe renal insufficiency who are at risk for nephrogenic systemic fibrosis (8). Another concern involves the accumulation of gadolinium deposits in tissues, including the brain, following repeated exposure to gadolinium-based contrast agents (110), a risk that is particularly important for breast cancer patients who undergo multiple DCE-MRI scans (111). Additionally, DCE-MRI is both time-consuming and costly. These concerns and limitations have created a need for an alternative imaging technique that can provide equivalent perfusion- and cellularity-related measurements for evaluating tumours, without the need for intravenous contrast injection.

2.8.2 Diffusion weighted imaging (DWI) MRI and advanced models of diffusion

Diffusion-weighted imaging (DWI) MRI is a technique that measures the thermally driven random, Brownian, movement of water molecules in tissue to generate contrast in an image. The diffusivity of water molecules in tissue is impeded by the cellular membranes and other hindrances (112). Thus, the motion of water molecules is not truly Brownian and is affected by changes in the tissue microstructure, including tissue cellularity and membrane integrity (10).

DWI is commonly acquired using a pulsed gradient spin echo (PGSE) sequence, which is a conventional spin-echo sequence with a pair of diffusion-sensitizing gradients placed before and after the 180° RF pulse, based on methods originally developed by Stejskal and Tanner (113), Figure 2.6. DWI sensitivity to water molecules mobility depends on the proton's gyromagnetic ratio (γ), gradient strength (G), gradient duration (δ), and the time delay between the two sensitizing gradients (Δ), and is defined as the b-value (unit: s/mm^2) of the sequence as shown below (10):

$$b = \gamma^2 G^2 \delta^2 (\Delta - \frac{\delta}{3})$$
Equation [1]

Water molecules that move into different locations between the two diffusion gradients will be not exactly rephased at the time of readout, causing the MR signal intensity to be reduced (10). Thus, the intensity of the MR signal is inversely proportional to the movement of water molecules. More restricted water diffusion,

due to the restricted environment, exhibits a larger signal intensity and appears brighter on the diffusion images compared with the less restricted diffusion (112).
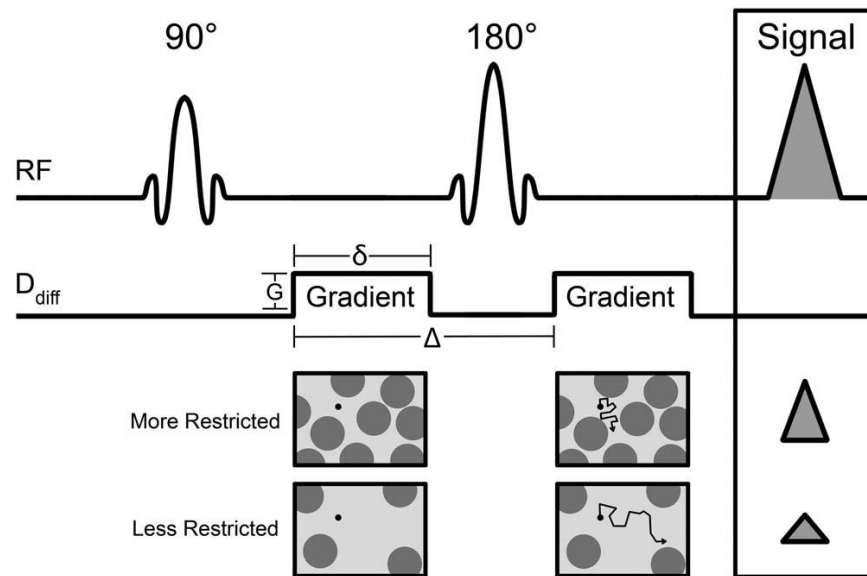
Figure 2.6 The diagram of a diffusion-weighted sequence, based on a PGSE technique developed by Stejskal and Tanner. Equal pairs of diffusion-sensitizing gradients are applied on either side of the 180° refocusing RF pulse. The degree of diffusion weighting (b-value) is determined by the proton's gyromagnetic ratio (γ), gradient strength (G), gradient duration (δ), and the timing between the two sensitizing gradients (Δ). The intensity of the MRI signal is directly inversely proportional to the diffusivity of water molecules, where more-restricted diffusion of water exhibits a larger signal intensity compared with the less-restricted diffusion (10).

2.8.2.1 Background of the apparent diffusion coefficient (ADC)

The mobility of water protons in tissue can be quantified via calculating the apparent diffusion coefficient (ADC), which is found through the monoexponential model equation:

$$S(b) = S(0) . exp(-b . ADC) \qquad \text{Equation [2]}$$

where S(b) is the signal intensity obtained with diffusion weighting b, and S(0) is the signal intensity acquired without diffusion weighting (b=0 s/mm^2). In general, the ADC value is determined for each voxel in the diffusion image and displayed as a parametric map on a voxel-by-voxel basis (10). Since the water concentration and diffusivity in biological tissues vary according to the type and condition of the tissue, the use of the DWI technique can be useful for imaging diseases, such as

breast cancer. Several studies have indicated that malignant breast lesions usually present low ADC value and appear darker on the ADC map than normal fibroglandular tissues. This low ADC value is due to the increased cellular density of the malignant lesions, which leads to a smaller extracellular volume fraction and results in restricted diffusion (114-116), (Figure 2.7). It is worth noting that raw DWIs are inherently T_2-weighted, meaning that tissues with longer T_2 relaxation times but higher ADC values can appear brighter than tissues with shorter T_2 but lower ADC values, highlighting the need for careful interpretation of DWIs and the advantages of calculating ADC maps, which largely overcome this limitation.
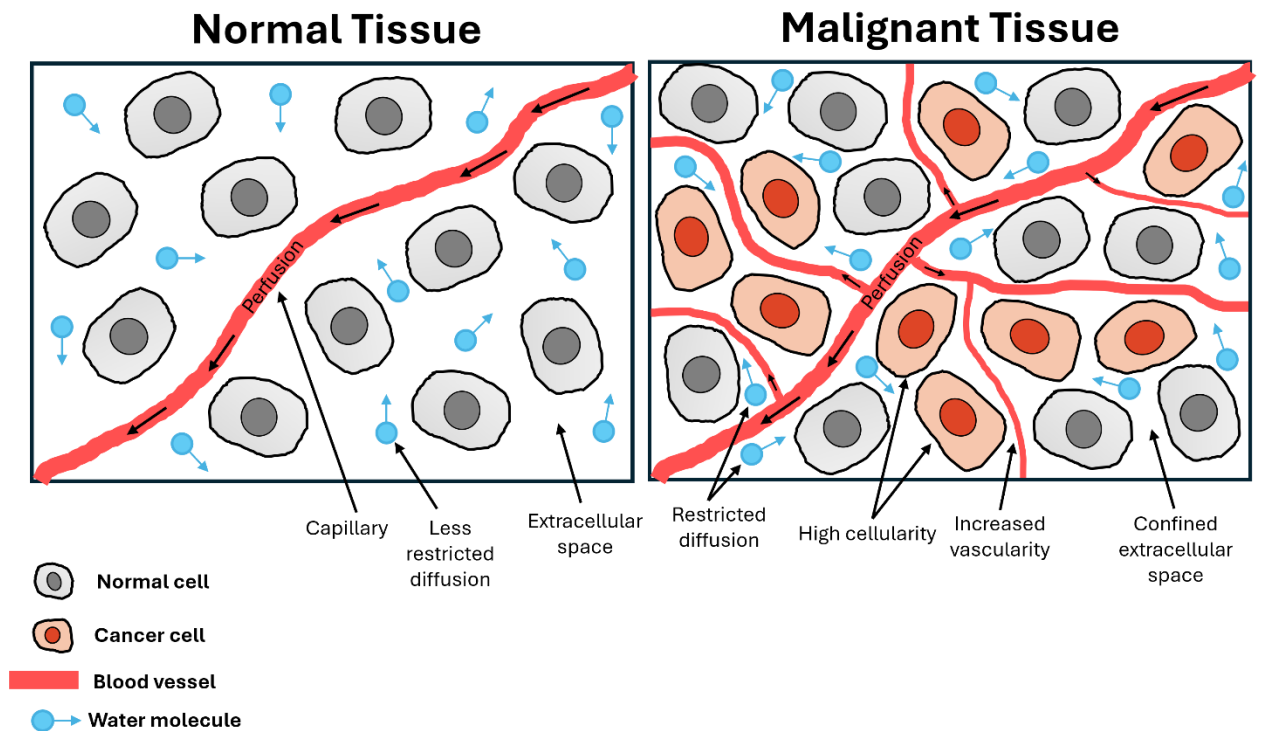
Figure 2.7 Diffusion of water molecules in normal and malignant breast tissue. The diffusivity of water molecules in malignant breast tumour tissue (right) is restricted due to high cellular density, causing a more confined extracellular space, thereby resulting in a low ADC value in comparison with normal breast tissue microenvironments (left).

The DWI sequence is not yet included in the clinical standard MRI protocol for breast imaging and is also not included in the BI-RADS lexicon for assessing breast lesions. Additionally, the literature lacks consistency regarding the b-values used (117). However, the international Breast DWI working group recently published a consensus to encourage the use of DWI in clinical practice,

recommending a lowest b-value of 0 s/mm² and a highest b-value of 800 s/mm² (24).

2.8.2.1.1   Role of ADC in assessing NACT response

Researchers examining changes in tumour specimens following NACT noted substantial reductions in tumour cellularity (118). Changes in the ADC value of a tumour can reflect changes in tumour cellularity, where an increase in tumour ADC during or after NACT is associated with increased cell lysis and necrosis, with larger increases observed in pathological responders than in non-responders (10, 119). Interestingly, significant change in tumour ADC in response to chemotherapy has been noted to precede tumour size reduction (120, 121), highlighting the potential utility of ADC in assessing treatment response at an earlier time point than measurement of tumour size.

Previous studies have demonstrated that changes in ADC values can predict treatment response after one cycle (122), two cycles (123), and after the completion of NACT(124). However, the American College of Radiology Imaging Network (ACRIN) 6698 trial, which is the largest multicentre trial, assessed the ability of ADC to predict NACT response at pretreatment, after one and four NACT cycles, and post-treatment. It found that changes in ADC values were only predictive of response to NACT after four cycles (12 weeks, mid-treatment) and post-treatment (25). This finding could be attributed to the fact that no imaging time point was included between cycles one and four, and that ADC changes after one cycle may be too early to distinguish responders from non-responders and predict treatment response, as also observed in this thesis' findings (125). The ACRIN 6698 trial paper proposed future investigations, including exploring alternative image analysis approaches to improve the ability of ADC to detect changes in tumour cellularity, such as characterising the worst tumour subregion (i.e., the area with the lowest ADC) (25). The international Breast DWI working group also recommended in their consensus statement measuring ADC values from a small region of interest (ROI) placed on the darkest region of the breast tumour on ADC maps (24), which is occasionally referred to as the diffusion cold-spot. This approach is considered analogous to that used for DCE-MRI image analysis (24), selecting the tumour region with the greatest mean maximum enhancement, often referred to as a perfusion hot-spot (26, 100).

Furthermore, the ACRIN 6698 trial suggests analysing DWI data using advanced models, such as IVIM or SEM, to better depict the effects of NACT, rather than solely relying on ADC calculated using a monoexponential decay model (25).

Consistent with this suggestion, diffusion data obtained from breast tumours in previous studies do not follow the expected monoexponential decay (21, 116, 126), as demonstrated by Bedair et al. (19) and this thesis' findings (125), which further supports the use of more advanced diffusion models when analysing diffusion data.

2.8.2.2 Advanced diffusion models: intravoxel incoherent motion (IVIM) and stretched-exponential (SEM)

Le Bihan et al. indicated that there is an extra source that contributes to the MR signal (and the ADC value) is that from microcapillary perfusion in pseudo-random capillary networks within imaging voxels (12, 127, 128), particularly at the low b-values (115). In general, the molecular diffusion of water includes the molecules moving due to their thermal energy and colliding with each other, which results in a change in their direction. This pattern of motion is random and described as a Brownian movement. However, intravascular water molecules flow and change direction between pseudo-randomly oriented capillaries within imaging voxels and can therefore mimic the random walk process and contribute to the calculated ADC value as a type of 'pseudo-diffusion'. Le Bihan et al. proposed an approach to diffusion imaging called IVIM model. The IVIM allows separation of the microcirculation perfusion effects from the molecular diffusion using multiple b-values (low and high) and a biexponential model. Figure 2.8 illustrates signal decay and monoexponential and biexponential model fits across different b-values. Thus, this enables the estimation of quantitative parameters that can separately reflect cellularity and vascularity (12), as shown in the following equation:

$$S(b) = S(0) \cdot \left[(1 - f) \, exp(-b \cdot D_t) + f \, exp(-b \cdot D_p) \right] \quad \text{Equation [3]}$$

Here, f is the perfusion fraction reflecting the fraction of diffusion linked to microcirculation, D_t represents the true molecular diffusion, D_p denotes the pseudo-diffusion coefficient (128), and the product f×D_p reflects the microvascular blood flow (20).
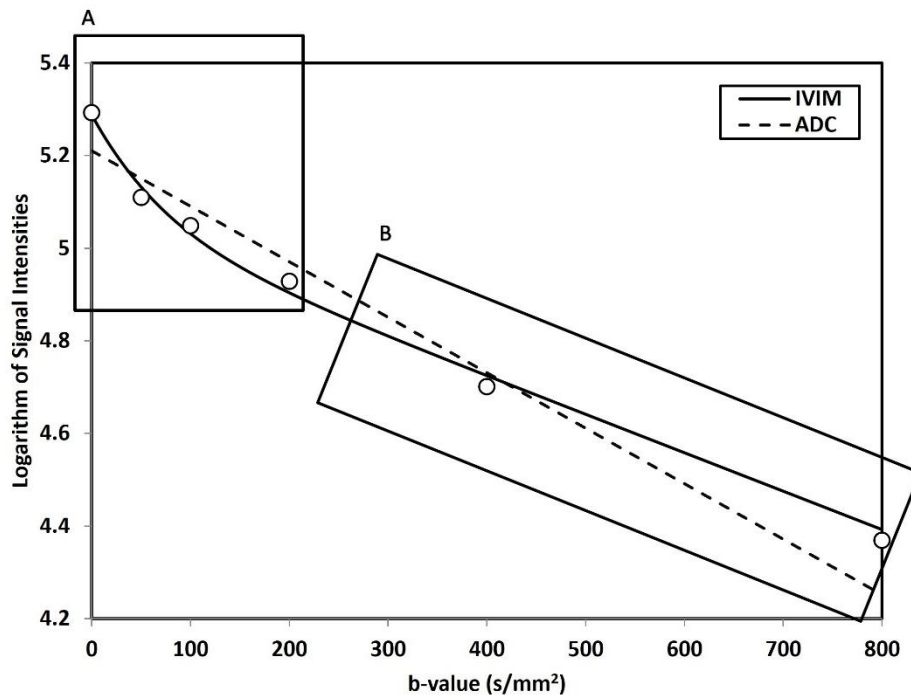
Figure 2.8 Monoexponential model fit (dashed line) and biexponential model fit (solid line, IVIM) of the signal intensity value decay as a function of b-value. Rectangular box A shows fast decaying signal at low b-values due to the effects of both pseudo-diffusion associated with blood microcirculation perfusion and diffusion, while rectangular box B shows a more gradual decay of signal at higher b-values where purely diffusion effects reside. This figure demonstrates that if the diffusion is calculated using a monoexponential ADC fit with low b-values, the microcirculation perfusion effects will affect this and hence the ADC may not be accurate. Adapted from Figure 2 of (125).

Furthermore, Bennett et al. proposed the SEM model to assess diffusion and intravoxel heterogeneity by measuring the distributed diffusion coefficient (DDC) and the water diffusion heterogeneity index (α) using the following equation:

$$S(b) = S(0).exp(-((b .\ DDC)^{\alpha}))$$ Equation [4]

Where DDC represents the mean intravoxel diffusion rate, and α describes the deviation of the signal attenuation from the monoexponential behaviour and has a value between 0 and 1. A low α index (close to 0) indicates a high degree of intravoxel diffusion heterogeneity, demonstrated as multiexponential signal decay. In contrast, a high α index (close to 1) denotes a low degree of diffusion heterogeneity, suggesting monoexponential diffusion signal decay and indicating

that the function will be the same as Equation [2] (13). While the DDC can be interpreted as the diffusion coefficient, the interpretation of α is less straightforward as there is no clear direct link between the parameter and a physiological basis (129).

2.8.2.2.1   Role of IVIM and SEM in assessing NACT response

Since the first investigation of IVIM in breast cancer in 2011 (126), growing interest in the potential applications of IVIM in breast has led to numerous studies on the differentiation between benign and malignant lesions and the association with receptor status (21, 27, 116, 130-135). Investigations comparing benign and malignant lesions reported that malignant lesions exhibited significantly lower D_t and higher f values than benign lesions, which could reflect the higher cellularity and vascularity characteristic of malignant lesions (21, 27, 130-133). Similarly, though less abundant, studies on SEM in breast cancer have pursued investigative objectives similar to those of IVIM. Findings from these SEM studies revealed that malignant lesions possessed significantly lower DDC and higher α values compared to benign lesions (135-138), which could also reflect greater cellular density in malignant lesion. These promising roles of IVIM and SEM parameters have underscored their potential usefulness in assessing treatment response to NACT.

Limited studies have assessed the capability of the IVIM and SEM models in monitoring and predicting early breast cancer response to NACT. The methodologies used in these studies vary in terms of the number and characteristics of the patient population that participated, the number and distribution of b-values used, the approach followed for pathological response evaluation, the imaging time points for assessing early NACT response, and the signal-fitting method employed for estimating IVIM parameters (19, 23, 139-141). Nevertheless, the results from these studies, summarised in Table 2.3, showed that after two or three NACT cycles, the parameters of the SEM and IVIM models may predict therapeutic response. For instance, Che et al.(23) reported that pre-treatment f values were significantly higher in responders than in non-responders. However, after two NACT cycles, responders showed significantly higher D_t values and lower f values compared to non-responders. In contrast, Cho et al. (139) found that only pre-treatment pseudo-diffusion D_p significantly differed between the response groups, stratified according to RECIST guidelines.

Bedair et al. (19) demonstrated that pre-treatment diffusion coefficients (D_t and DDC) were significantly lower in responders than in non-responders. After three

NACT cycles, only the percentage increase in DDC was significantly higher in responders, while D_t showed no significant change between the two groups. In contrast, Kim et al. (140) found that D_t at both pre-treatment and after two NACT cycles was significantly higher in responders compared to non-responders. Suo et al. (141) further demonstrated that the change in diffusion coefficients (D_t and DDC) after two NACT cycles was substantially greater in the responders' group.

The authors of these studies have recommended further investigation at earlier time points during the NACT course (i.e., after one cycle) (19, 23, 140). Notably, none of these studies examined the ability of the IVIM parameter that was suggested to reflect blood flow ($f{\times}D_p$) in predicting treatment response, and none of them explored the predictive value of IVIM and SEM parameters when derived from the diffusion cold-spot of the tumour. Furthermore, most of these results were obtained from a single ROI drawn freehand on the imaging slice with the largest tumour dimension (19, 23, 139); however, volumetric sampling has been recommended by the international Breast DWI working group when evaluating tumour response (24).

Minimal research has evaluated the variability in monoexponential and IVIM model measurements in breast lesions by calculating the coefficient of variation, and the results were promising for the ADC (4.8%) (142) and f (8.83–16.8%) (143). Table 2.4 provides an overview of the results of studies that have examined the repeatability and reproducibility of monoexponential, IVIM, and SEM model parameters in the breast and other body regions, demonstrating that the variability of these parameters may depend on the area under investigation. Notably, the variability of SEM parameters in both normal and malignant breast tissues has yet to be assessed.

Table 2.3 Summary of findings from studies assessing early treatment response to NACT in breast cancer using intravoxel incoherent motion and stretched-exponential models.

Author	Year	Intravoxel incoherent motion model											
		Pre-treatment (Baseline)						During treatment					
		Responders			Non-Responders			Responders			Non-Responders		
		D_t (×10⁻³ mm²/s)	D_p (×10⁻³ mm²/s)	f (%)	D_t (×10⁻³ mm²/s)	D_p (×10⁻³ mm²/s)	f (%)	D_t (×10⁻³ mm²/s)	D_p (×10⁻³ mm²/s)	f (%)	D_t (×10⁻³ mm²/s)	D_p (×10⁻³ mm²/s)	f (%)
* Che et al. (23)	2016	0.92 (0.77, 0.95)	10.10 (2.48, 33.65)	**32.40 (25.40, 40.55)**	0.83 (0.75, 0.92)	9.40 (4.88, 32.20)	**24.40 (21.60, 31.50)**	**1.36±0.3**	8.98 (7.52, 12.35)	**14.51±7.25**	**0.98±0.23**	20.00 (4.62, 31.70)	**20.69±5.10**
†Bedair et al.(19)	2017	**0.85 ± 0.05**	NA	12.10 ± 2.02	**1.02 ± 0.05**	NA	10.32±1.15	Δ ↑36%	NA	Δ ↓29%	Δ ↑23%	NA	Δ ↑5%
Cho et al.(139)	2017	0.99 (0.55, 2.16)	**25.54 (15.99, 37.14)**	8.70 (4.80,19.3)	1.05 (0.96, 1.21)	**17.16 (16.9, 25.79)**	11.70 (5.20, 14.2)	NA	NA	NA	NA	NA	NA
* Kim et al.(140)	2018	**1.22 (1.10, 1.49)**	5.87 (4.77, 7.94)	45.17 (37.96, 47.73)	**1.10 (1.01, 1.22)**	7.33 (5.26, 10.16)	43.33 (36.04, 53.90)	**1.37 (1.25, 1.60)**	6.04 (3.60, 7.34)	49.56 (38.81, 59.85)	**1.15 (1.10, 1.34)**	6.58 (5.28, 9.14)	45.23 (33.82, 57.18)
* Suo et al.(141)	2021	0.79 ± 0.15	15.62 ± 4.18	9.27 ± 3.66	0.77 ± 0.20	15.44 ± 3.70	9.27 ± 2.98	Δ **0.50 ± 0.26**	Δ − 3.06 ± 6.36	Δ 1.78 ± 4.33	Δ **0.19 ± 0.22**	Δ − 1.97 ± 6.35	Δ 0.82 ± 3.86

Author	Year	Stretched-exponential model							
		DDC (×10⁻³ mm²/s)	α (unitless)	DDC (×10⁻³ mm²/s)	α (unitless)	DDC (×10⁻³ mm²/s)	α (unitless)	DDC (×10⁻³ mm²/s)	α (unitless)
†Bedair et al.(19)	2017	**0.93±0.04**	0.84±0.02	**1.25±0.03**	0.81±0.02	Δ ↑**43%**	Δ ↑7%	Δ ↑**32%**	Δ ↑5%
* Suo et al.(141)	2021	1.00 ± 0.83	0.68 ± 0.08	0.98 ± 0.80	0.67 ± 0.08	Δ **0.78 ± 0.68**	Δ − 0.02 ± 0.12	Δ **0.25 ± 0.35**	Δ − 0.003 ± 0.09

D_t: tissue diffusion. D_p: pseudo-diffusion coefficient. f: perfusion fraction. DDC: distributed diffusion coefficient. α: diffusion heterogeneity index.
* Studies derived the parameters at pre-treatment and after two cycles of NACT. † Studies derived the parameters at pre-treatment and after three cycles of NACT. Values in bold indicate statistically significant differences between the response groups. NA: Not assessed. Data presented are mean ± standard deviation, median (interquartile range), or Δ change.

Table 2.4 Repeatability and reproducibility of monoexponential, IVIM, and SEM model parameters in healthy and cancerous tissues.

Authors	Parameter assessed	Body region	Result (%Coefficient of variation)
Kakite et al. (144)	ADC, D_t, D_p, f	Healthy liver	ADC= 8.8%. D_t= 13.2%. D_p= 59%. f= 25.3%
Lee et al. (145)	ADC, D_t, D_p, f	Healthy liver	Right lobe: ADC= 4.33%. D_t= 4.11%. D_p= 74.16%. f= 15.77%.
			Left lobe: ADC= 4.74%. D_t= 12.51%. D_p= 156.61%. f= 16.81%.
Sigmund et al. (146)	ADC, D_t, D_p, f	Healthy kidney	Cortex: ADC= 3.4%. D_t= 3.1%. D_p= 24.8%. f= 13.7%.
			Medulla: ADC= 5.6%. D_t= 3.7%. D_p= 29.5%. f= 24.2%.
Jakab et al. (147)	D_t, D_p, f	Healthy Foetal MRI (Kidneys, Liver, Lungs)	Kidneys: D_t= 17%. D_p= 30.1%. f= 36.2%.
			Lung: D_t= 14.1%. D_p= 25.3%. f= 20.4%.
			Liver: D_t= 13.8%. D_p= 16.8%. f= 14.4%.
Jerome et al. (148)	D_t, D_p, f, f×D_p, DDC, α	Paediatric solid tumours	D_t= 2.5%. D_p= 35.1%. f= 41.0%. f×D_p= 38.1%. DDC= 4.3%. α= 3.5%.
Reischauer et al. (149)	ADC, D_t, D_p, f, f×D_p, DDC, α	Prostate cancer bone metastases	ADC= 5.0%. D_t= 7.8%. D_p= 42.5%. f= 19.8%. f×D_p= 20.4%. DDC= 5.1%. α= 5%.
Pan et al. (150)	D_t, D_p, f	Renal tumors	D_t= 11.8–19.1%. D_p= 75.5–101.4%. f= 26.8–50.5%.
Iima et al. (143)	D_p, f	Malignant and benign breast lesions	D_p= 33.4–34.0%. f= 8.83–16.8%.
Newitt et al. (142)	ADC	Breast cancer	ADC= 4.8%.
ADC: Apparent diffusion coefficient. D_t: tissue diffusion. D_p: pseudo-diffusion coefficient. f: perfusion fraction. f×D_p: microvascular blood flow. DDC: distributed diffusion coefficient. α: diffusion heterogeneity index.			

2.8.3 Correlation between the perfusion parameters estimated by the IVIM and DCE-MRI techniques in breast cancer.

The promising roles of IVIM perfusion-related parameters in differentiating benign and malignant breast tumours and evaluating breast tumour response to NACT over the past decade have, in turn, reopened the question of whether IVIM could be used as a contrast-agent-free alternative to DCE-MRI for measuring breast tumour perfusion.

Few studies have investigated the correlations between IVIM and DCE-MRI perfusion-related parameters in breast tumours, and they have produced contradictory results (27-29). Table 2.5 summarises the main findings. These studies examined correlations at a single visit; however, a correlation between perfusion parameter changes caused by treatment is meaningful and suggests that IVIM could be a contrast agent-free surrogate for the DCE-MRI method in monitoring serial changes in tumour perfusion. Furthermore, none of these studies' DCE data provided an absolute estimation of tumour blood flow, but rather K^{trans}. The K^{trans} may not solely reflect tumour blood flow but also vessel permeability (151). Thus, these studies did not perform a direct comparison with the IVIM parameter purported to measure microvascular blood flow ($f \times D_p$). Also, the DCE and IVIM parameters in two studies were estimated from a single ROI manually drawn on the slice with the largest tumour area enclosing the whole tumour (27, 28), which may involve sampling bias (152).

The ADC is expected to be directly proportional to DCE-MRI cellularity-related measures (i.e., v_e, and v_d: $v_e + v_p$, extracellular volume fraction). However, although few studies have examined this relationship (153), one study on breast tumours has challenged this expectation by assessing it at a single visit, suggesting that ADC is incompletely understood (30).

Table 2.5 Summary of the breast studies' results assessing the correlation between IVIM and DCE-MRI parameters.

Author	Sample size	DCE-MRI temporal resolution	AIF measurement used for DCE analysis	Model used for DCE analysis	DCE parameters extracted	IVIM parameters extracted	No. of b-value (s/mm^2)	Main results
Jiang et al. (28)	59 patients (with 31 malignant and 35 benign lesions)	11 second	Individuals' AIF was not measured; Automatic AIF was used	Tofts model	K^{trans}, k_{ep}, v_e	D_p, f	12 b-values (0, 10, 30, 50, 70, 100, 150, 200, 400, 600, 1000, 1500)	Only correlation was found between f and k_{ep} (r=0.425, p<0.001).
Liu et al. (27)	36 patients (with 36 breast cancers) and 20 patients (with 23 benign lesions)	10.9 second	Individuals' AIF was not measured; the AIF from another study was used	Extended Tofts model	K^{trans}, k_{ep}, v_e, v_p	D_t, D_p, f	12 b-values (0, 10, 20, 30, 50, 70, 100, 150, 200, 400, 600, 1,000)	• f was correlated with v_p (r=0.692, p<0.001), K^{trans} (r=0.456, p<0.001), and k_{ep} (r=0.440, p<0.001). • D_p was negatively correlated with v_p (r=-0.335, p = 0.010). • D_t was negatively correlated with K^{trans} (r=-0.305, p=0.013), k_{ep} (r=-0.373, p =0.004), and v_p (-0.455, p<0.001).
Li et al. (29)	26 patients (with 14 malignant and 14 benign lesions)	14–18 seconds	Individuals' AIF was not measured; AIF from another study was used	Shutter-speed variant of the Tofts model	K^{trans}, k_{ep}	D_t, D_p, f	11 b-values (0, 10, 25, 50, 75, 100, 150, 250, 450, 800, 1000)	No significant correlations across IVIM and DCE-MRI parameters (f or D_p vs K^{trans} or k_{ep}).

K^{trans}: forward volume transfer constant. k_{ep}: reverse volume transfer constant. v_e: extravascular-extracellular volume fraction. v_p: blood plasma volume fraction. D_t: tissue diffusion. D_p: pseudo-diffusion coefficient. f: perfusion fraction. AIF: arterial input function.

2.9 Thesis aims and hypotheses

The primary aims and corresponding hypotheses of this thesis were as follows:

Aim 1 – To investigate the value of parameters obtained from the monoexponential, SEM and IVIM models derived from MRI data acquired pretreatment and after one and three NACT cycles, using volumetric sampling to assess early breast cancer response to NACT.

Hypothesis 1 – Parameters obtained from the monoexponential, SEM, and IVIM models derived from MRI data acquired pretreatment and after one and three NACT cycles, using volumetric sampling, have the potential to assess early breast cancer response to NACT.

Aim 2 – To investigate the value of monoexponential, SEM and IVIM models for the diffusion cold-spot and perfusion hot-spot regions of the tumour at pretreatment, and after one and three cycles of NACT in assessing the early breast cancer response to NACT.

Hypothesis 2 – Parameters obtained from the monoexponential, SEM, and IVIM models for the diffusion cold-spot and perfusion hot-spot regions of the tumour at pretreatment and after one and three cycles of NACT could be effective in assessing early breast cancer response to NACT.

Aim 3 – To investigate whether the IVIM technique can offer a contrast-agent-free alternative to DCE-MRI for measuring breast tumour perfusion and to explore the relationship between ADC and DCE-MRI cellularity-related measures.

Hypothesis 3 – The IVIM technique can serve as a contrast-agent-free alternative to DCE-MRI for measuring breast tumour perfusion, and the diffusion measure (ADC) correlates with DCE-MRI cellularity-related measures.

These aims were worked on using a retrospective MRI dataset of patients with breast cancer acquired as part of a Breast Cancer Now-funded project at three points in time: before NACT and after one and three NACT cycles. Figure 2.9 illustrates the pathway for performing the investigations (Aims 1 to 3). The implementation of each step in Figure 2.9 required substantial work and time. A variety of curve-fitting methods are available for estimating the IVIM parameters in breast cancer. Thus, a study involving computer simulations, along with in vivo measurements was performed first to identify the optimum IVIM curve-fitting method for the DWI data utilised in this thesis, which was then employed in the subsequent investigations in the IVIM analysis.

The work undertaken to perform the investigations (Aims 1 to 3)
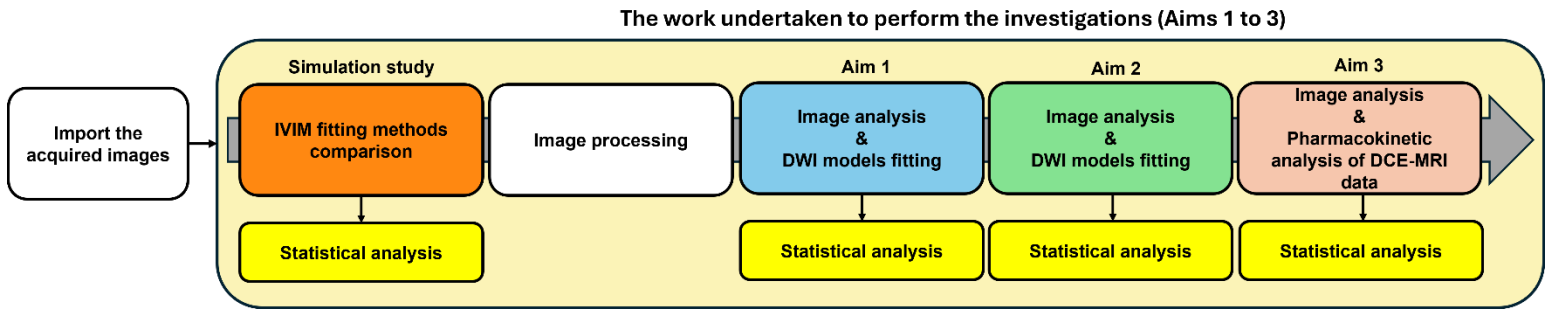
Figure 2.9 Flow diagram depicting the work to perform the investigations listed in Aims 1 to 3.

After importing the MRI dataset, a simulation study comparing IVIM curve-fitting methods was undertaken to identify the optimum method, which was employed in following investigations for the IVIM analysis. Then, DWI and DCE-MRI images were processed. The DWI images were analysed, and the monoexponential, SEM, and IVIM models were fitted to investigate the value of these DWI models using volumetric sampling to assess the early breast cancer response to NACT (Aim 1). Subsequently, the DWI and DCE-MRI images were analysed based on diffusion cold-spot and perfusion hot-spot regions of the tumour, and the monoexponential, SEM, and IVIM models were fitted to investigate the value of these DWI models derived from tumour focused ROIs to assess the early breast cancer response to NACT (Aim 2). Ultimately, DCE-MRI data were extracted from whole-tumour ROIs and diffusion cold-spot and perfusion hot-spot regions of the tumour and were analysed to derive the DCE-MRI perfusion and cellularity-related measures to investigate whether the IVIM technique can offer a contrast-agent-free alternative to DCE-MRI to measure breast tumour perfusion, and explore the relationship between the ADC and DCE-MRI cellularity-related measures (Aim 3).

Chapter 3 Comparison of curve-fitting methods for IVIM analysis in breast cancer: Simulation study

3.1 Introduction

Despite the promising applications of IVIM in breast cancer (section 2.8.2.2.1), the reported estimates of IVIM parameters vary considerably both across breast studies (27, 28, 116, 126, 154, 155), and within the same patient group (156) (Table 3.1). Furthermore, the precision of the D_p and f parameter estimates is typically less than that for the D_t estimate (144, 145, 157, 158). Alongside the characteristics of the patient population, data acquisition strategy, image noise level, and the number and distribution of b-values, signal-fitting methods have been shown to influence estimates of IVIM parameters to an extent (156, 159).

Previous studies have estimated IVIM parameters for breast cancer using either the full bi-exponential fitting method, involving the simultaneous estimation of all parameters, a segmented-fitting method that estimates IVIM parameters in a two-step manner (first estimating D_t and then D_p and f), or an oversegmented-fitting method that estimates IVIM parameters in a three-step manner (estimating D_t, f and D_p in the order). Further, some have also applied constraints on each parameter (27, 28, 116, 126, 154-156). However, the influence of the fitting method on the accuracy, bias, and precision of IVIM parameter estimates for breast cancer has scarcely been investigated (156, 160). For clinical interpretation of IVIM in breast tissue, determining which fitting method results in IVIM parameters that agree well with the underlying "true" values is critical.

Therefore, the objective of this exploratory study was to compare commonly used IVIM curve-fitting methods in breast cancer to identify the method that offers the highest accuracy, minimal bias, and superior precision of IVIM parameter estimates, with an emphasis on f and the product f×D_p, specifically for the clinical DWI data used in this thesis research. The study was performed using simulated data representing the range of IVIM parameters observed in breast cancer data obtained in Leeds, along with the same distribution of six b-values (125). Additionally, the repeatability of the IVIM parameter estimates in vivo was compared across the different fitting methods. The curve-fitting method identified as providing more precise estimates of IVIM parameters (f and f×D_p) with minimal error and bias values (systematic error in parameter estimates based on only six b-values), and found to achieve the best in vivo repeatability, was employed in subsequent studies on extracting IVIM parameters (Chapters 4 to 6).

Table 3.1 Summary of several studies on breast cancer IVIM imaging highlights variations in the IVIM-derived parameter estimates.

Authors, year	Lesion no.	Field strength	DWI sequence	b-values s/mm²	Image analysis	Fitting method	D_t (×10⁻³ mm²/s)	D_p (×10⁻³ mm²/s)	f (%)
Sigmund et al., 2011 (126)	24 19 IDC	3.0T	Single shot spin-echo TSE	0, 30, 70, 100, 150, 200, 300, 400, 500, 800	Mean SI	Over-segmented	1.15±0.35	15.1±10.4	9.8±4.8
Iima et al., 2013 (154)	16	3.0T	Single shot spin-echo EPI	0, 5, 10, 20, 30, 50, 70, 100, 200, 400, 600, 800, 1000, 1500, 2000, 2500	Voxel-by-voxel	Segmented	0.98±0.22	6.8±1.2	13.6±2.2
Nilsen et al., 2013 (155)	24 18 IDC	1.5T	Single shot spin-echo EPI	0, 50, 100, 250, 800	Voxel-by-voxel	Full	0.90±0.30	N/A	N/A
* Suo et al., 2016 (156)	30 IDC	3.0T	Single shot spin-echo EPI	0, 50, 100, 150, 200, 500, and 800	Voxel-by-voxel	Full	0.70±0.11	98.24±59.25	16.33±5.21
* Suo et al., 2016 (156)	30 IDC	3.0T	Single shot spin-echo EPI	0, 50, 100, 150, 200, 500, and 800	Voxel-by-voxel	Segmented	0.83±0.19	159.50±90.32	7.61±2.33
* Suo et al., 2016 (156)	30 IDC	3.0T	Single shot spin-echo EPI	0, 50, 100, 150, 200, 500, and 800	Voxel-by-voxel	Over-segmented	0.77±0.15	69.28±46.19	6.10±3.19
Liu et al., 2016 (27)	36 27 IDC	1.5T	Single shot spin-echo EPI	0, 10, 20, 30, 50, 70, 100, 150, 200, 400, 600 and 1,000	Pixel-by-pixel	Segmented	0.85 (0.79, 0.96)	109.78 (99.13, 128.80)	10.23 (7.72, 13.57)
KIM et al., 2016 (116)	274 228 IDC	3.0T	Single shot EPI	0,30,70, 100, 150, 200, 300, 400, 500 and 800	Mean SI	Over-segmented	0.90(0.21, 1.77)	13.89(2.12, 72.91)	11.87(4.83, 42.42)
Jiang et al., 2018 (28)	31 26 IDC	3.0T	Single shot spin-echo EPI	0, 10, 30, 50, 70, 100, 150, 200, 400, 600, 1000, and 1500	Voxel-by-voxel	Full	N/A	63.70 (44.90)	6.30 (2.10)

IDC: invasive ductal carcinoma. ss-EPI: single-shot echo-planar imaging. TSE: turbo spin-echo. D_t: tissue diffusion. D_p: pseudo-diffusion coefficient. f: perfused fraction. D_t, D_p and f values are summarised as mean ± standard deviation or median (Interquartile range or quartile interval). N/A: not available. (*) This is one study performed on one patient group.

3.2 Material and Methods

3.2.1 Simulation study

The simulated data were built on DWI data from a cohort of patients with breast cancer who underwent MRI scans at three time points during NACT (i.e., baseline, after one cycle, and after three cycles of treatment) in Leeds, which form the primary foundation of this thesis's experimental work (Chapters 4 to 6). At the initial stage of this PhD, the acquired clinical DWI data at the three MRI time points were aggregated for all patients, and the monoexponential, SEM, and IVIM models were fitted to the data at that time for the purpose of the published, un-updated version of the Chapter 4 study, which demonstrated promising results for IVIM (125). Subsequently, the idea for Chapter 3 to explore the optimal IVIM fitting method for these clinical DWI data arose and was implemented as follows. The DWI data that were best fitted by the IVIM model compared to the monoexponential and SEM models were selected based on F-test results. The selected IVIM data were then organised in descending order of perfusion fraction (f) values, and the average values of $S(0)$, D_t, D_p, and f for data within similar ranges of f were calculated. These average values ultimately formed 14 distinct sets of $S(0)$, f, D_t, and D_p (Table 3.2).

Table 3.2 True value sets of IVIM parameters for simulation study.

No.	S(0)	D_t $(\times 10^{-3}\,mm^2/s)$	D_p $(\times 10^{-3}\,mm^2/s)$	f (no units)	$f \times D_p$ $(\times 10^{-3}\,mm^2/s)$
1	200	1.08	6.10	0.213	1.30
2	200	1.21	5.57	0.208	1.15
3	200	1.20	6.80	0.197	1.34
4	200	0.98	6.47	0.184	1.19
5	200	0.90	5.95	0.174	1.03
6	200	1.01	5.45	0.164	0.89
7	200	0.95	6.47	0.154	1.00
8	200	0.90	6.46	0.145	0.94
9	200	0.81	5.97	0.132	0.78
10	200	0.91	5.59	0.126	0.70
11	200	0.79	6.49	0.114	0.74
12	200	0.70	6.53	0.107	0.69
13	200	0.82	8.08	0.093	0.75
14	200	0.68	7.23	0.081	0.59
15	200	1.16	0	0	0
$S(0)$: the signal intensity with b-value of zero. D_t: tissue diffusion. D_p: pseudo-diffusion coefficient. f: perfused fraction. $f \times D_p$: microvascular blood flow.					

Using MATLAB, the simulated signal data were generated according to the IVIM model using 14 IVIM parameter sets, along with one additional dataset where f was set to 0 (i.e., assuming no perfused fraction; Table 3.2) to evaluate the bias of the fitting algorithms in estimating the f value. For each IVIM parameter-value set, the signals were sampled at 12 b-values (b = 0, 10, 20, 30, 50, 70, 100, 150, 200, 400, 800 and 1000 s/mm^2).These 12 b-values were selected based on a previous study in breast imaging that explored the ability of IVIM to predict response to NACT (23), and they encompass the six b-values used in Chapters 4 to 6. The sampled signals (i.e., noise-free) were fitted using six fitting algorithms detailed in the subsequent section 3.2.2 (i.e., full, segmented, and oversegmented methods each with and without constraints). The same data-fitting process was performed using six b-values (b = 0, 50, 100, 200, 400 and 800 s/mm^2) employed in the studies of Chapters 4 to 6, to test the performance of fitting algorithms at fewer b-values.

Then, Rician noise was added to the sampled signals (i.e., at each of the 12 b-values) to achieve two different noise levels that are observed in the clinical breast DWI data at the image analysis stage of Chapters 4 and 5: a level similar to that observed in the whole-tumour region of interest (ROI) averaged signals and a level similar to that observed in the 5×5 pixel single-slice ROI averaged signals (i.e., the tumour diffusion cold-spot). These levels were identified by analysing curve plots of signal intensity (SI) derived from both whole-tumour and cold-spot regions for a number of acquired breast DWI datasets, focusing on the standard deviation of residuals between measured and fitted signals. This analysis ensured the added Rician noise closely reflected the noise characteristics seen in the targeted clinical breast DWI data, thereby aligning the simulation closely with the clinical data. The number entered for the Rician noise distribution in the noise simulation of whole-tumour ROI averaged signals was 1.5, and for cold-spot ROI averaged signals, it was 3.5. The number represents the noise level and is the same as the SD of a Gaussian distribution if SNR > 3. Finally, noisy signals were fitted using the six fitting algorithms, and the fitting process was repeated using six b-values. Each pseudo-random noisy simulation trial was repeated 1,000 times. An example of the noisy signal fitting process is shown in Figure 3.1. The MATLAB-based code for IVIM simulated signal data generation and curve-fitting was developed by the candidate.
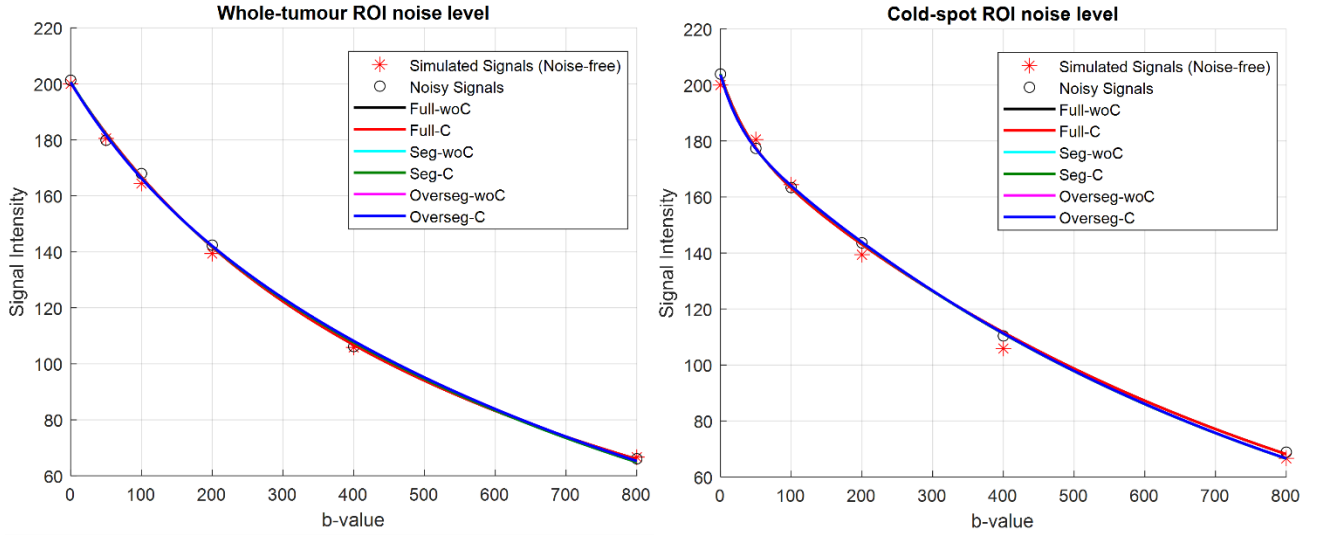
Figure 3.1 Example of noisy signal fitting for dataset number 1 (from Table 3.2) using six fitting algorithms at six b-values and two noise levels (whole-tumour ROI and cold-spot ROI). The noisy signals were fitted using full-fitting without constraints (Full-woC), full-fitting with constraints (Full-C), segmented-fitting without constraints (Seg-woC), segmented-fitting with constraints (Seg-C), oversegmented-fitting without constraints (Overseg-woC), and oversegmented-fitting with constraints (Overseg-C). The two plots represent one fit out of 1,000 pseudo-random noisy simulations performed. The simulated noise-free signals are included for reference and marked with (*).

The relative bias (RB) and relative error (RE) in the parameter estimate were calculated compared to the true parameter values in Table 3.2, as follows (159):

- RB = $\dfrac{(Fitted\ parameter\ value - True\ parameter\ value)}{True\ parameter\ value}$,

- RE = $\dfrac{\sqrt{(Fitted\ parameter\ value - True\ parameter\ value)^2}}{True\ parameter\ value}$.

Moreover, the standard deviation (SD) of the estimated IVIM parameters was calculated after 1,000 trials, indicating the precision of the parameter estimates.

The normality of the calculated measures (i.e., the RB, RE and SD) was assessed using the Shapiro–Wilk test and histogram evaluations, and a log transformation was applied to those measures that were not normally distributed. The RB, RE and SD values were summarised as the means with 95% confidence intervals (CIs), categorised according to the fitting methods, number of b-values (i.e., 6 and 12), and noise level (i.e., noise-free, whole-tumour ROI and single-slice ROI). The

comparison of the six fitting methods for each b-value set and noise level was based on the means and 95% CIs of the RB, RE and SD.

3.2.2 IVIM fitting methods

The decay of DWI signals is described using the following IVIM bi-exponential equation:

$$S(b) = S(0) . \left[(1 - f) \, exp(-b . D_t) + f \, exp(-b . D_p)\right], \qquad \text{Equation [3]}$$

where S(b) represents the SI at a given b-value, and S(0) denotes the SI at a b-value of 0 s/mm² (127). All simulated data were fitted using full-fitting, segmented-fitting, and oversegmented-fitting methods (156), each applied with and without bound constraints on the parameter values; thus, the same data were fitted using six different fitting methods, as follows.

A. Full-fitting without constraints

In the full-fitting method without constraints (full-woC), the IVIM model in Eq. [3] is fitted to the signal decay data, and all four parameters (S(0), D_t, D_p and f) are estimated simultaneously using a nonlinear least-squares approach without any parameter-value bound constraints. Then, the product f×D_p is calculated.

B. Full-fitting with constraints

The full-fitting method with constraints (full-C) is similar to the full-woC method but includes bound constraints of the parameter values: $0 \leq D_t \leq 5$ (×10^{-3} mm²/s), $D_t < D_p \leq 100 \times 10^{-3}$ mm²/s, and $0 \leq f \leq 1$ (156). Then, the product f×D_p is calculated. The constraints were chosen based on physiological plausibility and consistent with established ranges reported in a prior IVIM study on breast cancer (156), ensuring robust and realistic parameter estimates for meaningful and interpretable results while maintaining methodological comparability.

C. Segmented-fitting without constraints

In the segmented-fitting method without constraints (seg-woC), assuming that the pseudo-diffusion (D_p) contribution to the signal is negligible when the b-value is greater than 200 s/mm² (19), the D_t is estimated by first fitting the b-value data (>200 s/mm²) using the monoexponential fit as described in Eq. [5].

$$S(b) = S(I) . exp(-b . D_t) \qquad \text{Equation [5]}$$

S(I) is the fitted SI at a b-value of 0 s/mm². Finally, S(0), D_p and f are simultaneously estimated as in the full-woC method, and the product f×D_p is calculated.

D. Segmented-fitting with constraints

In the segmented-fitting method with constraints (seg-C), D_t is estimated first as in the seg-woC method but with the following bound constraints: $0 \leq D_t \leq 5$ ($\times 10^{-3}$ mm^2/s), followed by S(0) and the constrained estimation of D_p and f as in the full-C method. Then, product f$\times D_p$ is calculated.

E. Oversegmented-fitting without constraints

In the oversegmented-fitting method without constraints (overseg-woC), the D_t and f are estimated first, and then D_p is estimated. The D_t value is obtained as in the seg-woC method. Then, the monoexponential fit is extrapolated back to b = 0 to estimate f as f = (S(0)"measured" − intercept)/S(0)"measured", where where the "intercept" is the fitted S(I) in Eq. [5] (159). Finally, by fixing the D_t and f values, D_p is obtained as in the full-woC method, and the product f$\times D_p$ is calculated.

F. Oversegmented-fitting with constraints

In the oversegmented-fitting method with constraints (overseg-C), the value of D_t is obtained as in the seg-C method. Then, f is estimated as in the overseg-woC method, followed by the constrained estimation of D_p as in the full-C method. Then, the product f$\times D_p$ is calculated. If f < 0, f is forced to be 0 and D_p is not estimated; thus, the fitting is considered monoexponential.

3.2.3 Repeatability analysis in vivo

An upper estimate of the repeatability of IVIM parameters for each fitting method, derived from the whole-tumour ROI averaged signals, was assessed following the image analysis and the pathologist's evaluation of tumour response in Chapter 4 (illustrated in sections 4.2.3 and 4.2.4). This assessment was achieved by calculating the within-subject coefficient of variation (wCV) (161) in the data from the baseline and after one cycle of NACT in a subgroup of patients identified as pathological non-responders (pNRs) and demonstrated minimal changes in tumour volume following the first cycle. The RECIST guidelines indicate that, for a tumour to be classified as demonstrating a partial response, a reduction in volume of at least 66% is required, or an increase of more than 73% is needed for it to be considered a progressive disease (5).

Ten pNRs were included in the repeatability analysis, with changes in tumour volume observed between a decrease of 21.60% and an increase of 18.90%, averaging a volume change of -3.64%. The wCV values of the IVIM parameters across six fitting methods were compared.

3.3 Results

3.3.1 Simulation study

Without noise, the full-fitting methods produced the correct results (i.e., true parameter values listed in Table 3.2) as they displayed minimal error and bias for all IVIM parameter estimates (RE and RB ≈ 0), which in turn provided validation of the software (MATLAB code). In contrast, the segmented and oversegmented methods introduced error and bias, regardless of the number of b-values (Tables 3.3 and 3.4, Figures 3.2 and 3.3). However, when noise was added to the data, the full-woC method produced the highest errors in estimating D_t, f and f×D_p parameters, except for f×D_p at the cold-spot ROI noise level with six b-values (Tables 3.5-3.8, Figures 3.4-3.7). Moreover, the overseg-woC method consistently resulted in the highest errors in D_p estimates. The errors in the D_t estimates were marginally different between the segmented and oversegmented methods, and the D_t estimates had the lowest errors. In contrast, the errors in D_p were the highest, irrespective of the b-value count.

Table 3.3 Comparisons of mean relative bias and relative error of IVIM parameters among different fitting methods (6 b-values, Noise-free).

Parameter	Fitting methods	RE	RB
		Mean (95% CIs)	Mean (95% CIs)
D_t ($\times 10^{-3}$ mm^2/s)	Full-woC	0.000 (0.000, 0.000)	0.000 (0.000, 0.000)
	Full-C	0.000 (0.000, 0.000)	0.000 (0.000, 0.000)
	Seg-woC	0.049 (0.039, 0.060)	0.049 (0.039, 0.060)
	Seg-C	0.049 (0.039, 0.060)	0.049 (0.039, 0.060)
	Overseg-woC	0.049 (0.039, 0.060)	0.049 (0.039, 0.060)
	Overseg-C	0.049 (0.039, 0.060)	0.049 (0.039, 0.060)
D_p ($\times 10^{-3}$ mm^2/s)	Full-woC	0.000 (0.000, 0.000)	0.000 (0.000, 0.000)
	Full-C	0.000 (0.000, 0.000)	0.000 (0.000, 0.000)
	Seg-woC	0.206 (0.174, 0.238)	0.206 (0.174, 0.238)
	Seg-C	0.206 (0.174, 0.238)	0.206 (0.174, 0.238)
	Overseg-woC	0.276 (0.231, 0.320)	0.276 (0.231, 0.320)
	Overseg-C	0.276 (0.231, 0.320)	0.276 (0.231, 0.320)
f (no units)	Full-woC	0.000 (0.000, 0.000)	0.000 (0.000, 0.000)
	Full-C	0.000 (0.000, 0.000)	0.000 (0.000, 0.000)
	Seg-woC	0.181 (0.150, 0.212)	-0.181 (-0.212, -0.150)
	Seg-C	0.181 (0.150, 0.212)	-0.181 (-0.212, -0.150)
	Overseg-woC	0.224 (0.188, 0.259)	-0.224 (-0.259, -0.188)
	Overseg-C	0.224 (0.188, 0.259)	-0.224 (-0.259, -0.188)
f$\times$D$_p$ ($\times 10^{-3}$ mm^2/s)	Full-woC	0.000 (0.000, 0.000)	0.000 (0.000, 0.000)
	Full-C	0.000 (0.000, 0.000)	0.000 (0.000, 0.000)
	Seg-woC	0.020 (0.010, 0.030)	-0.015 (-0.028, -0.002)
	Seg-C	0.020 (0.010, 0.030)	-0.015 (-0.028, -0.002)
	Overseg-woC	0.016 (0.007, 0.025)	-0.014 (-0.024, -0.003)
	Overseg-C	0.016 (0.007, 0.025)	-0.014 (-0.024, -0.003)

RE: Relative error. RB: relative bias. CI: confidence interval. D_t: tissue diffusion. D_p: pseudo-diffusion coefficient. f: perfused fraction. f$\times$D$_p$: microvascular blood flow. Full-woC: full-fitting without constraints. Full-C: full-fitting with constraints. Seg-woC: segmented-fitting without constraints. Seg-C: segmented-fitting with constraints. Overseg-woC: Oversegmented-fitting without constraints. Overseg-C: Oversegmented-fitting with constraints.

Figure 3.2 Bar plots of the mean relative error (RE) and relative bias (RB) results for the IVIM parameters (D_t, D_p, f, and f×D_p) obtained with full-fitting without constraints (Full-woC), full-fitting with constraints (Full-C), segmented-fitting without constrain (Full-woC), full-fitting with constraints (Full-C), segmented-fitting without constraints (Seg-woC), segmented-fitting with constraints (Seg-C), oversegmented-fitting without constraints (Overseg-woC), and oversegmented-fitting with constraints (Overseg-C) at 6 b-values and Noise-free. Error bars represent 95% confidence interval for the mean.

Table 3.4 Comparisons of mean relative bias and relative error of IVIM parameters among different fitting methods (12 b-values, Noise-free).

Parameter	Fitting methods	RE	RB
		Mean (95% CIs)	Mean (95% CIs)
D_t (×10^{-3} mm²/s)	Full-woC	0.000 (0.000, 0.000)	0.000 (0.000, 0.000)
	Full-C	0.000 (0.000, 0.000)	0.000 (0.000, 0.000)
	Seg-woC	0.041 (0.032, 0.049)	0.041 (0.032, 0.049)
	Seg-C	0.041 (0.032, 0.049)	0.041 (0.032, 0.049)
	Overseg-woC	0.041 (0.032, 0.049)	0.041 (0.032, 0.049)
	Overseg-C	0.041 (0.032, 0.049)	0.041 (0.032, 0.049)
D_p (×10^{-3} mm²/s)	Full-woC	0.000 (0.000, 0.000)	0.000 (0.000, 0.000)
	Full-C	0.000 (0.000, 0.000)	0.000 (0.000, 0.000)
	Seg-woC	0.193 (0.163, 0.223)	0.193 (0.163, 0.223)
	Seg-C	0.193 (0.163, 0.223)	0.193 (0.163, 0.223)
	Overseg-woC	0.257 (0.216, 0.298)	0.257 (0.216, 0.298)
	Overseg-C	0.257 (0.216, 0.298)	0.257 (0.216, 0.298)
f (no units)	Full-woC	0.000 (0.000, 0.000)	0.000 (0.000, 0.000)
	Full-C	0.000 (0.000, 0.000)	0.000 (0.000, 0.000)
	Seg-woC	0.164 (0.134, 0.193)	-0.164 (-0.193, -0.134)
	Seg-C	0.164 (0.134, 0.193)	-0.164 (-0.193, -0.134)
	Overseg-woC	0.202 (0.169, 0.234)	-0.202 (-0.234, -0.169)
	Overseg-C	0.202 (0.169, 0.234)	-0.202 (-0.234, -0.169)
f×D_p (×10^{-3} mm²/s)	Full-woC	0.000 (0.000, 0.000)	0.000 (0.000, 0.000)
	Full-C	0.000 (0.000, 0.000)	0.000 (0.000, 0.000)
	Seg-woC	0.014 (0.007, 0.022)	-0.004 (-0.016, 0.007)
	Seg-C	0.014 (0.007, 0.022)	-0.004 (-0.016, 0.007)
	Overseg-woC	0.012 (0.006, 0.018)	1.804 x10^{-4} (-0.010, 0.010)
	Overseg-C	0.012 (0.018, 0.006)	9.847 x10^{-5} (-0.009, 0.009)

RE: Relative error. RB: relative bias. CI: confidence interval. D_t: tissue diffusion. D_p: pseudo-diffusion coefficient. f: perfused fraction. f×D_p: microvascular blood flow. Full-woC: full-fitting without constraints. Full-C: full-fitting with constraints. Seg-woC: segmented-fitting without constraints. Seg-C: segmented-fitting with constraints. Overseg-woC: Oversegmented-fitting without constraints. Overseg-C: Oversegmented-fitting with constraints.
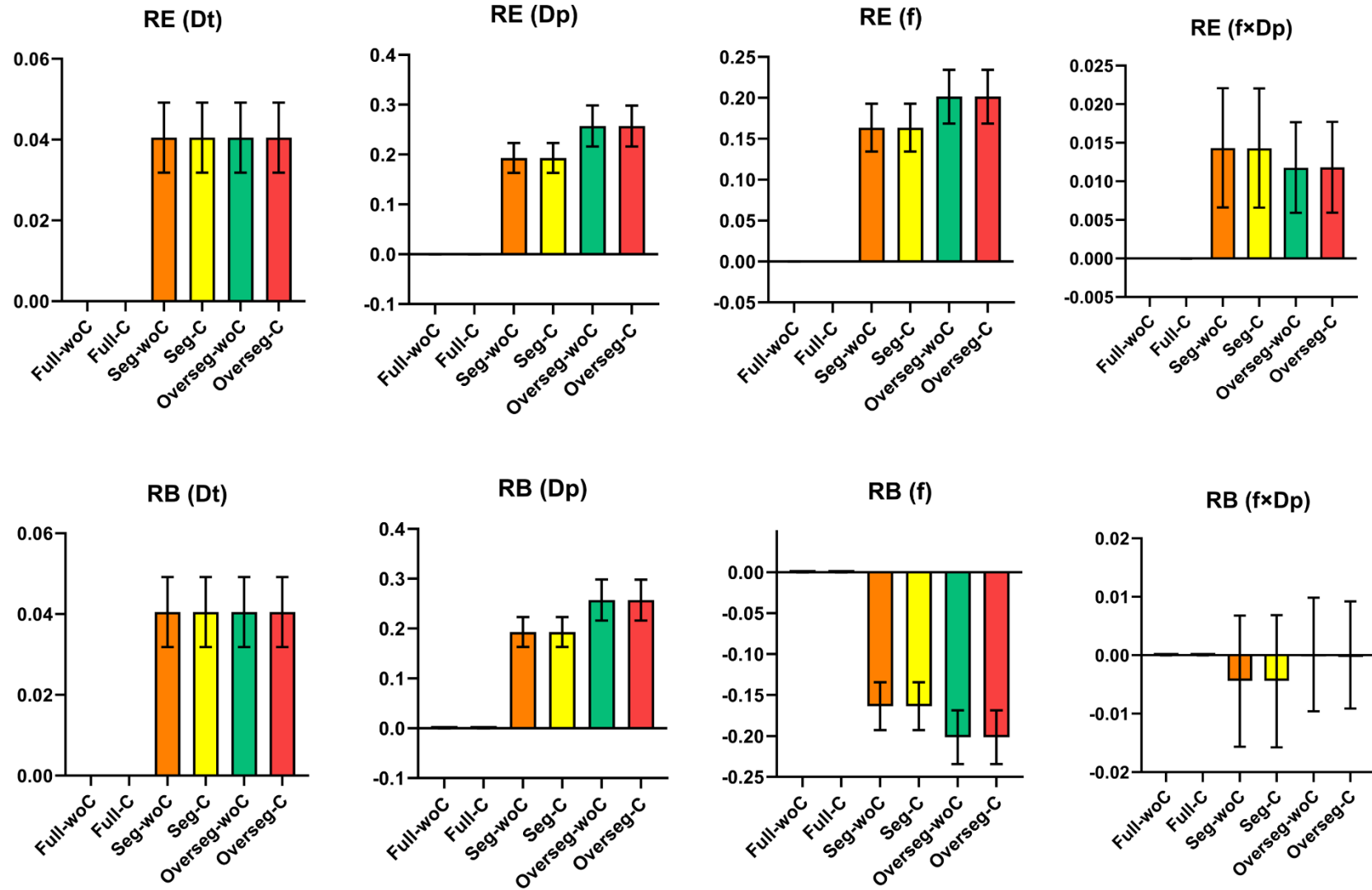
Figure 3.3 Bar plots of the mean relative error (RE) and relative bias (RB) results for the IVIM parameters (D_t, D_p, f, and f×D_p) obtained with full-fitting without constraints (Full-woC), full-fitting with constraints (Full-C), segmented-fitting without constrains (Seg-woC), segmented-fitting with constraints (Seg-C), oversegmented-fitting without constraints (Overseg-woC), and oversegmented-fitting with constraints (Overseg-C) at 12 b-values and Noise-free. Error bars represent 95% confidence interval for the mean.

Table 3.5 Comparisons of mean relative bias, relative error, and standard deviation of IVIM parameters among different fitting methods (6 b-values, whole-tumour ROI averaged signals noise level).

Parameter	Fitting methods	RE	RB	SD
		Mean (95% CIs)	Mean (95% CIs)	Mean (95% CIs)
D_t ($\times 10^{-3}$ mm^2/s)	Full-woC	0.317 (0.215, 0.469)	-0.155 (-0.027, -0.282)	1.078 (0.557, 2.084)
	Full-C	0.168 (0.147, 0.189)	-0.102 (-0.121, -0.083)	0.248 (0.214, 0.274)
	Seg-woC	0.065 (0.060, 0.070)	0.049 (0.039, 0.059)	0.056 (0.051, 0.062)
	Seg-C	0.066 (0.060, 0.072)	0.050 (0.039, 0.060)	0.057 (0.051, 0.062)
	Overseg-woC	0.065 (0.060, 0.071)	0.050 (0.040, 0.060)	0.056 (0.051, 0.061)
	Overseg-C	0.066 (0.061, 0.071)	0.050 (0.040, 0.060)	0.057 (0.052, 0.061)
D_p ($\times 10^{-3}$ mm^2/s)	Full-woC	0.595 (0.398, 0.891)	0.176 (0.081, 0.383)	12.164 (4.394, 33.678)
	Full-C	0.482 (0.404, 0.560)	0.145 (0.098, 0.192)	4.980 (3.704, 6.695)
	Seg-woC	0.519 (0.339, 0.795)	0.424 (0.270, 0.665)	7.206 (2.819, 18.421)
	Seg-C	0.439 (0.379, 0.499)	0.344 (0.298, 0.389)	4.036 (3.052, 5.336)
	Overseg-woC	0.795 (0.486, 1.300)	0.758 (0.463, 1.242)	21.195 (6.045, 74.31)
	Overseg-C	0.476 (0.423, 0.528)	0.427 (0.386, 0.469)	4.109 (3.011, 5.607)
f (no units)	Full-woC	0.832 (0.619, 1.045)	0.561 (0.380, 0.741)	0.195 (0.168, 0.222)
	Full-C	0.735 (0.591, 0.879)	0.490 (0.357, 0.624)	0.166 (0.147, 0.184)
	Seg-woC	0.254 (0.228, 0.284)	-0.166 (-0.192, -0.140)	0.051 (0.036, 0.071)
	Seg-C	0.247 (0.230, 0.265)	-0.154 (-0.188, -0.119)	0.035 (0.032, 0.038)
	Overseg-woC	0.257 (0.239, 0.275)	-0.228 (-0.261, -0.195)	0.027 (0.026, 0.029)
	Overseg-C	0.258 (0.240, 0.277)	-0.228 (-0.263, -0.194)	0.028 (0.026, 0.029)
f×D_p ($\times 10^{-3}$ mm^2/s)	Full-woC	0.265 (0.176, 0.400)	0.184 (0.112, 0.302)	0.613 (0.258, 1.460)
	Full-C	0.216 (0.176, 0.265)	0.165 (0.123, 0.207)	0.259 (0.223, 0.294)
	Seg-woC	0.189 (0.122, 0.292)	0.102 (-0.048, 0.276)	0.376 (0.176, 0.805)
	Seg-C	0.158 (0.131, 0.191)	0.025 (-0.002, 0.053)	0.201 (0.177, 0.227)
	Overseg-woC	0.218 (0.138, 0.343)	0.130 (-0.020, 0.303)	0.770 (0.314, 1.887)
	Overseg-C	0.155 (0.130, 0.185)	0.009 (-0.008, 0.026)	0.194 (0.177, 0.212)

RE: Relative error. RB: relative bias. SD: standard deviation. CI: confidence interval. D_t: tissue diffusion. D_p: pseudo-diffusion coefficient. f: perfused fraction. f×D_p: microvascular blood flow. Full-woC: full-fitting without constraints. Full-C: full-fitting with constraints. Seg-woC: segmented-fitting without constraints. Seg-C: segmented-fitting with constraints. Overseg-woC: Oversegmented-fitting without constraints. Overseg-C: Oversegmented-fitting with constraints.
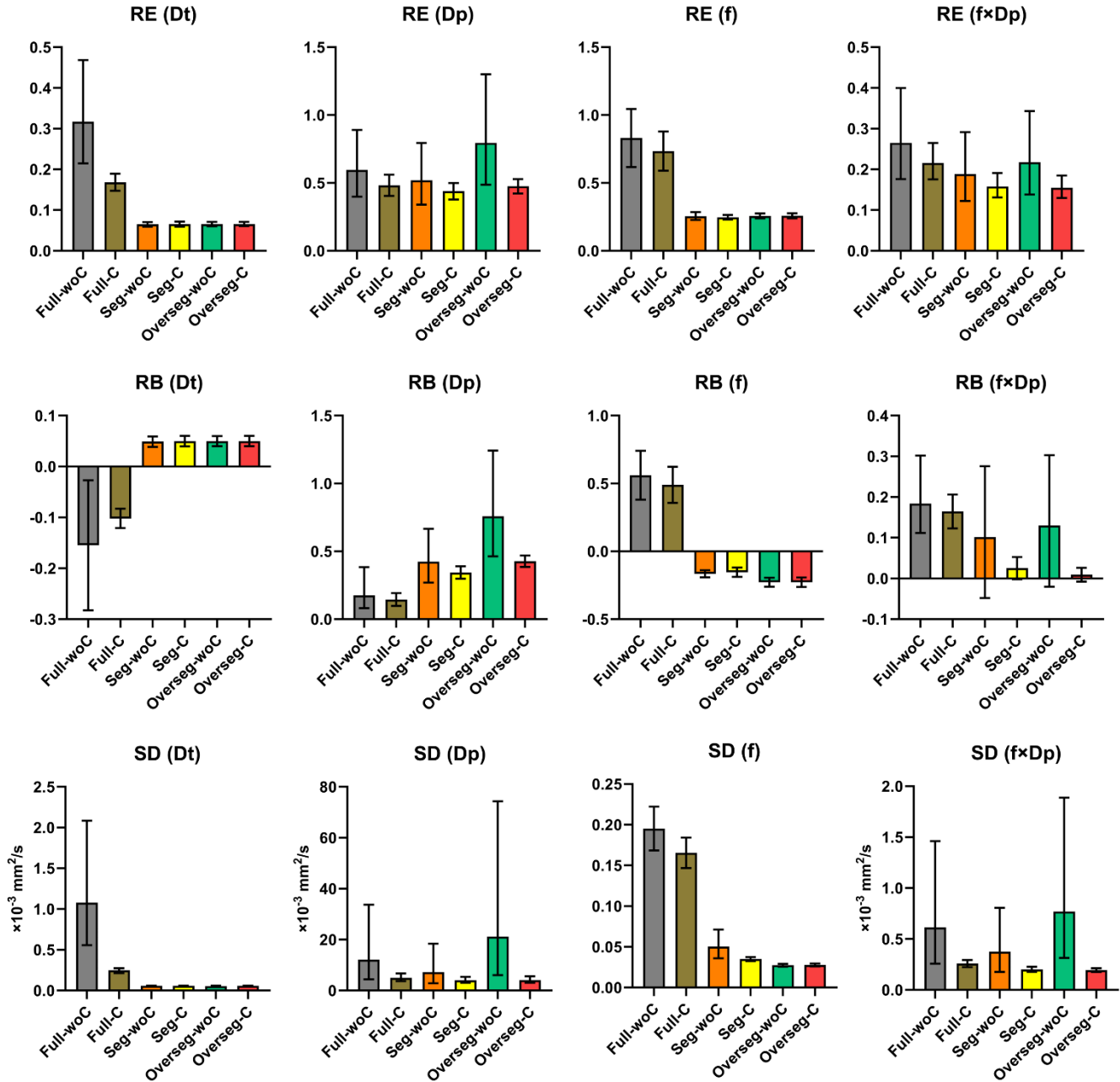
Figure 3.4 Bar plots of the mean relative error (RE), relative bias (RB), and standard deviation (SD) results for the IVIM parameters (D_t, D_p, f, and f×D_p) obtained with full-fitting without constraints (Full-woC), full-fitting with constraints (Full-C), segmented-fitting without constraints (Seg-woC), segmented-fitting with constraints (Seg-C), oversegmented-fitting without constraints (Overseg-woC), and oversegmented-fitting with constraints (Overseg-C) at 6 b-values and whole-tumour ROI averaged signals noise level. Error bars represent 95% confidence interval for the mean.

Table 3.6 Comparisons of mean relative bias, relative error, and standard deviation of IVIM parameters among different fitting methods (6 b-values, cold-spot ROI averaged signals noise level).

Parameter	Fitting methods	RE	RB	SD
		Mean (95% CIs)	Mean (95% CIs)	Mean (95% CIs)
D_t ($\times 10^{-3}$ mm^2/s)	Full-woC	3.009 (2.313, 3.916)	-1.743 (-2.456, -1.031)	11.278 (6.859, 18.545)
	Full-C	0.362 (0.341, 0.382)	-0.252 (-0.273, -0.232)	0.422 (0.379, 0.465)
	Seg-woC	0.121 (0.119, 0.124)	0.050 (0.040, 0.060)	0.131 (0.119, 0.144)
	Seg-C	0.129 (0.126, 0.132)	0.034 (0.019, 0.049)	0.161 (0.146, 0.176)
	Overseg-woC	0.121 (0.119, 0.124)	0.050 (0.039, 0.060)	0.131 (0.119, 0.144)
	Overseg-C	0.124 (0.121, 0.126)	0.044 (0.033, 0.056)	0.141 (0.129, 0.153)
D_p ($\times 10^{-3}$ mm^2/s)	Full-woC	7.464 (5.802, 9.127)	6.882 (5.256, 8.509)	393.352 (273.328, 513.377)
	Full-C	1.605 (1.409, 1.802)	1.088 (0.923, 1.252)	21.332 (19.085, 23.578)
	Seg-woC	6.797 (4.838, 9.548)	6.440 (4.549, 9.117)	325.067 (215.799, 489.661)
	Seg-C	1.566 (1.348, 1.785)	1.262 (1.088, 1.436)	21.054 (18.418, 23.689)
	Overseg-woC	16.761 (13.675, 19.847)	16.493 (13.444, 19.543)	823.281 (711.384, 935.179)
	Overseg-C	1.303 (1.181, 1.425)	1.012 (0.927, 1.097)	18.451 (16.664, 20.237)
f (no units)	Full-woC	2.068 (1.591, 2.545)	1.510 (1.139, 1.88)	0.400 (0.364, 0.435)
	Full-C	1.507 (1.257, 1.757)	1.144 (0.890, 1.399)	0.268 (0.257, 0.280)
	Seg-woC	1.897 (1.045, 3.442)	-0.642 (-0.275, -1.103)	1.972 (1.325, 2.619)
	Seg-C	0.559 (0.462, 0.677)	0.082 (-0.033, 0.210)	0.129 (0.111, 0.146)
	Overseg-woC	0.416 (0.380, 0.453)	-0.242 (-0.276, -0.209)	0.065 (0.061, 0.069)
	Overseg-C	0.400 (0.371, 0.431)	-0.229 (-0.266, -0.192)	0.061 (0.057, 0.066)
f×D_p ($\times 10^{-3}$ mm^2/s)	Full-woC	3.093 (2.181, 4.005)	2.919 (2.047, 3.790)	22.097 (13.560, 30.635)
	Full-C	0.780 (0.625, 0.936)	0.675 (0.536, 0.815)	1.044 (0.957, 1.131)
	Seg-woC	2.597 (1.646, 4.097)	1.888 (1.168, 3.053)	17.033 (12.143, 23.891)
	Seg-C	0.554 (0.437, 0.671)	0.304 (0.209, 0.400)	0.899 (0.822, 0.975)
	Overseg-woC	3.590 (2.625, 4.910)	3.176 (2.267, 4.45)	32.108 (25.390, 38.826)
	Overseg-C	0.499 (0.411, 0.587)	0.093 (0.054, 0.132)	0.761 (0.707, 0.814)

RE: Relative error. RB: relative bias. SD: standard deviation. CI: confidence interval. D_t: tissue diffusion. D_p: pseudo-diffusion coefficient. f: perfused fraction. f×D_p: microvascular blood flow. Full-woC: full-fitting without constraints. Full-C: full-fitting with constraints. Seg-woC: segmented-fitting without constraints. Seg-C: segmented-fitting with constraints. Overseg-woC: Oversegmented-fitting without constraints. Overseg-C: Oversegmented-fitting with constraints.
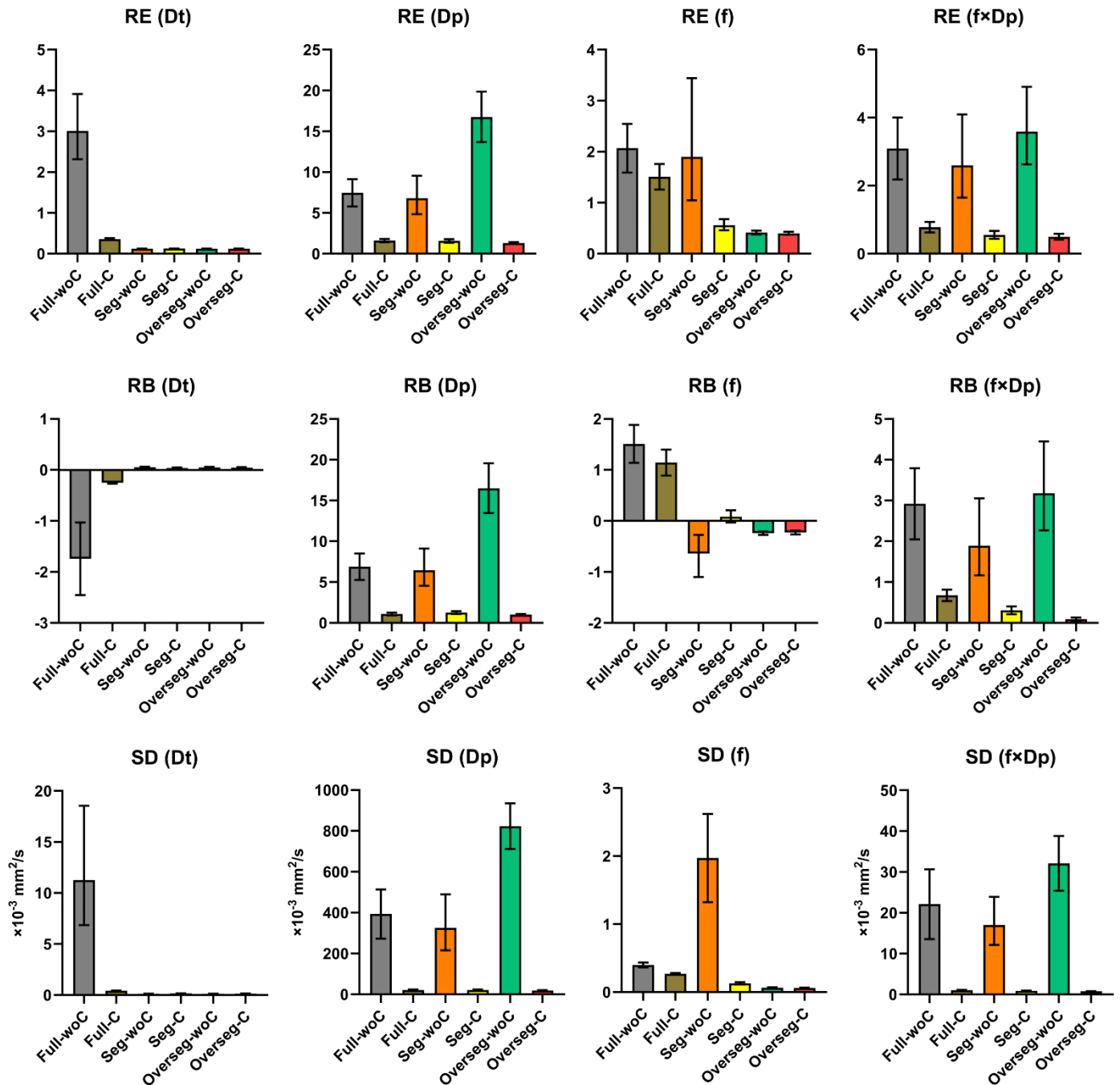
Figure 3.5 Bar plots of the mean relative error (RE), relative bias (RB), and standard deviation (SD) results for the IVIM parameters (D_t, D_p, f, and f×D_p) obtained with full-fitting without constraints (Full-woC), full-fitting with constraints (Full-C), segmented-fitting without constraints (Seg-woC), segmented-fitting with constraints (Seg-C), oversegmented-fitting without constraints (Overseg-woC), and oversegmented-fitting with constraints (Overseg-C) at 6 b-values and cold-spot ROI averaged signals noise level. Error bars represent 95% confidence interval for the mean.

Table 3.7 Comparisons of mean relative bias, relative error, and standard deviation of IVIM parameters among different fitting methods (12 b-values, whole-tumour ROI averaged signals noise level).

Parameter	Fitting methods	RE Mean (95% CIs)	RB Mean (95% CIs)	SD Mean (95% CIs)
D_t ($\times 10^{-3}$ mm^2/s)	Full-woC	0.105 (0.087, 0.123)	-0.041 (-0.059, -0.024)	0.233 (0.149, 0.363)
	Full-C	0.088 (0.078, 0.098)	-0.041 (-0.049, -0.033)	0.130 (0.114, 0.149)
	Seg-woC	0.049 (0.044, 0.054)	0.040 (0.031, 0.049)	0.039 (0.035, 0.043)
	Seg-C	0.049 (0.044, 0.054)	0.040 (0.032, 0.049)	0.038 (0.034, 0.041)
	Overseg-woC	0.049 (0.044, 0.055)	0.041 (0.032, 0.049)	0.039 (0.035, 0.042)
	Overseg-C	0.049 (0.043, 0.055)	0.040 (0.031, 0.048)	0.039 (0.035, 0.043)
D_p ($\times 10^{-3}$ mm^2/s)	Full-woC	0.324 (0.282, 0.365)	0.062 (0.050, 0.074)	2.828 (2.297, 3.360)
	Full-C	0.324 (0.280, 0.368)	0.057 (0.042, 0.077)	2.796 (2.290, 3.301)
	Seg-woC	0.320 (0.290, 0.350)	0.253 (0.224, 0.283)	2.230 (1.870, 2.658)
	Seg-C	0.320 (0.290, 0.351)	0.257 (0.228, 0.286)	2.212 (1.850, 2.644)
	Overseg-woC	0.371 (0.336, 0.407)	0.337 (0.295, 0.379)	2.242 (1.872, 2.686)
	Overseg-C	0.361 (0.329, 0.393)	0.325 (0.288, 0.362)	2.207 (1.824, 2.671)
f (no units)	Full-woC	0.447 (0.350, 0.544)	0.238 (0.158, 0.318)	0.111 (0.092, 0.131)
	Full-C	0.424 (0.345, 0.504)	0.228 (0.161, 0.296)	0.100 (0.086, 0.115)
	Seg-woC	0.201 (0.187, 0.216)	-0.145 (-0.177, -0.113)	0.026 (0.024, 0.028)
	Seg-C	0.201 (0.187, 0.216)	-0.147 (-0.178, -0.116)	0.026 (0.024, 0.028)
	Overseg-woC	0.225 (0.206, 0.246)	-0.205 (-0.238, -0.172)	0.022 (0.021, 0.024)
	Overseg-C	0.222 (0.203, 0.242)	-0.201 (-0.232, -0.169)	0.022 (0.021, 0.024)
f$\times$D$_p$ ($\times 10^{-3}$ mm^2/s)	Full-woC	0.142 (0.113, 0.170)	0.081 (0.060, 0.102)	0.155 (0.138, 0.174)
	Full-C	0.138 (0.111, 0.165)	0.082 (0.060, 0.103)	0.148 (0.135, 0.162)
	Seg-woC	0.118 (0.097, 0.140)	0.016 (0.001, 0.032)	0.132 (0.124, 0.141)
	Seg-C	0.118 (0.096, 0.140)	0.018 (0.001, 0.035)	0.133 (0.123, 0.144)
	Overseg-woC	0.116 (0.096, 0.136)	0.012 (0.003, 0.021)	0.131 (0.124, 0.137)
	Overseg-C	0.116 (0.097, 0.135)	0.010 (-3.560 x10^{-4}, 0.019)	0.131 (0.125, 0.137)

RE: Relative error. RB: relative bias. SD: standard deviation. CI: confidence interval. D$_t$: tissue diffusion. D$_p$: pseudo-diffusion coefficient. f: perfused fraction. f$\times$D$_p$: microvascular blood flow. Full-woC: full-fitting without constraints. Full-C: full-fitting with constraints. Seg-woC: segmented-fitting without constraints. Seg-C: segmented-fitting with constraints. Overseg-woC: Oversegmented-fitting without constraints. Overseg-C: Oversegmented-fitting with constraints.
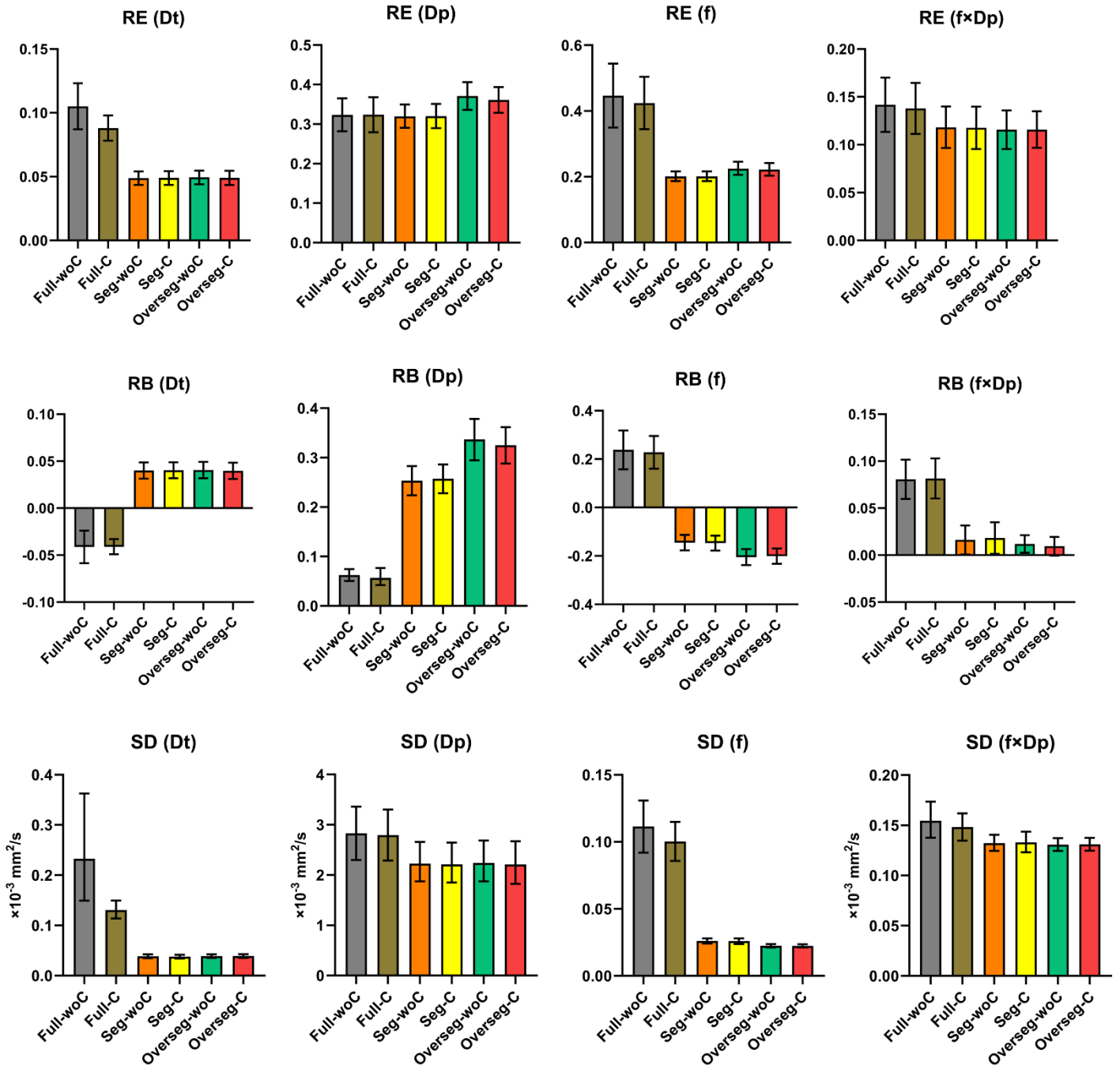
Figure 3.6 Bar plots of the mean relative error (RE), relative bias (RB), and standard deviation (SD) results for the IVIM parameters (D_t, D_p, f, and f×D_p) obtained with full-fitting without constraints (Full-woC), full-fitting with constraints (Full-C), segmented-fitting without constraints (Seg-woC), segmented-fitting with constraints (Seg-C), oversegmented-fitting without constraints (Overseg-woC), and oversegmented-fitting with constraints (Overseg-C) at 12 b-values and whole-tumour ROI averaged signals noise level. Error bars represent 95% confidence interval for the mean.

Table 3.8 Comparisons of mean relative bias, relative error, and standard deviation of IVIM parameters among different fitting methods (12 b-values, cold-spot ROI averaged signals noise level).

Parameter	Fitting methods	RE	RB	SD
		Mean (95% CIs)	Mean (95% CIs)	Mean (95% CIs)
D_t (×10^{-3} mm^2/s)	Full-woC	0.739 (0.538, 0.939)	-0.512 (-0.656, -0.368)	1.843 (1.364, 2.490)
	Full-C	0.261 (0.242, 0.281)	-0.180 (-0.199, -0.160)	0.343 (0.309, 0.377)
	Seg-woC	0.084 (0.082, 0.087)	0.038 (0.029, 0.047)	0.090 (0.081, 0.099)
	Seg-C	0.085 (0.082, 0.087)	0.037 (0.027, 0.046)	0.093 (0.084, 0.101)
	Overseg-woC	0.084 (0.082, 0.087)	0.038 (0.029, 0.047)	0.090 (0.081, 0.099)
	Overseg-C	0.085 (0.082, 0.087)	0.037 (0.028, 0.046)	0.092 (0.083, 0.100)
D_p (×10^{-3} mm^2/s)	Full-woC	1.634 (1.135, 2.353)	1.063 (0.638, 1.771)	144.404 (69.166, 219.642)
	Full-C	0.968 (0.825, 1.11)	0.516 (0.409, 0.622)	11.909 (9.805, 14.013)
	Seg-woC	2.497 (1.473, 3.521)	2.252 (1.270, 3.234)	202.770 (95.051, 310.490)
	Seg-C	0.898 (0.739, 1.056)	0.675 (0.547, 0.804)	11.237 (8.837, 13.637)
	Overseg-woC	3.084 (1.744, 4.423)	2.896 (1.588, 4.205)	240.853 (135.240, 346.465)
	Overseg-C	0.788 (0.686, 0.890)	0.596 (0.525, 0.668)	9.262 (7.447, 11.077)
f (no units)	Full-woC	1.459 (1.111, 1.807)	1.035 (0.784, 1.286)	0.303 (0.273, 0.333)
	Full-C	1.197 (0.984, 1.411)	0.889 (0.678, 1.100)	0.236 (0.222, 0.250)
	Seg-woC	0.495 (0.353, 0.696)	-0.131 (-0.225, -0.026)	0.203 (0.114, 0.361)
	Seg-C	0.375 (0.329, 0.427)	-0.044 (-0.104, 0.019)	0.072 (0.066, 0.078)
	Overseg-woC	0.340 (0.310, 0.370)	-0.204 (-0.240, -0.168)	0.052 (0.049, 0.054)
	Overseg-C	0.336 (0.308, 0.365)	-0.200 (-0.237, -0.163)	0.051 (0.048, 0.054)
f×D_p (×10^{-3} mm^2/s)	Full-woC	0.873 (0.555, 1.190)	0.732 (0.456, 1.008)	6.467 (2.961, 9.972)
	Full-C	0.491 (0.390, 0.593)	0.411 (0.319, 0.504)	0.626 (0.554, 0.698)
	Seg-woC	0.689 (0.413, 1.150)	0.364 (0.172, 0.771)	8.624 (4.063, 13.185)
	Seg-C	0.359 (0.277, 0.442)	0.138 (0.096, 0.199)	0.545 (0.472, 0.618)
	Overseg-woC	0.541 (0.352, 0.831)	0.169 (0.069, 0.414)	3.415 (1.580, 7.381)
	Overseg-C	0.323 (0.264, 0.381)	0.025 (0.010, 0.040)	0.459 (0.420, 0.499)

RE: Relative error. RB: relative bias. SD: standard deviation. CI: confidence interval. D_t: tissue diffusion. D_p: pseudo-diffusion coefficient. f: perfused fraction. f×D_p: microvascular blood flow. Full-woC: full-fitting without constraints. Full-C: full-fitting with constraints. Seg-woC: segmented-fitting without constraints. Seg-C: segmented-fitting with constraints. Overseg-woC: Oversegmented-fitting without constraints. Overseg-C: Oversegmented-fitting with constraints.
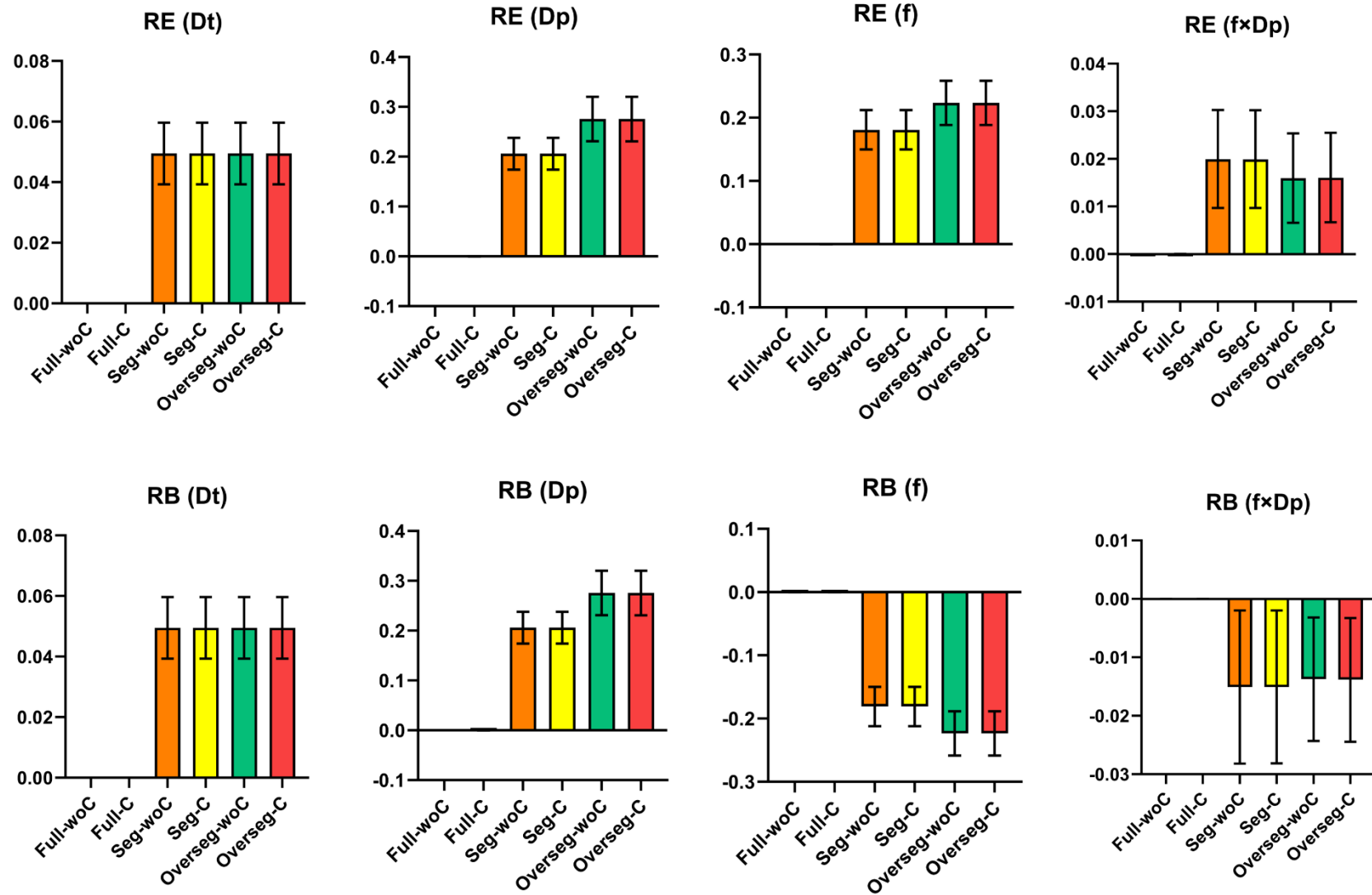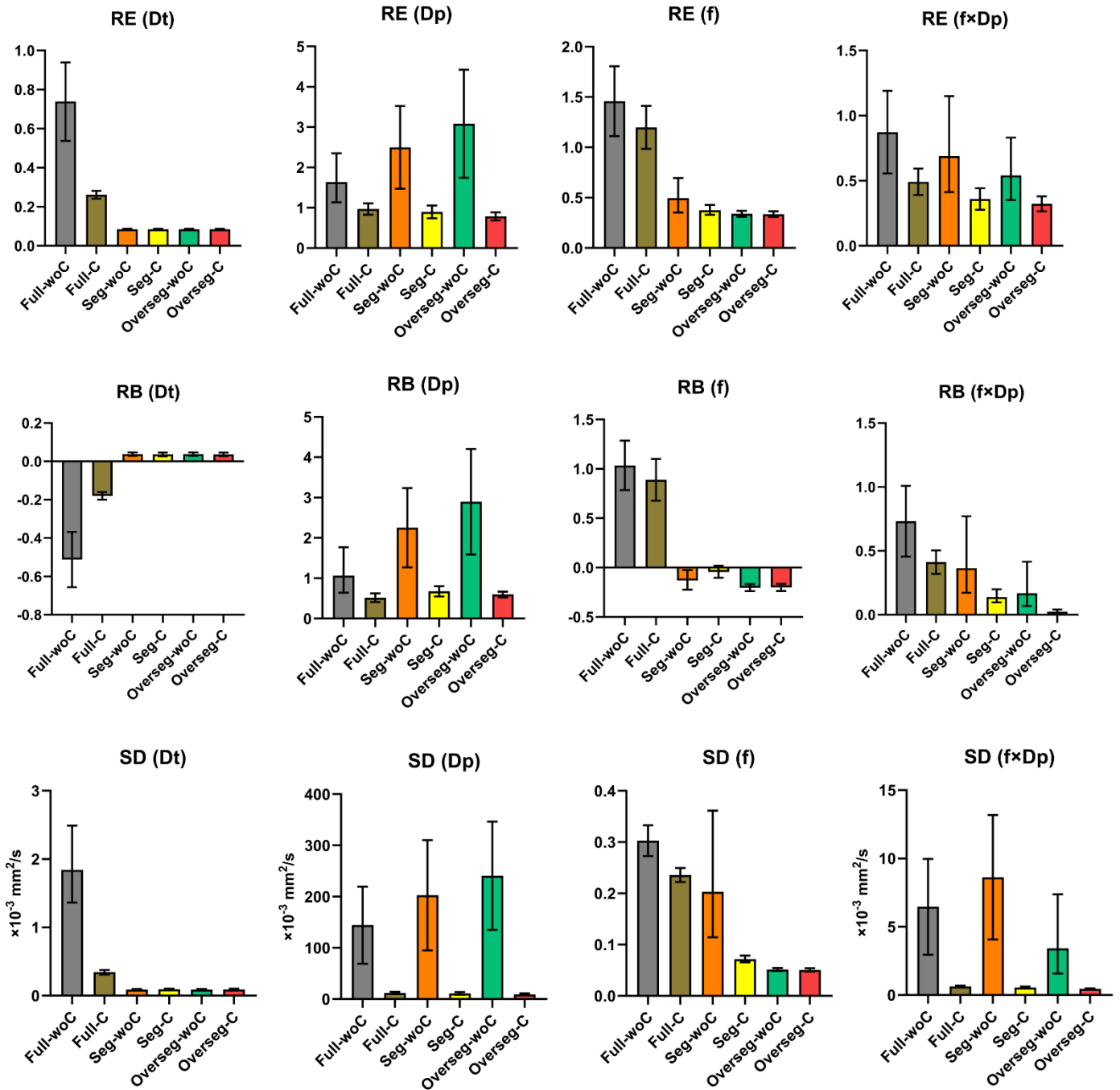
Figure 3.7 Bar plots of the mean relative error (RE), relative bias (RB), and standard deviation (SD) results for the IVIM parameters (D_t, D_p, f, and f×D_p) obtained with full-fitting without constraints (Full-woC), full-fitting with constraints (Full-C), segmented-fitting without constraints (Seg-woC), segmented-fitting with constraints (Seg-C), oversegmented-fitting without constraints (Overseg-woC), and oversegmented-fitting with constraints (Overseg-C) at 12 b-values and cold-spot ROI averaged signals noise level. Error bars represent 95% confidence interval for the mean.

For the D_p, f and f$\times$$D_p$ estimates at the whole-tumour ROI noise level, the seg-C method resulted in the lowest errors for D_p and f, and the overseg-C method resulted in the lowest errors for f$\times$$D_p$ (Tables 3.5 and 3.7, Figures 3.4 and 3.6). Conversely, at the cold-spot ROI noise level, the overseg-C method consistently exhibited the smallest errors and SD in estimating D_p, f and f$\times$$D_p$, independent of the b-value number (Tables 3.6 and 3.8, Figures 3.5 and 3.7).

The full-fitting methods produced the least precise (measured by SD) estimates for D_t and f in the presence of noise, except for f at the cold-spot ROI noise level with six b-values. Across the parameters, the precision of estimates for D_p and f$\times$$D_p$ was markedly lower than that for D_t and f when obtained with segmented and oversegmented methods, and the precision of the D_t estimates was roughly similar across the four methods (Tables 3.5-3.8, Figures 3.4-3.7).

Concerning the relative bias, trends similar to the results of the relative error upon introducing noise were observed. The full-woC method exhibited the greatest bias in estimating D_t, f and f$\times$$D_p$, except for f$\times$$D_p$ at the cold-spot ROI noise level with six b-values. In addition, the overseg-woC method displayed the most bias in the D_p estimates (Tables 3.5-3.8). The bias direction in D_t and f varied based on the fitting method, where the full-fitting methods underestimated D_t and overestimated f. The segmented and oversegmented methods exhibited the opposite trend consistently with six and 12 b-values (Figures 3.4-3.7).

The application of constraints in any fitting method resulted in lower bias and imprecision in estimating D_t, f and f$\times$$D_p$ compared to their unconstrained counterparts (Figures 3.4-3.7). The noise level clearly influenced the accuracy, bias, and precision of all IVIM parameter estimates, where estimates from the cold-spot noise level exhibited larger error and SD than those from the whole-tumour ROI noise level. The overestimation of D_p and f$\times$$D_p$ at the cold-spot noise level was higher than that at the whole-tumour ROI noise level (Tables 3.5 vs 3.6 and 3.7 vs 3.8).

The number of b-values also prominently affected all IVIM parameters when estimated using full-fitting methods, where the relative error, relative bias, and SD values were larger at six b-values than at 12 b-values (Tables 3.5 vs 3.7 and 3.6 vs 3.8). However, the D_t and f estimates were less affected by the number of b-values than D_p and f$\times$$D_p$ when obtained using the segmented and oversegmented methods.

For dataset 15, which assumed no perfusion (f = 0), the oversegmented methods consistently yielded the smallest error, bias, and SD values in estimating f across

all noise levels and numbers of b-values (the mean f value ranged from -0.004 to 0.026; Tables 3.9 and 3.10).

Table 3.9 Comparisons of the mean values of IVIM parameter estimates among different fitting methods in the simulation number 15 (6 b-values).

Noise-free							
Fitting methods	D_t (×10^{-3} mm^2/s)		D_p (×10^{-3} mm^2/s)		f (no units)		f×D_p (×10^{-3} mm^2/s)
	Mean		Mean		Mean		Mean
Full-woC	1.160		6.039		0.000		0.000
Full-C	1.156		1.261		0.035		0.044
Seg-woC	1.160		6.369		0.000		0.000
Seg-C	1.160		1.160		0.016		0.019
Overseg-woC	1.160		6.369		0.000		0.000
Overseg-C	1.160		0.000		0.000		0.000
Whole-tumour ROI averaged signals noise level							
	Mean	SD	Mean	SD	Mean	SD	Mean	SD
Full-woC	-1.154	15.840	22.076	126.338	0.049	1.087	0.071	2.772
Full-C	0.928	0.437	9.362	23.860	0.209	0.351	0.407	0.548
Seg-woC	1.159	0.056	75.225	735.380	0.022	5.726	0.387	13.977
Seg-C	0.906	0.427	3.935	11.675	0.403	0.425	0.533	0.496
Overseg-woC	1.160	0.057	111.265	829.510	-0.001	0.031	0.100	9.046
Overseg-C	1.108	0.220	4.742	14.779	0.013	0.018	0.077	0.168
Cold-spot ROI averaged signals noise level							
Full-woC	-0.855	15.465	82.948	558.697	-0.095	1.845	1.531	20.461
Full-C	0.918	0.436	11.456	25.216	0.198	0.324	0.639	0.935
Seg-woC	1.164	0.131	79.071	739.835	0.346	10.592	0.489	29.599
Seg-C	0.909	0.401	7.497	20.128	0.459	0.429	0.782	0.744
Overseg-woC	1.164	0.131	101.948	692.454	-0.004	0.072	0.778	15.345
Overseg-C	1.129	0.223	5.833	17.754	0.026	0.039	0.192	0.511
True value	1.16		0		0		0

SD: standard deviation. D_t: tissue diffusion. D_p: pseudo-diffusion coefficient. f: perfused fraction. f×D_p: microvascular blood flow. Full-woC: full-fitting without constraints. Full-C: full-fitting with constraints. Seg-woC: segmented-fitting without constraints. Seg-C: segmented-fitting with constraints. Overseg-woC: Oversegmented-fitting without constraints. Overseg-C: Oversegmented-fitting with constraints.

Table 3.10 Comparisons of the mean values of IVIM parameter estimates among different fitting methods in the simulation number 15 (12 b-values).

Fitting methods	D_t (×10⁻³ mm²/s)		D_p (×10⁻³ mm²/s)		f (no units)		f×D_p (×10⁻³ mm²/s)	
	Noise-free							
	Mean		Mean		Mean		Mean	
Full-woC	1.160		5.956		0.000		0.000	
Full-C	1.158		1.224		0.035		0.043	
Seg-woC	1.160		6.369		0.000		0.000	
Seg-C	1.160		1.160		0.015		0.017	
Overseg-woC	1.160		6.369		0.000		0.000	
Overseg-C	1.160		0.000		0.000		0.000	
	Whole-tumour ROI averaged signals noise level							
	Mean	SD	Mean	SD	Mean	SD	Mean	SD
Full-woC	0.873	14.034	36.954	281.777	0.117	0.903	0.208	3.655
Full-C	0.998	0.367	5.783	15.780	0.161	0.305	0.287	0.445
Seg-woC	1.160	0.040	24.642	185.625	-0.045	3.300	-0.125	4.532
Seg-C	0.913	0.423	3.712	10.517	0.315	0.381	0.419	0.455
Overseg-woC	1.161	0.040	37.449	370.441	-0.002	0.025	0.002	0.882
Overseg-C	1.115	0.208	3.768	11.367	0.009	0.013	0.045	0.098
	Cold-spot ROI averaged signals noise level							
Full-woC	4.155	137.177	118.065	615.027	0.119	0.896	2.517	23.181
Full-C	0.962	0.398	8.928	21.932	0.176	0.312	0.506	0.834
Seg-woC	1.162	0.092	71.124	713.355	0.248	6.235	0.705	21.630
Seg-C	0.937	0.383	7.133	19.749	0.439	0.424	0.702	0.698
Overseg-woC	1.162	0.092	57.697	483.603	-0.004	0.059	-0.452	12.391
Overseg-C	1.127	0.200	4.264	13.806	0.021	0.032	0.112	0.263
True value	1.16		0		0		0	

SD: standard deviation. D_t: tissue diffusion. D_p: pseudo-diffusion coefficient. f: perfused fraction. f×D_p: microvascular blood flow. Full-woC: full-fitting without constraints. Full-C: full-fitting with constraints. Seg-woC: segmented-fitting without constraints. Seg-C: segmented-fitting with constraints. Overseg-woC: Oversegmented-fitting without constraints. Overseg-C: Oversegmented-fitting with constraints.

3.3.2 In vivo repeatability

The upper estimate of the repeatability of IVIM parameters derived from whole-tumour ROI averaged signals generally exhibited patterns similar to the results of the simulations at a similar noise level (Table 3.11). Full-fitting methods had the poorest repeatability for D_t (wCV: 77.78% to 135.98%) and f (wCV: 57.79% to 63.19%), whereas segmented and oversegmented methods demonstrated better repeatability for both D_t (wCV: 5.53%) and f (wCV: 9.74% to 23.1%).

Across the parameters, the repeatability of D_p and f×D_p was notably lower than that of D_t and f when derived using the segmented and oversegmented methods. However, the best repeatability for D_p, f and f×D_p together was achieved using only the seg-C and overseg-C methods, with wCV values of 16.4% and 10.91% for D_p, 9.74% and 10.64% for f, and 18.1% and 17.85% for f×D_p, respectively.

Table 3.11 Upper estimate of the repeatability of IVIM parameters for each fitting method.

Fitting method	wCV (%)			
	D_t	D_p	f	f×D_p
Full-woC	135.98	54.96	63.19	27.17
Full-C	77.78	61.02	57.79	22.06
Seg-woC	5.53	74.6	23.1	80.71
Seg-C	5.53	16.4	9.74	18.1
Overseg-woC	5.53	47.75	10.64	50.16
Overseg-C	5.53	10.89	10.64	17.84

wCV: within-subject coefficient of variation. D_t: tissue diffusion. D_p: pseudo-diffusion coefficient. f: perfused fraction. f×D_p: microvascular blood flow. Full-woC: full-fitting without constraints; Full-C: full-fitting with constraints; Seg-woC: segmented-fitting without constraints; Seg-C: segmented-fitting with constraints; Overseg-woC: Oversegmented-fitting without constraints; Overseg-C: Oversegmented-fitting with constraints.

3.4 Discussion

This simulation study demonstrated that, in the absence of noise, full-fitting methods produce the smallest relative error and bias values for all IVIM parameter estimates (approximately 0). However, fitting the data with full-woC methods in the presence of noise leads to a substantial error and reduced precision in most IVIM parameters, particularly at higher noise levels (i.e., cold-spot ROI averaged signals). This outcome aligns with the outcomes of prior studies (159, 160, 162, 163), which might have been due to the statistical instability of the full-fitting method. The full-fitting method fits all four parameters simultaneously using a nonlinear least-squares approach; thus, noisy data points could result in erroneous and non-physiological parameter values with the full-woC method, a situation that could be aggravated at higher noise levels. A previous study stated that the full-fitting method is reliable only when a sufficiently high signal-to-noise ratio (SNR) exists (156).

In contrast, the results of the simulations revealed that the segmented and oversegmented methods could improve the accuracy and precision of IVIM parameters D_t and f in noisy settings, where using these methods resulted in lower RE and SD values for D_t and f compared to the full-woC method. The results of the upper estimate of the repeatability also indicated a similar trend where segmented and oversegmented methods demonstrated lower wCV values of D_t and f compared with the full-fitting methods. This improvement could be attributed to the stability of these methods, which estimate the IVIM parameters sequentially.

An additional advantage of the segmented and oversegmented methods over full-fitting methods is that the estimates of D_t and f were less affected by the number of b-values. The simulation results indicated that the number of b-values appreciably affected the accuracy and precision of all IVIM parameters when estimated using full-fitting methods. In contrast, its influence on D_t and f was less when obtained using segmented and oversegmented methods. The results revealed that the RB and SD values of D_t, f and $f \times D_p$ estimated using any fitting method that applies constraints were lower than those estimated with the same fitting method without constraints, indicating that applying constraints can offer another approach to reducing bias and imprecision in the parameter estimates. Thus, these advantages might have contributed to the seg-C and overseg-C methods producing the lowest errors and imprecision for the parameters D_p, f and $f \times D_p$ at the whole-tumour ROI noise level and six b-values. The results of the upper estimate of the repeatability

also aligned with these observations, where the best repeatability for D_p, f and f×D_p together was achieved using the seg-C and overseg-C methods.

Nevertheless, in this study, the overseg-C method consistently produced the smallest relative errors and SD in estimating D_p, f and f×D_p at cold-spot ROI noise level, and this became more evident with six b-values. This superiority of the overseg-C method could be due to the step-by-step estimation of the IVIM parameters, in which D_t and f were estimated first, and the bi-exponential fit was performed with only one free parameter to determine D_p. This approach has more stability than the seg-C method, where D_t was estimated first. Then, the bi-exponential fit was performed with two free parameters to estimate f and D_p simultaneously. The results of statistical fitting with a greater number of free parameters display more scatter (164).

The estimation of the f value with the overseg-C method uses $S(0)_{'measured'}$ and the intercept fitted from the higher b-value regime, without relying on a full fit across all b-values. In contrast, the seg-C method estimates f by fitting all b-values. While fitting all b-values in seg-C should theoretically lower its sensitivity to noise compared to overseg-C, the simulation results suggest that Overseg-C performed slightly better. Based on the results of the simulation study, to ensure methodological consistency in image analyses, the overseg-C method should be employed in subsequent research when analysing clinical breast DWI data acquired with six b-values to extract IVIM parameters from whole-tumour and single-slice small ROIs (i.e., Chapters 4 and 5).

In contrast, segmented and oversegmented methods overestimate D_t and D_p and underestimate f. In these methods, the data at b-values larger than 200 s/mm² (in this study at 400, 800 and 1,000 s/mm²) are presumed to be free from perfusion effects (156). However, the signal at b-values larger than 200 s/mm² might contain a perfusion contribution (165), leading to a slightly elevated SI compared to that expected in a perfusion-absent scenario. This approach results in an overestimation of D_t when fitting a straight line between these three data points. Consequently, f, which is derived as the difference between 1 and the intercept of this line at the y-axis, is underestimated. This underestimation of f necessitates an overestimation of D_p to align with the rapid signal decline observed at lower b-values (<400 s/mm²), partly attributed to perfusion effects. The increased D_p value compensates for the reduced f, enabling a better fit of the model to the rapid signal decline at these lower b-values.

On the other hand, the full-fitting methods tend to underestimate D_t and overestimate D_p and f in the presence of noise. This pattern might be attributable to the systematic influence of noise. The noise does not solely introduce imprecision; instead, it introduces consistent bias. In the full-fitting methods, all parameters are estimated simultaneously; thus, a plausible explanation for this observation could be related to the noise floor problem. The noise has a fixed level, and as the b-values get higher, the data get closer and closer to the noise floor; therefore, the signal at higher b-values will be overestimated because it includes both signal and noise (i.e., signal + noise). Given that the simulation study accounted for the Rician distribution of errors, the noise floor may have caused an artificial elevation in the tail of the signal decay curve, leading to an underestimation of D_t.

Consequently, this underestimation necessitates a compensatory overestimation of D_p and f to maintain the balance in the signal decay model to fit the model with the observed rapid signal decline at lower b-values. These observations of the systematic patterns in the estimations of the IVIM parameters observed with these three fitting methods were also observed in a previous clinical breast IVIM study. The mean D_t values estimated with the full-fitting method were lower than those estimated with the segmented and oversegmented methods, and the mean f values estimated with the full-fitting method were higher than those determined with the segmented and oversegmented methods (156).

This simulation study revealed that the parameter D_p exhibited larger error and SD compared to all IVIM parameters when derived using segmented and oversegmented methods. Previous research has consistently reported on the poor repeatability of D_p in vivo (144, 145, 157, 158). The simulation results further reinforced this observation, revealing notably high RE and SD values for D_p. In addition, the results of the upper estimate of the repeatability displayed a similar trend, where the wCv value for D_p was higher than that of D_t and f. The determination of D_p primarily relies on the fast-declining segment of the DWI signal curve at lower b-values (typically ≤200 s/mm2). Therefore, estimating D_p with high accuracy and precision may necessitate multiple data sampling in the lower b-value range and a considerably higher SNR, as illustrated by Pekar et al. (162), than that typically achievable in most clinical breast DW imaging (166). Additionally, this interpretation could be further supported by comparing the results of D_p estimates obtained from six b-values vs 12 b-values and the three noise levels (noise-free, whole-tumour and tumour cold-spot ROIs averaged signals). Thus, the application of D_p as an imaging biomarker should be limited to the conditions in which the observed variation in D_p for diagnosis, differentiating

pathological conditions, or the alteration in D_p during longitudinal monitoring markedly surpasses its estimation error.

3.4.1 Limitations

The simulated IVIM data were derived from clinical breast DWI data obtained from a specific patient population with breast cancer. Moreover, the simulations were conducted using only two b-value distributions (six and 12) and two noise levels (whole-tumour and cold-spot ROI averaged signals). These factors could limit the generalisability of the results and affect their applicability to various patient populations. However, the primary aim of this study was to identify the curve-fitting method that provides the most precise estimates of IVIM parameters (particularly f and f×D_p), with minimal error and bias based on only six b-values, using simulated data representing the range of IVIM parameters observed in breast cancer data obtained in Leeds, to be employed in subsequent research (i.e., Chapters 4 to 6).

Further, the actual repeatability of the IVIM parameters for each curve-fitting method in vivo was not examined. Alternatively, an upper estimate of the repeatability of the IVIM parameters for each fitting method was calculated from the baseline and after one-cycle NACT DWI studies for a subset of patients identified as pNR and showed the smallest changes in tumour volume at cycle one. The calculations were performed to serve as complementary to the simulation study. However, the results generally aligned with the findings of the simulation study.

Finally, other recently introduced IVIM curve-fitting methods, such as the Bayesian method, were not compared. The Bayesian method might be one approach to mitigate the noise floor problem by incorporating the noise floor into the Bayesian model for the signal. However, the current study focused on commonly used fitting methods in breast IVIM analysis. Nevertheless, the accuracy of the Bayesian method is heavily dependent on the choice of priors and is more computationally demanding, requiring a longer time for analysis than simpler methods (167). This approach could make its implementation more cumbersome. Importantly, the breast DWI data utilised in the current thesis were acquired with a maximum b-value of 800 s/mm² in which the SNR was observed to remain good without hitting the noise floor. A previous study argued that the Bayesian method provides performance similar to the oversegmented method, rendering the oversegmented method preferable due to the reduced numerical complexity and shorter computational time (167).

3.5 Conclusions

This simulation study compared commonly used IVIM curve-fitting methods in breast cancer, with the primary aim of identifying a method that provides more precise estimates of IVIM parameters (particularly f and $f{\times}D_p$), with minimal error and bias, using only six b-values. The study revealed that IVIM parameter estimates are susceptible to error, bias, and imprecision, varying according to the chosen fitting algorithm, number of b-values, and noise level. Constrained segmented and oversegmented fitting methods yielded the lowest errors and highest precision for the parameters D_p and f, and $f{\times}D_p$ together at the whole-tumour noise level. However, at the cold-spot ROI noise level, the constrained oversegmented fitting method consistently produced the lowest errors and highest precision in estimating D_p, f and $f{\times}D_p$. Therefore, for methodological consistency in image analyses, the constrained oversegmented method is employed in subsequent research when analysing clinical breast DWI data extracted from both whole-tumour and single-slice small ROIs (i.e., in Chapters 5 and 6).

Chapter 4 Evaluation of monoexponential, SEM and IVIM DWI MRI diffusion models estimated from the whole-tumour region of interest in early response monitoring to NACT in patients with breast cancer

Notes: This chapter is an updated version of the originally published paper (125), as it includes three additional patients in the pretreatment analysis. The IVIM parameters were estimated using an oversegmented-fitting with constraints method, based on the results from Chapter 3, whereas previously they were estimated using a segmented method with constraints.

4.1 Introduction

Previous studies have explored potential diagnostic roles for the SEM and IVIM models in breast cancer; however, there are few studies examining their ability to evaluate the response of breast cancer to NACT (section 2.8.2.2.1). Two preliminary studies have indicated that, after two or three NACT cycles, the parameters of the SEM and IVIM models obtained from a single region of interest (ROI) drawn freehand on the imaging slice with the largest tumour dimension may predict breast cancer response to NACT (19, 23). The authors of these studies recommended further investigation at earlier treatment points (i.e., after one cycle). Furthermore, the International Breast DWI Working Group recommended volumetric sampling when evaluating tumour response (24).

The primary aim of this study was to investigate the value of parameters obtained from the monoexponential (ADC), SEM (DDC, α), and IVIM (D_t, D_p, f, f×D_p) models derived from MRI data acquired pretreatment and after one and three NACT cycles, using volumetric sampling to assess early breast cancer response to NACT. The secondary aim was to estimate the repeatability of monoexponential and SEM models parameters by utilising a subset of DWI data from the baseline and after one cycle of NACT.

4.2 Materials and methods

4.2.1 Patients

A local research ethics committee approved the study, and written informed consent was obtained from each subject. The patient inclusion criteria were individuals [1] at least 18 years of age, [2] with pathological confirmation of invasive

breast cancer via core needle biopsy, and [3] planned to undergo NACT. Patients were ineligible if they received previous treatment for breast cancer (e.g., radiotherapy or chemotherapy) or had recurrent breast cancer, impaired kidney function, or contraindications to MRI. Recruited patients were treated with a standardised protocol of at least six NACT cycles. During treatment, all patients received epirubicin with cyclophosphamide for the first three cycles (one cycle every three weeks), followed by three cycles of docetaxel (one cycle every three weeks). In patients with human epidermal growth factor receptor 2 (HER2) positive tumours, docetaxel was accompanied by trastuzumab and, in some later cases, pertuzumab.

4.2.2 Magnetic resonance imaging

All patients were imaged on a 1.5 T MRI scanner (Aera; Siemens) using a 16-channel bilateral breast coil (Sentinelle; Siemens) with the patient in a head-first prone position.

The MRI protocol included axial T_1-weighted 3D spoiled gradient echo (FLASH), axial T_2-weighted turbo spin-echo, DWI, and dynamic contrast-enhanced (DCE) series. Axial DWI was performed before DCE-MRI using a spectral attenuated inversion-recovery (SPAIR) fat-suppressed, 2D single-shot spin echo–echo planar imaging (ss-EPI) sequence at six b-values (0, 50, 100, 200, 400, and 800 s/mm^2) with the following parameters: repetition time (TR)/echo time (TE): 7200/59 ms, field of view (FoV): 340×136 mm, matrix size: 280×116, slice thickness: 4 mm, and parallel imaging factor: 2. The acquisition time of the DWI sequence was 5 min, 31 s. ADC maps were created by the scanner software immediately following DWI acquisition.

DCE-MRI was performed using a fat-suppressed T_1-weighted 3D FLASH sequence (TR/TE: 4.1/1.2 ms, FoV: 340×340×180 mm, matrix size: 384×384×128, flip angle (FA): 10°, parallel imaging factor: 3, and acquisition time: 36 s) to acquire images before and at multiple time points following an intravenous bolus contrast injection of 0.1 mmol/kg Gd-DOTA (Dotarem, Guerbet Laboratories). For the purpose of this study, only the precontrast and the approximately 2-minute postcontrast images were included in the image analysis.

MRI was performed at four time points: before NACT (pretreatment) and after one, three (mid-treatment), and six NACT cycles (images acquired after six cycles were not included in this analysis; Figure 4.1).
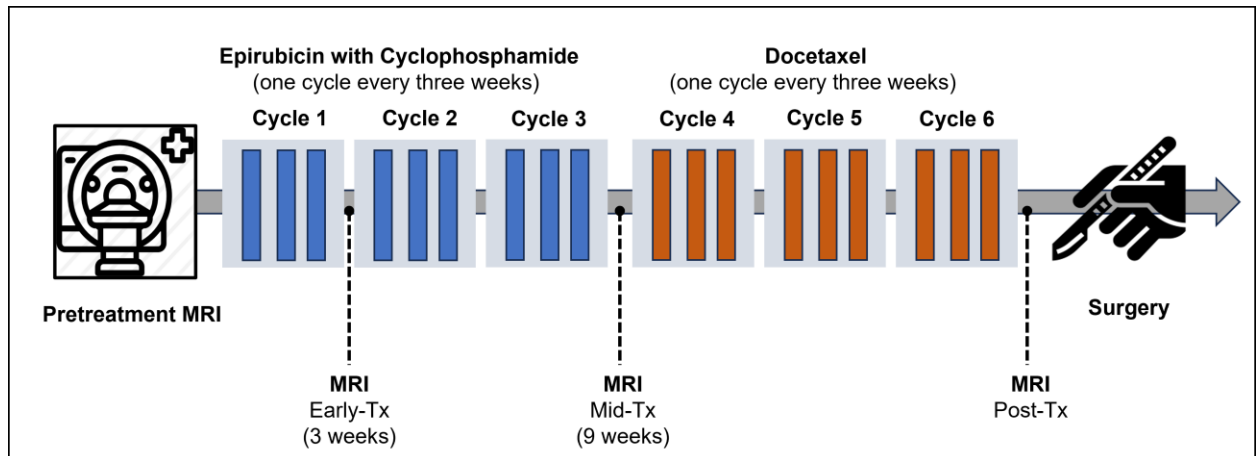
Figure 4.1 Diagram of the trial illustrating MRI time-points in relation to neoadjuvant chemotherapies. Tx = treatment.

4.2.3 Image analysis

MRI data were processed using an in-house program developed in MATLAB (MathWorks, USA) by a medical physicist in Leeds. The DCE images were rigidly aligned to match the DWI images (and therefore the ADC maps); there was no interpolation of the DWI data. DCE subtraction images were generated for each patient by subtracting the precontrast from the postcontrast (i.e., ~2 minutes) images to enhance tumour visibility. Using only rigid registration, however, may not be sufficient to fully correct inherent DWI distortions; thus, spatial co-registration accuracy between DWI and DCE images might be affected, and this may potentially lead to slight misalignment of the whole-volume ROI when generated on one image set and transferred to the corresponding image set.

For each patient, the location of the largest tumour was identified in the DCE images of the pretreatment MRI and confirmed by an experienced breast radiologist. Then, the author used the in-house program to seed the tumour and generate a whole-volume ROI using a 3D-region growing algorithm based on a threshold SI of the enhanced lesion in the DCE subtraction images. Obvious necrotic areas were avoided manually. The tumour volume was calculated from the sum of all enhanced tumour voxels. This ROI was transferred to the corresponding DWI, and the average SI value for every b-value was extracted (168) and displayed in the MATLAB command window for the subsequent step (DWI models' parameters estimation) (Figure 4.2). A screenshot with descriptions of the in-house

program used for generating the tumour's whole-volume ROI is shown in Figure 4.3.
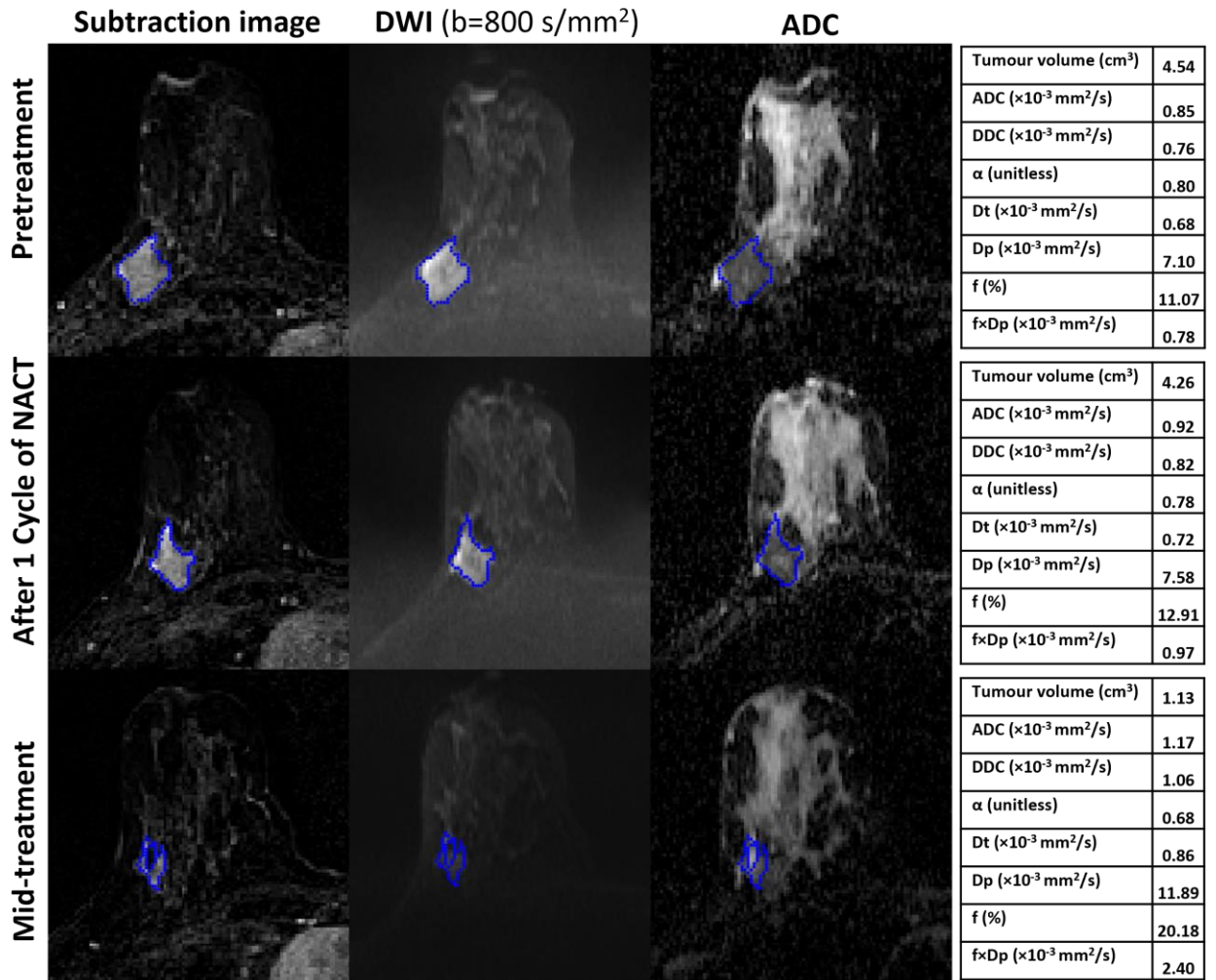
Figure 4.2 MRI scans of a 39-year-old woman with invasive ductal carcinoma who was a non-responder (RCB-II). Each row includes images acquired pretreatment, after one cycle of NACT, and at mid-treatment. The seeded ROI for the given slice is shown in blue. The tables represent the parameter estimates of monoexponential (ADC), SEM (DDC, α) and IVIM (D_t, D_p, f, f×D_p) models at each time point. The ADC, DDC, D_t, D_p, f, and f×D_p values increased during the treatment, while α was decreased.

Figure 4.3 Screenshot with descriptions of the in-house program used for generating the tumour's whole-volume ROI.
[1] Window for image display, where four images are open for analysis (A: ADC map, B: DWI (b = 800 s/mm^2), C: HSR-DCE subtraction image, D: HTR-DCE subtraction image (the latter is only used in Chapters 5 and 6)). [2] Zoom button, where the user can zoom in/out toward the affected breast. [3] Seed button, which is used to seed the tumour (by clicking on an enhanced pixel inside the tumour on the HSR-DCE subtraction image) and create a whole-tumour ROI using a 3D-region growing algorithm based on a threshold SI of the enhanced lesion pixels. The whole-tumour ROI covers all the slices where the tumour is present; however, the seeded ROI for the given slice is shown in blue. [4] Undo button to undo any step in case of a mistake. [5] Threshold slider, which can be used to increase/decrease the threshold SI, allowing the inclusion of more/fewer pixels based on their signal intensity and the selected threshold SI. [6] Readings window, which displays measurements extracted from the whole-tumour ROI (blue) for each image (i.e., 6A to 6D correspond to 1A to 1D). However, only tumour volume measurement is considered for this thesis work.

The parameters of the monoexponential (ADC), SEM (DDC, α), and IVIM (D_t, D_p, f) models were estimated using MATLAB. The IVIM model was fitted to the average SI values versus b-value data by employing the oversegmented-fitting with constraints method (described in section 3.2.2), based on the findings of Chapter 3, to estimate the parameters D_t, D_p, f, and f×D_p values. For the monoexponential and SEM models, the average SI versus b-value curves for each model were fitted using the nonlinear least-squares method with the following mathematical models (Figure 4.4):
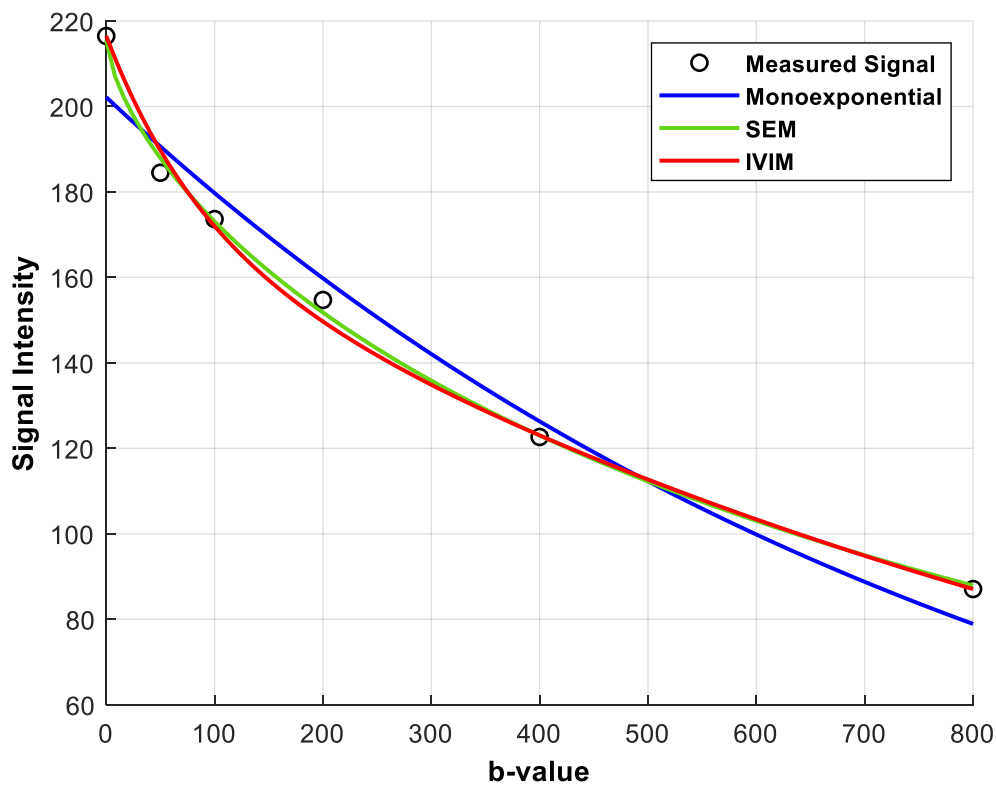
Figure 4.4 The measured DWI signals and best-fit curves of the tumour of the non-responder patient in Figure 4.2 at mid-treatment.

1. Monoexponential model:

$$S(b) = S(0).exp(-b.ADC),$$ Equation [2]

Where S(b) is the mean SI with diffusion weighting b, and S(0) is the mean SI without diffusion weighting (b = 0 s/mm^2). The S(0) and ADC values were simultaneously estimated from a monoexponential fit using the entire b-value range. The ACRIN 6698 multicentre trial reported using SIs acquired at all b-values for ADC calculation (25).

2. SEM:

$$S(b) = S(0).exp(-((b.\ DDC)^\alpha)),$$ Equation [4]

Where DDC represents the mean intravoxel diffusion rate, and α is the heterogeneity index describing the deviation of the signal attenuation from monoexponential behaviour with a value between 0 and 1. The entire range of b-values was used to provide best-fit estimates for S(0), DDC, and α simultaneously.

The parameter estimates and tumour volume were obtained and recorded for each patient at each MRI time-point. In addition, the percentage changes in the parameters and tumour volume compared to the values for pretreatment and after one NACT cycle were calculated for each patient as follows:

$$\Delta \text{ Parameter (\%)} = \frac{Value_{after\ one\ or\ three\ cycles} - Value_{at\ pretreatment\ or\ after\ one\ cycle}}{Value_{\ at\ pretreatment\ or\ after\ one\ cycle}} \times 100$$

The inter- and intra-observer variability in the tumour volume measurements was assessed by comparison with previous single measurements made by the same reader (the author) and a second reader, a colleague, using the same ROI generation method for the published, un-updated version of this chapter (125). These previous tumour volume measurements, acquired approximately 12 months before the repeated measurements, included 37 tumours at pretreatment and after one NACT cycle, and 35 tumours after three NACT cycles. All conducted steps were blinded to the evaluation of the pathological responses of the patients.

4.2.4 Pathological response evaluation

As previously reported (169), a pathologist assessed the tumour response, deriving an RCB index by dissecting and histologically examining the resected surgical specimen after the patients completed all NACT cycles. The RCB can be separated into four classes (RCB-0 to RCB-III), where RCB-0 denotes a

pathological complete response to NACT (pCR), which is associated with a good prognosis, and RCB-III denotes extensive residual disease, which is associated with a poor prognosis. Patients with an RCB of class I have the same five-year prognosis as those with an RCB of class 0 (64).

Patients were divided into two groups: pathological responders (pR), with an RCB class of 0 or I (RCB index ≤ 1.36) and pathological non-responders (pNR), with an RCB class of II or III (RCB index > 1.36).

4.2.5 Repeatability analysis

Consistent with the approach followed for the IVIM model (section 3.2.3), an upper estimate of the repeatability of the monoexponential and SEM model parameters was assessed by calculating the wCV (161) for the data from the pretreatment and after one NACT cycle for the same pNR subset, who displayed tumour volume changes between -66% (shrinkage) and +73% (increase) at cycle 1. It is indicated that the tumour volume changes would have to shrink by -66% to be considered a partial responder or increase by +73% to be considered progressive disease (5).

4.2.6 Statistical analysis

Median and interquartile ranges (IQR) were used to summarise the DWI model parameters due to the nonnormal data distribution. Inter- and intraobserver agreement in the tumour volume measurements at all three time points was assessed using the intraclass correlation coefficient (ICC < 0.5: poor agreement, 0.5 ≤ ICC < 0.75: moderate agreement, 0.75 ≤ ICC < 0.9: good agreement, 0.9 ≤ ICC: excellent agreement) (170). The parameter differences before NACT (pretreatment), after one cycle, and after three cycles were compared for all patients using Friedman's test with the Bonferroni correction (Bonferroni post hoc test). The parameter estimates for the pR and pNR groups were compared using the Mann–Whitney test. The percentage change in the parameter values after one and three NACT cycles for the pR and pNR groups was also compared using the Mann–Whitney test. The Spearman correlation test assessed the correlation between the diffusion coefficients (r < 0.2: very weak, 0.2 ≤ r <0.4: weak, 0.4 ≤ r < 0.7: moderate, 0.7 ≤ r < 0.9: strong: r ≥ 0.9: very strong) (171).

Receiver operating characteristic (ROC) curves were generated to assess the parameter performance to predict treatment outcomes, summarised by calculating the area under the ROC curve (AUC; 0.5 ≤ AUC < 0.7: poor performance and 0.7 ≤ AUC < 0.9: reasonable performance) (23). All analyses were performed using IBM SPSS (v.25.0). This study is preliminary; thus, the p-values for the predictive tests

were presented as raw values and were uncorrected for multiple comparisons. Thus, a p-value < 0.05 was considered statistically significant.

4.3 Results

4.3.1 Clinical characteristics of enrolled patients

Between August 2015 and April 2018, 40 female patients (mean age 46, range 25 to 69) were eligible and recruited for this study. Table 4.1 summarises the characteristics of the enrolled patients and tumours. According to the RCB assessment following surgery, 17 (42.5%) patients were classified as pR, whereas 23 (57.5%) patients were considered pNR. Compared with the pR patients, pNR patients were older (49 years, SD ±8 vs. 42 years, SD ±12) and had a higher proportion of grade-III tumours (70% (16) vs. 53% (9)).

However, three pNR patients withdrew following their pretreatment study and did not undergo further MRI (after one NACT cycle: pR = 17 and pNR = 20). Further, two pR patients were excluded from the analyses at mid-treatment because no tumour was visible in the MR images of these patients who went on to have a complete pathological response (Figure 4.5; at mid-treatment: pR = 15 and pNR = 20).

Table 4.1 Tumour characteristics of enrolled patients.

Characteristic	Number
Age, years (mean ± SD)	46 ± 10
Tumour grade	
II	15
III	25
Tumour histology	
Invasive ductal carcinoma	38
Inflammatory breast cancer	1
Mucinous carcinoma	1
Oestrogen receptor (ER) status	
Positive (+)	28
Negative (-)	12
Progesterone receptor (PR) status	
Positive (+)	18
Negative (-)	20
Not evaluable	2
Human epidermal growth factor 2 (HER2) status	
Positive (+)	15
Negative (-)	25
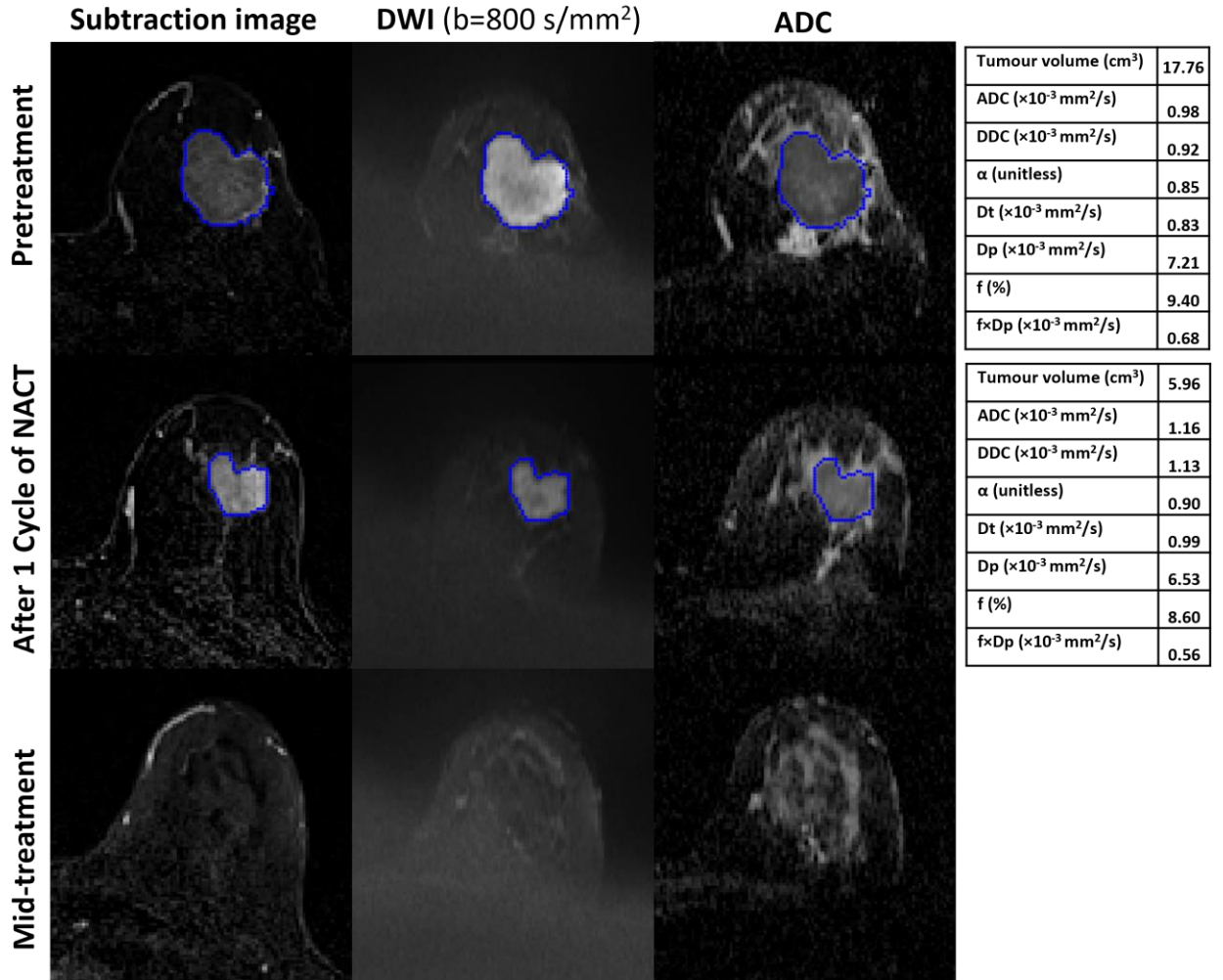
Figure 4.5 MRI scans of a 45-year-old woman with invasive ductal carcinoma in the left breast who showed a complete pathological response after surgery (RCB-0). Each row includes images acquired at pretreatment, after one cycle of NACT, and at mid-treatment. The seeded ROI for the given slice is shown in blue. The tables represent the parameter estimates of monoexponential (ADC), SEM (DDC, α) and IVIM (D_t, D_p, f, f×D_p) models at each time point. At mid-treatment, no tumour was visible on the DCE and DW images obtained. The ADC, DDC, α, and D_t values were increased after one cycle, while D_p, f, and f×D_p were decreased.

4.3.2 Parameter values for the cohort

Table 4.2 presents values at pretreatment and after one and three NACT cycles across the cohort. In two cases, estimates of the IVIM parameters D_p and f reached their constrained values, and these parameters were excluded from the statistical analyses. The pretreatment tumour volume was significantly higher than the tumour volume after three NACT cycles (median: 4.93 and 2.15 cm^3, respectively; p<0.001). The ADC, DDC, and D_t values for pretreatment and after one cycle were significantly lower than those after three cycles (median: ADC: 1.04, 1.08, and 1.18 $\times 10^{-3}$ mm^2/s, DDC: 0.96, 1.01, and 1.12 $\times 10^{-3}$ mm^2/s, and D_t: 0.81, 0.85, and 0.95 $\times 10^{-3}$ mm^2/s, respectively; p<0.001). However, no significant differences were observed in the α, D_p, f, and f×D_p values between pretreatment and after one and three cycles (p = 0.16, 0.10, 0.76, and 0.80, respectively).

Table 4.2 Tumour volume and parameters of monoexponential, SEM, and IVIM models pretreatment, after one cycle of NACT, and at mid-treatment.

Parameter	N	Pretreatment (a)	After one cycle of NACT (b)	After three cycles of NACT (c)	P	Post hoc**
Tumour volume (cm^3)	35	**4.93 (2.14, 11.65)**	**4.1 (1.44, 9.01)**	**2.15 (0.53, 5.8)**	**<0.001**	**a>c**
ADC ($\times 10^{-3}\,mm^2/s$)	35	**1.04 (0.91, 1.22)**	**1.08 (0.99, 1.29)**	**1.18 (1.06, 1.39)**	**<0.001**	**a<c, b<c**
DDC ($\times 10^{-3}\,mm^2/s$)	35	**0.96 (0.82, 1.16)**	**1.01 (0.91, 1.23)**	**1.12 (0.99, 1.36)**	**<0.001**	**a<c, b<c**
α (unitless)	35	0.82 (0.79, 0.85)	0.85 (0.8, 0.89)	0.84 (0.81, 0.88)	0.16	-
D_t ($\times 10^{-3}\,mm^2/s$)	35	**0.81 (0.73, 0.95)**	**0.85 (0.79, 1.01)**	**0.95 (0.84, 1.12)**	**<0.001**	**a<b, a<c**
D_p ($\times 10^{-3}\,mm^2/s$) (*)	33	7.17 (6.5, 7.85)	7.02 (5.83, 7.71)	6.37 (5.69, 7.47)	0.10	-
f (%) (*)	33	13.16 (11.07, 14.83)	12.85 (9.12, 15.62)	13.89 (10.72, 17.81)	0.76	-
f×D_p ($\times 10^{-3}\,mm^2/s$) (*)	33	0.95 (0.79, 1.13)	0.88 (0.55, 1.18)	0.94 (0.66, 1.27)	0.80	-

Data represented by medians (interquartile ranges). *P*-value for a difference between the three visits was found using Friedman's non-parametric test. Pairwise comparisons** (Bonferroni-corrected) significance at the 0.05 level. ADC: apparent diffusion coefficient. DDC: distributed diffusion coefficient. α: diffusion heterogeneity index. D_t: tissue diffusion. D_p: pseudo-diffusion coefficient. f: perfusion fraction. f×D_p: microvascular blood flow. (*) Estimates of the IVIM parameters D_p and f were excluded in two cases where they reached one of their limiting values.

4.3.3 Difference in parameters between response groups

Table 4.3 compares the parameter values for pR and pNR at pretreatment and after one and three cycles of NACT. Tumour volume for the pR group was significantly lower than that for the pNR group at all time-points (median: pretreatment: pR = 2.16 cm^3 and pNR = 10.47 cm^3; p<0.001; post one cycle: pR= 1.57 cm^3 and pNR = 8.71 cm^3; p<0.001; and post three cycles: pR= 0.51 cm^3 and pNR = 4.98 cm^3; p<0.001). No significant differences were found in ADC, DDC, D_t, and D_p between the pR and pNR groups at all time-points (pretreatment: p = 0.64, 0.78, 1, 0.97; after one cycle: p = 0.46, 0.72, 0.75, 0.07; and after three cycles: p = 0.93, 0.80, 0.61, 0.11, respectively). Figures 4.2 and 4.4 show examples of pNR and pR patients, respectively, where ADC, DDC, and D_t values were increased during the NACT course. After one NACT cycle, α values were significantly higher in the pR group (median: pR = 0.89 and pNR = 0.81; p = 0.003). In contrast, pNR patients exhibited considerably higher f and f×D_p values (median: pR = 9.13% and pNR = 15.21% for f; p = 0.001; and pR = 0.57×10^{-3} mm^2/s and pNR = 1.08×10^{-3} mm^2/s for f×D_p; p = 0.001). Figures 4.2 and 4.4 demonstrate that α was decreased, while f and f×D_p were increased in a pNR patient during NACT, whereas α was increased, and f and f×D_p were decreased in a pR patient. However, no significant differences between the response groups occurred in the α, f, and f×D_p values after three cycles (p = 0.17, 0.39, and 0.14, respectively).

Table 4.4 summarizes the ROC curve analyses for all parameters. The tumour volume demonstrated reasonable performance in predicting treatment response at all time-points (AUC = 0.848 to 0.881; p<0.001). In contrast, the AUCs for ADC, DDC, D_t, and D_p demonstrated poor performance at all time-points (AUC = 0.510–0.574 for ADC; p = 0.44–0.92; AUC = 0.527–0.535 for DDC; p = 0.71–0.79; AUC = 0.501–0.553 for D_t; p = 0.59–0.98; and AUC = 0.504–0.674 for D_p; p = 0.07–0.96). After one NACT cycle, the response prediction was reasonable for α (AUC = 0.782; p = 0.003), f (AUC = 0.832; p = 0.001), and f×D_p (AUC = 0.802; p = 0.002). At mid-treatment, the response prediction was poor for α, f, and f×D_p (AUC = 0.637, 0.590, and 0.654; p = 0.17, 0.38, and 0.13, respectively).

Table 4.3 Comparisons of tumour volume and parameter values at pretreatment, after one cycle of NACT, and at mid-treatment for the pR and pNR groups.

Parameter	Pretreatment (n=40)			After one cycle of NACT (n=37)			After three cycles of NACT (n=35)		
	pR (n=17)	pNR (n=23)	P	pR (n=17)	pNR (n=20)	P	pR(n=15)	pNR(n=20)	P
Tumour volume (cm^3)	**2.16 (1.83, 5.37)**	**10.47 (5.12, 24.11)**	**<0.001**	**1.57 (1.01, 2.61)**	**8.71 (4.18, 26.59)**	**<0.001**	**0.51 (0.29, 1.38)**	**4.98 (2.1, 13.32)**	**<0.001**
ADC (×10^{-3} mm^2/s)	0.98 (0.91, 1.08)	1.06 (0.89, 1.28)	0.64	1.08 (0.98, 1.14)	1.07 (0.99, 1.37)	0.46	1.17 (1.06, 1.34)	1.2 (1.05, 1.4)	0.93
DDC (×10^{-3} mm^2/s)	0.92 (0.86, 1.03)	0.98 (0.79, 1.23)	0.78	1.02 (0.93, 1.1)	1.01 (0.89, 1.34)	0.72	1.13 (1, 1.31)	1.12 (0.97, 1.38)	0.80
α (unitless)	0.84 (0.79, 0.86)	0.8 (0.78, 0.83)	0.24	**0.89 (0.86, 0.92)**	**0.81 (0.78, 0.86)**	**0.003**	0.88 (0.82, 0.95)	0.84 (0.77, 0.87)	0.17
D$_t$ (×10^{-3} mm^2/s)	0.81 (0.76, 0.9)	0.8 (0.71, 0.98)	1.00	0.87 (0.83, 0.94)	0.82 (0.77, 1.06)	0.75	0.95 (0.87, 1.08)	0.95 (0.82, 1.14)	0.61
D$_p$ (×10^{-3} mm^2/s) (*)	7.27 (6.26, 8.08)	7.17 (6.59, 7.79)	0.97	6.05 (5.42, 7.06)	7.08 (6.2, 7.84)	0.07	6.08 (5.13, 6.99)	6.59 (6.12, 7.69)	0.11
f (%) (*)	11.07 (10.18, 13.18)	13.83 (11.12, 15.51)	0.10	**9.13 (8.6, 11.54)**	**15.21 (12.96, 16.74)**	**0.001**	13.77 (8.64, 16.18)	14.71 (11.3, 18.22)	0.39
f×D$_p$ (×10^{-3} mm^2/s) (*)	0.83 (0.65, 1.06)	0.98 (0.81, 1.19)	0.18	**0.57 (0.51, 0.82)**	**1.08 (0.78, 1.27)**	**0.001**	0.93 (0.44, 1.03)	1 (0.71, 1.31)	0.14

Data are represented by medians (interquartile ranges). P-value calculated using independent samples for the Mann-Whitney U test. ADC: apparent diffusion coefficient. DDC: distributed diffusion coefficient. α: diffusion heterogeneity index. D$_t$: tissue diffusion. D$_p$: pseudo-diffusion coefficient. f: perfusion fraction. f×D$_p$: microvascular blood flow. pR: pathological responders. pNR: pathological non-responders. (*) Estimates of the IVIM parameters D$_p$ and f were excluded in two cases where they reached one of their limiting values.

Table 4.4 Diagnostic performance of tumour volume and monoexponential, SEM, and IVIM parameters in predicting NACT treatment outcomes.

Parameter	Pretreatment (n=37)			After 1 cycle of NACT (n=37)			After 3 cycles of NACT (n=35)		
	AUC	95% Confidence Interval	*P*	AUC	95% Confidence Interval	*P*	AUC	95% Confidence Interval	*P*
Tumour volume (cm^3)	**0.848**	**0.725-0.970**	**<0.001**	**0.881**	**0.767-0.995**	**<0.001**	**0.877**	**0.759-0.994**	**<0.001**
ADC ($\times 10^{-3}$ mm^2/s)	0.545	0.363-0.727	0.63	0.574	0.382-0.765	0.44	0.510	0.314-0.706	0.92
DDC ($\times 10^{-3}$ mm^2/s)	0.527	0.343-0.710	0.77	0.535	0.340-0.730	0.71	0.527	0.332-0.722	0.79
α (unitless)	0.611	0.423-0.799	0.23	**0.782**	**0.631-0.934**	**0.003**	0.637	0.446-0.828	0.17
D_t ($\times 10^{-3}$ mm^2/s)	0.501	0.319-0.683	0.98	0.532	0.337-0.728	0.73	0.553	0.358-0.748	0.59
D_p ($\times 10^{-3}$ mm^2/s)	0.504	0.315-0.692	0.96	0.674	0.490-0.857	0.07	0.665	0.472-0.859	0.10
f (%)	0.652	0.480-0.825	0.10	**0.832**	**0.687-0.978**	**0.001**	0.590	0.386-0.794	0.38
f$\times$D$_p$ ($\times 10^{-3}$ mm^2/s)	0.627	0.447-0.807	0.17	**0.802**	**0.658-0.948**	**0.002**	0.654	0.463-0.846	0.13
AUC: Area under the receiver operating characteristic curve. ADC: apparent diffusion coefficient. DDC: distributed diffusion coefficient. α: diffusion heterogeneity index. D_t: tissue diffusion. D_p: pseudo-diffusion coefficient. f: perfusion fraction. f$\times$D$_p$: microvascular blood flow.									

4.3.4 Relative parameters change differences between response groups

Tables 4.5 and 4.6 compare the relative (percentage) change in parameter values for the pR and pNR groups after one and three NACT cycles. The relative changes in α and $f \times D_p$ values after one NACT cycle and D_p values after three NACT cycles were significantly different between the pR and pNR groups (median: pR = 6.23% and pNR = -0.6% for α; p = 0.01; pR = -17.1% and pNR = 16.01% for $f \times D_p$; p = 0.04; and pR = -14.8% and pNR = -3.6% for D_p; p = 0.02). However, no statistically significant relationship was found between the pathological response and relative changes in ADC, DDC, D_t, D_p, and f values after one NACT cycle; in ADC, DDC, D_t, α, f, and $f \times D_p$ after three NACT cycles; or in the relative changes in tumour volume after one and three NACT cycles (after one cycle: p = 0.06 to 1 and after three cycles: p = 0.06 to 0.84; Tables 4.5 and 4.6).

Table 4.7 summarises the ROC curve analyses for the relative changes in all parameters. The changes in tumour volume, ADC, DDC, D_t, f, and $f \times D_p$ after one and three NACT cycles displayed poor performance in predicting NACT response (AUC = 0.500–0.691; p = 0.06–1). In contrast, changes in α (after one NACT cycle) and D_p (after three NACT cycles) demonstrated reasonable performance (AUC = 0.741 for α; p = 0.01, and AUC = 0.729 for D_p; p = 0.02). However, changes in α (after three cycles) and D_p (after one NACT cycle) exhibited poor performance (AUC = 0.683 for α; p = 0.06, and AUC = 0.632 for D_p; p = 0.71).

Table 4.5 Comparisons of the percentage change in tumour volume and DWI parameter values for the pR and pNR groups.

Cycle 1 - Pretreatment					
Parameter	**N**	**pR**	**N**	**pNR**	*P*
Tumour volume	17	-38.21 (-48.62, -26.23)	20	-15.93 (-31.6, -5.95)	0.06
ADC	17	4.54 (-1.12, 11.2)	20	6.58 (-2.03, 10.62)	1.00
DDC	17	7.34 (0.54, 12.21)	20	7.87 (-2.32, 13.94)	0.84
α	**17**	**6.23 (0.98, 10.46)**	**20**	**-0.6 (-4.07, 3.76)**	**0.012**
D_t	17	5.92 (1.52, 18.36)	20	4.73 (-1.47, 11.93)	0.28
D_p	17	-13.52 (-24.77, 8.08)	20	0.75 (-15.01, 19.18)	0.17
f	17	-18.45 (-32.28, 7.89)	20	12.94 (-3.38, 17.49)	0.06
f×D_p	**17**	**-17.1 (-44.02, 15.11)**	**20**	**16.04 (-14.27, 28.76)**	**0.048**
Cycle 3 - Pretreatment					
Tumour volume	15	-60.51 (-81.37, -35.66)	20	-49.07 (-68.56, -13.21)	0.15
ADC	15	12.29 (3.07, 34.9)	20	13.43 (-0.39, 24.25)	0.45
DDC	15	18.77 (6.36, 40.05)	20	16.04 (-0.1, 28.45)	0.4
α	15	6.12 (3.62, 8.15)	20	1.31 (-5.94, 6.39)	0.06
D_t	15	19.05 (3.41, 31.74)	20	12.17 (-0.74, 23.93)	0.34
D_p (*)	**14**	**-14.8 (-26.61, -8.4)**	**19**	**-3.6 (-15.32, 11.96)**	**0.026**
f (*)	14	2.97 (-18.19, 36.1)	19	8.69 (-7.77, 16.33)	0.84
f×D_p (*)	14	-6.4 (-29.11, 9.89)	19	0.12 (-13.54, 19.66)	0.37

Data are represented by medians (interquartile ranges). P-value calculated using independent samples for the Mann-Whitney U test. ADC: apparent diffusion coefficient. DDC: distributed diffusion coefficient. α: diffusion heterogeneity index. D_t: tissue diffusion. D_p: pseudo-diffusion coefficient. f: perfusion fraction. f×D_p: microvascular blood flow. pR: pathological responders. pNR: pathological non-responders. (*) Estimates of the IVIM parameters D_p and f were excluded in two cases where they reached one of their limiting values.

Δ parameter (%)= [(Value $_{after\ one/three\ cycles}$) - (Value $_{at\ pretreatment}$)]/(Value $_{at\ pretreatment}$) × 100

Table 4.6 Comparisons of the percentage change in tumour volume and DWI parameter values for the pR and pNR groups.

Cycle 3 – Cycle 1					
Parameter	**N**	**pR**	**N**	**pNR**	***P***
Tumour volume	15	-51.61 (-67.85, -14.81)	20	-31.49 (-52.56, -4.28)	0.54
ADC	15	5.99 (0.2, 14.18)	20	6.67 (-0.39, 15.15)	0.65
DDC	15	9.08 (0.5, 15.9)	20	7.12 (1.3, 18.2)	0.47
α	15	-1.51 (-4.32, 5.07)	20	0.28 (-3.14, 4.78)	0.65
D_t	15	4.75 (-1.38, 13.22)	20	9.28 (0.1, 16.93)	0.80
D_p (*)	14	-8.75 (-20.7, 7.21)	19	-2.78 (-11.06, 12.17)	0.33
f (*)	14	7.4 (-11.3, 56.46)	19	-4.5 (-19.96, 25.4)	0.50
f×D_p (*)	14	12.05 (-27.58, 46.24)	19	0.86 (-16.49, 34.24)	0.62
Data are represented by medians (interquartile ranges). P-value calculated using independent samples for the Mann-Whitney U test. ADC: apparent diffusion coefficient. DDC: distributed diffusion coefficient. α: diffusion heterogeneity index. D_t: tissue diffusion. D_p: pseudo-diffusion coefficient. f: perfusion fraction. f×D_p: microvascular blood flow. pR: pathological responders. pNR: pathological non-responders. (*) Estimates of the IVIM parameters D_p and f were excluded in two cases where they reached one of their limiting values. Δ parameter (%)= [(Value $_{after\ three\ cycles}$) - (Value $_{after\ one\ cycle}$)]/(Value $_{after\ one\ cycle}$) × 100					

Table 4.7 Diagnostic performance of the percentage change in tumour volume and monoexponential, SEM, and IVIM parameters in predicting NACT treatment outcomes.

Parameter	Cycle 1 - Pretreatment			Cycle 3 - Pretreatment			Cycle 3 – Cycle 1		
	AUC	95% Confidence Interval	P	AUC	95% Confidence Interval	P	AUC	95% Confidence Interval	P
Tumour volume (cm^3)	0.682	0.500-0.865	0.06	0.643	0.455-0.831	0.15	0.563	0.364-0.763	0.52
ADC ($\times 10^{-3}$ mm^2/s)	0.500	0.309-0.691	1.00	0.577	0.382-0.772	0.44	0.547	0.349-0.744	0.64
DDC ($\times 10^{-3}$ mm^2/s)	0.521	0.330-0.711	0.83	0.587	0.393-0.780	0.38	0.573	0.378-0.769	0.46
α (unitless)	**0.741**	**0.577 – 0.905**	**0.012**	0.683	0.504-0.863	0.06	0.547	0.349-0.744	0.64
D_t ($\times 10^{-3}$ mm^2/s)	0.606	0.421-0.790	0.27	0.597	0.405-0.788	0.33	0.527	0.325-0.728	0.79
D_p ($\times 10^{-3}$ mm^2/s)	0.632	0.450-0.815	0.17	**0.729**	**0.553 – 0.905**	**0.026**	0.602	0.394-0.809	0.32
f (%)	0.685	0.496-0.875	0.06	0.523	0.311-0.734	0.82	0.571	0.370-0.773	0.48
f×D_p ($\times 10^{-3}$ mm^2/s)	**0.691**	**0.515 – 0.868**	**0.048**	0.594	0.394-0.794	0.36	0.553	0.349-0.757	0.61
AUC: Area under the receiver operating characteristic curve. ADC: apparent diffusion coefficient. DDC: distributed diffusion coefficient. α: diffusion heterogeneity index. D_t: tissue diffusion. D_p: pseudo-diffusion coefficient. f: perfusion fraction. f×D_p: microvascular blood flow.									

4.3.5 Inter- and intraobserver agreement and correlation analysis

The inter- and intraobserver agreement in tumour volume, measured at pretreatment, after one NACT cycle, and after three cycles, was excellent: ICCs for interobserver = 0.93, 0.97, and 0.98 and ICCs for intraobserver = 0.97, 0.99, and 0.99, respectively (Table 4.8). A significant positive correlation occurred between ADC, DDC, and D_t at all time-points (r = 0.87 to 0.99; p<0.001). Figure 4.6 illustrates the correlations between the diffusion coefficients at each MRI time-point.

Table 4.8 Inter- and intraobserver agreement measures of the tumour volume at all three time points.

Parameter	N	Interobserver agreement	Intraobserver agreement
		ICC (95%CI)	ICC (95%CI)
Tumour volume (at pretreatment)	37	0.937 [0.881, 0.967]	0.977 [0.953, 0.989]
Tumour volume (post one cycle)	37	0.976 [0.919, 0.990]	0.995 [0.990, 0.997]
Tumour volume (post three cycles)	35	0.988 [0.969, 0.995]	0.998 [0.995, 0.999]
ICC: intraclass correlation coefficient. CI: Confidence interval.			
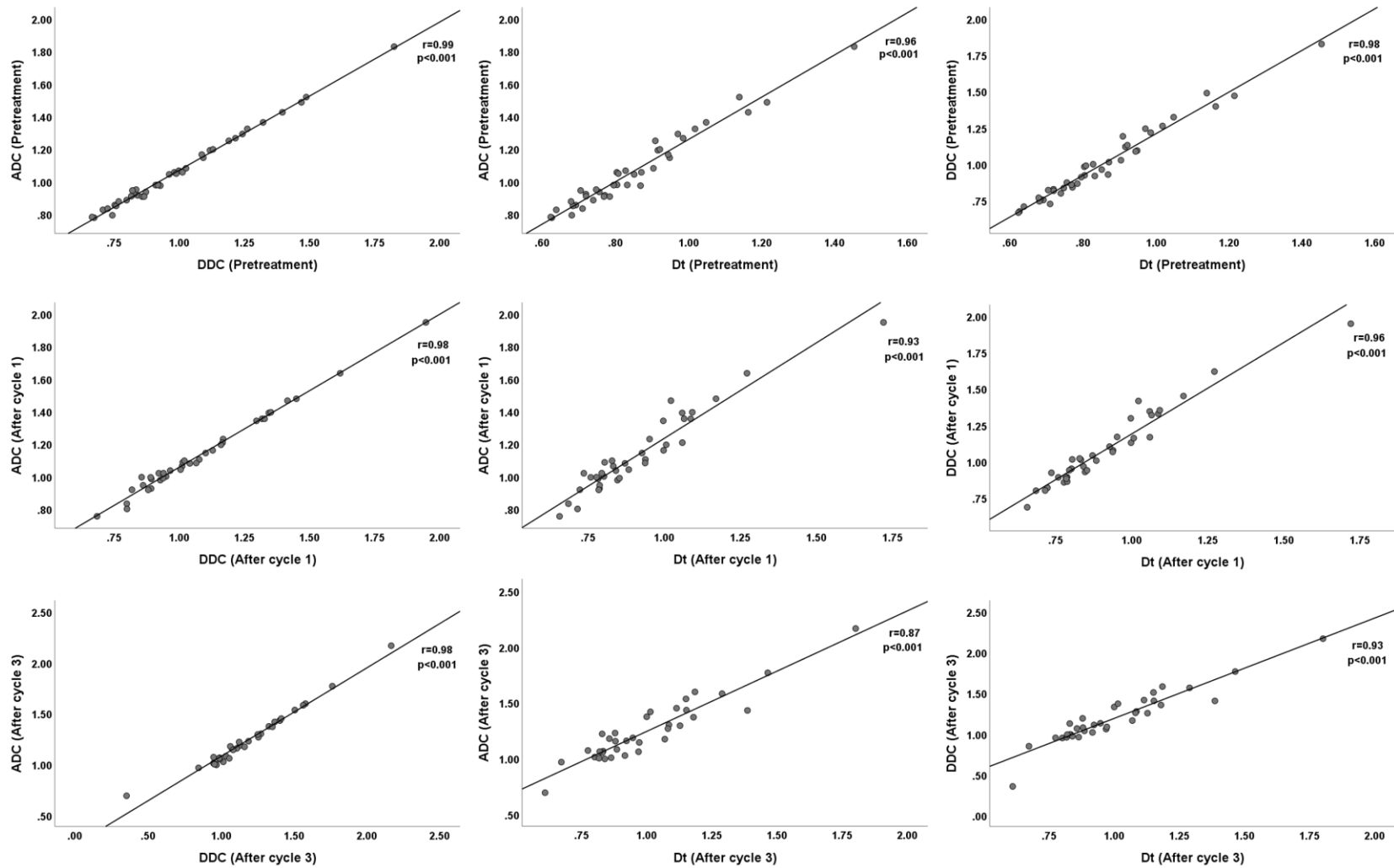
Figure 4.6 Scatter plots for the diffusion coefficients show the significant relationship between the ADC, DDC, and D_t parameters. The correlation coefficients (r-values) were obtained from the Spearman correlation tests, and the corresponding P-values were annotated for each plot.

4.3.6 Upper estimate of repeatability of the DWI model parameters

As indicated in section 3.2.3, ten pNRs were included in the repeatability analysis. The ten tumours showed changes in volume between -21.60% (shrinkage) and +18.90% (increase), with an average volume change of -3.64%. The upper estimate of the wCV for ADC was 4.9%; for the SEM parameters, it was 5.7% for DDC and 3.8% for α; for the IVIM parameters (derived from Table 3.11, Overseg-C), it was 5.5% for D_t, 10.9% for D_p, 10.6% for f, and 17.8% for $f \times D_p$.

4.4 Discussion

Early prediction and monitoring of the NACT response are advantageous for individualising an optimal and cost-effective treatment plan for patients with breast cancer by avoiding exposure to ineffective NACT. This preliminary study examined potential predictions that could alter treatment early (i.e., by the third cycle at the latest). The predictive power of the monoexponential, SEM, and IVIM DWI models for determining NACT outcomes for breast cancer in 40 patients was evaluated. The parameters of the DWI models were measured at three points: pretreatment, after one NACT cycle, and after three cycles.

The findings revealed that tumour volumes measured using the semi-automated method at the three time-points for pR were significantly smaller than those for pNR, and tumour volume was able to predict response to NACT with reasonable performance (AUC = 0.848 to 0.881; p<0.001). This confirms the finding shown in a recent study (169) that tumour volume, measured using manually drawn ROIs, is a good predictor pretreatment and after one cycle of NACT. The present study showed that this prediction remains valid after three cycles. Moreover, the semi-automated method used in this study for tumour volume estimation has excellent inter- and intraobserver agreement.

Although pR tumours shrank by slightly greater percentages than pNR tumours after one and three NACT cycles, the difference was not significant (p = 0.06 to 0.54). A recent ACRIN 6698 multicentre trial reported that the percentage change in tumour volume between pretreatment, one and four NACT cycles, and post-treatment was predictive in (HR+/HER2-) tumours at all time-points and in triple-negative (HR-/HER2-) tumours at post-treatment only. However, the change was not predictive in (HR-/HER2+) and (HR+/HER2+) tumours at all time-points (25). The results may explain the lack of a significant difference in the percentage

change in tumour volume between the response groups in the present study, as only 12 patients (2 pR and 10 pNR) in the sample had (HR+/HER2-) tumours.

The results revealed that the D_t values are consistently lower than those for ADC, similar to previous studies (19, 126). This outcome was anticipated when the contamination from the perfusion element was excluded using b-values greater than 200 s/mm^2 in the D_t calculation. Furthermore, a strong positive correlation of ADC with DDC and D_t was found at each MRI time-point in the present study, suggesting that DDC and D_t can be interpreted similarly to ADC in terms of observing diffusion components within the microenvironment. Similar to the findings by Surov et al.(172), the results illustrated that none of the pretreatment diffusion coefficients predict response to NACT. Nonetheless, pNR in the present study had slightly higher pretreatment ADC and DDC values than pR, as previously reported (19, 173). This result could be attributed to low ADC and DDC values being indicative of viable tissue with high cellularity, while high ADC and DDC values are indicative of necrotic, less viable tissue characterised by low cellularity (173).

After one NACT cycle, no significant difference in the ADC was noted between the response groups (p = 0.46). This outcome conflicts with the results Li et al. (174) reported, which may reflect technical differences in ADC calculation, the use of different treatment regimens, and how pathological response was assessed.

Following one NACT cycle, the percentage change in the tumour diffusion coefficients was not predictive of response, aligning with a previous report (25). At mid-treatment, no significant difference was observed between the response groups in the relative increase in the ADC, DDC, and D_t (p = 0.34–0.80). This finding is partially inconsistent with the results Bedair et al. (19), reported, finding a substantial difference at mid-therapy between responders and non-responders in the percentage of increase in the ADC and DDC values but not in the D_t value. This inconsistency may occur for the following possible reasons: [1] In the present study, the ROIs were generated around the whole-tumour volume on the DCE subtraction images, and the ROIs were then copied to the DWIs, and the average SI value for every b-value was calculated. In contrast, Bedair et al. generated parametric maps of all diffusion parameters, and then the single-section ROIs were analysed on a voxel-wise basis, and the parameters were expressed as means over the single-section ROIs (19). Estimation of model parameters is more accurate when performed using the ROI averaged signals, compared to the

average of parameter values estimated on a voxel-by-voxel basis (168). Moreover, volumetric sampling of the entire tumour may minimize sampling bias in comparison with the single-section ROI method (152), and this method is recommended when evaluating tumour response (24). [2] The ADC value in the present study was determined using all six b-values. In contrast, Bedair et al. (19) calculated it from only two values (0 and 900 s/mm^2). The choice of b-value may affect the calculation of the ADC value (175). [3] There were differences in the number of patients included in the mid-treatment analysis and in the method of categorising the response groups. In this study, 35 patients categorised as pR (15 patients with RCB 0/I) and pNR (20 patients with RCB II/III) were included in the mid-treatment analysis. In the study by Bedair et al. (19), 22 patients were classified as pCR (eight patients) and non-pCR (14 patients) at the mid-therapy analysis. However, the ACRIN 6698 multicentre trial found that the percentage change in the ADC value was predictive only in (HR+/HER2−) tumours after four NACT cycles (25).

Theoretically, D_p is related to the capillary blood flow velocity and the average capillary segment length (20). At mid-treatment, a significant difference was observed between the pR and pNR groups in the percentage decrease in D_p values. The pR group exhibited a greater reduction in the D_p value than the pNR group (pR = -14.8% and pNR = -3.6%; p = 0.02). This result may indicate that blood flow velocity was reduced more in responder tumours than in non-responder tumours relative to the baseline values. However, this study revealed no significant difference in D_p values between pRs and pNRs at each MRI time-point (p = 0.07–0.97). This finding could be attributed to the considerable variability of the D_p estimates in this study, as supported by the upper estimate of its repeatability (i.e., wCV = 10.9%), possibly overwhelming the difference between the two groups. This result has also been demonstrated in several studies that highlighted the large variability in D_p estimates (144, 157). Further studies exploring the nature of the D_p parameter and assessing its repeatability in the breast should be conducted to assess the D_p change and accurately interpret it. This could be conducted by acquiring DWI images for breast cancer patients at multiple NACT time points beyond the one used in this study, along with repeating the DWI acquisition for a subset of patients at pretreatment. This approach would help track how D_p evolves during treatment, explore its nature and relationship to tumour response, and assess its repeatability in breast cancer. An additional approach would be to correlate D_p with comparable measures, such as blood flow, which can be derived

from other imaging techniques like PET or DCE-MRI. Such an analysis may offer additional understanding of the nature of the D_p parameter. This could be done by acquiring both DWI and DCE-MRI scans for breast cancer patients at multiple NACT stages and investigating the longitudinal correlations between D_p and F_b (DCE-MRI derived measure of blood flow) parameter changes induced by NACT.

The values of f and f×D_p at the three time-points were consistently higher in pNR compared to pR, and both were able to differentiate the two groups and predict response with reasonable performance after one cycle of NACT (f: AUC = 0.832; p = 0.001; and f×D_p: AUC = 0.802; p = 0.002). Le Bihan et al. stated that the f parameter reflects the fractional volume of capillary blood in a voxel, whereas f×D_p reflects the microvascular blood flow (20). Thus, higher f and f×D_p values in the pNR group might be attributed to the richer blood supply in the non-responder tumours. Moreover, Lee et al. found a significant positive correlation between f and the histological microvessel density (176), a surrogate marker of tumour angiogenesis, where high scores are often associated with poor prognosis after chemotherapy (177). This finding may have an indirect relationship to the high f values in pNR tumours. A recent study discovered that breast tumours with higher blood scores using optical imaging were associated with a poorer pathological response to NACT (178). However, further investigation is necessary to determine the nature of the f and f×D_p parameters and their relationships to the response to NACT. One approach to achieve this would be to expand imaging assessments to additional time points, such as after each cycle of NACT. This would provide a more detailed understanding of how f and f×D_p evolve throughout the treatment and their role in predicting response. Additionally, investigating the correlation between f and f×D_p parameters and histopathological markers, such as microvessel density (MVD), could clarify whether these parameters reflect tumour perfusion and microvascular changes. This could be achieved by scanning breast cancer patients with DWI to derive f and f×D_p parameters of the tumour, followed by tumour surgical resection and MVD calculation to examine their correlation. Alternatively, imaging patients with multiple DWI scans during NACT cycles, combined with biopsies taken from different tumour locations to calculate averaged tumour MVD values, and then examining the longitudinal correlations between f, f×D_p of the tumour, and tumour MVD may also provide insight into the biophysiological nature of f and f×D_p parameters. Furthermore, comparing the DWI technique with other functional imaging techniques, such as DCE-MRI, which provides an absolute measure of tumour blood flow (F_b) along with blood volume

fraction (v_b), may offer additional insights. By acquiring DWI and DCE-MRI scans at multiple NACT time points and examining the longitudinal correlations between these parameter changes caused by NACT (i.e., f and f×D_p versus F_b and v_b), this approach could also provide an understanding of the nature of f and f×D_p parameters and their relationships to NACT response (Chapter 6 investigated these correlations).

Like Bedair et al. (19), pR in the present study had higher α values than pNR at all time-points. However, after one NACT cycle, the percentage change in α between the response groups was significantly different and α was significantly higher in pR, which showed an ability to differentiate the two groups and predict response with reasonable performance (pR = 6.23% and pNR = -0.6%; AUC = 0.741; p = 0.01). The biological interpretation of the heterogeneity index α is still under consideration, it could reflect the complexity of the tissue microstructure (179). High α values in pR tumours could be indicative of more structural homogeneity, while low α values observed in pNR tumours may be suggestive of a more heterogeneous microenvironment; vascular heterogeneity and the existence of microscopic necrosis, resulting in a more aggressive tumour with less sensitivity to chemotherapy (180).

4.4.1 Limitations

Although this is the first study, to the best of the candidate's knowledge, which addressed the point raised in the previous study about investigating the SEM model's value in predicting patient response to NACT at an earlier time point than cycle three (19), this study had some limitations. The study was conducted in a single centre using one scanner (1.5 T MRI; Aera; Siemens), and the sample size was small, limiting its interpretation and impeding the assessment of the prediction performance of DWI models between the response groups according to breast tumour subtypes. A subsequent study in multiple centres using assorted scanners with a larger sample cohort (responders and non-responders) with various breast tumour subtypes is recommended to validate the prediction performance of the DWI models.

Moreover, the effects of voxel-wise analysis and estimation of the ADC using different b-value combinations on the prediction performance were not investigated. Instead, this study followed the recommendation that the parameter value directly estimated from the ROI-averaged signals is more accurate than the average of parameter values estimated on a voxel-by-voxel basis (168). However,

an alternate analytic approach, explored in a subsequent study (Chapter 5), is to derive the parameters from a focused ROI positioned on the darkest part of the tumour on the ADC map (i.e., the lowest ADC value). The area with the lowest ADC value within a tumour may potentially reflect the most active part of the tumour (24). Finally, the repeatability of the monoexponential, SEM and IVIM models' parameters was not examined. An upper estimate of the repeatability of these diffusion model parameters was calculated (181).

4.5 Conclusions

This preliminary study demonstrated that analysing diffusion data with non-monoexponential models offers a better prediction of NACT response than an analysis with a monoexponential model. The IVIM-derived parameters f and $f{\times}D_p$ and the SEM-derived parameter α predicted the response in patients with breast cancer with reasonable performance after one NACT cycle (AUC = 0.832, 0.802, 0.782; p = 0.001, 0.002, and 0.003, respectively). The results indicated that the ADC, DDC, and D_t values could not predict the response at pretreatment or after one or three cycles. Tumour volumes in the responders were smaller than in non-responders at all three time-points (p<0.001). Patients with a small tumour volume, higher α value, and lower f fraction and $f{\times}D_p$ after one NACT cycle responded better to NACT. The promising role of the perfusion-related parameters f and $f{\times}D_p$ supports further investigations to explore whether IVIM can offer a contrast-agent-free alternative to the DCE-MRI method for measuring breast tumour perfusion (Chapter 6).

Chapter 5 Evaluation of monoexponential, SEM and IVIM DWI MRI diffusion models estimated from tumour diffusion cold-spot and perfusion hot-spot regions in early response monitoring to NACT in patients with breast cancer

5.1 Introduction

The ACRIN 6698 trial, which is the largest multicentre trial evaluating the effectiveness of the ADC to assess the breast cancer response to NACT, found that a relative increase in whole-tumour ADC value was only predictive of breast cancer response to NACT after four cycles (12 weeks). The trial recommended further investigation of alternative analytical methods, such as characterising the worst tumour subregion (i.e., the area with the lowest ADC) to improve the detectability of changes in tumour cellularity (25). Similarly, the International Breast DWI Working Group suggested using a small ROI on the darkest region of the tumour on ADC maps, occasionally known as the diffusion cold-spot, to calculate ADC values, potentially reflecting the most active part of the tumour (24). This method is analogous to that used for DCE-MRI image analyses, which involves selecting the region of greatest mean maximum enhancement, often called a perfusion hot-spot (24, 26). The rationale for characterising the cold-spot is that it may represent the area of the tumour with the highest cell density, whereas the hot-spot is likely to reflect the tumour area with abundant angiogenesis. However, the ability of the ADC derived from tumour diffusion cold-spot and perfusion hot-spot to predict the early breast cancer response to NACT requires exploration. The ADC value calculated from the tumour perfusion hot-spot region might be largely influenced by perfusion effects impacting DWI signal characteristics, making the IVIM model a potential suitable candidate for characterising this region.

Preliminary studies have found that analysing DWI data derived from an ROI of the whole-tumour or a large single-section tumour using SEM and IVIM models could predict early breast cancer response to NACT (19, 23, 125). However, the predictive capability of these models, when focused on the most active region (i.e., the diffusion cold-spot and perfusion hot-spot) of the tumour, requires further exploration. Therefore, the purpose of this study is to investigate the value of monoexponential, SEM and IVIM models for the diffusion cold-spot and perfusion hot-spot regions of the tumour at pretreatment, and after one and three cycles of NACT in assessing the early breast cancer response to NACT.

5.2 Materials and methods

5.2.1 Patient population

The cohort of patients included, the recruitment eligibility criteria used, and the NACT regimen plan delivered are the same as detailed in Chapter 4, section 4.2.1.

5.2.2 MRI acquisition

The MRI scan time points and imaging protocol are the same as described in Chapter 4 (section 4.2.2); however, this section provides more details on the DCE-MRI sequences used.

After the acquisition of DWI, interleaved high temporal resolution (HTR) and high spatial resolution (HSR) DCE sequences were employed (7). The dynamic series comprised 93 HTR images interleaved with eight HSR images sequenced in the order of 10×HTR, 1×HSR, and 43×HTR. Then, a cycle of [1×HSR, 5×HTR] was repeated seven times and ended with five HTR images (Figure 5.1). The HTR dynamic images were acquired by employing a T1-weighted 3D FLASH sequence (TR/TE: 2.37/0.73 ms, FA: 25°, FOV: 340×340×180 mm, matrix size: 128×128×36, slice thickness: 5 mm, parallel imaging factor: 2×2, acquisition time: 2 s). For the HSR images (as described in section 4.2.2), a fat-suppressed T1-weighted 3D FLASH sequence (TR/TE: 4.1/1.2 ms, FA: 10°, FoV: 340×340×180 mm, matrix size: 384×384×128, slice thickness: 1.4 mm, parallel imaging factor: 3, acquisition time: 36 s) was used. An automated power injector (Spectris Solaris EP) intravenously injected 0.1 mmol/kg of gadoteric acid (Gd-DOTA, Dotarem, Guerbet Laboratories) as the 11th HTR image acquisition commenced, followed by saline (20 mL at a rate of 3 mL/s).
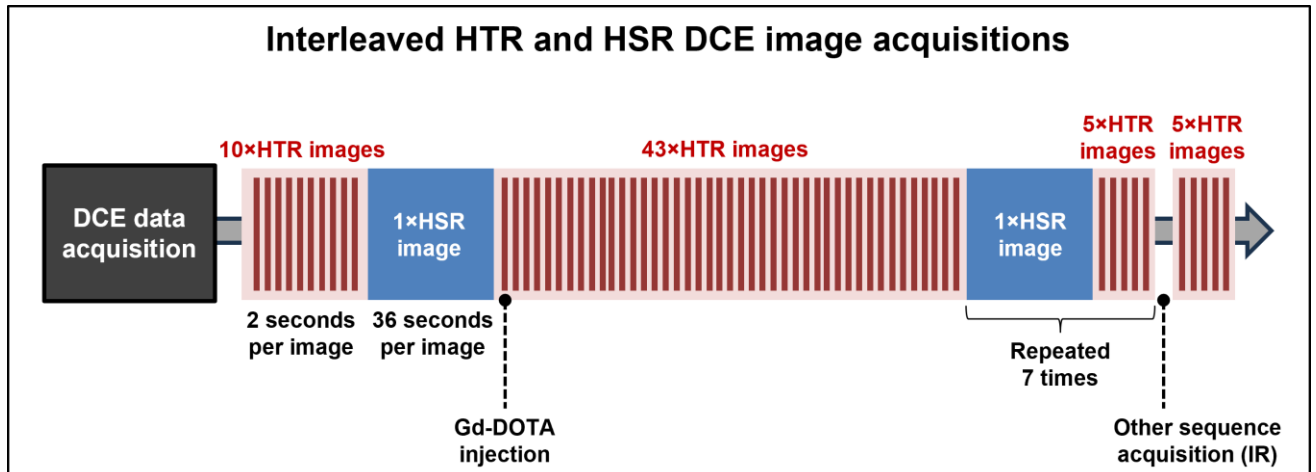
Figure 5.1 Schematic of the interleaved acquisition of high temporal resolution (HTR) and high spatial resolution (HSR) DCE images. The acquisitions comprised 93 HTR images interleaved with eight HSR images sequenced in the order of 10×HTR, 1×HSR, and 43×HTR. Then, a cycle of [1×HSR, 5×HTR] was repeated seven times and ended with five HTR images. The contrast agent (Gd-DOTA) was injected as the 11th HTR image acquisition commenced. An inversion recovery (IR) sequence was performed (for the study in Chapter 6) before the last five HTR images were obtained.

5.2.3 Image analysis

All MRI data were processed through the same in-house program developed in MATLAB (MathWorks, USA), used in Chapter 4 work. Expanding to section 4.2.3, the HTR, and HSR images were rigidly aligned to match the DWI images (and therefore the ADC maps) without interpolation of the DWI data. The HTR and HSR DCE subtraction images were created by subtracting the precontrast images from the postcontrast images to enhance the clarity of the tumour.

For each patient, the generated whole-tumour ROI (section 4.2.3) was propagated to the corresponding DWI, ADC, and HTR images. Two focused single-slice ROIs (5×5 pixels) were generated within the whole-tumour ROI, comprising a diffusion cold-spot and perfusion hot-spot. The cold-spot ROI was the tumour region with the lowest ADC value on the ADC map (24), and the hot-spot ROI was the tumour region with the highest SI on the HTR subtraction images. The spatial location of the cold-spot and hot-spot ROIs for each tumour were allowed to vary at each MRI visit as the tumour responded to NACT. The mean SI for every b-value was extracted from the cold-spot and hot-spot ROIs transferred to the corresponding DWI (168) (Figure 5.2).
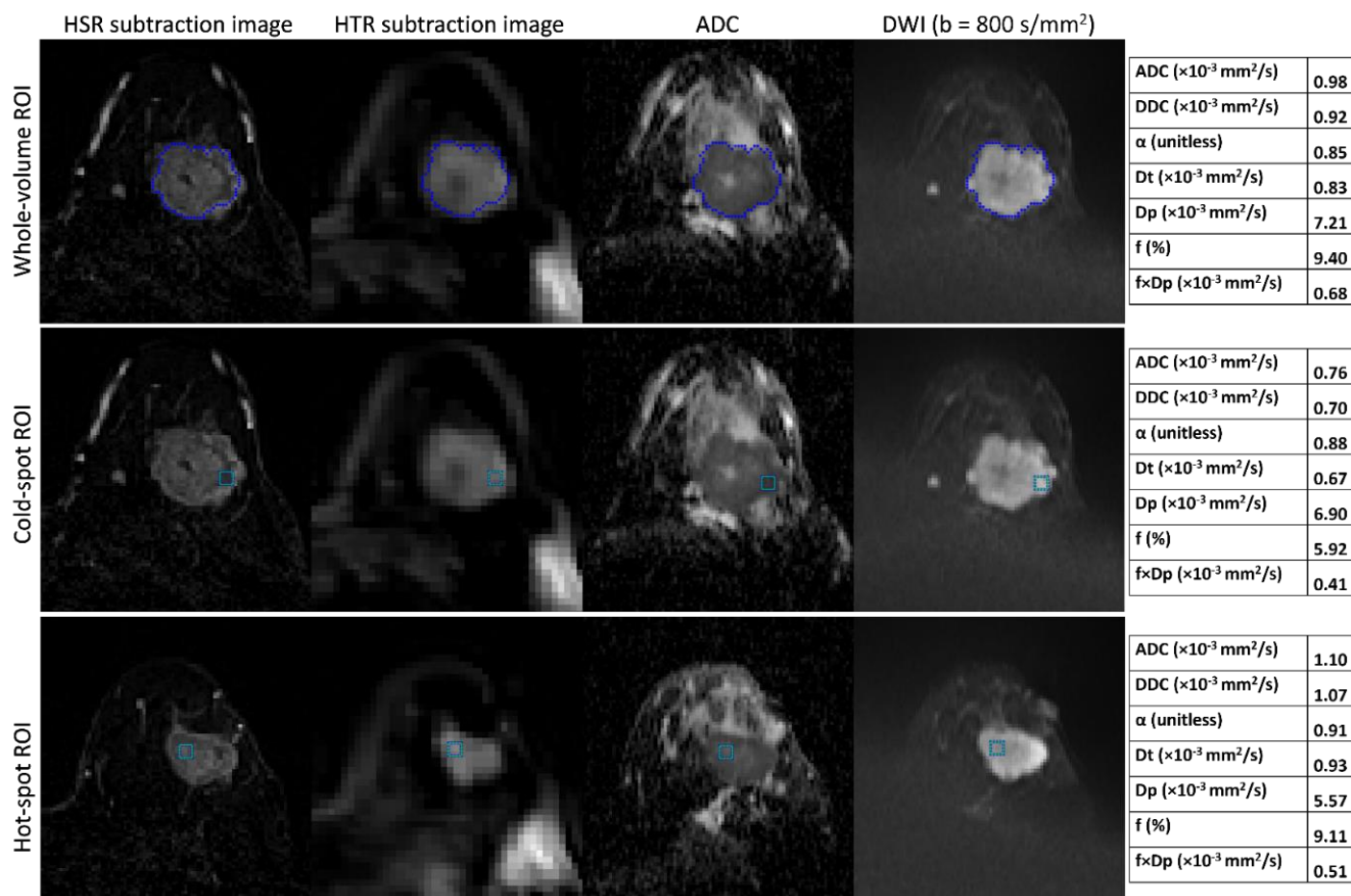
Figure 5.2 Example of MRI images for an invasive ductal carcinoma tumour in the left breast of a 45-year-old woman who was a responder (RCB-0). The top row illustrates the whole-tumour region of interest (ROI) created on the HSR subtraction images. The middle and bottom rows demonstrate the cold-spot and hot-spot ROIs (5×5 pixels) respectively, generated within the whole-tumour ROI. The whole-tumour ROI covers all the slices where the tumour is present, whereas the cold-spot and hot-spot regions originate in only a single slice (not necessarily the same slice). All three regions were transferred to the corresponding DWI for subsequent analysis. The tables represent the parameter estimates of monoexponential, SME, and IVIM models from each tumour ROI.

The parameters for the monoexponential (ADC) and SEM (DDC, α) models were estimated in the same manner as described in section 4.2.3, while the IVIM parameters (D_t, D_p, f, and f×D_p) were estimated using the oversegmented-fitting with constraints approach (illustrated in section 3.2.2) based on the results of Chapter 3. Figure 5.3 shows an example of DWI signals derived from tumour cold-spot and hot-spot ROIs and the curve-fittings performed.
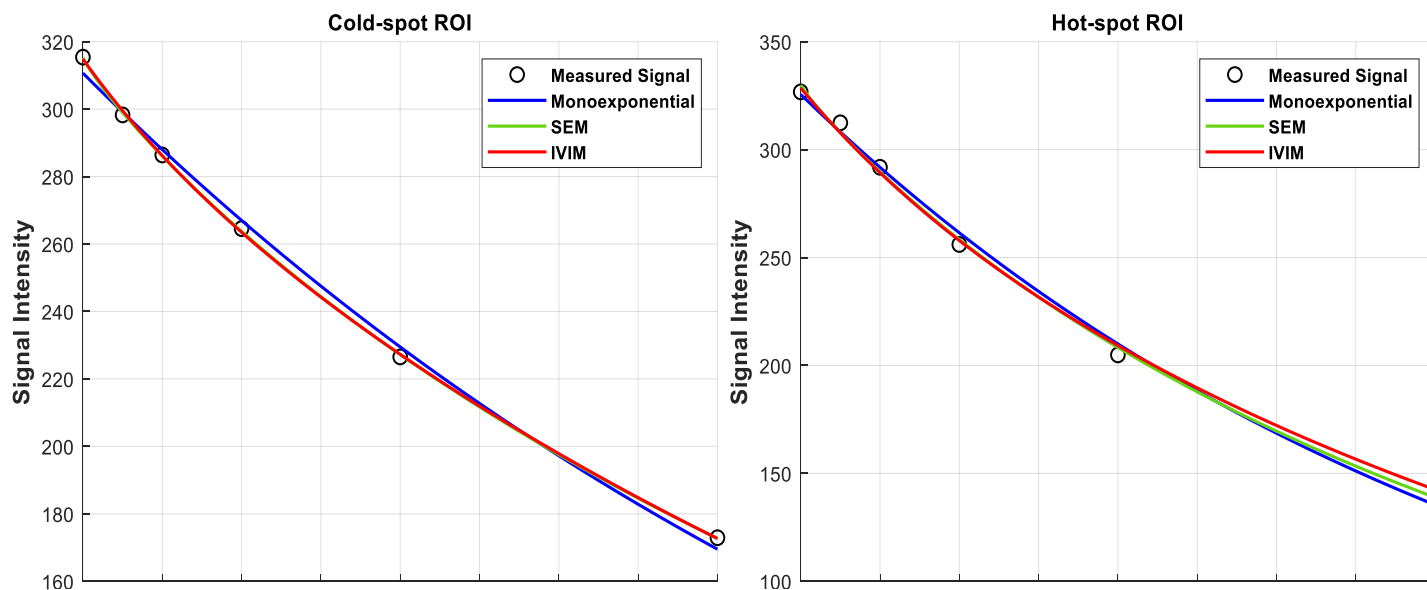
Figure 5.3 The measured DWI signals from the tumour's cold-spot and hot-spot ROIs, along with the best-fit curves of the monoexponential, SEM, and IVIM models, for the tumour of the responder patient in Figure 5.2 at pretreatment.

The parameter values were estimated and documented for each patient during the three MRI visits (pretreatment, and after one and three cycles of NACT). The percentage changes in the parameters were computed for each patient relative to the values for pretreatment and after one NACT cycle:

$$\Delta \text{ Parameter (\%)} = \frac{Value_{after\ one\ or\ three\ cycles} - Value_{at\ pretreatment\ or\ after\ one\ cycle}}{Value_{\ at\ pretreatment\ or\ after\ one\ cycle}} \times 100$$

All steps were performed blind to the evaluation of pathological responses to NACT.

5.2.4 Pathological response evaluation

The method for assessing tumour response and classifying patients into pR and pNR groups was as detailed in section 4.24.

5.2.5 Statistical analysis

The DWI parameters were reported as the median and IQR due to the non-normal data distribution. The parameter differences between pretreatment, after one cycle, and after three cycles were assessed for the entire cohort using Friedman's test with the Bonferroni correction. The parameter estimates and relative changes (%) in parameter values after one and three NACT cycles were compared between the pR and pNR groups using the Mann–Whitney test. The performance of the parameters and their corresponding relative changes in predicting treatment outcomes was evaluated by calculating the AUC (AUC; $0.5 \leq AUC < 0.7$: poor performance and $0.7 \leq AUC < 0.9$: reasonable performance) (23). The IBM SPSS software (v.25.0) was used for all analyses. As this is a preliminary study, p-values were reported as raw values and were not corrected for multiple comparisons; thus, a p-value of less than 0.05 was considered statistically significant.

5.3 Results

5.3.1 Tumour segmentations

As illustrated in section 4.3.1, 40 MRI studies were analysed at pretreatment (pR = 17 and pNR = 23), 37 after one NACT cycle (pR = 17 and pNR = 20), and 35 after three NACT cycles (pR = 15 and pNR = 20).

Focused ROIs (cold-spot/hot-spot) were generated in 37/34 tumours at pretreatment (pR = 15 and pNR = 22/pR = 13 and pNR = 21), 33/33 tumours after one NACT cycle (pR = 14 and pNR = 19), and 25/24 tumours after three NACT cycles (pR = 7 and pNR = 18/pR = 7 and pNR = 17). Three tumours at pretreatment were smaller than the 5x5 pixel size threshold, and some during NACT cycles were reduced below this threshold. Four HTR-DCE scans—two at pretreatment and two after three NACT cycles—were excluded at the step of whole-tumour ROI propagation due to patient intolerance of the whole scan (one case), coil technical problems (two cases), and excessive patient movement (one case). Furthermore one HTR-DCE scan at pretreatment was excluded from the hot-spot identification step due to unsuccessful image alignment because the initial scan was performed without contrast and repeated on another day only for the DCE imaging, not the DWI (Figure 5.4).
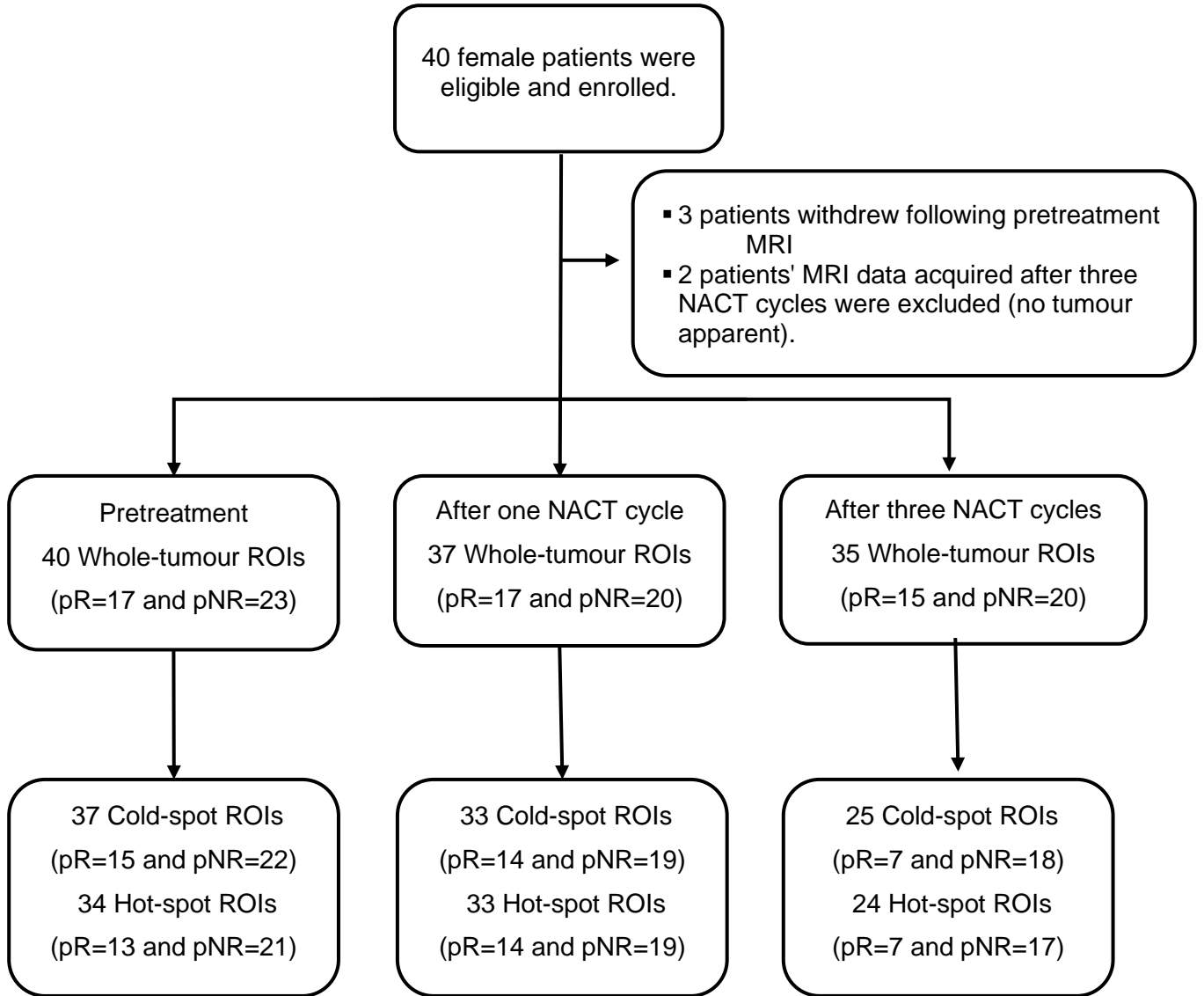
Figure 5.4 The flow chart illustrates the number of recruited patients, responders (pR) and non-responders (pNR), and the number of generated tumor cold-spot and hot-spot ROIs at each MRI time-point.

5.3.2 Parameter values for the cohort

The IVIM parameter estimates D_p and f reached one of their constrained values in eight cases from the cold-spot region (at pretreatment) and four cases from the hot-spot region (three at pretreatment and one after three NACT cycles) and were excluded from the statistical analyses. Tables 5.1 and 5.2 summarise the values at pretreatment and after one and three NACT cycles across the cohort in cold-spot and hot-spot ROIs. The ADC and DDC values in the cold-spot and hot-spot ROIs

were significantly lower at pretreatment than after three NACT cycles (median: ADC: 0.73 and 0.97 $\times 10^{-3}$ mm^2/s; p = 0.001, and DDC: 0.64 and 0.90 $\times 10^{-3}$ mm^2/s; p = 0.03 in cold-spot ROIs; ADC: 0.93 and 1.12 $\times 10^{-3}$ mm^2/s; p = 0.01, and DDC: 0.86 and 1.05 $\times 10^{-3}$ mm^2/s; p = 0.02 in hot-spot ROIs, respectively). Pretreatment f values derived from hot-spot ROIs were significantly less than those after three cycles (median: f: 10.15 and 12.34; p = 0.03, respectively). Additionally, α values estimated from cold-spot ROIs were significantly higher at pretreatment than after cycle three (median: α: 0.88 and 0.81; p = 0.02, respectively). However, no significant differences were observed in the α (in hot-spot ROIs), D_t, D_p, f (in cold-spot ROIs) and f$\times$$D_p$ values between pretreatment and after one and three cycles (p = 0.054 and 0.81).

Table 5.1 DWI parameters of monoexponential, SEM and IVIM models pretreatment, after one cycle of NACT, and at mid-treatment in tumour cold-spot ROI.

Parameter	N	Pretreatment (a)	After one cycle of NACT (b)	After three cycles of NACT (c)	P	Post hoc**
ADC ($\times 10^{-3}$ mm^2/s)	25	**0.73 (0.65, 0.86)**	**0.87 (0.75, 1)**	**0.97 (0.81, 1.14)**	**0.001**	**a<c**
DDC ($\times 10^{-3}$ mm^2/s)	25	**0.64 (0.58, 0.81)**	**0.80 (0.66, 0.91)**	**0.90 (0.73, 1.06)**	**0.03**	**a<c**
α (unitless)	25	**0.88 (0.79, 0.89)**	**0.83 (0.74, 0.89)**	**0.81 (0.7, 0.87)**	**0.02**	**a>c**
D_t ($\times 10^{-3}$ mm^2/s)	25	0.64 (0.59, 0.78)	0.66 (0.57, 0.84)	0.77 (0.6, 0.92)	0.054	-
D_p ($\times 10^{-3}$ mm^2/s) (*)	19	7.12 (5.69, 10.77)	6.38 (4.96, 10.17)	7.13 (5.73, 9.27)	0.81	-
f (%) (*)	19	9.3 (4.61, 11.69)	9.25 (7.17, 11.88)	12.15 (7.84, 16.11)	0.33	-
f×D_p ($\times 10^{-3}$ mm^2/s) (*)	19	0.53 (0.44, 1.07)	0.57 (0.42, 1.16)	0.87 (0.53, 1.73)	0.50	-

Data represented by medians (interquartile ranges). P-value for a difference between the three visits was found using Friedman's non-parametric test. Pairwise comparisons** (Bonferroni-corrected) significance at the 0.05 level. ADC: apparent diffusion coefficient. DDC: distributed diffusion coefficient. α: diffusion heterogeneity index. D_t: tissue diffusion. D_p: pseudo-diffusion coefficient. f: perfusion fraction. f×D_p: microvascular blood flow. (*) Number of the IVIM parameter D_p and f estimates is different due to the exclusion of the estimates that reached one of their limiting values.

Table 5.2 DWI parameters of monoexponential, SEM and IVIM models pretreatment, after one cycle of NACT, and at mid-treatment in tumour hot-spot ROI.

Parameter	N	Pretreatment (a)	After one cycle of NACT (b)	After three cycles of NACT (c)	P	Post hoc**
ADC ($\times 10^{-3}$ mm^2/s)	22	**0.93 (0.85, 1.11)**	**1.03 (0.86, 1.26)**	**1.12 (0.96, 1.27)**	**0.016**	**a<c**
DDC ($\times 10^{-3}$ mm^2/s)	22	**0.86 (0.79, 1.06)**	**0.97 (0.82, 1.21)**	**1.05 (0.86, 1.2)**	**0.025**	**a<c**
α (unitless)	22	0.85 (0.81, 0.88)	0.85 (0.78, 0.88)	0.81 (0.75, 0.88)	0.17	-
D_t ($\times 10^{-3}$ mm^2/s)	22	0.78 (0.74, 0.94)	0.85 (0.74, 1.01)	0.85 (0.76, 0.93)	0.28	-
D_p ($\times 10^{-3}$ mm^2/s) (*)	21	7.83 (6.07, 8.7)	7.06 (5.99, 8.86)	7.13 (5.6, 8.67)	0.82	-
f (%) (*)	21	**10.15 (7.56, 11.61)**	**10.36 (9.07, 12.92)**	**12.34 (11.06, 14.03)**	**0.03**	**a<c**
f×D_p ($\times 10^{-3}$ mm^2/s) (*)	21	0.72 (0.54, 1)	0.67 (0.54, 1)	0.95 (0.68, 1.72)	0.055	-

Data represented by medians (interquartile ranges). P-value for a difference between the three visits was found using Friedman's non-parametric test. Pairwise comparisons** (Bonferroni-corrected) significance at the 0.05 level. ADC: apparent diffusion coefficient. DDC: distributed diffusion coefficient. α: diffusion heterogeneity index. D_t: tissue diffusion. D_p: pseudo-diffusion coefficient. f: perfusion fraction. f×D_p: microvascular blood flow. (*) Number of the IVIM parameter D_p and f estimates is different due to the exclusion of the estimates that reached one of their limiting values.

5.3.3 Difference in parameters between response groups

Table 5.3 compares the parameter values for pR and pNR at pretreatment and after one and three cycles of NACT in tumour cold-spot regions. No significant differences were found in ADC, D_p and $f{\times}D_p$ between the pR and pNR groups at all time points (pretreatment: p = 0.09, 1 and 1; after one cycle: p = 0.07, 0.92, and 0.14; and after three cycles: p = 0.27, 0.70, and 0.57, respectively). After one NACT cycle, pR patients exhibited considerably higher DDC, α and D_t values (median: pR = $0.9{\times}10^{-3}$ mm^2/s and pNR = $0.72{\times}10^{-3}$ mm^2/s; p = 0.01 for DDC; pR = 0.89 and pNR = 0.77; p = 0.01 for α; and pR = $0.8{\times}10^{-3}$ mm^2/s and pNR = $0.63{\times}10^{-3}$ mm^2/s; p = 0.005 for D_t). In contrast, f values were significantly higher in the pNR group (median: pR = 7.91% and pNR = 9.85%; p = 0.04). However, no significant differences between the response groups existed in the DDC, α, D_t and f values at pretreatment and after three cycles (pretreatment: p = 0.17, 0.72, 0.23 and 0.77 and after three cycles: p = 0.15, 0.49, 0.19 and 0.53, respectively; Table 5.3).

Table 5.3 Comparisons of DWI parameter values at pretreatment, after one cycle of NACT, and at mid-treatment for the pR and pNR groups in tumour cold-spot ROI.

Parameter	Pretreatment (n=37)			After one cycle of NACT (n=33)			After three cycles of NACT (n=25)		
	pR (n=15)	pNR (n=22)	P	pR (n=14)	pNR (n=19)	P	pR(n=7)	pNR(n=18)	P
ADC ($\times 10^{-3}$ mm^2/s)	0.81 (0.73, 0.86)	0.71 (0.63, 0.95)	0.09	0.96 (0.87, 1.02)	0.8 (0.73, 0.99)	0.07	1.03 (0.97, 1.13)	0.92 (0.76, 1.15)	0.27
DDC ($\times 10^{-3}$ mm^2/s)	0.7 (0.65, 0.81)	0.6 (0.56, 0.81)	0.17	**0.9 (0.81, 1)**	**0.72 (0.63, 0.85)**	**0.01**	0.96 (0.9, 1.07)	0.83 (0.54, 0.99)	0.15
α (unitless)	0.88 (0.76, 0.91)	0.84 (0.76, 0.89)	0.72	**0.89 (0.85, 0.96)**	**0.77 (0.71, 0.89)**	**0.01**	0.83 (0.8, 0.85)	0.79 (0.59, 0.89)	0.49
D_t ($\times 10^{-3}$ mm^2/s)	0.68 (0.63, 0.76)	0.64 (0.56, 0.72)	0.23	**0.8 (0.75, 0.91)**	**0.63 (0.54, 0.79)**	**0.005**	0.84 (0.78, 0.88)	0.69 (0.54, 0.93)	0.19
D_p ($\times 10^{-3}$ mm^2/s) (*)	6.94 (5.53, 14.81)	9.09 (5.9, 11.06)	1.00	6.47 (5.41, 8.41)	6.38 (4.83, 10.17)	0.92	7.69 (6.45, 8.31)	7.6 (5.6, 20.74)	0.70
f (%) (*)	8.12 (6.22, 12.24)	9.77 (4.88, 12.15)	0.77	**7.91 (5.76, 9.7)**	**9.85 (8.04, 18.07)**	**0.04**	12.15 (9.54, 13.28)	12.82 (7.95, 16.89)	0.53
f×D_p ($\times 10^{-3}$ mm^2/s) (*)	0.86 (0.41, 1.63)	0.64 (0.47, 1.07)	1.00	0.51 (0.33, 0.77)	0.89 (0.42, 1.44)	0.14	0.87 (0.69, 1.03)	0.88 (0.67, 3.47)	0.57

Data are represented by medians (interquartile ranges). P-value calculated using independent samples for the Mann-Whitney U test. ADC: apparent diffusion coefficient. DDC: distributed diffusion coefficient. α: diffusion heterogeneity index. D_t: tissue diffusion. D_p: pseudo-diffusion coefficient. f: perfusion fraction. f×D_p: microvascular blood flow. pR: pathological responders. pNR: pathological non-responders. (*) Number of the IVIM parameter D_p and f estimates is different due to the exclusion of the estimates that reached one of their limiting values (at pretreatment: pR = 13 and pNR = 16).

Table 5.4 presents the parameter values for pR and pNR at pretreatment and after one and three cycles of NACT in tumour hot-spot regions. No significant differences were observed between the response groups in ADC, DDC, D_t and D_p at all time points (pretreatment: p = 0.50, 0.80, 0.97 and 0.07; after one cycle: p = 0.55, 0.73, 1 and 0.46; and after three cycles: p = 0.85, 0.90, 1 and 0.82, respectively). The α values were significantly higher in the pR group at pretreatment and after one cycle (median: pretreatment: pR = 0.87 and pNR = 0.82; p = 0.04, after one cycle: pR = 0.9 and pNR = 0.84; p = 0.01). Conversely, pNR patients exhibited significantly higher values of f and f×D_p at pretreatment, and higher f values after one cycle (median: pretreatment: pR = 8.78% and pNR = 11.44%; p = 0.03 for f; and pR = 0.56×10^{-3} mm^2/s and pNR = 0.98×10^{-3} mm^2/s; p = 0.006 for f×D_p; and after one cycle: pR = 9.12% and pNR = 11.84%; p = 0.03 for f). However, no significant differences were found between the response groups in the values of f×D_p after one cycle and in α, f and f×D_p after three cycles (p = 0.08, 0.41, 0.13 and 0.34, respectively; Table 5.4).

Table 5.4 Comparisons of DWI parameter values at pretreatment, after one cycle of NACT, and at mid-treatment for the pR and pNR groups in tumour hot-spot ROI.

Parameter	Pretreatment (n=34)			After one cycle of NACT (n=33)			After three cycles of NACT (n=24)		
	pR (n=13)	pNR (n=21)	*P*	pR (n=14)	pNR (n=19)	*P*	pR(n=7)	pNR(n=17)	*P*
ADC ($\times10^{-3}$ mm^2/s)	0.91 (0.87, 1.02)	0.97 (0.85, 1.11)	0.50	1.01 (0.95, 1.19)	1.09 (0.89, 1.28)	0.55	1.13 (0.97, 1.21)	1.11 (0.97, 1.25)	0.85
DDC ($\times10^{-3}$ mm^2/s)	0.85 (0.81, 0.96)	0.94 (0.79, 1.06)	0.80	0.98 (0.88, 1.15)	1.03 (0.83, 1.24)	0.73	1.06 (0.9, 1.14)	1.04 (0.89, 1.16)	0.90
α (unitless)	**0.87 (0.84, 0.9)**	**0.82 (0.76, 0.86)**	**0.042**	**0.9 (0.86, 0.93)**	**0.84 (0.8, 0.86)**	**0.014**	0.83 (0.79, 0.88)	0.81 (0.73, 0.88)	0.41
D_t ($\times10^{-3}$ mm^2/s)	0.8 (0.74, 0.85)	0.81 (0.71, 0.94)	0.97	0.86 (0.78, 1.05)	0.92 (0.76, 1.03)	1.00	0.84 (0.8, 0.93)	0.89 (0.78, 0.97)	1.00
D_p ($\times10^{-3}$ mm^2/s) (*)	6.15 (5.57, 7.56)	8.25 (6.11, 12.12)	0.07	6.89 (5.28, 7.73)	7.06 (6.43, 9.01)	0.46	7.69 (6.45, 8.34)	7.38 (5.51, 11.51)	0.82
f (%) (*)	**8.78 (7.17, 10.42)**	**11.44 (9.21, 12.69)**	**0.039**	**9.12 (7.51, 11.47)**	**11.84 (9.95, 13.56)**	**0.032**	11.35 (9.31, 12.8)	12.52 (12.08, 19.69)	0.13
f$\times$D$_p$ ($\times10^{-3}$ mm^2/s) (*)	**0.56 (0.44, 0.75)**	**0.98 (0.7, 1.32)**	**0.006**	0.59 (0.45, 0.98)	0.8 (0.58, 1.18)	0.08	0.9 (0.66, 1.09)	1.17 (0.7, 2.06)	0.34

Data are represented by medians (interquartile ranges). P-value calculated using independent samples for the Mann-Whitney U test. ADC: apparent diffusion coefficient. DDC: distributed diffusion coefficient. α: diffusion heterogeneity index. D_t: tissue diffusion. D_p: pseudo-diffusion coefficient. f: perfusion fraction. f$\times$D$_p$: microvascular blood flow. pR: pathological responders. pNR: pathological non-responders. (*) Number of the IVIM parameter D_p and f estimates is different due to the exclusion of the estimates that reached one of their limiting values (at pretreatment: pR = 12 and pNR = 19, after three cycles: pR = 7 and pNR = 16).

Table 5.5 reports the AUCs of the ROC curves for parameters that differentiated between the pR and pNR groups. The α, f and f×D_p in hot-spot regions demonstrated reasonable performance in predicting treatment response at pretreatment (AUC = 0.711, 0.724 and 0.794; p = 0.04, 0.03, and 0.007, respectively). After one NACT cycle, the response prediction was reasonable for DDC and D_t in cold-spot regions (AUC = 0.752 and 0.786; p = 0.01 and 0.006), and for α and f in both hot-spot (AUC = 0.752 and 0.722; p = 0.01 and 0.03) and cold-spot regions (AUC = 0.744 and 0.711; p = 0.01 and 0.04), respectively.

Table 5.5 The diagnostic performance of monoexponential, SEM and IVIM parameters that differentiated between pR and pNR groups.

Parameter	Tumour region	Time point	AUC	95% Confidence Interval	P
α (unitless)	Hot-spot	Pretreatment	0.711	0.535 – 0.886	0.042
f (%)	Hot-spot	Pretreatment	0.724	0.538 – 0.910	0.039
f×D_p (×10^{-3} mm^2/s)	Hot-spot	Pretreatment	0.794	0.637 – 0.951	0.007
α (unitless)	Hot-spot	Cycle 1	0.752	0.571 – 0.932	0.015
f (%)	Hot-spot	Cycle 1	0.722	0.538 – 0.906	0.032
DDC (×10^{-3} mm^2/s)	Cold-spot	Cycle 1	0.752	0.585 – 0.918	0.015
α (unitless)	Cold-spot	Cycle 1	0.744	0.572 – 0.916	0.018
D_t (×10^{-3} mm^2/s)	Cold-spot	Cycle 1	0.786	0.627 – 0.944	0.006
f (%)	Cold-spot	Cycle 1	0.711	0.531 – 0.890	0.041
AUC: Area under the receiver operating characteristic curve. DDC: distributed diffusion coefficient. α: diffusion heterogeneity index. D_t: tissue diffusion. f: perfusion fraction. f×D_p: microvascular blood flow.					

5.3.4 Relative parameter change differences between response groups

In the cold-spot regions, the changes in the DDC and D_t values after one NACT cycle relative to their pretreatment values and in the f values after three NACT cycles relative to their values after one NACT cycle significantly differed between the pR and pNR groups (median: pR = 31.86% and pNR = 10.41%; p = 0.009 for DDC; pR = 23.88% and pNR = -8.03%; p = 0.003 for D_t; and pR = 107.36% and pNR = 3.44%; p = 0.02 for f; Tables 5.6 and 5.7). Nevertheless, no statistically significant relationship was determined between the pathological response and the relative changes in the ADC, α, D_p, f and f×D_p values after one NACT cycle, nor in the ADC, DDC, α, D_t, D_p and f×D_p values after three NACT cycles (after one cycle: p = 0.06 to 0.56 and after three cycles: p = 0.11 to 0.92; Tables 5.6 and 5.7).

Table 5.6 Comparisons of the relative change in DWI parameter values for the pR and pNR groups in tumour cold-spot ROI.

Cycle 1 - Pretreatment					
Parameter	**N**	**pR**	**N**	**pNR**	**_P_**
ADC	14	20.97 (14.69, 36.87)	19	5.61 (-3.64, 28.57)	0.065
DDC	**14**	**31.86 (16.37, 41.89)**	**19**	**10.41 (-7.29, 16.36)**	**0.009**
α	14	2.15 (-3.14, 12.69)	19	-5.82 (-21.14, 6.91)	0.077
D_t	**14**	**23.88 (7.6, 32.98)**	**19**	**-8.03 (-17.1, 4.4)**	**0.003**
D_p (*)	12	-4.11 (-50.26, 22.86)	14	7.18 (-59.06, 72.74)	0.56
f (*)	12	-12.23 (-44.63, 21.35)	14	30.92 (-7.51, 102.24)	0.095
f×D_p (*)	12	-3.48 (-65.64, 49.58)	14	15.15 (-45.46, 166.43)	0.274
Cycle 3 - Pretreatment					
ADC	7	35.74 (32.44, 46.51)	18	17.75 (0.32, 39.6)	0.27
DDC	7	48.05 (37.82, 49.36)	18	14.15 (-7, 40.05)	0.14
α	7	-4.53 (-7.01, -0.25)	18	-10.7 (-28.81, -0.32)	0.24
D_t	7	20.74 (17.21, 34.65)	18	4.44 (-14.08, 36.99)	0.11
D_p (*)	6	1.71 (-74.45, 30.49)	13	-11.92 (-17.92, 77.75)	0.46
f (*)	6	58.22 (-18.98, 177.78)	13	51.95 (-22.65, 92.57)	0.76
f×D_p (*)	6	28.98 (-46.55, 212.36)	13	36.78 (-36.94, 263.9)	0.52

Data are represented by medians (interquartile ranges). P-value calculated using independent samples for the Mann-Whitney U test. ADC: apparent diffusion coefficient. DDC: distributed diffusion coefficient. α: diffusion heterogeneity index. D_t: tissue diffusion. D_p: pseudo-diffusion coefficient. f: perfusion fraction. f×D_p: microvascular blood flow. pR: pathological responders. pNR: pathological non-responders. (*) Number of the IVIM parameter D_p and f estimates is different due to the exclusion of the estimates that reached one of their limiting values.

Δ parameter (%)= [(Value _after one/three cycles_) - (Value _at pretreatment_)]/(Value _at pretreatment_) × 100

Table 5.7 Comparisons of the relative change in DWI parameter values for the pR and pNR groups in tumour cold-spot ROI.

Cycle 3 – Cycle 1					
Parameter	**N**	**pR**	**N**	**pNR**	**P**
ADC	7	10.01 (7.08, 22.45)	18	6.77 (-1.28, 29.91)	0.65
DDC	7	6.19 (4.33, 22.38)	18	14.35 (-21.21, 34.53)	0.74
α	7	-7.98 (-13.17, -3.3)	18	-7.84 (-18.95, 11.24)	0.79
D_t	7	6.85 (-3.72, 9.24)	18	16.81 (2.05, 32.17)	0.14
D_p	7	-5.35 (-16.61, 38.67)	18	13.28 (-39.29, 167.74)	0.92
f	**7**	**107.36 (47.12, 132.15)**	**18**	**3.44 (-26.57, 74.36)**	**0.02**
f×D_p	7	96.26 (59.89, 160.98)	18	84.31 (-52.97, 261.38)	0.74
Data are represented by medians (interquartile ranges). P-value calculated using independent samples for the Mann-Whitney U test. ADC: apparent diffusion coefficient. DDC: distributed diffusion coefficient. α: diffusion heterogeneity index. D_t: tissue diffusion. D_p: pseudo-diffusion coefficient. f: perfusion fraction. f×D_p: microvascular blood flow. pR: pathological responders. pNR: pathological non-responders.					
Δ parameter (%)= [(Value after three cycles) - (Value after one cycle)]/(Value after one cycle) × 100					

In the hot-spot regions, no statistically significant relationship existed between the pathological response and relative changes in all parameter values after one and three NACT cycles (after one cycle: $p = 0.37$ to 0.87 and after three cycles: $p = 0.20$ to 0.97; Tables 5.8 and 5.9).

Table 5.8 Comparisons of the relative change in DWI parameter values for the pR and pNR groups in tumour hot-spot ROI.

Cycle 1 - Pretreatment					
Parameter	**N**	**pR**	**N**	**pNR**	**_P_**
ADC	13	11.09 (8.2, 17.71)	18	5.1 (-5.55, 19.65)	0.37
DDC	13	11.64 (7.42, 18.45)	18	6.72 (-4.67, 23.77)	0.51
α	13	0.1 (-5.16, 3.46)	18	0.37 (-10.78, 10.79)	0.56
D_t	13	12.08 (3.47, 15.14)	18	3.58 (-6.74, 17.22)	0.37
D_p (*)	12	-1.95 (-15.37, 17.53)	17	-7.74 (-48.08, 20.42)	0.52
f (*)	12	0.32 (-12.15, 25.69)	17	4.42 (-13.44, 22.2)	0.71
f×D_p (*)	12	13.29 (-30.35, 38.88)	17	-15.22 (-32.37, 73.33)	0.87
Cycle 3 - Pretreatment					
ADC	6	23.38 (5.12, 46.6)	16	7.4 (-0.11, 18.41)	0.17
DDC	6	26.1 (3.58, 47.79)	16	7.25 (-2.52, 19.74)	0.20
α	6	-4.21 (-5.27, 1.73)	16	-7.51 (-14.03, 3.42)	0.44
D_t	6	13.24 (0.27, 24.19)	16	4.71 (-11.69, 13.71)	0.23
D_p (*)	6	1.41 (-25.43, 31.54)	15	7.33 (-37.27, 15.73)	0.85
f (*)	6	41.14 (13.21, 52.59)	15	41.86 (5, 91.29)	0.91
f×D_p (*)	6	40.92 (11.32, 144.94)	15	23.09 (-16.05, 121.4)	0.51

Data are represented by medians (interquartile ranges). P-value calculated using independent samples for the Mann-Whitney U test. ADC: apparent diffusion coefficient. DDC: distributed diffusion coefficient. α: diffusion heterogeneity index. D_t: tissue diffusion. D_p: pseudo-diffusion coefficient. f: perfusion fraction. f×D_p: microvascular blood flow. pR: pathological responders. pNR: pathological non-responders. (*) Number of the IVIM parameter D_p and f estimates is different due to the exclusion of the estimates that reached one of their limiting values.

Δ parameter (%)= [(Value ₐfter one/three cycles) - (Value ₐt pretreatment)]/(Value ₐt pretreatment) × 100

Table 5.9 Comparisons of the relative change in DWI parameter values for the pR and pNR groups in tumour hot-spot ROI.

Cycle 3 – Cycle 1					
Parameter	**N**	**pR**	**N**	**pNR**	**P**
ADC	7	10.01 (-2.74, 21.06)	17	4.64 (-7.16, 19.82)	0.85
DDC	7	6.19 (-3.36, 21.14)	17	1.94 (-10.26, 20.27)	0.75
α	7	-3.45 (-10.61, -0.29)	17	-1.62 (-7.65, 7.66)	0.61
D_t	7	2.64 (-5.56, 8.64)	17	-3.48 (-4.3, 14.13)	0.85
D_p (*)	7	-6.88 (-14.84, 34.29)	16	1.62 (-16.92, 26.42)	0.72
f (*)	7	25.25 (14.84, 51.76)	16	44.61 (-5.08, 98.33)	0.97
f×D_p (*)	7	33.96 (2.46, 128.8)	16	41 (-0.23, 94.65)	0.76
Data are represented by medians (interquartile ranges). P-value calculated using independent samples for the Mann-Whitney U test. ADC: apparent diffusion coefficient. DDC: distributed diffusion coefficient. α: diffusion heterogeneity index. D_t: tissue diffusion. D_p: pseudo-diffusion coefficient. f: perfusion fraction. f×D_p: microvascular blood flow. pR: pathological responders. pNR: pathological non-responders.					
Δ parameter (%)= [(Value after three cycles) - (Value after one cycle)]/(Value after one cycle) × 100					

Table 5.10 presents the AUCs of the ROC curves for the relative changes in the parameters that differentiated between the response groups. The changes in DDC and D_t (after one NACT cycle relative to pretreatment) and f (after three NACT cycles relative to one cycle) demonstrated reasonable performance in predicting treatment response (AUC = 0.767; p = 0.01 for DDC, AUC = 0.797; p = 0.004 for D_t, and AUC = 0.802; p = 0.02 for f).

Table 5.10 The diagnostic performance for the relative change in monoexponential, SEM and IVIM parameters that differentiated between pR and pNR groups.

Parameter	Tumour region	Time point	AUC	95% Confidence Interval	P
DDC	Cold-spot	Cycle 1 - Pretreatment	0.767	0.600 – 0.934	0.010
D_t	Cold-spot	Cycle 1 - Pretreatment	0.797	0.639 – 0.955	0.004
f	Cold-spot	Cycle 3 – Cycle 1	0.802	0.617 – 0.986	0.021
AUC: Area under the receiver operating characteristic curve. DDC: distributed diffusion coefficient. α: diffusion heterogeneity index. D_t: tissue diffusion. f: perfusion fraction. f×D_p: microvascular blood flow.					

5.4 Discussion

None of the pretreatment diffusion coefficients—ADC, DDC and D_t—from cold-spot and hot-spot regions were predictive of the response to NACT. This finding aligns with observations from the whole-tumour ROI in the same cohort (Chapter 4) and with those reported from a meta-analysis study on ADC (172). However, in cold-spot regions after one NACT cycle, the percentage change in DDC and D_t between the response groups significantly differed, and DDC and D_t were significantly higher in the pR group (pR = 31.86% and pNR = 10.41%; p = 0.009 for DDC; pR = 23.88% and pNR = -8.03%; p = 0.003 for D_t), demonstrating the ability to differentiate the two groups and predict the response with reasonable performance (AUC = 0.767; p = 0.01 for DDC, AUC = 0.797; p = 0.004 for D_t). This increased and higher DDC and D_t values in pR tumours after one NACT cycle may reflect the reduction of cellularity in the tumour cold-spot region as a response to treatment. The cytotoxic effects of NACT lead to tumour cell lysis, where cells begin to die, breaking down cell walls (182). This process in turn results in a reduction in cellular density, implying that water molecules in the cold-spot region of the tumour can move with less restriction, translating into increased DDC and D_t values (10). In contrast, the absence of a significant difference in the cold-spot ADC between pR and pNR groups could be attributed to the diffusion and perfusion oppositely influencing the ADC value, where increased diffusion with decreased perfusion in response to treatment may cause an underestimation of the diffusion reduction by ADC. This attribution may be supported by the significantly higher D_t and lower f observed in the pR tumour cold-spot regions compared to those in pNR tumour after one NACT cycle.

Similar to the results found using the whole-tumour ROI (Chapter 4), f and $f{\times}D_p$ values derived from cold-spot and hot-spot regions were higher in the pNR group than in the pR group at almost all time points. However, pretreatment f and $f{\times}D_p$ values from the hot-spot region, and the f value after one cycle from hot-spot and cold-spot regions were significantly higher in the pNR group (pretreatment hot-spot: pR = 8.78% and pNR = 11.44%; p = 0.03 for f; pR = $0.56{\times}10^{-3}$ mm²/s and pNR = $0.98{\times}10^{-3}$ mm²/s; p = 0.006 for $f{\times}D_p$; after one cycle: pR = 9.12% and pNR = 11.84%; p = 0.03 for f in hot-spot; pR = 7.91% and pNR = 9.85%; p = 0.04 for f in cold-spot), differentiating between the response groups and predicting the response with reasonable performance (pretreatment hot-spot: AUC = 0.724; p = 0.03 for f, AUC = 0.794; p = 0.007 for $f{\times}D_p$; after one cycle: AUC = 0.722; p = 0.03 for f in hot-spot, AUC = 0.711; p = 0.04 for f in cold-spot). It has been suggested

that f represents the reflects the fractional volume of capillary blood in a voxel, and $f \times D_p$ indicates the microvascular blood flow (20). Furthermore, a previous study found that f is positively correlated with the histological microvessel density, a surrogate marker of tumour angiogenesis (176). As such, greater f and $f \times D_p$ values in the pNR group might be linked to the higher blood flow and volume in pNR tumours. Given that the measurements of f and $f \times D_p$ pretreatment and f after one cycle from hot-spot ROIs are predictive of the response, and that these ROIs were identified based on DCE images, an interesting question arises: Could IVIM potentially serve as a contrast-agent-free alternative to DCE-MRI to acquire comparable information on breast tumour perfusion? A few studies have been conducted; Chapter 6 comprehensively investigates this question (27-29).

Consistent with the findings from the same cohort using the whole-tumour ROI (Chapter 4), and those reported in a previous study using large single-section tumour ROI (19), the pR group in the present study exhibited higher α values than the pNR group in cold-spot and hot-spot regions at all time points. Unlike the whole-tumour ROIs (Chapter 4), α values from the hot-spot region pretreatment and both hot-spot and cold-spot regions after one cycle were able to distinguish between the two groups (pretreatment hot-spot: pR = 0.87 and pNR = 0.82; p = 0.04 ; after one cycle: pR = 0.9 and pNR = 0.84; p = 0.01 in hot-spot; pR = 0.89 and pNR = 0.77; p = 0.01 in cold-spot), and predict the response with reasonable performance (pretreatment hot-spot: AUC = 0.711; p = 0.04; after one cycle: AUC = 0.752; p = 0.01 in hot-spot, AUC = 0.744; p = 0.01 in cold-spot). Although the biological interpretation of the heterogeneity index α still requires investigation, it has been suggested to reflect the complexity of the tissue microstructure in imaging voxels to a certain extent (15). High α values in the hot- and cold-spots of pR tumours could therefore indicate a more homogeneous microenvironment, whereas low α values in pNR tumours may suggest a high degree of heterogeneity in the microenvironment.

Although some parameters derived from cold-spot and hot-spot regions were predictive of the response, their AUCs, corresponding 95% confidence intervals and statistical significance are less powerful than those derived from whole-tumour ROIs. The range of values for the promising parameters derived from these small focused regions across patients exhibits more variability than those from whole-tumour ROIs. This is demonstrated by the IQR of α (cold- and hot-spots), D_t and f (cold-spot), and $f \times D_p$ (cold- and hot-spots), as presented in Tables 5.1 and 5.2 versus Table 4.2 in Chapter 4. Thus, based on the present results, analysing DWI

images using cold-spot and hot-spot ROIs appears to be less robust for evaluating tumour response and more variable than employing whole-tumour ROIs, particularly as very few tumours at pretreatment were below the 5x5 pixel size threshold, and the number increased during NACT as some tumours responded and reduced below this threshold size.

5.4.1 Limitations

Although this is the first study (to the best of the candidate's knowledge) investigating the value of characterising the tumour subregion (lowest ADC) in assessing the early breast cancer response to NACT, it has some limitations. The study was performed at a single centre using a single scanner (1.5 T MRI; Aera; Siemens) with a limited sample size, restricting its interpretation and hindering the evaluation of the predictive performance of the DWI models according to breast tumour subtypes. A future multicentre study with various scanners and a larger cohort of patients with diverse breast tumour subtypes is recommended to validate the predictive performance of DWI models on tumour cold-spot and hot-spot regions. Moreover, the DCE images were rigidly aligned to the DWI images, which may not have been sufficient to correct DWI distortions. Thus, the spatial co-registration accuracy could have been affected, potentially influencing the results reported.

5.5 Conclusions

This preliminary study demonstrated that analysing diffusion data from breast tumour diffusion cold-spot and perfusion hot-spot regions using SEM and IVIM models predicts the NACT response better than the monoexponential model. The IVIM parameters f and $f \times D_p$ and the SEM parameter α derived from hot-spot regions at pretreatment exhibited reasonable performance in predicting the response (AUC = 0.724, 0.794, 0.711; p = 0.03, 0.007, and 0.04, respectively). After one cycle of NACT, f and α continued having reasonable predictive performance when analysed from tumour cold-spot and hot-spot regions, with higher α and lower f and $f \times D_p$ values indicating a favourable response (in hot-spot: AUC = 0.722; p = 0.03 for f, AUC = 0.752; p = 0.01 for α; and in cold-spot: AUC = 0.711; p = 0.04 for f, AUC = 0.744; p = 0.01 for α). The promising results of the perfusion-related parameters f and $f \times D_p$ from hot-spot ROIs support that further investigation into whether IVIM could offer a contrast-agent-free alternative to the DCE-MRI method to measure breast tumour perfusion. Moreover, only the

diffusion coefficients (DDC and D_t) from cold-spot regions after one NACT cycle were reasonably predictive of the pathological response, with higher DDC and D_t values correlating with a favourable response (AUC = 0.767; p = 0.01 for DDC, AUC = 0.797; p = 0.004 for D_t). However, the results indicate that sampling diffusion data from small tumour subregions (cold-spot/hot-spot) introduces more variability in parameter estimates and diminishes the predictive performance compared to the whole-tumour ROI approach. Thus, the entire tumour should be characterised when evaluating NACT response.

Chapter 6 The relationship between parameters measured using IVIM and DCE-MRI in patients with breast cancer undergoing NACT: a longitudinal cohort study

6.1 Introduction

Patients with breast cancer undergoing NACT often undergo repeated DCE-MRI scans for treatment monitoring via morphological assessment (3). Quantitative estimation of perfusion-related parameters of breast tumours, including tumour blood flow (F_b), blood volume fraction (v_b), along with haemodynamic and cellularity-related parameters: capillary permeability–surface area product (PS); interstitial volume fraction (v_e), and extracellular volume fraction (v_d; calculated from the combination of v_p and v_e) can be achieved by employing a recently developed DCE-MRI technique (7). However, certain safety concerns exist regarding gadolinium administration, particularly in patients with cancer who undergo repeated contrast-enhanced scans (9). Therefore, alternative imaging techniques that can provide equivalent perfusion and cellularity-related measurements without administering a contrast agent are of interest.

The ADC, obtained via DWI, measures the diffusivity of water molecules in the tissue and is assumed to serve as an indicator of cellular density. As such, as tumour cellularity decreases in response to treatment, the ADC value increases (10). The ADC is therefore expected to be related to the DCE-MRI cellularity-related measures (v_e and v_d). However, few studies have examined this relationship (153), and one study in breast tumours has challenged this expectation by assessing it at a single visit, suggesting that ADC is incompletely understood (30).

In contrast, IVIM perfusion-related (f and f$\times$D$_p$) parameters have shown promising roles in differentiating benign and malignant breast tumours and evaluating breast tumour response to NACT over the past decade, as described in section 2.8.2.2.1 of Chapter 2 and also found in Chapters 4 and 5. This in turn has reopened the question of whether IVIM could be used as a contrast-agent-free alternative to DCE-MRI for measuring breast tumour perfusion. Few studies have investigated the correlations between IVIM and DCE-MRI perfusion-related parameters in breast tumours and have produced contradictory results (summarised in Table 2.5,

Chapter 2). These studies examined correlations at a single visit; however, a correlation between perfusion parameter changes caused by treatment is also meaningful and suggests that IVIM could be a contrast-agent-free surrogate to the DCE-MRI method in monitoring serial changes in tumour perfusion. Further, none of these studies provided an absolute estimation of tumour blood flow; they did not perform a direct comparison with the IVIM parameter purported to measure microvascular blood flow ($f{\times}D_p$).

The first aim of this study was to investigate whether IVIM and DCE-MRI perfusion-related parameters correlate and whether IVIM can offer a contrast-agent-free alternative to DCE-MRI for monitoring serial changes in tumour perfusion. The DCE-MRI data were analysed to estimate absolute F_b, v_b, PS, v_e, and v_d (7). This study assesses both between-subject and within-subject repeated measures correlations between the perfusion parameters estimated by IVIM and DCE-MRI (specifically f versus v_b and $f{\times}D_p$ versus F_b) in the same cohort of patients who underwent NACT in Chapter 4. Analysing both correlations is valuable; between-subject correlation reveals the potential for estimating DCE-MRI perfusion parameters using IVIM at a given time, whereas within-subject repeated measures correlations indicate the potential for estimating change in DCE-MRI perfusion parameters using IVIM when assessing longitudinal changes in the same patient. The second aim of this study was to examine the correlation between DWI tissue diffusion measures (D_t and ADC) and DCE-MRI measurements of the tissue's interstitial and extracellular volume fractions (v_e and v_d). This would improve the understanding of tissue diffusion measures and their changes in response to treatment further, which are of interest for translation into breast cancer imaging as markers of treatment response (25).

6.2 Materials and methods

6.2.1 Patient population

The cohort of patients included, the recruitment eligibility criteria used, and the NACT regimen plan delivered are the same as detailed in Chapter 4, section 4.2.1.

6.2.2 Image acquisition

The MRI time points, and scanning protocol are the same as specified in Chapters 4 and 5 (sections 4.2.2 and 5.2.2); however, this section introduces information on the inversion recovery (IR) sequence.

In conjunction with the 16-channel breast coil employed, a flexible array coil, placed on the patient's back, was employed to increase the signal from the descending aorta (183). A 3D non-selective IR-prepared FLASH sequence (TR / TE: 2.8/0.93 ms, FA: 8°, FOV: 340×340×180 mm, matrix size: 128×128×36, slice thickness: 5 mm, parallel imaging factor: 2, IR-TR: 3000 ms, overall scan time: 4 min 20 s), was performed before the interleaved HTR and HSR DCE sequences, at four inversion times (100, 600, 1200 and 2800 ms) to estimate T_1. Both breasts, the aortic arch and part of the descending aorta were included in the field of view (183). A second IR T_1 estimate (bookend) was performed (184) after all eight HSR (and 88 HTR) dynamic images were acquired. Then, the last five HTR images were obtained. The acquired HTR and HSR images have the same geometry as the IR sequence.

6.2.3 Image analysis

The MRI data were processed with the same in-house program developed in MATLAB (MathWorks, USA), employed in the work described in Chapter 4 work (section 4.2.3). Building on section 5.2.3, the rigid alignment of HTR, HSR to match DWI (with ADC maps) images also integrated IR images. The inclusion of IR images is highlighted here due to their relevance to the DCE data analysis.

The generated three ROIs for each patient (whole-tumour ROI (section 4.2.3), diffusion cold-spot and perfusion hot-spot ROIs (section 5.2.3)) were propagated to the corresponding IR and HTR images. Another key rationale for including the small focused ROIs (cold-spot and hot-spot regions) in the image analysis undertaken in this thesis was to reduce the possibility of tumour heterogeneity compromising subsequent correlation analysis. Then the author extracted the mean SI versus time data from the three ROIs on both IR and HTR images and provided to D.L.B. (DCE-MRI analysis expert and supervisor), who carried out the subsequent DCE-MRI quantitative analysis and parameter estimates using another in-house MATLAB program developed by a researcher at the Division of Biomedical Imaging at the University of Leeds.

The T1 relaxation times per ROI were estimated from both sets of IR images, according to Kershaw et al. (109) and Brix et al. (185). The detailed equations were derived and are provided in Appendix 1 of Kershaw's PhD thesis (186). A further ROI was drawn in the descending aorta to generate SI-time curves and estimate T1 before and after Gd-DOTA injection for measurement of the arterial input function (183). The SI-time data were converted to Gd-DOTA concentration-time using a bookend T1 correction (i.e., a combination of T1 estimate before and after Gd-DOTA injection) with an iterative scheme (183, 184). A two–compartment

exchange model was fitted to the DCE-MRI data, and F_b, v_b, PS and v_e were estimated (187). Then, the extracellular volume fraction (v_d: the sum of interstitial and blood plasma volume fractions) was calculated. For each ROI, a tissue uptake model (described by parameters F_b, v_b, and PS) and a one–compartment model (described by parameters F_b, and v_d) were also fitted to the DCE-MRI data (187). The final model to use in the correlation analysis was selected based on the corrected Akaike information criterion test (cAIC) to evaluate which model best fits the data (188, 189), (Figure 6.1).
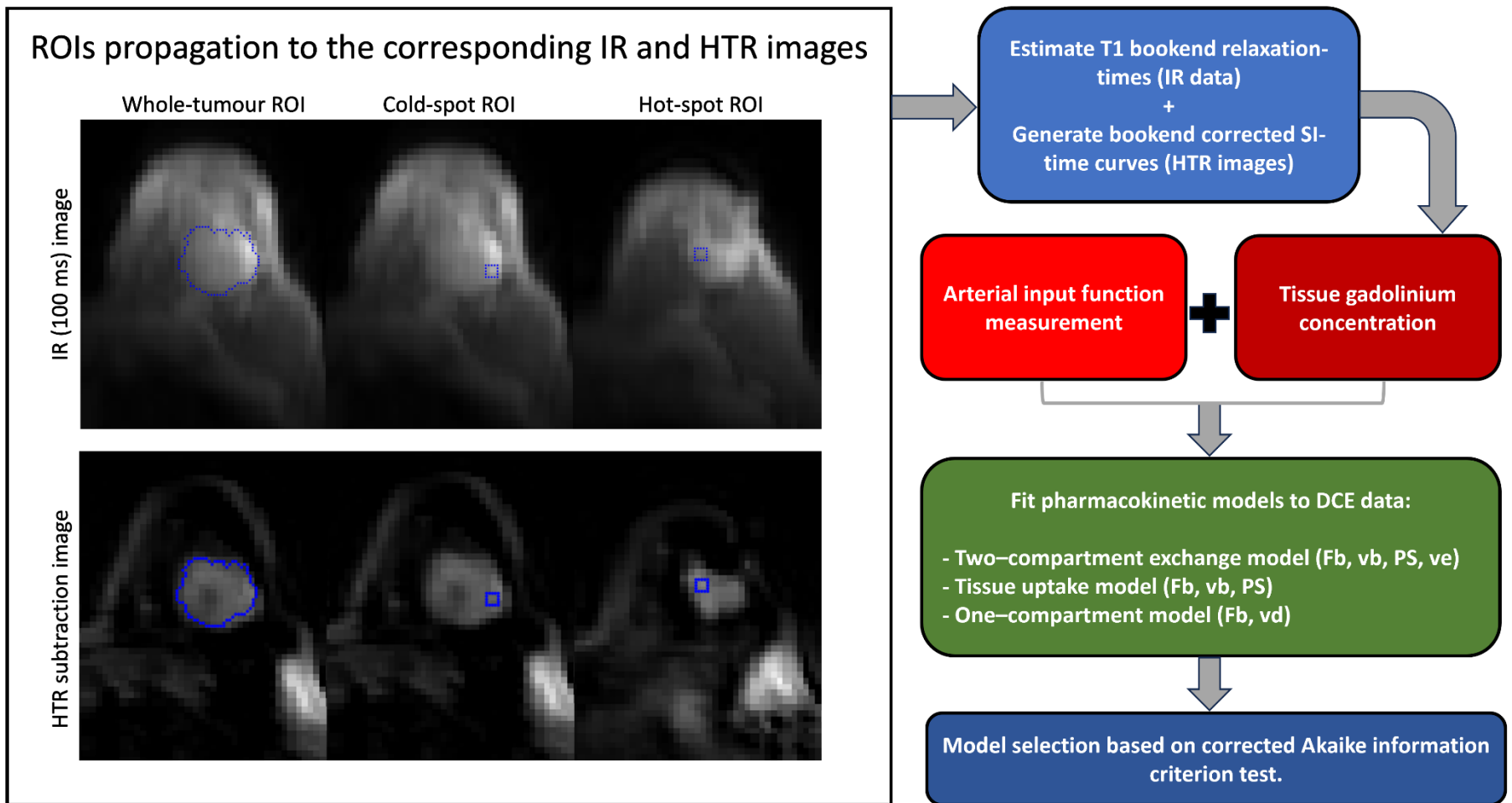
Figure 6.1 The flow chart illustrates the analysis steps followed for extracting quantitative DCE-MRI parameters, building upon the generation of ROIs performed in Chapter 5 and demonstrated in Figure 5.2.

For DWI analysis, the parameter values for IVIM (D_t, D_p, f, and f×D_p) and monoexponential (ADC) diffusion models for each ROI were those estimated in Chapters 4 and 5, conducted blinded to the DCE-MRI parameter values.

6.2.4 Statistical analysis

Due to the non-normal data distribution, the DCE-MRI data were summarised using the median (IQR). Friedman's test with Bonferroni correction (Bonferroni post hoc test) was performed for each parameter from the baseline MRI (i.e., pretreatment) to determine whether parameter differences existed between the three ROIs (whole-tumour, cold-spot, and hot-spot). To determine the between-subject correlation between IVIM parameters and ADC with the DCE-MRI parameters for each ROI, the mean value of each parameter for each patient was calculated by dividing the sum of parameter values from all MRI visits by the number of times the parameter was estimated; then, the parameter value for each visit where the parameter was estimated was replaced by its subject mean. The weighted correlation coefficient, r, was calculated between the mean DWI and DCE-MRI parameters for each ROI using the Spearman's rank correlation test (190) (r<0.2, very weak; 0.2≤r<0.4, weak; 0.4≤r<0.7, moderate; 0.7≤r<0.9, strong; r≥0.9, very strong correlation) (171). This statistical method was followed to exploit the properties of data with multiple measures while addressing the issue of non-independence among observations and the impact of NACT (190). Statistical analyses were performed using SPSS software for Windows (v.25.0, Chicago, IL). All tests were two-sided, and a p-value of less than 0.05 was considered statistically significant.

To determine the correlation between changes in the IVIM parameters and ADC with the DCE-MRI parameters induced by treatment, the repeated measures correlation test (rmcorr) was utilized via the rmcorr-shiny app (191, 192). The rmcorr-shiny app computes a repeated measures correlation coefficient (r_{rm}) that considers the dependence between repeated measurements. This analysis involves determining the correlation between two parameters while accounting for between-subject variation. The rmcorr-shiny app fits separate parallel lines to each patient's data utilizing a shared slope but permitting the intercept to differ per patient. The orientation of these parallel lines represents the correlation's sign (positive or negative), while the slope denotes the correlation's magnitude.

The results of repeated measures correlation for each region were summarised in tables as: r_{rm}, degrees of freedom, 95% confidence interval, and a p-value. The

95% confidence interval for each r_{rm} were determined using bootstrapping with 1000 resamples. The degrees of freedom (df) were computed based on the formula df = N(k-1) – 1, where N is the total number of patients and k is the (average) number of repeated measures per patient (191). The rmcorr test was initially conducted to identify statistically significant results (P-value < 0.05), then bootstrapped 95% confidence intervals were calculated. A correlation result was considered meaningful and significant only if the correlation coefficient was ≥ 0.4, the P-value was less than 0.05, and the bootstrapped 95% confidence intervals excluded zero. Since this is a preliminary exploration study focusing on hypothesis generation, P-values for the correlation tests were reported as raw values and were not corrected for multiple comparisons. An upper estimate of the repeatability of the DCE-MRI parameters was calculated from the same subset of baseline and cycle 1 studies selected for the repeatability analysis of DWI model parameters performed in Chapter 4 (section 4.2.5).

6.3 Results

As described in section 4.3.1, MRI scans of 40 patients at baseline, 37 after one NACT cycle, and 35 after three NACT cycles were collected for analysis, resulting in a total of 112 MRI studies with DWI and DCE-MRI acquisitions. Following the exclusion of DCE-MRI scans (detailed in section 5.3.1), 108 studies with paired DWI and DCE-MRI data acquisitions remained (Figure 6.2). Based on the cAIC results, 75 DCE-MRI data sets were analysed using the two–compartment exchange model, 20 using the tissue uptake model, and 13 using the one–compartment model.

Paired small focused ROIs (cold-spot and hot-spot regions) were generated from 91 of the 108 studies, as illustrated in section 5.3.1: 34 at baseline, 33 after one NACT cycle, and 24 after three NACT cycles. DCE data sets were fitted using the two-compartment exchange/tissue-uptake/one-compartment models for 68/13/10 cold-spot regions and for 72/9/10 hot-spot regions.

For the IVIM analysis, as indicated in sections 4.3.2 and 5.3.2, there were a number of cases in which parameter estimates D_p and f reached one of their constrained values and were excluded from the statistical analyses: 2 cases from the whole-tumour ROI, 8 from the cold-spot and 4 from the hot-spot ROIs.
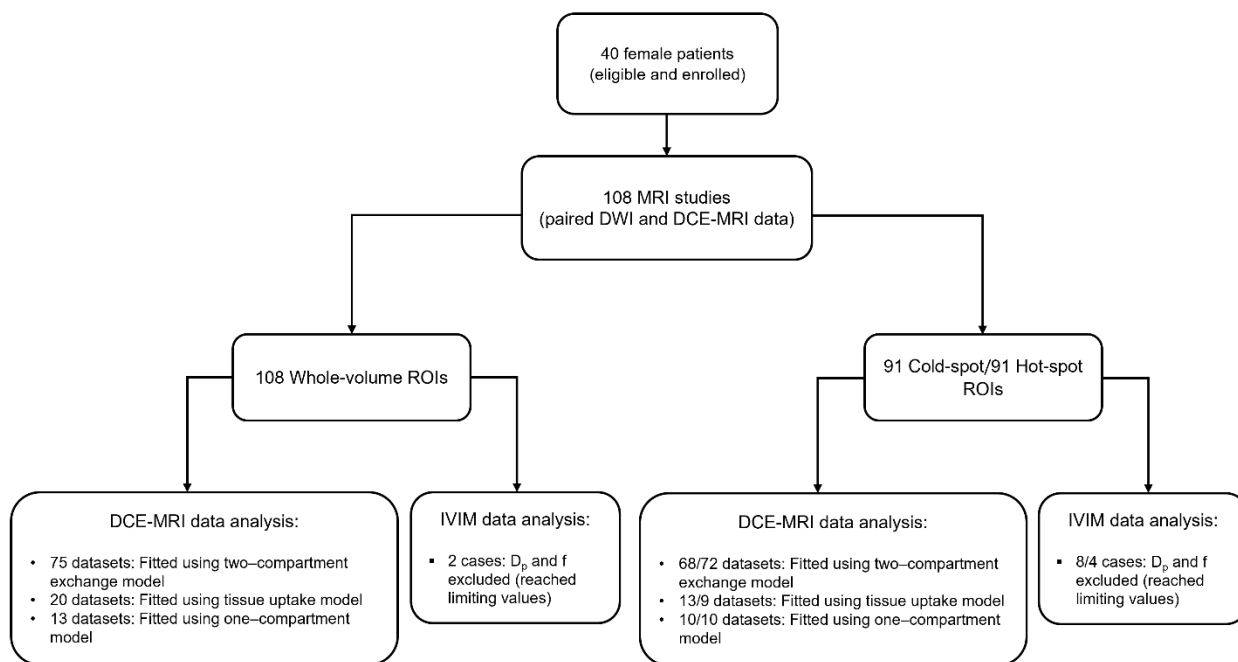
Figure 6.2 The flow chart summarises the final number of MRI studies with paired DWI and DCE-MRI data acquisitions, detailing the number of generated ROIs (whole-tumour, cold-spot, and hot-spot), the models selected for DCE-MRI data analysis based on cAIC results, and the number of cases with excluded D_p and f estimates.

6.3.1 Estimated DWI and DCE-MRI parameters from the three regions at baseline

There were significant differences between the parameter values estimated in whole-tumour, diffusion cold-spot, and perfusion hot-spot regions for all DWI and DCE-MRI parameters ($p<0.001$ to 0.04), with the exception of D_p and v_d ($p = 0.88$ and 0.2, respectively). Of particular interest, ADC and D_t values estimated from cold-spot ROIs were significantly lower than those from whole-tumour and hot-spot ROIs [(median: 0.73, 0.98, and 0.93 x 10^{-3} mm^2/s for ADC; $p< 0.001$; and 0.64, 0.80, and 0.81 x 10^{-3} mm^2/s for D_t; $p< 0.001$, respectively)], while F_b values from cold-spot and hot-spot ROIs were significantly higher than those from whole-tumour ROIs [(median: 0.36, 0.38, and 0.29 for F_b (ml/min/ml tissue); $p< 0.001$, respectively)]. Detailed results, including pairwise comparisons (Bonferroni-corrected), are presented in Table 6.1.

Table 6.1 Comparison of DCE-MR and DWI parameter values at baseline for the whole-tumour, cold-spot, and hot-spot regions.

Parameter	N	Whole-tumour ROI (a)	Cold-spot ROI (b)	Hot-spot ROI (c)	P	Post hoc**
ADC (10^{-3} mm^2/s)	34	**0.98(0.88, 1.20)**	**0.73(0.65, 0.88)**	**0.93(0.86, 1.10)**	<0.001	**b<a, b<c**
D_t (10^{-3} mm^2/s)	34	**0.80(0.72, 0.92)**	**0.64(0.59, 0.74)**	**0.81(0.72, 0.93)**	<0.001	**b<a, b<c**
D_p (10^{-3} mm^2/s)	25	7.13(6.47, 7.33)	6.94(5.53, 10.18)	7.29(5.69, 8.67)	0.88	-
f (no units)	25	**0.12 (0.11, 0.14)**	**0.09 (0.06, 0.12)**	**0.10(0.08, 0.12)**	<0.001	**b<a, c<a**
f×D_p (10^{-3} mm^2/s)	25	**0.90(0.68, 1.01)**	**0.62(0.43, 0.98)**	**0.71(0.49, 1.00)**	0.006	**b<a, c<a**
Tumour T_1 (ms)	34	**1264 (1230, 1322)**	**1252 (1201, 1298)**	**1303 (1256, 1349)**	<0.001	**b<c**
F_b (ml/min/ml tissue)	34	**0.29(0.22, 0.55)**	**0.36(0.28, 0.74)**	**0.38(0.27, 0.62)**	<0.001	**a<b, a<c**
PS (ml/min/ml tissue)	30	**0.05(0.04, 0.08)**	**0.06(0.04, 0.13)**	**0.09(0.05, 0.17)**	<0.001	**a<c, b<c**
v_b (no units)	30	**0.29(0.22, 0.47)**	**0.33(0.23, 0.49)**	**0.3(0.22, 0.44)**	0.048	**a<b**
v_e (no units)	24	**0.19(0.16, 0.25)**	**0.17(0.12, 0.22)**	**0.19(0.13, 0.23)**	0.03	**b<a**
v_d (no units)	27	0.38(0.35, 0.45)	0.39(0.32, 0.44)	0.36(0.29, 0.46)	0.2	-

Data represented by medians (interquartile ranges). *P* value for a difference between ROIs was found using Friedman's non-parametric test. (The N number differs for the DCE-MRI parameters due to the models used for analysing the DCE-MRI data, Number of patients= 24-34) Pairwise comparisons** (Bonferroni-corrected) significance at the 0.05 level. ADC: apparent diffusion coefficient. D_t: tissue diffusion. D_p: pseudo-diffusion coefficient. f: perfused fraction. f×D_p: microvascular blood flow. F_b: blood flow. PS: capillary permeability–surface area product. v_b: blood volume fraction. v_e: interstitial volume fraction. v_d: extracellular volume fraction.

6.3.2 Correlation between averaged DWI and DCE-MRI parameters from three MRI visits (between-subject correlation)

No statistically significant correlations were discovered between the IVIM and DCE-MRI perfusion-related parameters (f with v_b and $f \times D_p$ with F_b) in the three tumour regions (p = 0.146–0.379; Tables 6.2-6.4). However, for whole-tumour regions, ADC exhibited a statistically significant, moderate positive correlation with tumour T_1 and v_e (r = 0.603, p<0.001; and r = 0.461, p = 0.004, respectively; Figure 6.3, Table 6.2). Similarly, D_t demonstrated a statistically significant, moderate positive correlation with tumour T_1 and v_e (r = 0.631, p<0.001; and r = 0.405, p = 0.01, respectively; Figure 6.3, Table 6.2).

Table 6.2 Correlation between averaged DWI and DCE-MRI parameters from three MRI visits (whole-tumour region).

Parameter		Tumour T_1	F_b	PS	v_e	v_b	v_d
ADC	r	**0.603****	0.026	0.305	**0.461***	-0.173	0.302
	P-value	**<0.001**	0.873	0.056	**0.004**	0.286	0.058
	N	**40**	40	40	**37**	40	40
D_t	r	**0.631****	0.014	0.266	**0.405***	-0.135	0.302
	P-value	**<0.001**	0.932	0.097	**0.013**	0.406	0.058
	N	**40**	40	40	**37**	40	40
D_p	r	-0.251	0.172	-0.051	-0.360	-0.006	-0.213
	P-value	0.118	0.289	0.755	0.029	0.971	0.187
	N	40	40	40	37	40	40
f	r	0.187	0.121	0.186	0.093	-0.144	0.079
	P-value	0.248	0.457	0.251	0.584	0.375	0.628
	N	40	40	40	37	40	40
$f \times D_p$	r	-0.020	0.143	0.071	-0.126	-0.041	0.001
	P-value	0.903	0.379	0.663	0.457	0.802	0.995
	N	40	40	40	37	40	40

r: correlation coefficient. N: sample size. ADC: apparent diffusion coefficient. D_t: tissue diffusion. D_p: pseudo-diffusion coefficient. f: perfused fraction. $f \times D_p$: microvascular blood flow. F_b: blood flow. PS: capillary permeability–surface area product. v_e: interstitial volume fraction. v_b: blood volume fraction. v_d: extracellular volume fraction.

* r ≥ 0.4 and P<0.05.

** r ≥ 0.4 and P<0.001.
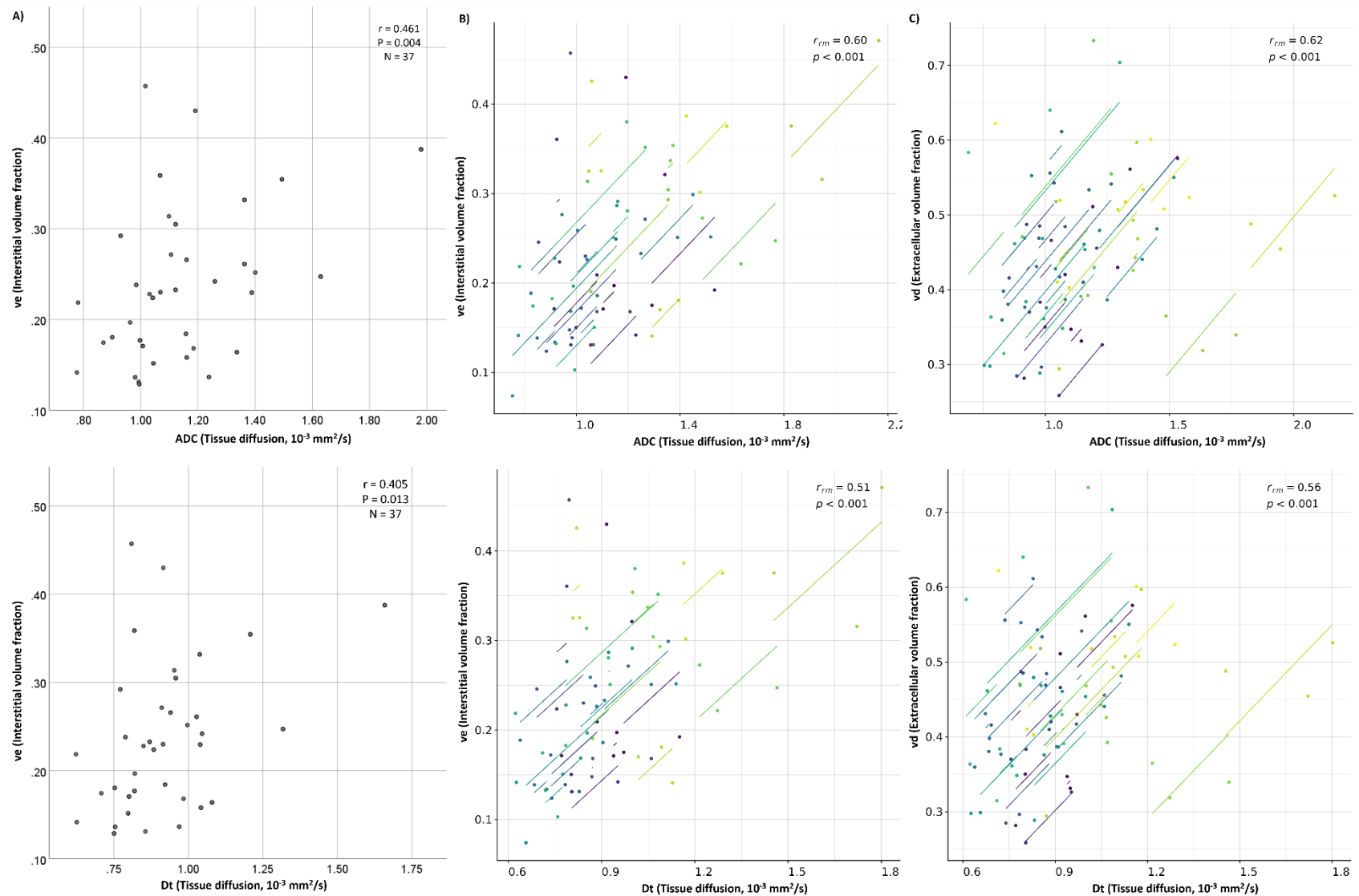
Figure 6.3 Scatter plots show moderate positive (A) between-subject and (B) within-subject repeated measures correlations between the diffusion coefficients (ADC and D_t) and the interstitial volume fraction (v_e), as well as moderate positive (C) within-subject repeated measures correlation between the diffusion coefficients (ADC and D_t) and the extracellular volume fraction (v_d). Each line in the scatter plots (B and C; repeated measures correlations) shows the fit for a single patient.

In the cold-spot regions, statistically significant, moderate positive correlations were found between tumour T_1 and both measures of tissue diffusion ADC and D_t (r = 0.632, p<0.001; and r = 0.588, p<0.001, respectively). D_p demonstrated a statistically significant, moderate negative correlation with F_b (r = -0.400, p = 0.01; Figure 6.4, Table 6.3). In hot-spot regions, ADC and D_t displayed statistically significant, moderate positive correlations with tumour T_1 (r = 0.520, p = 0.001; and r = 0.460, p = 0.005, respectively; Table 6.4).

Table 6.3 Correlation between averaged DWI and DCE-MRI parameters from three MRI visits (cold-spot region).

Parameter		Tumour T_1	F_b	PS	v_e	v_b	v_d
ADC	**r**	**0.632**[**]	-0.030	-0.028	0.219	-0.18	0.156
	P-value	**<0.001**	0.862	0.871	0.206	0.293	0.371
	N	**36**	36	36	35	36	35
D_t	**r**	**0.588**[**]	0.020	0.100	0.283	-0.253	0.115
	P-value	**<0.001**	0.908	0.562	0.099	0.137	0.511
	N	**36**	36	36	35	36	35
D_p	**r**	-0.139	**-0.400**[*]	-0.126	-0.074	-0.062	-0.149
	P-value	0.426	**0.017**	0.471	0.682	0.723	0.4
	N	35	**35**	35	33	35	34
f	**r**	0.231	-0.048	0.055	-0.045	-0.202	-0.031
	P-value	0.182	0.784	0.754	0.804	0.245	0.862
	N	35	35	35	33	35	34
f×D_p	**r**	0.040	-0.247	0.037	-0.020	-0.158	-0.143
	P-value	0.82	0.153	0.833	0.912	0.365	0.42
	N	35	35	35	33	35	34

r: correlation coefficient. N: sample size. ADC: apparent diffusion coefficient. D_t: tissue diffusion. D_p: pseudo-diffusion coefficient. f: perfused fraction. f×D_p: microvascular blood flow. F_b: blood flow. PS: capillary permeability–surface area product. v_e: interstitial volume fraction. v_b: blood volume fraction. v_d: extracellular volume fraction.

* r ≥ 0.4 and P<0.05.

** r ≥ 0.4 and P<0.001.
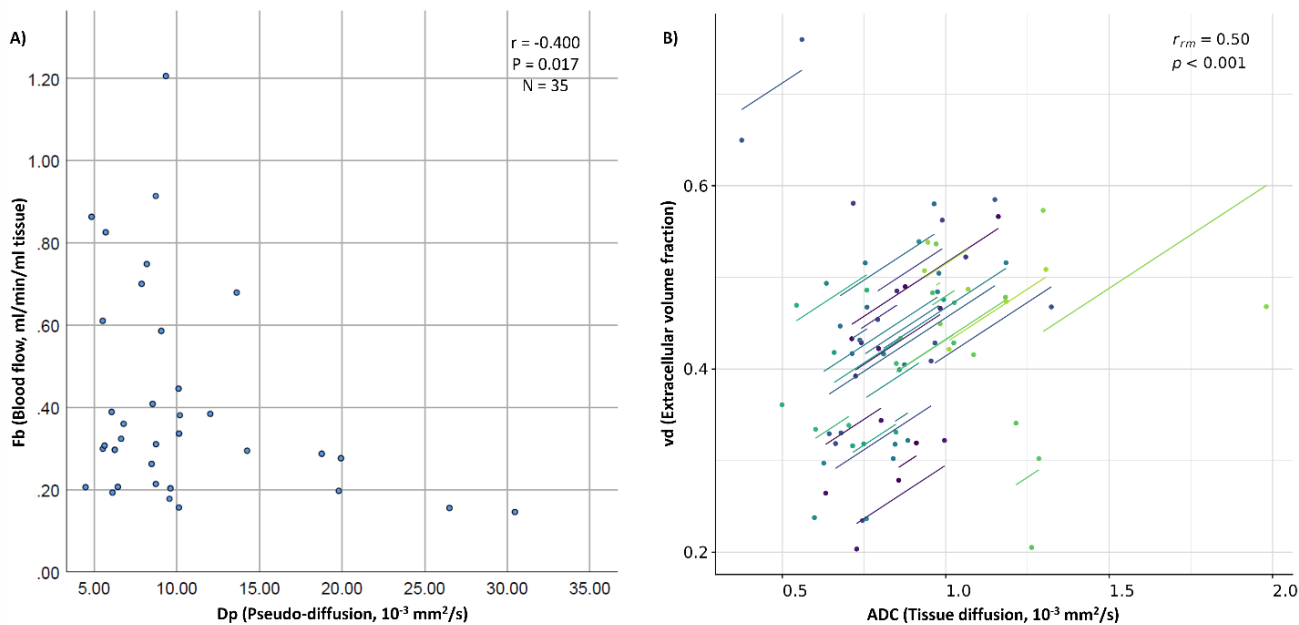
Figure 6.4 Scatter plots show a moderate negative between-subject correlation (A) between the pseudo-diffusion coefficient (D_p) and blood flow (F_b), as well as a moderate positive within-subject repeated measures correlation (B) between the diffusion coefficient (ADC) and the extracellular volume fraction (v_d) in the cold-spot regions.

Table 6.4 Correlation between averaged DWI and DCE-MRI parameters from three MRI visits (hot-spot region).

Parameter		Tumour T_1	F_b	PS	v_e	v_b	v_d
ADC	r	**0.520***	0.145	0.126	0.137	-0.146	0.203
	P-value	**0.001**	0.399	0.471	0.433	0.403	0.235
	N	**36**	36	35	35	35	36
D_t	r	**0.460***	0.042	0.056	0.194	-0.098	0.277
	P-value	**0.005**	0.808	0.749	0.264	0.575	0.102
	N	**36**	36	35	35	35	36
D_p	r	-0.039	0.070	0.138	0.081	-0.123	-0.172
	P-value	0.824	0.689	0.436	0.649	0.488	0.323
	N	35	35	34	34	34	35
f	r	0.343	0.329	0.368	0.103	-0.172	0.004
	P-value	0.044	0.054	0.032	0.562	0.331	0.982
	N	35	35	34	34	34	35
f×D_p	r	0.179	0.251	0.258	0.158	-0.148	-0.053
	P-value	0.304	0.146	0.141	0.372	0.404	0.762
	N	35	35	34	34	34	35

r: correlation coefficient. N: sample size. ADC: apparent diffusion coefficient. D_t: tissue diffusion. D_p: pseudo-diffusion coefficient. f: perfused fraction. f×D_p: microvascular blood flow. F_b: blood flow. PS: capillary permeability–surface area product. v_e: interstitial volume fraction. v_b: blood volume fraction. v_d: extracellular volume fraction.

* $r ≥ 0.4$ and $P<0.05$.

6.3.3 Repeated measures correlations between DWI and DCE-MRI parameters (within-subject correlation)

Table 6.5 lists the repeated measures correlation results computed between the DWI and DCE-MRI parameters estimated from the whole-tumour ROIs. No statistically significant correlations were discovered between the IVIM and DCE-MRI perfusion-related parameters of the study's primary interest (f versus v_b and f×D_p versus F_b; p = 0.815 and 0.229, respectively). However, ADC and D_t displayed statistically significant, moderate positive correlations with v_e ($r_{rm} = 0.597$, p<0.001; and $r_{rm} = 0.514$, p<0.001, respectively) and v_d ($r_{rm} = 0.619$, p<0.001; and $r_{rm} = 0.564$, p<0.001, respectively; Figure 6.3).

Table 6.5 Repeated measures correlations between DWI and DCE-MRI parameters estimated from whole-tumour region.

Parameter		Tumour T_1	F_b	PS	v_e	v_b	v_d
ADC	r_{rm}	0.035	-0.361	-0.138	**0.597****	0.226	**0.619****
	df	67	67	54	**37**	54	**47**
	P-value	0.775	0.002	0.309	**<0.001**	0.094	**<0.001**
	95% CI	-0.18, 0.253	-0.605, 0.01	-0.452, 0.253	**0.203, 0.785**	-0.012, 0.432	**0.383, 0.82**
D_t	r_{rm}	0.043	-0.32	-0.045	**0.514****	0.165	**0.564****
	df	67	67	54	**37**	54	**47**
	P-value	0.724	0.007	0.741	**<0.001**	0.224	**<0.001**
	95% CI	-0.217, 0.279	-0.544, 0.036	-0.339, 0.312	**0.103, 0.716**	-0.052, 0.373	**0.305, 0.785**
D_p	r_{rm}	0.125	0.336	0.157	-0.127	-0.208	0.078
	df	65	65	53	37	53	46
	P-value	0.313	0.005	0.253	0.442	0.127	0.597
	95% CI	-0.08, 0.268	0.092, 0.502	-0.08, 0.397	-0.311, 0.074	-0.402, -0.02	-0.221, 0.304
f	r_{rm}	0.04	-0.182	-0.237	0.354	0.165	0.297
	df	65	65	53	37	53	46
	P-value	0.748	0.139	0.081	0.027	0.229	0.04
	95% CI	-0.201, 0.229	-0.423, 0.137	-0.477, 0.034	0.017, 0.583	-0.19, 0.418	0.068, 0.509
f×D_p	r_{rm}	0.055	0.029	-0.059	0.215	-0.035	0.252
	df	65	65	53	37	53	46
	P-value	0.661	0.815	0.668	0.188	0.799	0.084
	95% CI	-0.178, 0.228	-0.169, 0.265	-0.222, 0.123	-0.066, 0.444	-0.261, 0.187	-0.023, 0.445

r_{rm}: repeated measures correlation coefficient. df: degrees of freedom. CI: confidence interval. ADC: apparent diffusion coefficient. D_t: tissue diffusion. D_p: pseudo-diffusion coefficient. f: perfused fraction. f×D_p: microvascular blood flow. F_b: blood flow. PS: capillary permeability–surface area product. v_e: interstitial volume fraction. v_b: blood volume fraction. v_d: extracellular volume fraction.
* $r_{rm} \geq 0.4$, P<0.05, and bootstrapped 95% CIs excluded zero.
** $r_{rm} \geq 0.4$, P<0.001 and bootstrapped 95% CIs excluded zero.

For cold-spot and hot-spot ROIs, no statistically significant correlations were observed between any DWI and DCE-MRI parameters, except for a moderate positive correlation between ADC and v_d in the cold-spot regions (r_{rm} = 0.501, p<0.001; Figure 6.4); repeated measures correlation results in the cold-spot and hot-spot regions are presented in Tables 6.6 and 6.7. The median DWI and DCE-MRI parameter values estimated at the three MRI visits from the cold-spot and hot-spot regions exhibited patterns similar to those of the whole-tumour regions but with much more variability (Figure 6.5 versus Figure 6.6).

Table 6.6 Repeated measures correlations between DWI and DCE-MRI parameters estimated from cold-spot region.

Parameter		Tumour T_1	F_b	PS	v_e	v_b	v_d
ADC	r_{rm}	0.103	-0.095	-0.026	0.126	0.263	**0.501**[**]
	df	54	54	44	32	44	**42**
	P-value	0.449	0.484	0.863	0.477	0.077	**<0.001**
	95% CI	-0.279, 0.389	-0.349, 0.113	-0.335, 0.293	-0.161, 0.499	-0.035, 0.478	**0.217, 0.773**
D_t	r_{rm}	0.03	0.029	0.043	0.113	0.092	0.266
	df	54	54	44	32	44	42
	P-value	0.826	0.829	0.778	0.525	0.545	0.081
	95% CI	-0.361, 0.284	-0.189, 0.264	-0.21, 0.309	-0.234, 0.61	-0.188, 0.303	0.019, 0.6
D_p	r_{rm}	0.036	0.085	0.071	-0.047	0.029	-0.003
	df	47	47	37	26	37	35
	P-value	0.807	0.56	0.666	0.812	0.861	0.988
	95% CI	-0.125, 0.211	-0.085, 0.32	-0.352, 0.394	-0.501, 0.219	-0.383, 0.643	-0.202, 0.253
f	r_{rm}	-0.031	-0.034	-0.082	0.109	0.102	0.116
	df	47	47	37	26	37	35
	P-value	0.834	0.814	0.618	0.582	0.536	0.493
	95% CI	-0.408, 0.277	-0.252, 0.217	-0.47, 0.275	-0.292, 0.442	-0.283, 0.431	-0.181, 0.372
f×D_p	r_{rm}	0.068	0.076	0.078	-0.023	0.002	0.039
	df	47	47	37	26	37	35
	P-value	0.64	0.602	0.638	0.909	0.99	0.818
	95% CI	-0.102, 0.251	-0.086, 0.291	-0.271, 0.325	-0.411, 0.228	-0.284, 0.497	-0.164, 0.295

r_{rm}: repeated measures correlation coefficient. df: degrees of freedom. CI: confidence interval. ADC: apparent diffusion coefficient. D_t: tissue diffusion. D_p: pseudo-diffusion coefficient. f: perfused fraction. f×D_p: microvascular blood flow. F_b: blood flow. PS: capillary permeability–surface area product. v_e: interstitial volume fraction. v_b: blood volume fraction. v_d: extracellular volume fraction.
**$r_{rm} \geq 0.4$, P<0.001, and bootstrapped 95% CIs excluded zero.

Table 6.7 Repeated measures correlations between DWI and DCE-MRI parameters estimated from hot-spot region.

Parameter		Tumour T_1	F_b	PS	v_e	v_b	v_d
ADC	r_{rm}	0.247	-0.012	0.004	0.36	0.078	0.34
	df	54	54	45	36	45	45
	P-value	0.067	0.929	0.979	0.026	0.603	0.019
	95% CI	-0.05, 0.511	-0.326, 0.248	-0.336, 0.364	-0.024, 0.622	-0.315, 0.425	0.153, 0.524
D_t	r_{rm}	0.246	0.022	0.063	0.254	-0.078	0.287
	df	54	54	45	36	45	45
	P-value	0.067	0.87	0.672	0.123	0.604	0.051
	95% CI	-0.012, 0.499	-0.279, 0.271	-0.191, 0.282	0.005, 0.476	-0.307, 0.181	0.09, 0.548
D_p	r_{rm}	0.048	-0.028	-0.085	-0.257	0.087	0.013
	df	51	51	43	34	43	42
	P-value	0.733	0.84	0.579	0.13	0.569	0.932
	95% CI	-0.25, 0.35	-0.34, 0.234	-0.44, 0.125	-0.736, -0.001	-0.4, 0.485	-0.565, 0.388
f	r_{rm}	-0.127	-0.147	-0.178	0.04	0.268	0.013
	df	51	51	43	34	43	42
	P-value	0.364	0.292	0.242	0.816	0.076	0.932
	95% CI	-0.388, 0.21	-0.461, 0.221	-0.526, 0.269	-0.567, 0.53	-0.208, 0.655	-0.279, 0.308
f×D_p	r_{rm}	-0.002	-0.066	-0.083	-0.094	0.148	0.109
	df	51	51	43	34	43	42
	P-value	0.99	0.637	0.586	0.587	0.331	0.481
	95% CI	-0.352, 0.362	-0.438, 0.279	-0.329, 0.127	-0.566, 0.094	-0.255, 0.424	-0.435, 0.441

r_{rm}: repeated measures correlation coefficient. df: degrees of freedom. CI: confidence interval. ADC: apparent diffusion coefficient. D_t: tissue diffusion. D_p: pseudo-diffusion coefficient. f: perfused fraction. f×D_p: microvascular blood flow. F_b: blood flow. PS: capillary permeability–surface area product. v_e: interstitial volume fraction. v_b: blood volume fraction. v_d: extracellular volume fraction.
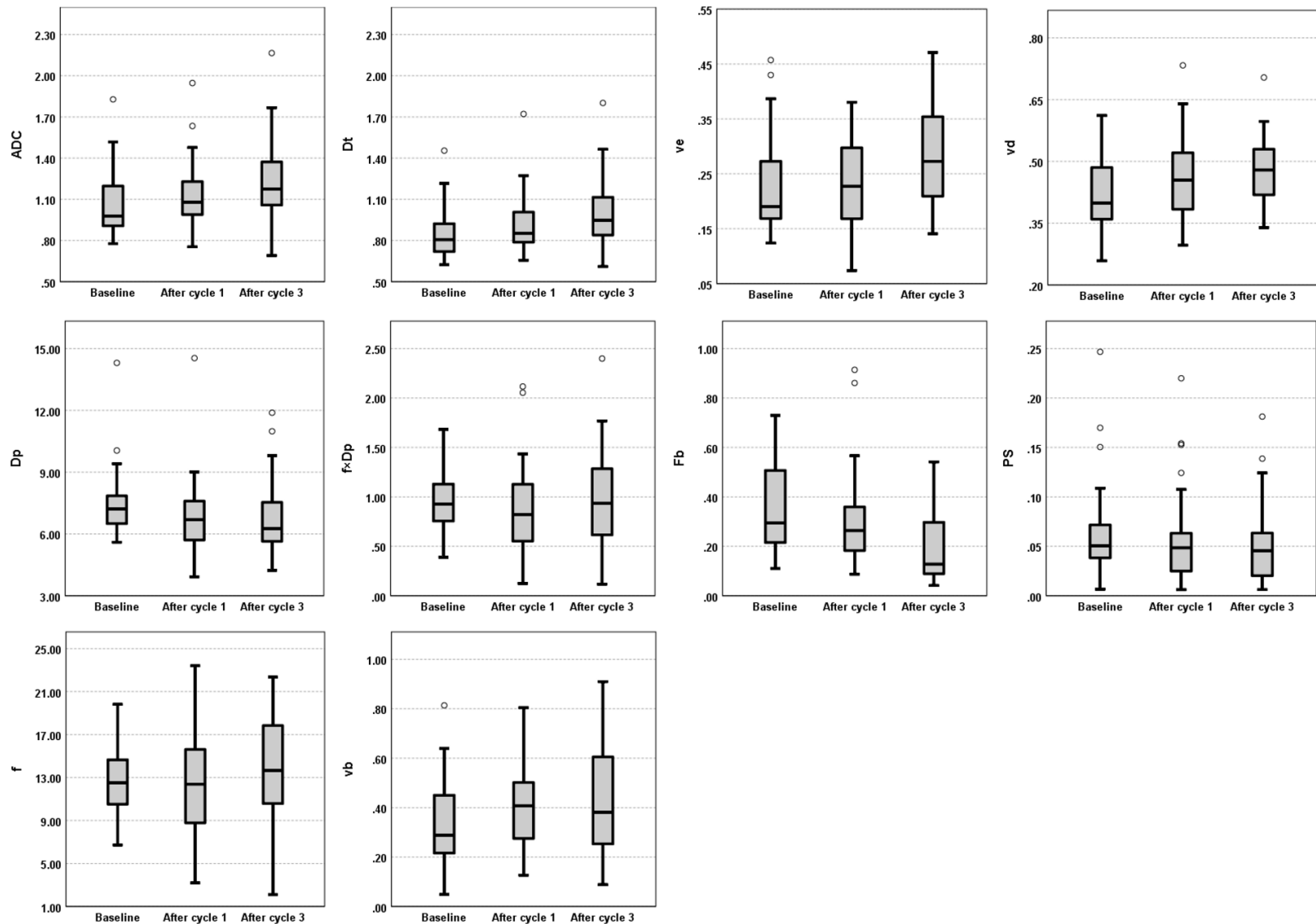
Figure 6.5 Evolution of DWI (ADC, D_t, D_p, f, and f×D_p) and DCE-MRI (F_b, v_b, PS, v_e, and v_d) parameters across the three MRI visits (baseline, and after one and three cycles of NACT). Box plots illustrate the median and interquartile range values of all patients for whole-tumour region at each MRI visit. ADC: apparent diffusion coefficient. D_t: tissue diffusion. v_e: interstitial volume fraction. v_d: extracellular volume fraction. D_p: pseudo-diffusion coefficient. f×D_p: microvascular blood flow. F_b: blood flow. PS: capillary permeability–surface area product. f: perfused fraction. v_b: blood volume fraction.
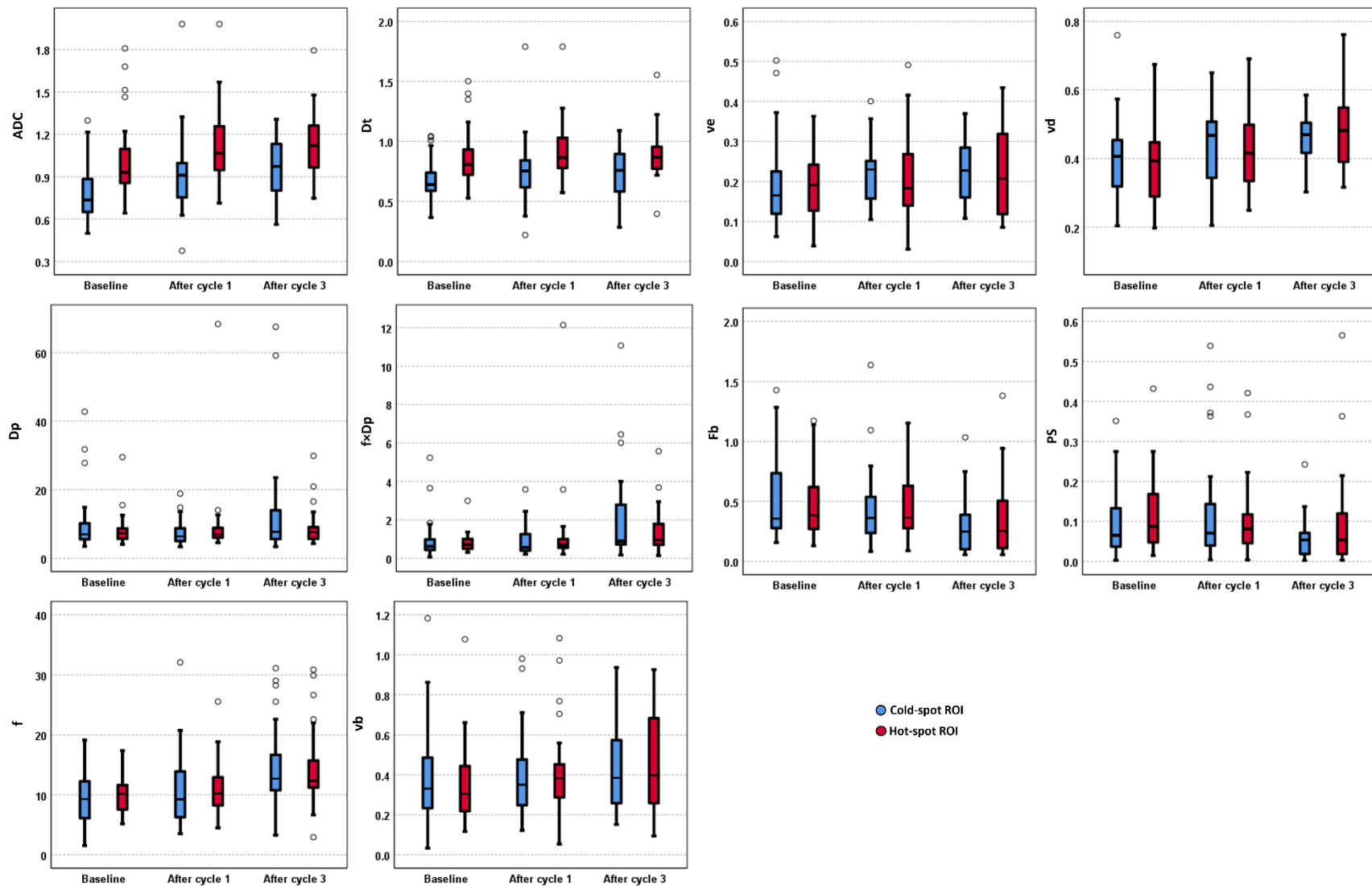
Figure 6.6 Evolution of DWI (ADC, D_t, D_p, f, and f×D_p) and DCE-MRI (F_b, v_b, PS, v_e, and v_d) parameters across the three MRI visits (baseline, and after one and three cycles of NACT). Box plots illustrate the median and interquartile range values of all patients for cold-spot and hot-spot regions at each MRI visit. ADC: apparent diffusion coefficient. D_t: tissue diffusion. v_e: interstitial volume fraction. v_d: extracellular volume fraction. D_p: pseudo-diffusion coefficient. f×D_p: microvascular blood flow. F_b: blood flow. PS: capillary permeability–surface area product. f: perfused fraction. v_b: blood volume fraction.

6.3.4 Upper estimate of repeatability of the DWI model parameters

The same ten pNRs selected for the repeatability analysis of DWI model parameters in Chapter 4 (section 4.3.6) were included in the repeatability analysis of the DCE-MRI parameters. The upper estimate of the wCV was 2.1% for tumour T_1, 13.9% for F_b, 54.8% for PS, 20.6% for v_e, 41.9% for v_b, and 10.2% for v_d. It should be noted that the wCV for v_e and v_d was calculated from 7 pNR patients' data, as it was not possible to estimate these parameters in one of the two chosen visits for 3 patients.

6.4 Discussion

In this study, the absolute blood flow (F_b) estimates were made from the HTR-DCE-MRI data after measuring patient-specific arterial input functions and are consistent with previously reported estimates obtained using [O-15] H_2O positron emission tomography in a comparable patient population (193). The correlations were examined in a total of 108 studies using paired DWI and DCE-MRI measurements.

No statistically significant between-subject or within-subject repeated measures correlations were found between the IVIM and DCE-MRI perfusion parameters of the study's primary interest (f versus v_b and f×D_p versus F_b; p = 0.054–0.99). These findings align with previous breast cancer studies, which also found no correlation between any IVIM perfusion parameters and DCE-MRI parameter related to perfusion, K^{trans} (28, 29). K^{trans} may not solely reflect tumour blood flow but also vessel permeability (151). The present study went further by estimating tumour blood flow and blood volume fraction from DCE-MRI during NACT, but still found no correlations. One possible explanation for the lack of correlation might be significant tissue heterogeneity in tumours; the parameters were estimated from the whole-tumour regions. Where possible, two small focused ROIs (diffusion cold-spot and perfusion hot-spot) in each whole-tumour region were generated to reduce the likelihood of heterogeneity. It was assumed that these smaller ROIs would be more homogenous. However, no clear correlations were found in these smaller regions, and the data were observed to be more variable than the whole-tumour ROI, as reflected by the number of outliers and a wider range in the box plot scale (Figure 6.5 versus Figure 6.6). An alternative method for future studies that might aid in selecting homogeneous tumour regions could be histogram analysis of pixel-wise IVIM and DCE-MRI parameter maps; however, the possibility of finding a homogeneous tumour region in the IVIM and DCE perfusion-related

parameter maps to examine the correlation (f versus v_b and f×D_p versus F_b) would require further investigation and validation.

Imprecision in the estimates of f×D_p and v_b, in particular, is a potential issue that may have masked correlations between the IVIM and DCE-MRI perfusion parameters. A previous report recognized that the precision with which the D_p parameter is estimated is poor (157), and the estimate of v_b in another study was reported to be very imprecise (109), which was reflected in our calculated upper estimate of its repeatability (wCV: 41.9%). The estimation of v_b, against which the f parameter derived from IVIM is compared, becomes difficult when tumour capillaries are excessively leaky (187). In this study, out of 108 DCE-MRI datasets, a one-compartment model was preferred in 13 cases, and an estimate of v_b and PS was not possible in those 13.

It is also possible that IVIM and DCE-MRI reflect different underlying physiology. IVIM does not estimate perfusion in a classical way but estimates flow in the direction of the diffusion encoding gradient, whereas DCE-MRI measures the delivery of blood and subsequent distribution of contrast agent in the tissue, on a different time scale (194). Furthermore, it has been suggested that a single pseudo-diffusion coefficient (D_p) is insufficient to describe the complex diffusion properties of the vascular signal (195). The inconsistent patterns of response to treatment seen in the median values of f versus v_b and f×D_p versus F_b may support this suggestion (Figure 6.5).

In contrast, this study found moderate positive between-subject and within-subject repeated measures correlations between the diffusion parameters (ADC and D_t) and v_e (between-subject: r = 0.461, p = 0.004; and r = 0.405, p = 0.01, and within-subject: r_{rm} = 0.597, p<0.001; and r_{rm} = 0.514, p<0.001 for (ADC & v_e) and (D_t & v_e), respectively), as well as a moderate positive within-subject repeated measures correlation between the diffusion parameters (ADC and D_t) and v_d (r_{rm} = 0.619, p<0.001; and r_{rm} = 0.564, p<0.001 for (ADC & v_d) and (D_t & v_d), respectively). These positive results are important, as this is the first time they have been observed in breast cancer (30), and support the current understanding of these imaging parameters. A positive between-subject correlation between ADC and v_e was previously determined in head and neck cancers and orofacial lesions (153, 196) suggesting that these parameters are related to tissue microstructure. The ADC and D_t values reflect the diffusion of water molecules in tissue, which is affected by cellular density, membrane permeability and extracellular volume (10),

and v_d is a direct measure of the extracellular volume fraction (187) while v_e is a parameter that reflects the volume fraction of the interstitial space within the tissue, which can be influenced by such factors as cellular density and extracellular matrix deposition. A prior study revealed that tumour cellularity is inversely proportional to v_e, v_d, and ADC values (197). Therefore, the observed between-subject correlation of the diffusion coefficients and v_e may suggest that breast tumours with a high cellular density tend to have a small interstitium and increased diffusion restriction, whereas tumours with a low cellular density tend to have a large interstitium and less diffusion restriction. The observed positive within-subject repeated measures correlations could result from the fact that ADC/D_t, v_e, and v_d exhibited similar patterns of change in response to treatment, wherein the values were increasing during the three MRI time-points (Figure 6.5).

Furthermore, a moderate positive between-subject correlation between the diffusion coefficients (ADC and D_t) and tumour T_1 was observed in this study (r = 0.603, p<0.001; and r = 0.631, p<0.001 for (ADC & tumour T_1) and (D_t & tumour T_1), respectively). Tumour T_1 measures tissue relaxation time, which can be affected by tissue water and fat content, macromolecule concentration and hydration state (198). Thus, this positive correlation may be because breast tumours with high cellular density and a small extracellular space have a decreased free-water content, resulting in low diffusion coefficient values and short tumour T_1 (198, 199).

6.4.1 Limitations

First, this study was performed on a limited sample size, which may limit the statistical power of the results. However, this is the first study that assesses both between-subject and within-subject repeated correlations between the perfusion parameters estimated by IVIM and DCE-MRI in a cohort of breast cancer patients undergoing NACT with a primary focus on hypothesis generation rather than testing; therefore, the results can be used to direct future studies. Second, the DWI data were acquired with only 6 b-values, four of which were low ($\leq$ 200 s/mm^2). In a clinical protocol, it is not practical to acquire DWI data with a large number of b-values. Nevertheless, the simulation study performed in Chapter 3 showed that acquiring DWI data with 6 b-values will not lead to appreciably biased and imprecise results for most IVIM parameters compared to acquiring DWI data with 12 b-values, though the precision of f×D_p was lower than with 12 b-values (refer to Chapter 3, Table 3.5 vs. Table 3.7 for RB and SD of Overseg-C). Further, a

previous study showed that a small number of b-values is not the main source of errors in IVIM parameter estimates. Intra-patient variability is significant; they found that the precision in the estimates of the IVIM parameters with only 4 b-values was better than the test-retest repeatability of those same parameters estimated with 16 b-values (157). Third, a pixel-wise comparison of IVIM and DCE-MRI parameter maps was not performed in this study, although it might be valuable. Instead, the images were analysed by following the recommended approaches of the International Breast Diffusion-Weighted Imaging Working Group (24), which included volumetric sampling and focused ROIs (i.e., smaller single-slice ROIs on the darkest part of the ADC map). No correlations were observed between f versus v_b and f$\times D_p$ versus F_b in these smaller regions, but they showed more variability in the estimates instead (Figure 6.6), suggesting that a pixel-wise analysis might yield similar outcomes. Fourth, the DCE images were rigidly aligned to the DWI images and this approach may not have been sufficient to correct DWI distortions. As such, the accuracy of spatial co-registration could have been affected, potentially influencing the findings reported, particularly in the smaller regions. Therefore, future work incorporating pixel-wise analysis following rigorous DWI and DCE-MRI image registration is needed to further investigate these relationships. Finally, the repeatability of the DCE-MRI parameters was not formally investigated. It was challenging to justify performing a repeated baseline DCE-MRI scan that required an additional injection of gadolinium contrast because the patients were due to undergo multiple NACT cycles and MRI scans. Instead, an upper estimate of the repeatability of the DCE-MRI parameters was calculated from the same subset of baseline and cycle 1 studies selected for the repeatability analysis of DWI model parameters, as performed in Chapter 4, section 4.3.6.

6.5 Conclusions

This preliminary study investigated both between-subject and within-subject repeated measures correlations between DWI and DCE-MRI parameters in a cohort of patients with breast cancer imaged before and after one and three cycles of NACT. No statistically significant correlations were observed between the perfusion parameters estimated by IVIM (f and f$\times D_p$) and those estimated by DCE-MRI (F_b and v_b) (p = 0.054–0.99). The two techniques may reflect different underlying physiology, and/or estimates of the IVIM and DCE-MRI parameters in the current study are imprecise. Therefore, care should be taken when interpreting the IVIM perfusion parameters as surrogates for those measured using DCE-MRI

until their underlying pathophysiologic interpretation and relationship to the DCE-MRI perfusion parameters are elucidated by further research. However, the moderate positive within-subject repeated measures correlations found between the diffusion parameters ADC and D_t and DCE-MRI parameters v_e and v_d confirm the expectation that as the interstitial and extracellular volume fractions increase, water diffusion increases.

Chapter 7 Thesis summary, limitations and future work

7.1 Introduction

There has been growing interest in exploring the applications of IVIM and SEM models of DWI in breast imaging, with a predominant focus on differentiating breast lesions. However, the use of IVIM and SEM models to predict early breast cancer response to NACT has received less attention. This thesis focused on evaluating the relative potential of basic monoexponential versus advanced (IVIM and SEM) diffusion models in predicting early response to NACT in patients with primary breast cancer scheduled to undergo NACT. Additionally, the relationships between IVIM and DCE-MRI perfusion-related measures, as well as between DWI tissue diffusion measures and DCE-MRI cellularity-related measures, were explored. The research projects were conducted using a retrospective MRI dataset of 40 breast cancer patients collected as part of a Breast Cancer Now-funded project at three time points: before NACT and after one and three NACT cycles.

7.2 Summary of the experimental works

7.2.1 Comparison of curve-fitting methods for IVIM analysis in breast cancer: Simulation study

There is considerable variability in IVIM parameters both across breast studies (27, 28, 116, 126, 154, 155) and within the same patient group (156), with no consensus on which fitting method to use for estimating IVIM parameters from DWI images. The influence of the fitting method on the accuracy, bias, and precision of IVIM parameter estimates for breast cancer has scarcely been investigated (156, 160). However, determining the fitting method that produces IVIM parameters closely aligned with the underlying 'true' values is crucial.

This chapter compared six commonly used IVIM curve-fitting methods in breast cancer, using simulated data that represents the range of IVIM parameters observed in breast cancer data obtained in Leeds with the same distribution of six b-values (125), along with in vivo measurements, to primarily determine the method providing superior precision, minimal error and bias, and achieving the best in vivo repeatability of IVIM parameter estimates (with an emphasis on f and $f \times D_p$) to be employed in analysing the clinical breast DWI data included in this thesis.

The comparisons were made across six fitting methods: full-fitting, segmented-fitting, and oversegmented-fitting, each with and without bound constraints of the parameter values, at 12 b-values (b = 0, 10, 20, 30, 50, 70, 100, 150, 200, 400, 800, and 1000 s/mm²) and six b-values (b = 0, 50, 100, 200, 400, and 800 s/mm²), and with three noise levels (noise-free, whole-tumour and tumour cold-spot ROIs averaged signals).

The study showed that IVIM parameter estimates are susceptible to error, bias, and imprecision, varying according to the applied fitting algorithm, number of b-values, and noise level. Constrained segmented- and oversegmented-fitting methods produced the lowest errors and highest precision for the parameters D_p, f, and $f \times D_p$ at the whole-tumour noise level. The in vivo repeatability results aligned with the simulation findings, where constrained segmented- and oversegmented-fitting methods achieved best repeatability for D_t, D_p, f, and $f \times D_p$. Nevertheless, the constrained oversegmented-fitting method consistently produced the smallest errors and highest precision for D_p, f, and $f \times D_p$ estimates at the tumour cold-spot ROI. Consequently, for methodological consistency, the constrained oversegmented method was employed in subsequent research (i.e., Chapters 4 and 5) when analysing clinical breast DWI data extracted from both whole-tumour and small focused ROIs. Although this work was built on and performed for specific clinical DWI data, the results from this chapter reveal a need for further investigation into the impact of noise and the number of b-values on in vivo IVIM parameter estimates to validate these findings and suggest that applying an absolute diagnostic cut-off value for any IVIM parameter in a tumour may not be valid in clinical practice unless the parameter is obtained using the same fitting algorithm and/or acquired with the same number of b-values and/or noise level as the reference scenario from which the cut-off value was derived.

7.2.2 Evaluation of monoexponential, SEM and IVIM DWI MRI diffusion models estimated from the whole-tumour region of interest in early response monitoring to NACT in patients with breast cancer.

Preliminary studies have reported that after two or three NACT cycles, the parameters of the SEM and IVIM models estimated from freehand single-section ROI drawn on the imaging slice with the largest tumour dimension may predict breast cancer response to NACT; however, the authors of these studies have recommended further investigation at earlier treatment points (i.e., after one cycle) (19, 23). Consistent with this direction, the ACRIN 6698 multicentre trial, which

evaluated the effectiveness of ADC in predicting early pathological response to NACT, suggests that further investigation into using IVIM or SEM for analysing DWI data may better depict therapeutic effects (25). Additionally, the International Breast DWI Working Group recommended volumetric sampling of the entire tumour when evaluating tumour response (24), and this approach may minimise sampling bias in comparison with the single-section ROI (152).

The Chapter 4 study aimed to address the identified research gap by investigating the value of parameters obtained from the monoexponential (ADC), SEM (DDC, α), and IVIM (D_t, D_p, f, f×D_p) models, derived from DWI data acquired pretreatment and after one and three NACT cycles, and estimated using whole-tumour ROI to assess early breast cancer response to NACT.

The corresponding hypothesis was that parameters obtained from the monoexponential, SEM, and IVIM models derived from MRI data acquired pretreatment and after one and three NACT cycles, using volumetric sampling, have the potential to assess early breast cancer response to NACT.

The results partially supported this hypothesis. Specifically, the study demonstrated that analysing breast cancer DWI data with the advanced diffusion models (IVIM and SEM) offers a better prediction of NACT response than analysis with the monoexponential model. The IVIM perfusion-related parameters values f and f×D_p were significantly lower, and the SEM heterogeneity index value α was significantly higher in pathological responders compared to non-responders after one NACT cycle (median: pR = 9.13% and pNR = 15.21% for f; p = 0.001, pR = 0.57×10^{-3} mm^2/s and pNR = 1.08×10^{-3} mm^2/s for f×D_p; p = 0.001, and pR = 0.89 and pNR = 0.81 for α; p = 0.003), and were predictive of response with reasonable performance (AUC = 0.832; p = 0.001 for f; AUC = 0.802; p = 0.002 for f×D_p; and AUC = 0.782; p = 0.003 for α). The diffusion coefficients (ADC, DDC, and D_t) could not predict the response at any of the three time-points. In contrast, tumour volumes in the responders were considerably smaller than in non-responders at all three time-points (median: pretreatment: pR = 2.16 cm^3 and pNR = 10.47 cm^3; p<0.001; post one cycle: pR = 1.57 cm^3 and pNR = 8.71 cm^3; p<0.001; and post three cycles: pR = 0.51 cm^3 and pNR = 4.98 cm^3; p<0.001), and showed reasonable performance for response prediction (AUC = 0.848 to 0.881; p<0.001). Thus, patients with a smaller tumour volume, higher α, and lower f and f×D_p after one NACT cycle responded better to NACT.

7.2.3 Evaluation of monoexponential, SEM and IVIM DWI MRI diffusion models estimated from tumour diffusion cold-spot and perfusion hot-spot regions in early response monitoring to NACT in patients with breast cancer.

The ACRIN 6698 trial further proposed future investigations into alternative analytical methods to improve the detectability of changes in tumour cellularity, such as by characterising the worst tumour subregion (i.e., the area with the lowest ADC) (25). Consistently, the International Breast DWI Working Group suggested using a small ROI placed on the darkest region of the tumour on ADC maps, potentially reflecting the most active part of the tumour and occasionally referred to as the diffusion cold-spot, as the preferred method for measuring ADC (24). This method is considered analogous to that used in DCE-MRI image analysis, where the tumour region with the greatest mean maximum enhancement, often referred to as a perfusion hot-spot, is selected (24, 26). However, the predictive capability of the ADC, along with SEM and IVIM model parameters, when focused on the most active region of the tumour (i.e., the diffusion cold-spot and perfusion hot-spot) requires exploration.

Accordingly, given the promising IVIM and SEM results from Chapter 4, the Chapter 5 study aimed to add to the body of knowledge by investigating the value of monoexponential, SEM and IVIM models for the diffusion cold-spot and perfusion hot-spot regions of the tumour in assessing the early breast cancer response to NACT.

The corresponding hypothesis was that parameters obtained from the monoexponential, SEM, and IVIM models for the diffusion cold-spot and perfusion hot-spot regions of the tumour at pretreatment and after one and three cycles of NACT could be effective in assessing early breast cancer response to NACT.

The results partially supported this hypothesis and aligned with those of Chapter 4. In particular, the study findings showed that the SEM and IVIM models outperformed the monoexponential model in predicting NACT response when fitted to diffusion data from breast tumour cold-spot and hot-spot regions. At pretreatment, IVIM perfusion-related parameters f and $f{\times}D_p$ were significantly lower and the SEM heterogeneity index α was significantly higher in responders compared to non-responders in the tumour hot-spot regions (median: pretreatment: pR = 8.78% and pNR = 11.44% for f; p = 0.03, and pR = 0.56×10^{-3} mm^2/s and pNR = 0.98×10^{-3} mm^2/s for $f{\times}D_p$; p = 0.006, and pR = 0.87 and pNR = 0.82 for α;

p = 0.04), and demonstrated reasonable performance in predicting response (AUC = 0.724; p = 0.03 for f; AUC = 0.794; p = 0.007 for f×D_p; and AUC = 0.711; p = 0.04 for α). After one NACT cycle, f and α continued to show reasonable predictive performance when estimated from tumour cold-spot and hot-spot regions (in hot-spot: AUC = 0.722; p = 0.03 for f, AUC = 0.752; p = 0.01 for α; and in cold-spot: AUC = 0.711; p = 0.04 for f, AUC = 0.744; p = 0.01 for α), with responders displaying significantly lower f and higher α values (median: in hot-spot: pR = 9.12% and pNR = 11.84% for f; p = 0.03, pR = 0.90 and pNR = 0.84 for α; p = 0.01; and in cold-spot: pR = 7.91% and pNR = 9.85% for f; p = 0.04, pR = 0.89 and pNR = 0.77 for α; p = 0.01). In contrast, only the diffusion coefficients (DDC and D_t) from cold-spot regions after one NACT cycle were significantly higher in responders compared to non-responders (median: pR = 0.90 × 10^{-3} mm^2/s and pNR = 0.72 × 10^{-3} mm^2/s for DDC; p = 0.01, and pR = 0.80 × 10^{-3} mm^2/s and pNR = 0.63 × 10^{-3} mm^2/s for D_t; p = 0.005), and exhibited reasonable performance for response prediction (AUC = 0.752; p = 0.01 for DDC, and AUC = 0.786; p = 0.006 for D_t). However, Chapter 5 results indicate that sampling diffusion data from small tumour subregions (cold-spot/hot-spot) introduces more variability in parameter estimates and reduces the predictive performance compared to the whole-tumour ROI approach, suggesting the entire tumour should be characterised when evaluating the NACT response.

7.2.4 The relationship between parameters measured using IVIM and DCE-MRI in patients with breast cancer undergoing NACT: a longitudinal cohort study.

The promising roles of IVIM perfusion-related parameters f and f×D_p in differentiating benign and malignant breast tumours over the past decade (21, 27, 130-133), and in evaluating breast tumour response to NACT as found by a previous study (23) and this thesis have, in turn, reopened the question of whether IVIM could be used as a contrast-agent-free alternative to DCE-MRI for measuring breast tumour perfusion. Studies that investigated the correlations between IVIM and DCE-MRI perfusion-related parameters in breast tumours were few, examined correlations at a single visit, and produced contradictory results (27-29). A correlation between perfusion parameter changes induced by treatment is meaningful and suggests that IVIM could be used as a contrast-agent-free surrogate for DCE-MRI in monitoring serial changes in tumour perfusion. Furthermore, none of these studies' DCE data provided an absolute estimation of

tumour blood flow (F_b); thus, the studies did not perform a direct comparison with the IVIM parameter purported to measure microvascular blood flow ($f \times D_p$).

On the other hand, ADC is expected to be directly proportional to DCE-MRI cellularity-related measures (i.e., v_e, and v_d); however, one study on breast tumours assessed the correlation at a single visit and found no relationship between ADC and v_e, suggesting that ADC is incompletely understood (30).

Therefore, the Chapter 6 study aimed to take a further novel step by investigating whether IVIM and DCE-MRI perfusion-related parameters correlate (f versus v_b and $f \times D_p$ versus F_b), and whether IVIM can offer a contrast-agent-free alternative to DCE-MRI for monitoring serial changes in tumour perfusion. It also aimed to examine the correlation between DWI tissue diffusion measures and DCE-MRI cellularity-related measures (ADC and D_t versus v_e and v_d), utilising the same MRI dataset of 40 patients who underwent NACT.

The stated hypothesis was that the IVIM technique can serve as a contrast-agent-free alternative to DCE-MRI for measuring breast tumour perfusion, and that the diffusion measure (ADC) correlates with DCE-MRI cellularity-related measures.

The results did not support the first part of this hypothesis but supported the second. The study found no statistically significant between-subject or within-subject repeated measures correlations between the IVIM and DCE-MRI perfusion-related parameters (f and $f \times D_p$ with F_b and v_b) in the whole-tumour, cold-spot, and hot-spot regions (p = 0.054–0.99). This may indicate that the two techniques reflect different underlying physiology, and/or that the estimates of the IVIM and DCE-MRI parameters ($f \times D_p$ and v_b) in the current study are imprecise. Potentially, significant tissue heterogeneity in tumours might have compromised correlations in the whole-tumour regions, and the large variability in parameter estimates observed within focused small tumour regions (cold-spot and hot-spot) may have also masked the correlations. In light of these findings, care should be taken when interpreting the IVIM perfusion parameters as surrogates for those measured using DCE-MRI until their underlying pathophysiologic interpretation and relationship to the DCE-MRI perfusion parameters are elucidated by further research.

In contrast, moderate positive between-subject and within-subject repeated measures correlations were found between the diffusion parameters (ADC and D_t) and v_e (between-subject: r = 0.461, p = 0.004; and r = 0.405, p = 0.01, and within-subject: r_{rm} = 0.597, p<0.001; and r_{rm} = 0.514, p<0.001 for (ADC & v_e) and (D_t & v_e), respectively), and moderate positive within-subject repeated measures

correlations between the diffusion parameters (ADC and D_t) and v_d in the whole-tumour regions (r_{rm} = 0.619, p<0.001; and r_{rm} = 0.564, p<0.001 for (ADC & v_d) and (D_t & v_d), respectively), confirm the expectation that as the interstitial and extracellular volume fractions increase, water diffusion increases.

7.3 Limitations and future work

I- The IVIM parameters were estimated with only 6 b-values (0-800 s/mm²), four of which were low (≤ 200 s/mm²). However, there is no consensus yet on the number of b-values lower and higher than 200 s/mm² to acquire, and also performing DWI with a large number of b-values is not currently practical in the clinical setting. The simulation study performed in Chapter 3 demonstrated that acquiring DWI data with the 6 b-values used in this thesis does not lead to biased or imprecise results for most IVIM parameters compared to acquiring data with 12 b-values (nine of which were ≤ 200 s/mm²), though the precision of $f×D_p$ was lower than with 12 b-values. Including a greater number of lower b-values may facilitate more accurate estimation of IVIM perfusion-related parameters but at the expense of increased scanning time and a risk of patient intolerance (motion and/or withdraw). Given that this study found f and $f×D_p$ as having potential clinical utility in predicting non-responders at early treatment time point, future work should focus on exploring the optimal number of b-values, particularly the lower b-values, for reliable IVIM parameter quantification in the breast, within a scanning time that is clinically feasible. This could be explored on 3 T MRI systems, where an improved SNR and a greater number of b-values with fewer averages could be acquired for the benefit of overall scanning time. Such work is essential for the future clinical adoption of IVIM. However, there are some challenges of using 3 T over 1.5 T MRI for DWI of breast cancer that need to be considered. Higher field strengths suffer from more susceptibility artefacts, particularly at air-tissue interfaces (e.g. skin folds), which can potentially lead to spatial distortions that make it difficult to define the tumour region accurately and alter signal intensity non-uniformly, thereby reducing the reliability of IVIM parameter estimation. Also, at 3 T the specific absorption rate (SAR) is higher, restricting the number of RF pulses that can be applied within a given scan. This restriction may limit the number of b-values or signal averages that can be clinically acquired, which in turn could affect the precision of IVIM parameter estimation. Additionally, fat suppression becomes more difficult at 3 T due to increased magnetic field inhomogeneity. Ineffective fat suppression may

result in artefacts that further complicate the accuracy and precision of IVIM-derived parameters.

II- The DWI model parameters were estimated from whole-tumour and small focused ROIs averaged signals, as recommended by the International Breast Diffusion-Weighted Imaging working group (24) and Iima et al (168). Investigating alternative analytical approaches, such as pixel-by-pixel fitting with corresponding mean and histogram-based analysis of DWI parametric maps, may provide additional information for assessing tumour response, though the high variability in the parameter estimates observed within the small regions in this thesis suggests that pixel-wise analysis might yield similar outcomes.

III- The repeatability of the DWI and DCE-MRI parameters was not formally investigated. It was challenging to justify performing a repeated baseline DCE-MRI scan that required an additional injection of gadolinium contrast, given that patients were scheduled to undergo multiple NACT cycles and MRI scans. Instead, an upper estimate of the repeatability of the DWI and DCE-MRI parameters was calculated from a selection of baseline and cycle 1 studies. Future work exploring the optimal number of b-values for IVIM should also assess the repeatability and reproducibility of the diffusion model parameters in breast cancer, with consideration for extending the assessment across multiple centres and MRI field strengths. Such work is required to bridge the gap before the first translation of SEM and IVIM models into routine clinical practice.

IV- The DWIs were acquired using the ss-EPI technique, which is the standard method for breast DWI. The ss-EPI technique is widely available and allows efficient and rapid acquisition of multiple DWIs (varied b-values) that minimizes motion artifacts; however, it suffers from blurring and geometric distortion. In this thesis, the DCE images were rigidly aligned to the DWI images and this approach may not have been sufficient to fully correct DWI distortions. As such, the accuracy of spatial co-registration could have been affected, potentially influencing the findings reported, particularly in the smaller regions. A promising technique is multi-shot DWI, one version of which called multiplexed sensitivity encoding (MUSE), has recently been explored in a breast study to address these limitations (200). The MUSE DWI demonstrated superior image quality compared to the ss-EPI DWI, improved spatial resolution, and significantly reduced blurring and geometric distortion, though at the cost of increased acquisition time. Future work should consider using the MUSE technique, or any other emerging

techniques from the literature that overcome ss-EPI limitations, and then optimising it to ensure clinically feasible scanning times (if required), to assess whether it can improve the diagnostic performance of monoexponential, SEM, and IVIM diffusion model parameters in predicting early breast cancer response to NACT, and carry out further investigation on the relationship between IVIM and DCE-MRI parameters.

V- The clinical studies in this thesis were conducted on a limited sample size at a single centre using one MRI scanner, which restricts the interpretation and limits the statistical power of the results. However, to the best of the candidate's knowledge, these studies were the initial ones to address the gaps identified in the literature on DWI studies of breast cancer patients undergoing NACT, with a primary focus on hypothesis generation rather than testing. Therefore, based on the current findings and after addressing the limitations, a future multicentre study with a larger cohort of patients (responders and non-responders) with diverse breast tumour subtypes is recommended to test the predictive performance of monoexponential, SEM, and IVIM diffusion models between the response groups on three tumour regions (whole-tumour, cold-spot and hot-spot), and also according to breast tumour subtypes. The ACRIN 6698 multicentre trial found that the percentage change in the ADC value was predictive only in (HR+/HER2−) tumours after four NACT cycles (25); however, the data utilised here included only 15 patients with (HR+/HER2−) tumours, with 2 responders and 13 non-responders, of which three non-responders withdrew following the pretreatment MRI, hence impeding assessment within this specific tumour subtype. Further, although MRI scans were performed at an earlier treatment point (i.e., after one cycle) than mid-treatment, acquiring DWI data following two NACT cycles which is still considered an early phase of treatment, would provide significant additional insights, enabling a comprehensive assessment of the predictive performance of the three diffusion models and determining the optimal early time point for predicting response, and possibly revealing additional predictive parameters. While this thesis focused on evaluating the relative potential of monoexponential, IVIM, and SEM diffusion models in predicting early response to NACT, future work testing the value of these models for predicting recurrence-free survival and/or overall survival, as study follow-up data mature, would be informative.

7.4 Thesis conclusions

This thesis performed a progressive evaluation of monoexponential and advanced (IVIM and SEM) DWI models in assessing the early response of breast cancer to NACT. A major contribution to the field is the demonstration of the superior predictive capabilities of IVIM and SEM models compared to the conventional monoexponential model in whole-tumour analysis after one NACT cycle, as well as in tumour diffusion cold-spot and perfusion hot-spot regions at pretreatment and after one cycle. Responders showed lower pretreatment IVIM perfusion-related parameters f and $f \times D_p$ and higher SEM heterogeneity index α in tumour hot-spot regions compared to non-responders. After one NACT cycle, responders demonstrated higher diffusion coefficients DDC and D_t in tumour cold-spot regions, continued to show lower f and higher α in hot-spot and cold-spot regions, and lower f and $f \times D_p$ and higher α in whole-tumour regions. Nevertheless, findings from Chapters 4 and 5 collectively underscore that sampling diffusion data from the whole tumour offers less variable parameter estimates and superior predictive performance, particularly for α and f and $f \times D_p$.

The novel methodology adopted in Chapter 6 provided new evidence to the existing knowledge on the lack of relationship between IVIM and DCE-MRI perfusion-related parameters (f versus v_b and $f \times D_p$ versus F_b) in breast cancer, underscoring the need for caution when interpreting IVIM perfusion parameters as surrogates for those measured using DCE-MRI at this stage of development. In contrast, the novel finding of moderate positive correlations between diffusion parameters (ADC and D_t) and DCE-MRI cellularity-related measures (v_e and v_d) confirms that as the interstitial and extracellular volume fractions increase, water diffusion increases.

Overall thesis findings underscore the promising clinical utility of IVIM and SEM models in assessing early breast cancer response to NACT in patients.

References

1. Organization, W.H. *Breast cancer*. [Online]. 2023. [Accessed 12 July]. Available from: https://www.who.int/news-room/fact-sheets/detail/breast-cancer

2. Kaufmann, M., Von Minckwitz, G., Mamounas, E.P., Cameron, D., Carey, L.A., Cristofanilli, M., Denkert, C., Eiermann, W., Gnant, M. and Harris, J.R. Recommendations from an international consensus conference on the current status and future of neoadjuvant systemic therapy in primary breast cancer. *Annals of Surgical Oncology*. 2012, **19**(5), pp.1508-1516.

3. Shenoy, H., Peter, M., Masannat, Y., Dall, B., Dodwell, D. and Horgan, K.J.S.O. Practical advice on clinical decision making during neoadjuvant chemotherapy for primary breast cancer. *Surgical Oncology*. 2009, **1**(18), pp.65-71.

4. Fowler, A.M., Mankoff, D.A. and Joe, B.N. Imaging neoadjuvant therapy response in breast cancer. *Radiology*. 2017, **285**(2), pp.358-375.

5. Eisenhauer, E.A., Therasse, P., Bogaerts, J., Schwartz, L.H., Sargent, D., Ford, R., Dancey, J., Arbuck, S., Gwyther, S. and Mooney, M. New response evaluation criteria in solid tumours: revised RECIST guideline (version 1.1). *European Journal of Cancer*. 2009, **45**(2), pp.228-247.

6. Li, S. and Padhani, A. Tumor response assessments with diffusion and perfusion MRI. *Journal of Magnetic Resonance Imaging*. 2012, **35**(4), pp.745-763.

7. Georgiou, L., Sharma, N., Broadbent, D.A., Wilson, D.J., Dall, B.J., Gangi, A. and Buckley, D.L. Estimating breast tumor blood flow during neoadjuvant chemotherapy using interleaved high temporal and high spatial resolution MRI. *Magnetic Resonance in Medicine*. 2018, **79**(1), pp.317-326.

8. Schieda, N., Blaichman, J.I., Costa, A.F., Glikstein, R., Hurrell, C., James, M., Jabehdar Maralani, P., Shabana, W., Tang, A. and Tsampalieros, A. Gadolinium-based contrast agents in kidney disease: a comprehensive review and clinical practice guideline issued by the Canadian Association of Radiologists. *Canadian Journal of Kidney Health Disease*. 2018, **5**, p.2054358118778573.

9. Mazhar, S.M., Shiehmorteza, M., Kohl, C.A., Middleton, M.S. and Sirlin, C.B. Nephrogenic Systemic Fibrosis in Liver Disease: A Systematic Review. *Journal of Magnetic Resonance Imaging*. 2009, **30**(6), p.1313.

10. Partridge, S., Nissan, N., Rahbar, H., Kitsch, A. and Sigmund, E. Diffusion-weighted breast MRI: Clinical applications and emerging techniques. *Journal of Magnetic Resonance Imaging*. 2017, **45**(2), pp.337-355.

11. Guo, R., Yang, S.-H., Lu, F., Han, Z.-H., Yan, X., Fu, C.-X., Zhao, M.-L. and Lin, J. Evaluation of intratumoral heterogeneity by using diffusion kurtosis imaging and stretched exponential diffusion-weighted imaging in an orthotopic hepatocellular carcinoma xenograft model. *Quantitative Imaging in Medicine and Surgery*. 2019, **9**(9), p.1566.

12. Le Bihan, D., Breton, E., Lallemand, D., Grenier, P., Cabanis, E. and Laval-Jeantet, M. MR imaging of intravoxel incoherent motions: application to

diffusion and perfusion in neurologic disorders. *Radiology*. 1986, **161**(2), pp.401-407.

13. Bennett, K.M., Schmainda, K.M., Bennett, R., Rowe, D.B., Lu, H. and Hyde, J.S. Characterization of continuously distributed cortical water diffusion rates with a stretched-exponential model. *Magnetic Resonance in Medicine*. 2003, **50**(4), pp.727-734.

14. Liu, C., Wang, K., Li, X., Zhang, J., Ding, J., Spuhler, K., Duong, T., Liang, C. and Huang, C. Breast lesion characterization using whole-lesion histogram analysis with stretched-exponential diffusion model. *Journal of Magnetic Resonance Imaging*. 2018, **47**(6), p.1701.

15. Jin, Y.N., Zhang, Y., Cheng, J.L., Zheng, D.D. and Hu, Y. Monoexponential, Biexponential, and stretched-exponential models using diffusion-weighted imaging: A quantitative differentiation of breast lesions at 3.0 T. *Journal of Magnetic Resonance Imaging*. 2019, **50**(5), pp.1461-1467.

16. Chen, X., Jiang, J., Shen, N., Zhao, L., Zhang, J., Qin, Y., Zhang, S., Li, L. and Zhu, W. Stretched-exponential model diffusion-weighted imaging as a potential imaging marker in preoperative grading and assessment of proliferative activity of gliomas. *American Journal of Translational Research*. 2018, **10**(8), p.2659.

17. Hu, Y., Tang, H., Li, H., Li, A., Li, J., Hu, D., Li, Z. and Kamel, I.R. Assessment of different mathematical models for diffusion-weighted imaging as quantitative biomarkers for differentiating benign from malignant solid hepatic lesions. *Cancer Medicine*. 2018, **7**(7), pp.3501-3509.

18. Li, H., Liang, L., Li, A., Hu, Y., Hu, D., Li, Z. and Kamel, I.R. Monoexponential, biexponential, and stretched exponential diffusion-weighted imaging models: Quantitative biomarkers for differentiating renal clear cell carcinoma and minimal fat angiomyolipoma. *Journal of Magnetic Resonance Imaging*. 2017, **46**(1), pp.240-247.

19. Bedair, R., Priest, A., Patterson, A., McLean, M., Graves, M., Manavaki, R., Gill, A., Abeyakoon, O., Griffiths, J. and Gilbert, F. Assessment of early treatment response to neoadjuvant chemotherapy in breast cancer using non-mono-exponential diffusion models: a feasibility study comparing the baseline and mid-treatment MRI examinations. *European Radiology*. 2017, **27**(7), pp.2726-2736.

20. Le Bihan, D. and Turner, R. The capillary network: a link between IVIM and classical perfusion. *Magnetic Resonance in Medicine*. 1992, **27**(1), pp.171-178.

21. Liu, C., Liang, C., Liu, Z., Zhang, S. and Huang, B. Intravoxel incoherent motion (IVIM) in evaluation of breast lesions: comparison with conventional DWI. *European Journal of Radiology*. 2013, **82**(12), pp.e782-e789.

22. Iima, M., Yano, K., Kataoka, M., Umehana, M., Murata, K., Kanao, S., Togashi, K. and Le Bihan, D. Quantitative non-Gaussian diffusion and intravoxel incoherent motion magnetic resonance imaging: differentiation of malignant and benign breast lesions. *Investigative Radiology*. 2015, **50**(4), pp.205-211.

23. Che, S., Zhao, X., Yanghan, O., Li, J., Wang, M., Wu, B. and Zhou, C. Role of the intravoxel incoherent motion diffusion weighted imaging in the pre-treatment prediction and early response monitoring to neoadjuvant chemotherapy in locally advanced breast cancer. *Medicine*. 2016, **95**(4), pp.1-12.

24. Baltzer, P., Mann, R.M., Iima, M., Sigmund, E.E., Clauser, P., Gilbert, F.J., Martincich, L., Partridge, S.C., Patterson, A. and Pinker, K. Diffusion-weighted imaging of the breast-a consensus and mission statement from the EUSOBI International Breast Diffusion-Weighted Imaging working group. *European Radiology*. 2020, **30**, pp.1436-1450.

25. Partridge, S.C., Zhang, Z., Newitt, D.C., Gibbs, J.E., Chenevert, T.L., Rosen, M.A., Bolan, P.J., Marques, H.S., Romanoff, J. and Cimino, L. Diffusion-weighted MRI findings predict pathologic response in neoadjuvant treatment of breast cancer: the ACRIN 6698 multicenter trial. *Radiology*. 2018, **289**(3), pp.618-627.

26. Pickles, M.D., Manton, D.J., Lowry, M. and Turnbull, L.W. Prognostic value of pre-treatment DCE-MRI parameters in predicting disease free and overall survival for breast cancer patients undergoing neoadjuvant chemotherapy. *European Journal of Radiology*. 2009, **71**(3), pp.498-505.

27. Liu, C., Wang, K., Chan, Q., Liu, Z., Zhang, J., He, H., Zhang, S. and Liang, C. Intravoxel incoherent motion MR imaging for breast lesions: comparison and correlation with pharmacokinetic evaluation from dynamic contrast-enhanced MR imaging. *European Radiology*. 2016, **26**(11), pp.3888-3898.

28. Jiang, L., Lu, X., Hua, B., Gao, J., Zheng, D. and Zhou, Y. Intravoxel incoherent motion diffusion-weighted imaging versus dynamic contrast-enhanced magnetic resonance imaging: comparison of the diagnostic performance of perfusion-related parameters in breast. *Journal of Computer Assisted Tomography*. 2018, **42**(1), pp.6-11.

29. Li, K., Machireddy, A., Tudorica, A., Moloney, B., Oh, K.Y., Jafarian, N., Partridge, S.C., Li, X. and Huang, W. Discrimination of malignant and benign breast lesions using quantitative multiparametric MRI: a preliminary study. *Tomography*. 2020, **6**(2), pp.148-159.

30. Arlinghaus, L.R., Li, X., Rahman, A.R., Welch, E.B., Xu, L., Gore, J.C. and Yankeelov, T.E. On the relationship between the apparent diffusion coefficient and extravascular extracellular volume fraction in human breast cancer. *Magnetic Resonance Imaging*. 2011, **29**(5), pp.630-638.

31. McGuire, K.P. Breast Anatomy and Physiology. In: Aydiner, A. et al. eds. *Breast Disease: Diagnosis and Pathology*. Switzerland: Springer International Publishing, 2016, pp.1-14.

32. Schnitt, S.J. and Collins, L.C. *Biopsy interpretation of the breast*. 2nd ed. Philadelphia: Lippincott Williams & Wilkins, 2009.

33. Jesinger, R.A. Breast anatomy for the interventionalist. *Techniques in vascular interventional radiology*. 2014, **17**(1), pp.3-9.

34. Waugh, A. and Grant, A. *Anatomy and physiology in health and illness*. 9th ed. London: Elsevier Health Sciences, 2001.

35. Cardiff, R.D., Jindal, S., Treuting, P.M., Going, J.J., Gusterson, B. and Thompson, H.J. 23 - Mammary Gland. In: Treuting, P.M. et al. eds. *Comparative Anatomy and Histology (Second Edition)*. San Diego: Academic Press, 2018, pp.487-509.

36. Bray, F., Laversanne, M., Sung, H., Ferlay, J., Siegel, R.L., Soerjomataram, I. and Jemal, A. Global cancer statistics 2022: GLOBOCAN estimates of incidence and mortality worldwide for 36 cancers in 185 countries. *CA: A Cancer Journal for Clinicians*. 2024, **74**(3), pp.229-263.

37. UK, C.R. *Breast cancer statistics*. [Online]. 2024. [Accessed 25 May]. Available from: https://www.cancerresearchuk.org/health-professional/cancer-statistics/statistics-by-cancer-type/breast-cancer#heading-Two

38. UK, C.R. *Cancer Statistics Data Hub*. [Online]. [Accessed 20 May]. Available from: https://crukcancerintelligence.shinyapps.io/CancerStatsDataHub/

39. UK, C.R. *Breast screening*. [Online]. 2023. [Accessed 25 May]. Available from: https://www.cancerresearchuk.org/about-cancer/breast-cancer/getting-diagnosed/screening-breast

40. UK, C.R. *Breast ultrasound scan*. [Online]. 2023. [Accessed 25 May]. Available from: https://www.cancerresearchuk.org/about-cancer/tests-and-scans/breast-ultrasound

41. Sardanelli, F. and Podo, F. *Breast MRI for High-risk Screening*. 1 ed. Cham: Springer International Publishing, 2020.

42. Polyak, K. Heterogeneity in breast cancer. *The Journal of clinical investigation*. 2011, **121**(10), pp.3786-3788.

43. Badve, S. Tumor Heterogeneity in Breast Cancer. In: Badve, S. and Gökmen-Polar, Y. eds. *Molecular Pathology of Breast Cancer*. 1 ed. Cham: Springer International Publishing, 2016, pp.121-132.

44. Makki, J. Diversity of breast carcinoma: histological subtypes and clinical relevance. *Clinical Medicine Insights: Pathology*. 2015, **8**, p.CPath. S31563.

45. Cancer Research UK. *Types of breast cancer and related breast conditions*. [Online]. 2023. [Accessed 03 June 2024]. Available from: https://www.cancerresearchuk.org/about-cancer/breast-cancer/types

46. Rakha, E.A., Reis-Filho, J.S., Baehner, F., Dabbs, D.J., Decker, T., Eusebi, V., Fox, S.B., Ichihara, S., Jacquemier, J. and Lakhani, S.R. Breast cancer prognostic classification in the molecular era: the role of histological grade. *Breast Cancer Research*. 2010, **12**, pp.1-12.

47. Tang, Y., Wang, Y., Kiani, M.F. and Wang, B. Classification, Treatment Strategy, and Associated Drug Resistance in Breast Cancer. *Clinical Breast Cancer*. 2016, **16**(5), pp.335-343.

48. Waks, A.G. and Winer, E.P. Breast cancer treatment. *JAMA*. 2019, **321**(3), pp.316-316.

49. Eroles, P., Bosch, A., Pérez-Fidalgo, J.A. and Lluch, A. Molecular biology in breast cancer: intrinsic subtypes and signaling pathways. *Cancer Treatment Reviews*. 2012, **38**(6), pp.698-707.

50. Podo, F., Buydens, L.M., Degani, H., Hilhorst, R., Klipp, E., Gribbestad, I.S., Van Huffel, S., van Laarhoven, H.W., Luts, J. and Monleon, D. Triple-negative breast

cancer: present challenges and new perspectives. *Molecular Oncology*. 2010, **4**(3), pp.209-229.

51. Pereira, H., Pinder, S., Sibbering, D., Galea, M., Elston, C., Blamey, R., Robertson, J. and Ellis, I. Pathological prognostic factors in breast cancer. IV: Should you be a typer or a grader? A comparative study of two histological prognostic features in operable breast carcinoma. *Histopathology*. 1995, **27**(3), pp.219-226.

52. Elston, C.W. and Ellis, I.O. Pathological prognostic factors in breast cancer. I. The value of histological grade in breast cancer: experience from a large study with long-term follow-up. *Histopathology*. 1991, **19**(5), pp.403-410.

53. Beresford, M.J., Wilson, G.D. and Makris, A. Measuring proliferation in breast cancer: practicalities and applications. *Breast Cancer Research and Treatment*. 2006, **8**, pp.1-11.

54. Yerushalmi, R., Woods, R., Ravdin, P.M., Hayes, M.M. and Gelmon, K.A. Ki67 in breast cancer: prognostic and predictive potential. *The Lancet Oncology*. 2010, **2**(11), pp.174-183.

55. Bamias, A. and Dimopoulos, M.A. Angiogenesis in human cancer: implications in cancer therapy. 2003, **14**(8), pp.459-469.

56. Kerbel, R.S. Inhibition of tumor angiogenesis as a strategy to circumvent acquired resistance to anti-cancer therapeutic agents. *Bioessays*. 1991, **13**(1), pp.31-36.

57. Siemann, D. The unique characteristics of tumor vasculature and preclinical evidence for its selective disruption by Tumor-Vascular Disrupting Agents. *Cancer Treatment Reviews*. 2011, **37**, pp.63-74.

58. Bergers, G. and Benjamin, L.E. Tumorigenesis and the angiogenic switch. *Nature Reviews Cancer*. 2003, **3**(6), pp.401-410.

59. Grubstein, A., Yepes, M. and Kiszonas, R. Magnetic resonance imaging of breast vascularity in medial versus lateral breast cancer. *European Journal of Radiology*. 2009, **75**(2), pp.e9-11.

60. Madu, C.O., Wang, S., Madu, C.O. and Lu, Y. Angiogenesis in Breast Cancer Progression, Diagnosis, and Treatment. *Journal of Cancer*. 2020, **11**(15), p.4474.

61. Slanetz, P.J., Moy, L., Baron, P., Green, E.D., Heller, S.L., Holbrook, A.I., Lee, S.-J., Lewin, A.A., Lourenco, A.P. and Niell, B. ACR appropriateness criteria® monitoring response to neoadjuvant systemic therapy for breast cancer. *Journal of the American College of Radiology*. 2017, **14**(11), pp.S462-S475.

62. Cleator, S., Parton, M. and Dowsett, M. The biology of neoadjuvant chemotherapy for breast cancer. *Endocrine-Related Cancer*. 2002, **9**(3), pp.183-195.

63. Untch, M., Rezai, M., Loibl, S., Fasching, P.A., Huober, J., Tesch, H., Bauerfeind, I., Hilfrich, J., Eidtmann, H. and Gerber, B. Neoadjuvant treatment with trastuzumab in HER2-positive breast cancer: results from the GeparQuattro study. 2010, **28**(12), pp.2024-2031.

64. Symmans, W., Peintinger, F., Hatzis, C., Rajan, R., Kuerer, H., Valero, V., Assad, L., Poniecka, A., Hennessy, B. and Green, M. Measurement of residual

breast cancer burden to predict survival after neoadjuvant chemotherapy. *Journal of Clinical Oncology*. 2007, **25**(28), p.4414.

65. Hamy, A.-S., Darrigues, L., Laas, E., De Croze, D., Topciu, L., Lam, G.-T., Evrevin, C., Rozette, S., Laot, L. and Lerebours, F. Prognostic value of the Residual Cancer Burden index according to breast cancer subtype: Validation on a cohort of BC patients treated by neoadjuvant chemotherapy. *PloS One*. 2020, **15**(6), p.e0234191.

66. Rahbar, H. and Partridge, S.C. Multiparametric MR imaging of breast cancer. *Magnetic Resonance Imaging Clinics*. 2016, **24**(1), pp.223-238.

67. Mann, R.M., Kuhl, C.K., Kinkel, K. and Boetes, C. Breast MRI: guidelines from the European society of breast imaging. *European Radiology*. 2008, **18**, pp.1307-1318.

68. Turnbull, L.W. Dynamic contrast-enhanced MRI in the diagnosis and management of breast cancer. *NMR in Biomedicine*. 2009, **22**(1), pp.28-39.

69. Evans, D.G., Graham, J., O'Connell, S., Arnold, S. and Fitzsimmons, D. Familial breast cancer: summary of updated NICE guidance. *BMJ*. 2013, **346**.

70. Radhakrishna, S., Agarwal, S., Parikh, P.M., Kaur, K., Panwar, S., Sharma, S., Dey, A., Saxena, K., Chandra, M. and Sud, S. Role of magnetic resonance imaging in breast cancer management. *South Asian Journal of Cancer*. 2018, **7**(02), pp.069-071.

71. Kuhl, C., Weigel, S., Schrading, S., Arand, B., Bieling, H., König, R., Tombach, B., Leutner, C., Rieber-Brambs, A. and Nordhoff, D. Prospective Multicenter Cohort Study to Refine Management Recommendations for Women at Elevated Familial Risk of Breast Cancer: The EVA Trial. *Journal of Clinical Oncology*. 2010, **28**, pp.1450-1457.

72. Mann, R.M., Athanasiou, A., Baltzer, P.A., Camps-Herrero, J., Clauser, P., Fallenberg, E.M., Forrai, G., Fuchsjäger, M.H., Helbich, T.H. and Killburn-Toppin, F. Breast cancer screening in women with extremely dense breasts recommendations of the European Society of Breast Imaging (EUSOBI). *European Radiology*. 2022, **32**(6), pp.4036-4045.

73. Leithner, D., Wengert, G., Helbich, T., Thakur, S., Ochoa-Albiztegui, R., Morris, E. and Pinker, K. Clinical role of breast MRI now and going forward. *Clinical Radiology*. 2018, **73**(8), pp.700-714.

74. Sharma, S., Vicenty-Latorre, F.G., Elsherif, S. and Sharma, S. Role of MRI in breast cancer staging: A case-based review. *Cureus*. 2021, **13**(12).

75. Panico, C., Ferrara, F., Woitek, R., D'Angelo, A., Di Paola, V., Bufi, E., Conti, M., Palma, S., Cicero, S.L. and Cimino, G. Staging breast cancer with MRI, the T. A key role in the neoadjuvant setting. *Cancers*. 2022, **14**(23), p.5786.

76. Sardanelli, F., Trimboli, R.M., Houssami, N., Gilbert, F.J., Helbich, T.H., Álvarez Benito, M., Balleyguier, C., Bazzocchi, M., Bult, P. and Calabrese, M. Magnetic resonance imaging before breast cancer surgery: results of an observational multicenter international prospective analysis (MIPA). *European Radiology*. 2022, pp.1-13.

77. Mariscotti, G., Houssami, N., Durando, M., Bergamasco, L., Campanino, P.P., Ruggieri, C., Regini, E., Luparia, A., Bussone, R. and Sapino, A. Accuracy of

mammography, digital breast tomosynthesis, ultrasound and MR imaging in preoperative assessment of breast cancer. *Anticancer Research.* 2014, **34**(3), pp.1219-1225.

78.   Partridge, S.C., Gibbs, J.E., Lu, Y., Esserman, L.J., Tripathy, D., Wolverton, D.S., Rugo, H.S., Hwang, E.S., Ewing, C.A. and Hylton, N.M. MRI measurements of breast tumor volume predict response to neoadjuvant chemotherapy and recurrence-free survival. *American Journal of Roentgenology.* 2005, **184**(6), pp.1774-1781.

79.   Marinovich, M.L., Macaskill, P., Irwig, L., Sardanelli, F., Mamounas, E., von Minckwitz, G., Guarneri, V., Partridge, S.C., Wright, F.C. and Choi, J.H. Agreement between MRI and pathologic breast tumor size after neoadjuvant chemotherapy, and comparison with alternative tests: individual patient data meta-analysis. *BMC Cancer.* 2015, **15**, pp.1-12.

80.   Scheel, J.R., Kim, E., Partridge, S.C., Lehman, C.D., Rosen, M.A., Bernreuter, W.K., Pisano, E.D., Marques, H.S., Morris, E.A. and Weatherall, P.T. MRI, Clinical Examination, and Mammography for Preoperative Assessment of Residual Disease and Pathologic Complete Response After Neoadjuvant Chemotherapy for Breast Cancer: ACRIN 6657 Trial. *American Journal of Roentgenology.* 2018, **210**(6), pp.1376-1385.

81.   Fangberget, A., Nilsen, L., Hole, K.H., Holmen, M., Engebraaten, O., Naume, B., Smith, H.-J., Olsen, D.R. and Seierstad, T. Neoadjuvant chemotherapy in breast cancer-response evaluation and prediction of response to treatment using dynamic contrast-enhanced and diffusion-weighted MR imaging. *European Radiology.* 2011, **21**, pp.1188-1199.

82.   McGuire, K.P., Toro-Burguete, J., Dang, H., Young, J., Soran, A., Zuley, M., Bhargava, R., Bonaventura, M., Johnson, R. and Ahrendt, G. MRI staging after neoadjuvant chemotherapy for breast cancer: does tumor biology affect accuracy? *Annals of Surgical Oncology.* 2011, **18**(11), pp.3149-3154.

83.   WOODHAMS, R., KAKITA, S., HATA, H., IWABUCHI, K., KURANAMI, M. and GAUTAM, S. Identification of Residual Breast Carcinoma Following Neoadjuvant Chemotherapy: Diffusion-weighted Imaging—Comparison with Contrast-enhanced MR Imaging and Pathologic Findings. *Radiology.* 2010, **254**(2), pp.357-366.

84.   Fukuda, T., Horii, R., Gomi, N., Miyagi, Y., Takahashi, S., Ito, Y., Akiyama, F., Ohno, S. and Iwase, T. Accuracy of magnetic resonance imaging for predicting pathological complete response of breast cancer after neoadjuvant chemotherapy: association with breast cancer subtype. *Springerplus.* 2016, **5**, pp.1-9.

85.   Denis, F., Desbiez-Bourcier, A., Chapiron, C., Arbion, F., Body, G. and Brunereau, L. Contrast enhanced magnetic resonance imaging underestimates residual disease following neoadjuvant docetaxel based chemotherapy for breast cancer. *European Journal of Surgical Oncology.* 2004, **30**(10), pp.1069-1076.

86.   Schrading, S. and Kuhl, C.K. Breast Cancer: Influence of Taxanes on Response Assessment with Dynamic Contrast-enhanced MR Imaging. *Radiology.* 2015.

87.   Hylton, N.M., Blume, J.D., Bernreuter, W.K., Pisano, E.D., Rosen, M.A., Morris, E.A., Weatherall, P.T., Lehman, C.D., Newstead, G.M. and Polin, S. Locally advanced breast cancer: MR imaging for prediction of response to neoadjuvant chemotherapy—results from ACRIN 6657/I-SPY TRIAL. *Radiology*. 2012, **263**(3), pp.663-672.

88.   Marinovich, M., Sardanelli, F., Ciatto, S., Mamounas, E., Brennan, M., Macaskill, P., Irwig, L., Von Minckwitz, G. and Houssami, N. Early prediction of pathologic response to neoadjuvant therapy in breast cancer: systematic review of the accuracy of MRI. *The Breast*. 2012, **21**(5), pp.669-677.

89.   Reig, B., Heacock, L., Lewin, A., Cho, N. and Moy, L. Role of MRI to assess response to neoadjuvant therapy for breast cancer. *Journal of Magnetic Resonance Imaging*. 2020, **52**(6).

90.   Radiology, A.C.o. *Breast Imaging Reporting and Data System*. [Online]. 2013. [Accessed 15 June]. Available from: https://www.acr.org/-/media/ACR/Files/RADS/BI-RADS/MRI-Reporting.pdf

91.   Kuhl, C.K., Mielcareck, P., Klaschik, S., Leutner, C., Wardelmann, E., Gieseke, J. and Schild, H.H. Dynamic breast MR imaging: are signal intensity time course data useful for differential diagnosis of enhancing lesions? *Radiology*. 1999, **211**(1), pp.101-110.

92.   Woolf, D.K., Padhani, A.R., Taylor, N.J., Gogbashian, A., Li, S.P., Beresford, M.J., Ah-See, M.-L., Stirling, J., Collins, D.J. and Makris, A. Assessing response in breast cancer with dynamic contrast-enhanced magnetic resonance imaging: Are signal intensity–time curves adequate? *Breast Cancer Research and Treatment*. 2014, **147**, pp.335-343.

93.   Navaei-Lavasani, S., Fathi-Kazerooni, A., Saligheh-Rad, H. and Gity, M. Discrimination of benign and malignant suspicious breast tumors based on semi-quantitative DCE-MRI parameters employing support vector machine. *Frontiers in Biomedical Technologies*. 2015, **2**(2), pp.87-92.

94.   Liang, X., Chen, X., Yang, Z., Liao, Y., Wang, M., Li, Y., Fan, W., Dai, Z. and Zhang, Y. Early prediction of pathological complete response to neoadjuvant chemotherapy combining DCE-MRI and apparent diffusion coefficient values in breast Cancer. *BMC Cancer*. 2022, **22**(1), p.1250.

95.   Marino, M.A., Helbich, T., Baltzer, P. and Pinker-Domenig, K. Multiparametric MRI of the breast: A review. *Journal of Magnetic Resonance Imaging*. 2018, **47**(2), pp.301-315.

96.   Tofts, P.S., Brix, G., Buckley, D.L., Evelhoch, J.L., Henderson, E., Knopp, M.V., Larsson, H.B., Lee, T.Y., Mayr, N.A. and Parker, G.J. Estimating kinetic parameters from dynamic contrast-enhanced T1-weighted MRI of a diffusable tracer: standardized quantities and symbols. *Journal of Magnetic Resonance Imaging*. 1999, **10**(3), pp.223-232.

97.   Jena, A., Taneja, S., Singh, A., Negi, P., Mehta, S.B. and Sarin, R. Role of pharmacokinetic parameters derived with high temporal resolution DCE MRI using simultaneous PET/MRI system in breast cancer: a feasibility study. *European Journal of Radiology*. 2017, **86**, pp.261-266.

98. Cheng, Z., Wu, Z., Shi, G., Yi, Z., Xie, M., Zeng, W., Song, C., Zheng, C. and Shen, J. Discrimination between benign and malignant breast lesions using volumetric quantitative dynamic contrast-enhanced MR imaging. *European Radiology*. 2018, **28**, pp.982-991.

99. Ah-See, M.-L.W., Makris, A., Taylor, N.J., Harrison, M., Richman, P.I., Burcombe, R.J., Stirling, J.J., d'Arcy, J.A., Collins, D.J. and Pittam, M.R. Early changes in functional dynamic magnetic resonance imaging predict for pathologic response to neoadjuvant chemotherapy in primary breast cancer. *Clinical Cancer Research*. 2008, **14**(20), pp.6580-6589.

100. Pickles, M.D., Lowry, M., Manton, D.J., Gibbs, P. and Turnbull, L.W. Role of dynamic contrast enhanced MRI in monitoring early response of locally advanced breast cancer to neoadjuvant chemotherapy. *Breast Cancer Research Treatment*. 2005, **91**, pp.1-10.

101. Dogan, B.E., Yuan, Q., Bassett, R., Guvenc, I., Jackson, E.F., Cristofanilli, M. and Whitman, G.J. Comparing the performances of magnetic resonance imaging size vs pharmacokinetic parameters to predict response to neoadjuvant chemotherapy and survival in patients with breast cancer. *Current Problems in Diagnostic Radiology*. 2019, **48**(3), pp.235-240.

102. Li, X., Arlinghaus, L.R., Ayers, G.D., Chakravarthy, A.B., Abramson, R.G., Abramson, V.G., Atuegwu, N., Farley, J., Mayer, I.A. and Kelley, M.C. DCE-MRI analysis methods for predicting the response of breast cancer to neoadjuvant chemotherapy: Pilot study findings. *Magnetic Resonance in Medicine*. 2014, **71**(4), pp.1592-1602.

103. Kontopodis, E., Venianaki, M., Manikis, G.C., Nikiforaki, K., Salvetti, O., Papadaki, E., Papadakis, G.Z., Karantanas, A.H. and Marias, K. Investigating the role of model-based and model-free imaging biomarkers as early predictors of neoadjuvant breast cancer therapy outcome. *IEEE Journal of Biomedical Health Informatics*. 2019, **23**(5), pp.1834-1843.

104. Jun, W., Cong, W., Xianxin, X. and Daqing, J. Meta-Analysis of Quantitative Dynamic Contrast-Enhanced MRI for the Assessment of Neoadjuvant Chemotherapy in Breast Cancer. *American Surgeon*. 2019, **85**(6).

105. Alonzi, R., Taylor, N.J., Stirling, J.J., d'Arcy, J.A., Collins, D.J., Saunders, M.I., Hoskin, P.J. and Padhani, A.R. Reproducibility and correlation between quantitative and semiquantitative dynamic and intrinsic susceptibility-weighted MRI parameters in the benign and malignant human prostate. *Journal of Magnetic Resonance Imaging*. 2010, **1**(32), pp.155-164.

106. Jackson, A., Jayson, G., Li, K., Zhu, X., Checkley, D., Tessier, J. and Waterton, J. Reproducibility of quantitative dynamic contrast-enhanced MRI in newly presenting glioma. *The British Journal of Radiology*. 2003, **76**(903), pp.153-162.

107. Galbraith, S.M., Lodge, M.A., Taylor, N.J., Rustin, G.J., Bentzen, S., Stirling, J.J. and Padhani, A.R. Reproducibility of dynamic contrast-enhanced MRI in human muscle and tumours: comparison of quantitative and semi-quantitative analysis. *NMR in Biomedicine*. 2002, **15**(2), pp.132-142.

108. Wang, H., Su, Z., Ye, H., Xu, X., Sun, Z., Li, L., Duan, F., Song, Y., Lambrou, T. and Ma, L. Reproducibility of dynamic contrast-enhanced MRI in renal cell

carcinoma: A prospective analysis on intra-and interobserver and scan-rescan performance of pharmacokinetic parameters. *Medicine*. 2015, **94**(37), p.e1529.

109. Kershaw, L.E., Hutchinson, C.E. and Buckley, D.L. Benign prostatic hyperplasia: Evaluation of T1, T2, and microvascular characteristics with T1-weighted dynamic contrast-enhanced MRI. *Journal of Magnetic Resonance Imaging*. 2009, **29**(3), pp.641-648.

110. Kanda, T., Ishii, K., Kawaguchi, H., Kitajima, K. and Takenaka, D. High signal intensity in the dentate nucleus and globus pallidus on unenhanced T1-weighted MR images: relationship with increasing cumulative dose of a gadolinium-based contrast material. *Radiology*. 2014, **270**(3), pp.834-841.

111. Sardanelli, F., Cozzi, A., Trimboli, R.M. and Schiaffino, S. Gadolinium retention and breast MRI screening: more harm than good? *American Journal of Roentgenology*. 2020, **214**(2), pp.324-327.

112. Woodhams, R., Ramadan, S., Stanwell, P., Sakamoto, S., Hata, H., Ozaki, M., Kan, S. and Inoue, Y. Diffusion-weighted imaging of the breast: principles and clinical applications. *Radiographics*. 2011, **31**(4), pp.1059-1084.

113. Stejskal, E.O. and Tanner, J.E. Spin diffusion measurements: spin echoes in the presence of a time-dependent field gradient. *The Journal of Chemical Physics*. 1965, **42**(1), pp.288-292.

114. Guo, Y., Cai, Y.Q., Cai, Z.L., Gao, Y.G., An, N.Y., Ma, L., Mahankali, S. and Gao, J.H. Differentiation of clinically benign and malignant breast lesions using diffusion-weighted imaging. *Journal of Magnetic Resonance Imaging*. 2002, **16**(2), pp.172-178.

115. Sinha, S., Lucas-Quesada, F.A., Sinha, U., DeBruhl, N. and Bassett, L.W. In vivo diffusion-weighted MRI of the breast: potential for lesion characterization. *Journal of Magnetic Resonance Imaging*. 2002, **15**(6), pp.693-704.

116. Kim, Y., Ko, K., Kim, D., Min, C., Kim, S.G., Joo, J. and Park, B. Intravoxel incoherent motion diffusion-weighted MR imaging of breast cancer: association with histopathological features and subtypes. *The British Journal of Radiology*. 2016, **89**(1063), p.20160140.

117. Chu, W., Jin, W., Liu, D., Wang, J., Geng, C., Chen, L. and Huang, X. Diffusion-weighted imaging in identifying breast cancer pathological response to neoadjuvant chemotherapy: A meta-analysis. *Oncotarget*. 2018, **9**(6), p.7088.

118. Rajan, R., Poniecka, A., Smith, T., Yang, Y., Frye, D., Pusztai, L., Fiterman, D., Gal-Gombos, E., Whitman, G. and Rouzier, R. Change in tumor cellularity of breast carcinoma after neoadjuvant chemotherapy as a variable in the pathologic assessment of response. *Cancer*. 2004, **100**(7), pp.1365-1373.

119. Fowler, A.M., Mankoff, D.A. and Joe, B.N. Imaging Neoadjuvant Therapy Response in Breast Cancer. *Radiology*. 2017.

120. Sharma, U., Danishad, K., Seenu, V. and Jagannathan, N. Longitudinal study of the assessment by MRI and diffusion-weighted imaging of tumor response in patients with locally advanced breast cancer undergoing neoadjuvant chemotherapy. *NMR in Biomedicine*. 2009, **22**(1), pp.104-113.

121. Pickles, M.D., Gibbs, P., Lowry, M. and Turnbull, L.W. Diffusion changes precede size reduction in neoadjuvant treatment of breast cancer. *Magnetic Resonance Imaging*. 2006, **24**(7), pp.843-847.

122. Pereira, N.P., Curi, C., Osório, C.A., Marques, E.F., Makdissi, F.B., Pinker, K. and Bitencourt, A.G. Diffusion-weighted magnetic resonance imaging of patients with breast cancer following neoadjuvant chemotherapy provides early prediction of pathological response–a prospective study. *Scientific Reports*. 2019, **9**(1), p.16372.

123. Hu, X.-Y., Li, Y., Jin, G.-Q., Lai, S.-L., Huang, X.-Y. and Su, D.-K. Diffusion-weighted MR imaging in prediction of response to neoadjuvant chemotherapy in patients with breast cancer. *Oncotarget*. 2017, **8**(45), p.79642.

124. Park, S.H., Moon, W.K., Cho, N., Chang, J.M., Im, S.-A., Park, I.A., Kang, K.W., Han, W. and Noh, D.-Y. Comparison of diffusion-weighted MR imaging and FDG PET/CT to predict pathological complete response to neoadjuvant chemotherapy in patients with breast cancer. *European Radiology*. 2012, **22**, pp.18-25.

125. Almutlaq, Z.M., Wilson, D.J., Bacon, S.E., Sharma, N., Stephens, S., Dondo, T. and Buckley, D.L. Evaluation of monoexponential, stretched-exponential and intravoxel incoherent motion MRI diffusion models in early response monitoring to neoadjuvant chemotherapy in patients with breast cancer—A preliminary study. *Journal of Magnetic Resonance Imaging*. 2022, **56**(4), pp.1079-1088.

126. Sigmund, E., Cho, G., Kim, S., Finn, M., Moccaldi, M., Jensen, J., Sodickson, D., Goldberg, J., Formenti, S. and Moy, L. Intravoxel incoherent motion imaging of tumor microenvironment in locally advanced breast cancer. *Magnetic Resonance in Medicine*. 2011, **65**(5), pp.1437-1447.

127. Le Bihan, D., Breton, E., Lallemand, D., Aubin, M., Vignaud, J. and Laval-Jeantet, M. Separation of diffusion and perfusion in intravoxel incoherent motion MR imaging. *Radiology*. 1988, **168**(2), pp.497-505.

128. Le Bihan, D., Turner, R., Moonen, C.T. and Pekar, J. Imaging of diffusion and microcirculation with gradient sensitization: design, strategy, and significance. *Journal of Magnetic Resonance Imaging*. 1991, **1**(1), pp.7-28.

129. Koh, D.-M., Collins, D.J. and Orton, M.R. Intravoxel incoherent motion in body diffusion-weighted MRI: reality and challenges. *American Journal of Roentgenology*. 2011, **196**(6), pp.1351-1361.

130. Bokacheva, L., Kaplan, J.B., Giri, D.D., Patil, S., Gnanasigamani, M., Nyman, C.G., Deasy, J.O., Morris, E.A. and Thakur, S. Intravoxel incoherent motion diffusion-weighted MRI at 3.0 T differentiates malignant breast lesions from benign lesions and breast parenchyma. *Journal of Magnetic Resonance Imaging*. 2014, **40**(4), pp.813-823.

131. Lin, N., Chen, J., Hua, J., Zhao, J., Zhao, J. and Lu, J. Intravoxel incoherent motion MR imaging in breast cancer: quantitative analysis for characterizing lesions. *International Journal of Clinical and Experimental Medicine*. 2017, **10**(1), pp.1705-1714.

132. Ma, D., Lu, F., Zou, X., Zhang, H., Li, Y., Zhang, L., Chen, L., Qin, D. and Wang, B. Intravoxel incoherent motion diffusion-weighted imaging as an adjunct to dynamic contrast-enhanced MRI to improve accuracy of the differential diagnosis of benign and malignant breast lesions. *Magnetic Resonance Imaging*. 2017, **36**, pp.175-179.

133. Xu, W., Zheng, B. and Li, H. Identification of the benignity and malignancy of BI-RADS 4 breast lesions based on a combined quantitative model of dynamic contrast-enhanced MRI and Intravoxel Incoherent Motion. *Tomography*. 2022, **8**(6), pp.2676-2686.

134. Cho, G.Y., Moy, L., Kim, S.G., Baete, S.H., Moccaldi, M., Babb, J.S., Sodickson, D.K. and Sigmund, E. Evaluation of breast cancer using intravoxel incoherent motion (IVIM) histogram analysis: comparison with malignant status, histological subtype, and molecular prognostic factors. *European Radiology*. 2016, **26**(8), pp.2547-2558.

135. Suo, S., Cheng, F., Cao, M., Kang, J., Wang, M., Hua, J., Hua, X., Li, L., Lu, Q. and Liu, J. Multiparametric diffusion-weighted imaging in breast lesions: Association with pathologic diagnosis and prognostic factors. *Journal of Magnetic Resonance Imaging*. 2017, **46**(3), p.740.

136. Ertas, G., Onaygil, C., Akin, Y., Kaya, H. and Aribal, E. Quantitative differentiation of breast lesions at 3T diffusion-weighted imaging (DWI) using the ratio of distributed diffusion coefficient (DDC). *Journal of Magnetic Resonance Imaging*. 2016, **44**(6), pp.1633-1641.

137. Jin, Y.N., Zhang, Y., Cheng, J.L., Zheng, D.D. and Hu, Y. Monoexponential, Biexponential, and stretched-exponential models using diffusion-weighted imaging: A quantitative differentiation of breast lesions at 3.0 T. *Journal of Magnetic Resonance Imaging*. 2019, **50**(5), pp.1461-1467.

138. Chen, B.-Y., Xie, Z., Nie, P., Yang, D., Hu, Y.-C., Liu, S.-T., Bao, G.-Q., Feng, J. and Yu, J. Multiple b-value diffusion-weighted imaging in differentiating benign from malignant breast lesions: comparison of conventional mono-, bi-and stretched exponential models. *Clinical Radiology*. 2020, **75**(8), pp.642. e641-642. e648.

139. Cho, G.Y., Gennaro, L., Sutton, E.J., Zabor, E.C., Zhang, Z., Giri, D., Moy, L., Sodickson, D.K., Morris, E.A., Sigmund, E.E. and Thakur, S.B. Intravoxel incoherent motion (IVIM) histogram biomarkers for prediction of neoadjuvant treatment response in breast cancer patients. *European Journal of Radiology Open*. 2017, **4**, pp.101-107.

140. Kim, Y., Kim, S.H., Lee, H.W., Song, B.J., Kang, B.J., Lee, A. and Nam, Y. Intravoxel incoherent motion diffusion-weighted MRI for predicting response to neoadjuvant chemotherapy in breast cancer. *Magnetic Resonance Imaging*. 2018, **48**, pp.27-33.

141. Suo, S., Yin, Y., Geng, X., Zhang, D., Hua, J., Cheng, F., Chen, J., Zhuang, Z., Cao, M. and Xu, J. Diffusion-weighted MRI for predicting pathologic response to neoadjuvant chemotherapy in breast cancer: evaluation with mono-, bi-, and stretched-exponential models. *Journal of Translational Medicine*. 2021, **19**(1), p.236.

142. Newitt, D.C., Zhang, Z., Gibbs, J.E., Partridge, S.C., Chenevert, T.L., Rosen, M.A., Bolan, P.J., Marques, H.S., Aliu, S. and Li, W. Test–retest repeatability and reproducibility of ADC measures by breast DWI: Results from the ACRIN 6698 trial. *Journal of Magnetic Resonance Imaging*. 2019, **49**(6), pp.1617-1628.

143. Iima, M., Kataoka, M., Kanao, S., Kawai, M., Onishi, N., Koyasu, S., Murata, K., Ohashi, A., Sakaguchi, R. and Togashi, K. Variability of non-Gaussian diffusion MRI and intravoxel incoherent motion (IVIM) measurements in the breast. *PloS One*. 2018, **13**(3), p.e0193444.

144. Kakite, S., Dyvorne, H., Besa, C., Cooper, N., Facciuto, M., Donnerhack, C. and Taouli, B. Hepatocellular carcinoma: short-term reproducibility of apparent diffusion coefficient and intravoxel incoherent motion parameters at 3.0 T. *Journal of Magnetic Resonance Imaging*. 2015, **41**(1), pp.149-156.

145. Lee, Y., Lee, S.S., Kim, N., Kim, E., Kim, Y.J., Yun, S.-C., Kühn, B., Kim, I.S., Park, S.H. and Kim, S.Y. Intravoxel incoherent motion diffusion-weighted MR imaging of the liver: effect of triggering methods on regional variability and measurement repeatability of quantitative parameters. *Radiology*. 2015, **274**(2), pp.405-415.

146. Sigmund, E.E., Vivier, P.-H., Sui, D., Lamparello, N.A., Tantillo, K., Mikheev, A., Rusinek, H., Babb, J.S., Storey, P. and Lee, V.S. Intravoxel incoherent motion and diffusion-tensor imaging in renal tissue under hydration and furosemide flow challenges. *Radiology*. 2012, **263**(3), pp.758-769.

147. Jakab, A., Tuura, R., Kottke, R., Kellenberger, C.J. and Scheer, I. Intra-voxel incoherent motion MRI of the living human foetus: technique and test–retest repeatability. *European Radiology Experimental*. 2017, **1**(1), p.26.

148. Jerome, N.P., Miyazaki, K., Collins, D.J., Orton, M.R., d'Arcy, J.A., Wallace, T., Moreno, L., Pearson, A.D., Marshall, L.V. and Carceller, F. Repeatability of derived parameters from histograms following non-Gaussian diffusion modelling of diffusion-weighted imaging in a paediatric oncological cohort. *European Radiology*. 2017, **27**, pp.345-353.

149. Reischauer, C., Patzwahl, R., Koh, D.-M., Froehlich, J.M. and Gutzeit, A. Non-mono-exponential analysis of diffusion-weighted imaging for treatment monitoring in prostate cancer bone metastases. *Scientific Reports*. 2017, **7**(1), pp.1-10.

150. Pan, J., Zhang, H., Man, F., Shen, Y., Wang, Y., Zhong, Y., Ma, L., Wang, H. and Ye, H. Measurement and scan reproducibility of parameters of intravoxel incoherent motion in renal tumor and normal renal parenchyma: a preliminary research at 3.0 T MR. *Abdominal Radiology*. 2018, **43**, pp.1739-1748.

151. Sourbron, S.P. and Buckley, D.L. On the scope and interpretation of the Tofts models for DCE-MRI. *Magnetic Resonance in Medicine*. 2011, **66**(3), pp.735-745.

152. Nougaret, S., Vargas, H.A., Lakhman, Y., Sudre, R., Do, R.K., Bibeau, F., Azria, D., Assenat, E., Molinari, N. and Pierredon, M.-A. Intravoxel incoherent motion–derived histogram metrics for assessment of response after combined chemotherapy and radiation therapy in rectal cancer: initial experience and

comparison between single-section and volumetric analyses. *Radiology*. 2016, **280**(2), pp.446-454.

153. Han, M., Kim, S.Y., Lee, S.J. and Choi, J.W. The correlations between MRI perfusion, diffusion parameters, and 18F-FDG PET metabolic parameters in primary head-and-neck cancer: a cross-sectional analysis in single institute. *Medicine*. 2015, **94**(47).

154. Iima, M., Kataoka, M., Le Bihan, D., Umehana, M., Imakita, T., Nakagawa, M., Kanao, S., Yano, K., Feiweier, T. and Togashi, K. Potential of perfusion imaging with IVIM MRI in breast cancer. In: *Proceedings of the 21st Annual Meeting of ISMRM, Salt Lake City*, 2013.

155. Nilsen, L.B., Fangberget, A., Geier, O. and Seierstad, T. Quantitative analysis of diffusion-weighted magnetic resonance imaging in malignant breast lesions using different b value combinations. *European Radiology*. 2013, **23**(4), pp.1027-1033.

156. Suo, S., Lin, N., Wang, H., Zhang, L., Wang, R., Zhang, S., Hua, J. and Xu, J. Intravoxel incoherent motion diffusion-weighted MR imaging of breast cancer at 3.0 tesla: comparison of different curve-fitting methods. *Journal of Magnetic Resonance Imaging*. 2015, **42**(2), pp.362-370.

157. Dyvorne, H., Jajamovich, G., Kakite, S., Kuehn, B. and Taouli, B. Intravoxel incoherent motion diffusion imaging of the liver: optimal b-value subsampling and impact on parameter precision and reproducibility. *European Journal of Radiology*. 2014, **83**(12), pp.2109-2113.

158. Lecler, A., Savatovsky, J., Balvay, D., Zmuda, M., Sadik, J.-C., Galatoire, O., Charbonneau, F., Bergès, O., Picard, H. and Fournier, L. Repeatability of apparent diffusion coefficient and intravoxel incoherent motion parameters at 3.0 Tesla in orbital lesions. *European Radiology*. 2017, **27**, pp.5094-5103.

159. Park, H.J., Sung, Y.S., Lee, S.S., Lee, Y., Cheong, H., Kim, Y.J. and Lee, M.g. Intravoxel incoherent motion diffusion-weighted MRI of the abdomen: The effect of fitting algorithms on the accuracy and reliability of the parameters. *Journal of Magnetic Resonance Imaging*. 2017, **45**(6), pp.1637-1647.

160. Cho, G.Y., Moy, L., Zhang, J.L., Baete, S., Lattanzi, R., Moccaldi, M., Babb, J.S., Kim, S., Sodickson, D.K. and Sigmund, E.E. Comparison of fitting methods and b-value sampling strategies for intravoxel incoherent motion in breast cancer. *Magnetic Resonance in Medicine*. 2015, **74**(4), pp.1077-1085.

161. Shukla-Dave, A., Obuchowski, N.A., Chenevert, T.L., Jambawalikar, S., Schwartz, L.H., Malyarenko, D., Huang, W., Noworolski, S.M., Young, R.J. and Shiroishi, M.S. Quantitative imaging biomarkers alliance (QIBA) recommendations for improved precision of DWI and DCE-MRI derived biomarkers in multicenter oncology trials. *Journal of Magnetic Resonance Imaging*. 2019, **49**(7), pp.e101-e121.

162. Pekar, J., Moonen, C.T. and van Zijl, P.C. On the precision of diffusion/perfusion imaging by gradient sensitization. *Magnetic Resonance in Medicine*. 1992, **23**(1), pp.122-129.

163. Lee, J.H., Cheong, H., Lee, S.S., Lee, C.K., Sung, Y.S., Huh, J.-W., Song, J.-A. and Choe, H. Perfusion assessment using intravoxel incoherent motion-based

analysis of diffusion-weighted magnetic resonance imaging: validation through phantom experiments. *Investigative Radiology*. 2016, **51**(8), pp.520-528.

164. Heusch, P., Wittsack, H.-J., Pentang, G., Buchbender, C., Miese, F., Schek, J., Kröpil, P., Antoch, G. and Lanzman, R.S. Biexponential analysis of diffusion-weighted imaging: comparison of three different calculation methods in transplanted kidneys. *Acta Radiologica*. 2013, **54**(10), pp.1210-1217.

165. Le Bihan, D. Intravoxel incoherent motion perfusion MR imaging: a wake-up call. *Radiology*. 2008, **249**(3), pp.748-752.

166. Han, X., Li, J. and Wang, X. Comparison and optimization of 3.0 T breast images quality of diffusion-weighted imaging with multiple b-values. *Academic Radiology*. 2017, **24**(4), pp.418-425.

167. Jalnefjord, O., Andersson, M., Montelius, M., Starck, G., Elf, A.-K., Johanson, V., Svensson, J. and Ljungberg, M. Comparison of methods for estimation of the intravoxel incoherent motion (IVIM) diffusion coefficient (D) and perfusion fraction (f). *Magnetic Resonance Materials in Physics, Biology and Medicine*. 2018, **31**, pp.715-723.

168. Iima, M., Partridge, S.C. and Le Bihan, D. Six DWI questions you always wanted to know but were afraid to ask: clinical relevance for breast diffusion MRI. *European Radiology*. 2020, **30**, pp.2561–2570.

169. Stevens, W., Farrow, I.M., Georgiou, L., Hanby, A.M., Perren, T.J., Windel, L.M., Wilson, D.J., Sharma, N., Dodwell, D. and Hughes, T.A. Breast tumour volume and blood flow measured by MRI after one cycle of epirubicin and cyclophosphamide-based neoadjuvant chemotherapy as predictors of pathological response. *The British Journal of Radiology*. 2021, **94**, p.20201396.

170. Koo, T.K. and Li, M.Y. A guideline of selecting and reporting intraclass correlation coefficients for reliability research. *Journal of Chiropractic Medicine*. 2016, **15**(2), pp.155-163.

171. Overholser, B.R. and Sowinski, K.M. Biostatistics primer: part 2. *Nutrition in Clinical Practice*. 2008, **23**(1), pp.76-84.

172. Surov, A., Wienke, A. and Meyer, H.J. Pretreatment apparent diffusion coefficient does not predict therapy response to neoadjuvant chemotherapy in breast cancer. *The Breast*. 2020, **53**, pp.59-67.

173. Park, S.H., Moon, W.K., Cho, N., Song, I.C., Chang, J.M., Park, I.-A., Han, W. and Noh, D.-Y. Diffusion-weighted MR imaging: pretreatment prediction of response to neoadjuvant chemotherapy in patients with breast cancer. *Radiology*. 2010, **257**(1), pp.56-63.

174. Li, X., Abramson, R.G., Arlinghaus, L.R., Kang, H., Chakravarthy, A.B., Abramson, V.G., Farley, J., Mayer, I.A., Kelley, M.C. and Meszoely, I.M. Multiparametric magnetic resonance imaging for predicting pathological response after the first cycle of neoadjuvant chemotherapy in breast cancer. *Investigative Radiology*. 2015, **50**(4), pp.195-204.

175. Partridge, S.C. and McDonald, E.S. Diffusion weighted MRI of the breast: Protocol optimization, guidelines for interpretation, and potential clinical applications. *Magnetic Resonance Imaging Clinics of North America*. 2013, **21**(3), p.601.

176. Lee, H.J., Rha, S.Y., Chung, Y.E., Shim, H.S., Kim, Y.J., Hur, J., Hong, Y.J. and Choi, B.W. Tumor perfusion-related parameter of diffusion-weighted magnetic resonance imaging: Correlation with histological microvessel density. *Magnetic Resonance in Medicine*. 2014, **71**(4), pp.1554-1558.

177. Hasan, J., Byers, R. and Jayson, G.C. Intra-tumoural microvessel density in human solid tumours. *British Journal of Cancer*. 2002, **86**(10), pp.1566-1577.

178. Zhang, J., Gao, S., Zheng, Q., Kang, Y., Li, J., Zhang, S., Shang, C., Tan, X., Ren, W. and Ma, Y. A Novel Model Incorporating Tumor Stiffness, Blood Flow Characteristics, and Ki-67 Expression to Predict Responses After Neoadjuvant Chemotherapy in Breast Cancer. *Frontiers in Oncology*. 2020, **10**, p.2750.

179. Kwee, T.C., Galbán, C.J., Tsien, C., Junck, L., Sundgren, P.C., Ivancevic, M.K., Johnson, T.D., Meyer, C.R., Rehemtulla, A. and Ross, B.D. Comparison of apparent diffusion coefficients and distributed diffusion coefficients in high-grade gliomas. *Journal of Magnetic Resonance Imaging*. 2010, **31**(3), pp.531-537.

180. Liang, C.-Y., Chen, M.-D., Zhao, X.-X., Yan, C.-G., Mei, Y.-J. and Xu, Y.-K. Multiple mathematical models of diffusion-weighted magnetic resonance imaging combined with prognostic factors for assessing the response to neoadjuvant chemotherapy and radiation therapy in locally advanced rectal cancer. *European Journal of Radiology*. 2019, **110**, pp.249-255.

181. Orton, M.R., Messiou, C., Collins, D., Morgan, V.A., Tessier, J., Young, H., Desouza, N. and Leach, M.O. Diffusion-weighted MR imaging of metastatic abdominal and pelvic tumours is sensitive to early changes induced by a VEGF inhibitor using alternative diffusion attenuation models. *European Radiology*. 2016, **26**(5), pp.1412-1419.

182. Moore, M.J. Clinical pharmacokinetics of cyclophosphamide. *Clinical Pharmacokinetics*. 1991, **20**(3), pp.194-208.

183. Georgiou, L., Wilson, D.J., Sharma, N., Perren, T.J. and Buckley, D.L. A functional form for a representative individual arterial input function measured from a population using high temporal resolution DCE MRI. *Magnetic Resonance in Medicine*. 2019, **81**(3), pp.1955-1963.

184. Cron, G.O., Santyr, G. and Kelcz, F. Accurate and rapid quantitative dynamic contrast-enhanced breast MR imaging using spoiled gradient-recalled echoes and bookend T1 measurements. *Magnetic Resonance in Medicine*. 1999, **42**(4), pp.746-753.

185. Brix, G., Schad, L.R., Deimling, M. and Lorenz, W.J. Fast and precise T1 imaging using a TOMROP sequence. *Magnetic Resonance Imaging*. 1990, **8**(4), pp.351-356.

186. Kershaw, L.E. *Measuring microvascular physiology using quantitative magnetic resonance imaging*. Ph.D. thesis, University of Manchester, 2008.

187. Sourbron, S.P. and Buckley, D.L. Classic models for dynamic contrast-enhanced MRI. *NMR in Biomedicine*. 2013, **26**(8), pp.1004-1027.

188. Buckley, D.L. Shutter-speed dynamic contrast-enhanced MRI: Is it fit for purpose? *Magnetic Resonance in Medicine*. 2019, **81**(2), pp.976-988.

189. Glatting, G., Kletting, P., Reske, S.N., Hohl, K. and Ring, C. Choosing the optimal fit function: comparison of the Akaike information criterion and the F-test. *Medical Physics*. 2007, **34**(11), pp.4285-4292.

190. Bland, J.M. and Altman, D.G. Calculating correlation coefficients with repeated observations: Part 2—Correlation between subjects. *BMJ*. 1995, **310**(6980), p.633.

191. Bakdash, J.Z. and Marusich, L.R. Repeated measures correlation. *Frontiers in Psychology*. 2017, **8**, p.456.

192. Marusich, L.R. and Bakdash, J.Z. rmcorrShiny: A web and standalone application for repeated measures correlation [version 1; peer review: 2 approved]. *F1000Research*. 2021, **10**, p.697.

193. Specht, J.M., Kurland, B.F., Montgomery, S.K., Dunnwald, L.K., Doot, R.K., Gralow, J.R., Ellis, G.K., Linden, H.M., Livingston, R.B. and Allison, K.H. Tumor Metabolism and Blood Flow as Assessed by Positron Emission Tomography Varies by Tumor Subtype in Locally Advanced Breast Cancer. *Clinical Cancer Research*. 2010, **16**(10), pp.2803-2810.

194. Henkelman, R.M. Does IVIM measure classical perfusion? *Magnetic Resonance in Medicine*. 1990, **16**(3), pp.470-475.

195. Zhang, X., Ingo, C., Teeuwisse, W.M., Chen, Z. and van Osch, M.J. Comparison of perfusion signal acquired by arterial spin labeling–prepared intravoxel incoherent motion (IVIM) MRI and conventional IVIM MRI to unravel the origin of the IVIM signal. *Magnetic Resonance in Medicine*. 2018, **79**(2), pp.723-729.

196. Chikui, T., Ohga, M., Kami, Y., Togao, O., Kawano, S., Kiyoshima, T. and Yoshiura, K. Correlation between diffusion-weighted image-derived parameters and dynamic contrast-enhanced magnetic resonance imaging-derived parameters in the orofacial region. *Acta Radiologica Open*. 2024, **13**(3), pp.20584601241244777-20584601241244777.

197. Aryal, M.P., Nagaraja, T.N., Keenan, K.A., Bagher-Ebadian, H., Panda, S., Brown, S.L., Cabral, G., Fenstermacher, J.D. and Ewing, J.R. Dynamic contrast enhanced MRI parameters and tumor cellularity in a rat model of cerebral glioma at 7 T. *Magnetic Resonance in Medicine*. 2014, **71**(6), pp.2206-2214.

198. Meng, L., Zhao, X., Guo, J., Lu, L., Cheng, M., Xing, Q., Shang, H., Wang, K., Zhang, B. and Lei, D. Evaluation of the differentiation of benign and malignant breast lesions using synthetic relaxometry and the Kaiser score. *Frontiers in Oncology*. 2022, **12**.

199. Iima, M., Kataoka, M., Kanao, S., Onishi, N., Kawai, M., Ohashi, A., Sakaguchi, R., Toi, M. and Togashi, K. Intravoxel incoherent motion and quantitative non-Gaussian diffusion MR imaging: evaluation of the diagnostic and prognostic value of several markers of malignant and benign breast lesions. *Radiology*. 2018, **287**(2), pp.432-441.

200. Baxter, G.C., Patterson, A.J., Woitek, R., Allajbeu, I., Graves, M.J. and Gilbert, F. Improving the image quality of DWI in breast cancer: comparison of multi-shot DWI using multiplexed sensitivity encoding to conventional single-shot echo-planar imaging DWI. *The British Journal of Radiology*. 2021, **94**(1119), p.20200427.

Appendix

NHS
Health Research Authority
NRES Committee Yorkshire & The Humber - Bradford Leeds

Jarrow Business Centre
Jarrow REC Centre
Room 001
Rolling Mill Road
Jarrow
NE32 3DT

Telephone: 0191 428 3565

28 May 2015

Professor David Buckley
Professor of Medical Physics
University of Leeds
Division of Biomedical Imaging
Room 8.001, Level 8, Worsley Building
Clarendon Way
Leeds LS2 9JT

Dear Professor Buckley

Study title:	**CHERNAC: characterising early response to neoadjuvant chemotherapy with quantitative breast MRI**
REC reference:	15/YH/0246
IRAS project ID:	173435

The Research Ethics Committee reviewed the above application at the meeting held on 19 May 2015. Thank you for attending to discuss the application.

We plan to publish your research summary wording for the above study on the HRA website, together with your contact details. Publication will be no earlier than three months from the date of this favourable opinion letter. The expectation is that this information will be published for all studies that receive an ethical opinion but should you wish to provide a substitute contact point, wish to make a request to defer, or require further information, please contact the REC Manager Ms Gillian Mayer, nrescommittee.yorkandhumber-bradfordleeds@nhs.net. Under very limited circumstances (e.g. for student research which has received an unfavourable opinion), it may be possible to grant an exemption to the publication of the study.

Ethical opinion

The members of the Committee present gave a **Favourable** ethical opinion of the above research on the basis described in the application form, protocol and supporting documentation, subject to the conditions specified below. .

Conditions of the favourable opinion

The favourable opinion is subject to the following conditions being met prior to the start of the study.

Additional conditions specified by the REC

1. The participant information sheet to be revised as follows –

    a.   Reproducibility study: NACT needs to be explained – 'Neo-Adjuvant chemotherapy which is a type of treatment to reduce the size of tumours during surgery' (page 1).

    b.   Section 6 - Remove the word 'in' from the following sentence - You will need to undertake an additional MRI scan and stay in the MRI scanner for a little longer (in) during 2 visits.

Recommendation: the title of the participant information sheet and consent form to be revised to a simpler version for easy understanding.

You should notify the REC in writing once all conditions have been met (except for site approvals from host organisations) and provide copies of any revised documentation with updated version numbers. The REC will acknowledge receipt and provide a final list of the approved documentation for the study, which can be made available to host organisations to facilitate their permission for the study. Failure to provide the final versions to the REC may cause delay in obtaining permissions.

Management permission or approval must be obtained from each host organisation prior to the start of the study at the site concerned.

Management permission ("R&D approval") should be sought from all NHS organisations involved in the study in accordance with NHS research governance arrangements.

Guidance on applying for NHS permission for research is available in the Integrated Research Application System or at http://www.rdforum.nhs.uk.

Where a NHS organisation's role in the study is limited to identifying and referring potential participants to research sites ("participant identification centre"), guidance should be sought from the R&D office on the information it requires to give permission for this activity.

For non-NHS sites, site management permission should be obtained in accordance with the procedures of the relevant host organisation.

Sponsors are not required to notify the Committee of approvals from host organisations.

Registration of Clinical Trials

All clinical trials (defined as the first four categories on the IRAS filter page) must be registered on a publically accessible database. This should be before the first participant is recruited but no later than 6 weeks after recruitment of the first participant.

There is no requirement to separately notify the REC but you should do so at the earliest opportunity e.g. when submitting an amendment. We will audit the registration details as part of the annual progress reporting process.

To ensure transparency in research, we strongly recommend that all research is registered but for non-clinical trials this is not currently mandatory.

If a sponsor wishes to request a deferral for study registration within the required timeframe, they should contact hra.studyregistration@nhs.net. The expectation is that all clinical trials will be registered, however, in exceptional circumstances non registration may be

permissible with prior agreement from NRES. Guidance on where to register is provided on the HRA website.

It is the responsibility of the sponsor to ensure that all the conditions are complied with before the start of the study or its initiation at a particular site (as applicable).

Ethical review of research sites

NHS Sites

The favourable opinion applies to all NHS sites taking part in the study taking part in the study, subject to management permission being obtained from the NHS/HSC R&D office prior to the start of the study (see "Conditions of the favourable opinion" below). No non-NHS sites were included in the application, however if you decide to include a non-NHS site in the future, then an application for Site Specific Assessment would need to be submitted for ethical approval.

Summary of discussion at the meeting

It was noted that members had enjoyed reading this interesting project.

Social or scientific value; scientific design and conduct of the study

The Committee noted that participants would be given the option to be included in the biopsy and additional blood sample tests and it was queried if it would be simpler and more practical to ask participants simply to adopt the whole package.

You informed the Committee that this issue had been discussed at length within the clinical and research team and it was decided to give participants the opportunity to choose which part of the study they wished to be involved in.

The Committee noted the importance of ensuring that all the study procedures would be robust and well considered.

The Committee asked about the additional blood samples and biopsies and the necessity to opt in/opt out of these.

You stated that it was considered appropriate to include the option in the additional tissue/biopsy forms and include a statement in the consent form to agree to future use of the samples in research (as suggested by the pathologists) and this would also correspond with the information in the application form.

Informed consent process and the adequacy and completeness of participant information

It was noted that the title on the participant information sheet and consent needs to be simplified so it is more meaningful for the participants.

You acknowledged this.

Other general comments

The Committee considered the application had been well presented.

You stated that you had tried to submit a good application although it had been a time consuming process. You noted that the radiation section had been completed but confirmed this was part of routine care.

Approved documents

The documents reviewed and approved at the meeting were:

Document	Version	Date
Evidence of Sponsor insurance or indemnity (non-NHS Sponsors only)	NHE-03CA02-0013	17 September 2014
Letter from funder	L. Wilde	13 June 2013
Letter from sponsor	J. Uniacke	06 May 2015
Participant consent form [CF]	1.0	01 May 2015
Participant consent form [Sub-study CF]	1.0	01 May 2015
Participant information sheet (PIS) [PIS]	1.0	01 May 2015
Participant information sheet (PIS) [Sub-study PIS]	1.0	01 May 2015
REC Application Form [REC_Form_08052015]		08 May 2015
Referee's report or other scientific critique report		
Research protocol or project proposal	1.0	01 May 2015
Summary CV for Chief Investigator (CI)	D. Buckley	

Membership of the Committee

The members of the Ethics Committee who were present at the meeting are listed on the attached sheet.

After ethical review

Reporting requirements

The attached document "After ethical review – guidance for researchers" gives detailed guidance on reporting requirements for studies with a favourable opinion, including:

- Notifying substantial amendments
- Adding new sites and investigators
- Notification of serious breaches of the protocol
- Progress and safety reports
- Notifying the end of the study

The HRA website also provides guidance on these topics, which is updated in the light of changes in reporting requirements or procedures.

User Feedback

The Health Research Authority is continually striving to provide a high quality service to all applicants and sponsors. You are invited to give your view of the service you have received and the application procedure. If you wish to make your views known please use the feedback form available on the HRA website: http://www.hra.nhs.uk/about-the-hra/governance/quality-assurance/
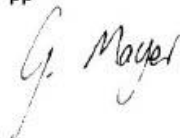
HRA Training

We are pleased to welcome researchers and R&D staff at our training days – see details at http://www.hra.nhs.uk/hra-training/

15/YH/0246	Please quote this number on all correspondence

With the Committee's best wishes for the success of this project.

Yours sincerely
pp

G. Mayes

Dr Janet Holt
Chair

E-mail: nrescommittee.yorkandhumber-bradfordleeds@nhs.net

Enclosures:	List of names and professions of members who were present at the meeting and those who submitted written comments
	"After ethical review – guidance for researchers"
Copy to:	Mr Derek Norfolk – R&D Dept, Leeds Teaching Hospitals NHS Trust
	Claire Skinner – R&D Dept, University of Leeds

NRES Committee Yorkshire & The Humber - Bradford Leeds

Attendance at Committee meeting on 19 May 2015

Committee Members:

Name	Profession	Present	Notes
Mr Sharif Al-Ghazal	Consultant Plastic Surgeon	Yes	
Professor Diana Anderson	Professor of Biomedical Sciences	No	
Miss Jennifer Blaikie	Research Administrator	Yes	(Co-opted member from Leeds East REC)
Ms Anne Davies (Vice Chair)	Clinical Research Consultant	Yes	
Mr David Dawson	Consultant Anaesthetist	Yes	
Dr Stan Dobrzanski	Clinical Services Manager Pharmacy	Yes	
Mrs Jenny Foggin	Senior Governance & Corporate Affairs Officer	Yes	
Ms Rebecca Forster	Research Fellow	No	
Mr Simon Gelsthorpe	Head of Psychological Therapies	Yes	
Dr Janet Holt (Chair)	Senior Lecturer	Yes	
Dr Kirste Mellish	Research Programme Manager	No	
Mr Andrew Scally	Senior Lecturer	Yes	
Dr Christopher Skidmore (Alternative Vice Chair)	Retired University Lecturer	No	
Mr Robert Thompson	Lay Member	No	

Also in attendance:

Name	Position (or reason for attending)
Ms Gillian Mayer	REC Manager

A Research Ethics Committee established by the Health Research Authority